The University of Nottingham

UNITED KINGDOM · CHINA · MALAYSIA

Faculty of Engineering

Department of Architecture and Built Environment

Integrated Hybrid Ventilative Cooling Technology for Residential Buildings in Tropical Savannah Climate

Eso Olamide Folakemi,

(B.Tech, M.Tech)

Thesis submitted in partial fulfilment of the requirements for the award of the degree of Doctorate of Philosophy in Sustainable Energy Technology

September 2024

Abstract

The tropical savannah climate, particularly in Sub-Saharan Africa, is characterised by daytime temperatures as high as 35–37°C and generally low wind speeds of 2–4 m/s. This complicates indoor thermal comfort without mechanical cooling. As a result, energy demand for residential air conditioning and ventilation increases. Meanwhile, residential air conditioning contributes significantly to greenhouse gas emissions.

The study presents the design, validation, and performance analysis of an Encapsulated Phase Change Material Hybrid solar fan assisted Multi-directional Windcatcher system. The study aimed to assess effective cooling, and temperature stabilisation performance without compromising on acceptable ventilation in residential buildings within tropical savannah climates, specifically in Sub-Saharan Africa. The novelty of this research lies in the vertical integration of encapsulated PCM tubes within the windcatcher's airstreams. The system also combines with hybrid ventilation through fan-assisted airflow during low wind speeds. The fan provides an additional 370L/s airflow. This ensured consistent ventilation and addressed the limitations of passive windcatcher systems, such as inconsistent airflow.

The optimal passive cooling material selected for this study was the RT28HC paraffin PCM, with a melting point of 27–29°C. It was chosen for its efficiency in regulating indoor temperatures without the energy-related costs of air conditioning systems. Encapsulating the PCM in tubes (EPCM-T) ensured consistent heat transfer, which improved the thermal storage capability. The study employed Computational Fluid Dynamics (CFD) simulations to evaluate the system's performance under different climatic conditions. Simulations explored various EPCM tube configurations and their effects on airflow, cooling, and thermal storage efficiency.

The findings have indicated that the EPCM-HMW system can reduce supply air temperature by up to 3.15°C (9% temperature reduction) compared to conventional windcatcher systems without PCM. Supply air dropped to 305 K (31.85 °C) in the best-case scenario. This occurred when outdoor air temperature was as high as 308 K (35 °C). This temperature drop was essential for maintaining indoor comfort without mechanical cooling, particularly during peak heat when outdoor air is or exceeds 308 K (35 °C). The study findings also showed that the air supply offered by the system achieved temperature stabilisation for approximately 5 hours. However, cooling (indoor temperature reduction) continued for 7 hours. The ventilation performance, although lower than that of a conventional windcatcher, was still within acceptable thermal comfort limits of 140.86 L/s air flow rate, sufficient for 14 to 17 occupants.

The EPCM-HMW system consumed 95% less energy than a ductless split AC unit, equating to 20 times lower energy consumption. Annual energy savings were estimated at $2,707.2 (£2,152), with net savings over 20 years amounting to $23,690.71 (£19,070.81). The system achieved a payback period of approximately 8.24 years and an ROI of 106.2%.

This research demonstrates the significant long-term financial benefits of adopting the EPCM-HMW system. It also advances windcatcher technology by integrating thermal energy storage to enhance cooling efficiency and temperature stabilisation. The outcomes of this research would be beneficial to broader applications of PCM-based hybrid cooling systems in tropical savannah climates. The study offers a practical, low-energy solution for residential ventilative cooling in high-temperature and low wind regions with limited energy infrastructure. The research also suggests future work in optimising PCM encapsulation techniques and conducting further field testing to further validate the system's real-world performance.

Acknowledgements

First and foremost, I express my gratitude to Almighty God, to whom I attribute my life and achievements.

I am truly blessed to have parents who deeply value educational excellence, hard work, and resilience—values that have guided me throughout this study. My entire family has been an unwavering pillar of support throughout this journey. I thank my dad, mum, Dapo, Dieko, Kunle, Julie, Stephen, Lorin, Jimi, and Zuri. Their consistent encouragement, prayers, meticulous review of my drafts, and insightful discussions were invaluable in propelling me forward.

I also extend my sincere appreciation to my primary supervisor, **Prof. Jo Darkwa**, and my secondary supervisor, **Dr. John Calautit**. Their profound subject knowledge, unwavering commitment to research ethics and quality and their continuous supervision support significantly influenced the development of this thesis. Special thanks also go to my internal assessor, Dr. Siddig Omer, whose insightful feedback and recommendations during yearly reviews have been instrumental in shaping my work.

My gratitude extends to my colleagues in the Department of Architecture and Built Environment and the Faculty of Engineering. Sharing the PhD journey with you has been enriching. Special thanks to my friends Murtaza Mohammad, Meruyert Sovetova, Olutola Adekeye, Sara Mohammed, Mahmoud Mohamed, Aminu Bena, Weijie Xu, Salah

Almazmumi, Wuzia Zhang, Anti Kur, Tomilola Kayode-Adedeji, Gertrude Kadzuwa, Ejiro Matilda Ikoko, and Sheriff Mohamed. To my fellow Commonwealth scholars in the UK, our research discussions were always motivating. A special thanks to Bolaji Okunola who happened to be the first person who believed I could do a PhD even when it had never crossed my mind!

Finally, I would like to express my gratitude to my mentors, including Dr. Liberty Mgbanyi and Dr. Deji Aremu, among others. Their patience in listening to my research updates and providing feedback from a non-specialist perspective has consistently added valuable insights to my work, enhancing its quality.

Thank you all for your unwavering support and encouragement.

Table of Contents

List of figures

List of tables

List of publications

Peer review Journals:

Olamide Eso, Jo Darkwa, John Calautit; **"Integrated Phase Change Materials (PCM) in a Hybrid Windcatcher Ventilation System"** Energies, 2024 (under review).

Conference Proceedings:

Olamide Eso, Jo Darkwa, John Calautit; **"Integrated Energy Storage Windcatcher Ventilation system"** - *presented as an oral presentation at the 18th Conference on Sustainable Development of Energy, Water and Environment systems (SDEWES 2023), Dubrovnik, Croatia on September 24-29, 2023.*

Olamide Eso, Jo Darkwa, John Calautit; **"Thermal Performance Study of Different Phase Change Material Arrangements within a hybrid Windcatcher"** – *presented as a poster presentation at the 18th Conference on Sustainable Development of Energy, Water and Environment systems (SDEWES 2023), Dubrovnik, Croatia on September 24-29, 2023.*

Olamide Eso, Jo Darkwa, John Calautit; ***"Numerical Study of Phase Change Material Nodal Arrangements in Multi-Directional Windcatcher"*** - *presented as oral presentation at the 20th International Conference on Sustainable Energy Technologies, Nottingham, UK on August 15-17, 2023.*

Olamide Eso, Jo Darkwa, John Calautit; **"Integrated Phase Change Material Windcatcher System for Hybrid Cooling and Ventilation in Tropical Buildings"** - *Conference paper presented as an oral presentation at the 2nd World Energy Storage Conference (WESC 2022), Istanbul Turkey on December 18-21, 2022.*

Nomenclature

Q	absorbed heat in a room per unit area surface
E_{AC}	AC energy consumption
$t_{operational}$	AC operation hours per day
dy_{year}	AC operation days per year
p	air pressure
T	air temperature
V	air velocity
C_p	CFD model predictions
$\bar{C}$	data set average
T_d	daytime room temperature
k_{eff}	effective heat conductivity
C_{elec}	electricity cost
$C_{1\varepsilon}$	empirical model constant
$C_{2\varepsilon}$	empirical model constant
$C_{3\varepsilon}$	empirical model constant
$E_{EPCM-HMW}$	energy consumption of the EPCM-HMW system
T_e	exhaust air temperature
V_e	exhaust air velocity
C_o	experiment observations
P_e	exhaust air pressure
h_i	fluid-specific enthalpy
ds	future discounted cost
$C_{elec,t}$	future electricity cost
h^{-1}	per hour
$P_{solarfan}$	power rating solar ventilation fan
T_{inlet}	inlet air temperature
V_{angle}	inlet wind angle
V_{inlet}	inlet wind speed
j_i	mass flux

R_i	net rate of production of species
T_n	nighttime room temperature
$T_{m,r}$	optimal PCM melting temperature.
T_{out}	outdoor temperature
t_c	PCM charging time.
t_d	PCM discharging time.
f_l	PCM liquid fraction
T_{pcm}	PCM temperature
ΔT_{pcm}	PCM temperature difference
T_s	PCM temperature at solid
D%	percentage deviation at every data point
P	point
RC	Radiative cooling
S_i	rate of creating species by addition
$\bar{T}_r$	set average room temperature.
S	simulation coefficient
V_{supply}	supply air velocity
i	species
e	specific internal energy
P_{supply}	supply air pressure
T_{supply}	supply air temperature
V_{supply}	supply air velocity
ΔT	temperature difference
t	time
G_k	TKE source caused by average velocity gradient.
G_b	TKE source based on buoyancy force.
T_{tube}	tube temperature
α_k	turbulent Prandtl constant
α_ε	turbulent Prandtl constant
τ_t	turbulence stress divergence due to the velocity fluctuations by the auxiliary stresses

Greek symbols

ρ	density of air
u	fluid velocity in the model
$\vec{J}_i$	fusion flux of species
g	gravitational acceleration
μ	molecular dynamic viscosity
β	thermal expansion coefficient

Abbreviations

AC	air conditioning
Case 1	EPCM-HMW system model when integrated with 48 EPCM-Ts placed within the supply airstream.
Case 2	EPCM-HMW system model when integrated with 48 EPCM-Ts placed within all four airstreams.
CFD	computational fluid dynamics
EPCM-HMW	encapsulated PCM integrated hybrid multi-directional windcatcher
EPCM-T	encapsulated phase change material tubes
GHG	global greenhouse gas
MVS	mechanical ventilation systems
PCM	phase change material
SBS	sick building syndrome
TES	thermal energy storage

Subscript

c	charging time
d	discharging time
l	liquid
s	solid
$supply$	supply
r	room

Chapter 1

1 Introduction

1.1 Research Background

Global warming stands out as one of the most urgent global challenges. This has led to erratic weather patterns and exceptionally elevated temperatures. Historical data depict a steady annual 0.2°C increase in global temperatures from 1951 to date, while a temperature increase of 89% was observed during the year 2021. The average temperature increased by about 1.09°C from 1951 to 2021 [1], [2], [3]. In the Intergovernmental Panel on Climate Change (IPCC) report of 2022 [4], it is stated that buildings emitted 12 GtCO2-eq in 2019. Buildings alone contributed 21% towards the global GHG emissions. Additionally, 50% of energy demand is from residential, while 32% is from non-residential buildings. This statistics highlight the significant role of energy emissions and consumption by buildings on global warming.

Residential buildings which consume more energy, are more impactful to global warming compared to commercial buildings [5]. As it stands, residential cooling constitutes the largest portion of energy consumption globally. According to the study by Santamouris et al. [6], about 55% of the 1.25 PWH of energy used in buildings globally [7] is attributed to residential cooling alone while the rest is used in commercial buildings.

In a typical hot climate residential building, 54% of the building's energy is used mainly for space cooling, primarily through air conditioning (AC) [8]. Since regions with a hot climate often face more challenging outdoor conditions such as high temperatures and humidity levels, there is a higher demand for space cooling. In some hot climates like the tropical savannah climate of sub-Saharan Africa, outdoor temperatures can soar to a peak of 35-37°C [9], [10], in addition to wind speeds as low as 2m/s [11], [12]. These extreme weather conditions often lead to uncomfortable

indoor environments that need cooling and ventilation. Hence, there is a common trend to rely on conventional AC and mechanical ventilation (MV) systems to meet this need. Still, only 5.6% of the population in sub-Saharan Africa has access to any form of indoor cooling [13].

Randazzo et al. [14] illustrated that in residential buildings with AC, energy use can be up to 35% - 42% higher than in buildings without such systems. An approximate 70% of these conventional AC and MV systems are powered by energy derived from fossil fuels, which emit greenhouse gases into the atmosphere. It is said that the estimated amount of such emitted gases from AC and MV systems stands at about double the amount produced from the whole aviation industry [15]. The environmental impact and high energy consumption of conventional cooling and ventilation systems underscore the importance of developing sustainable and cost-effective energy solutions. The development of eco-friendly and conventional AC systems with improved energy efficiency is the focus of ongoing research [16].

Another effective way of developing energy-efficient AC or MV systems includes the integration of phase change material with thermal energy storage (TES). The purpose is to increase efficiency in waste heat dissipation. As a result, a significant amount of energy saving is achieved. In this regard, Real et al. [17] showed that an MV system achieved energy saving of 18.97% upon integration with encapsulated-PCM-based TES. However, despite the energy savings and efficiency benefits of utilising PCM, AC and MV systems' energy consumption and emissions remain high.

Implementing passive cooling and ventilation systems can drastically reduce energy consumption and emissions while maintaining the desired indoor comfort levels. Such systems can potentially replace MV and AC operations in buildings. Many passive cooling systems have emerged as viable solutions for reducing energy use and emissions without a trade-

off in the effective indoor cooling in buildings. Examples of such systems include evaporative cooling, radiative cooling, and ground cooling.

The concerns of environmentalists and researchers go beyond the negative environmental impact and high energy consumption of MV and AC use in buildings. Recent studies indicate that the process of recirculating indoor air in these systems can contribute to the rapid spread of aerosol and airborne diseases including COVID-19, flu, and cold inside a building [18]. Indoor air can become 2 to 5 times more polluted than outdoor air due to the continuous re-circulation of stale air in an enclosed space [19]. According to Sundell et al. [20], a space with less than 0.5 ventilation rate per hour (h^{-1}) could increase the risk of child allergies and sick-building syndrome (SBS) symptoms in warm climates. All these findings suggest that the exchange of air between outdoor and indoor rather than re-circulation of indoor air improves overall indoor air quality (IAQ) [21]. An improved IAQ reduces the occurrence of SBS symptoms and the spread of airborne diseases inside buildings [22]. Moreover, studies show that optimising indoor-to-outdoor air exchange through passive ventilation improves the neutral temperature inside a building for improved thermal comfort [23].

Windcatcher systems can be employed to further enhance indoor-outdoor air exchange in buildings located in regions with enormous energy needs such as sub-Saharan Africa. Windcatchers rely on local weather and microclimate conditions. Therefore, local conditions must be considered in the design of windcatchers. Windcatchers, which are typically installed on building roofs capture the prevailing wind through their vents by directing airflow into the building for natural ventilation [24]. This process relies on stack and buoyancy effects caused by the difference in indoor-outdoor air pressures and temperatures [25]. Studies indicate that windcatchers with multiple openings, such as multi-directional windcatchers, effectively provide ventilation in low-wind, hot climates [26]. These include tropical savanna climates of sub-Saharan

Africa, where wind speeds can reach as low as 2 to 4 m/s [11], [12]. The study conducted by Jafari et al. [27] on a symmetric four-sided multi-directional windcatcher that was enhanced with blades and crowns revealed a significant 16 % increase in air flow rate. The multi-directional windcatcher displayed a beneficial turbulence effect that optimised the flow induction in the system during low wind conditions.

a. Room ventilated with single vent opening (without windcatcher)

b. Room ventilated with multi-directional windcatcher
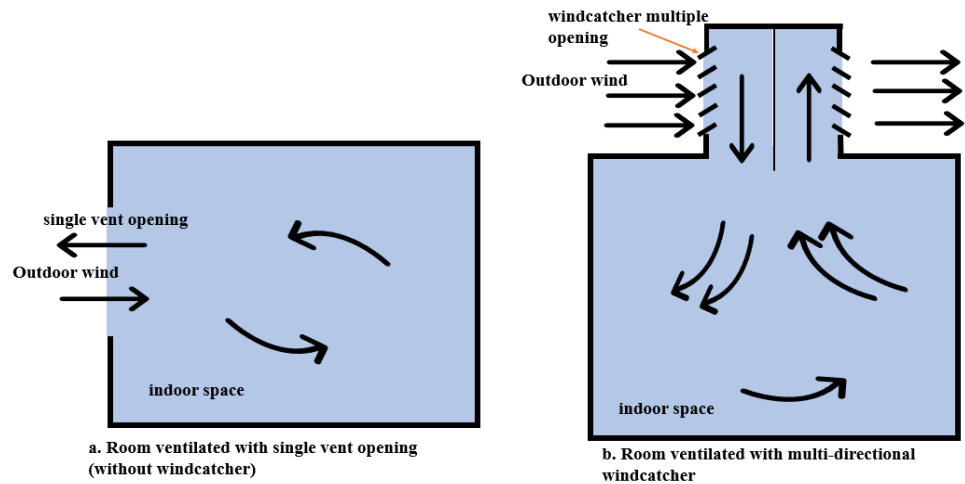
Figure 1.1 Contrast between the airflow patterns by a single window opening and a top-mounted multi-directional windcatcher

Multi-directional windcatchers also significantly enhance the efficiency of the indoor-air exchange. Figure 1.1 illustrates the improvement in indoor airflow patterns when using a roof-mounted multi-directional windcatcher compared to a single-sided window. The design of vents in multiple directions is crucial to achieving the improvement in indoor air exchange. Studies by Sadeghi et al. [28] and Li et al. [29] showed that multi-directional windcatchers achieved a higher indoor air velocity of 0.33 - 0.39 m/s compared to equivalent single-sided windows in urban settings. In essence, the ventilation performance of buildings can be further enhanced with multi-directional windcatchers.

1.2 Statement of problem

Time-varying flows and irregularity in outdoor air velocities affect the consistency of indoor ventilation supplied by multi-directional windcatchers [30]. According to Zhang et al. [31], opting for hybrid

ventilation in buildings, instead of relying solely on passive ventilation, can effectively reduce the airflow inconsistencies in many passive ventilation systems. Although commercial windcatchers exists, fan-integrated windcatcher operation still requires further understanding [32]. The significance of combining fans with windcatchers for hybrid ventilation to achieve consistent airflow in the absence of outdoor wind was further emphasised in the studies by Sangdeh and Nasrollahi [33] and Hughes et al. [34]. Although the existing windcatcher design shows satisfactory efficiency in ventilation, its implementation is impended, and its effectiveness is reduced in hot climates by high outdoor temperatures and temperature fluctuations. Therefore, design changes are necessary to improve the cooling performance and air temperature stabilisation of windcatchers in buildings located in hot climates.

A recent research work by Calautit et al. [35] was focused on improving windcatcher cooling performance. Passive cooling strategies such as heat pipes [36], evaporative cooling [37], solar chimneys [38], and radiative cooling [38] have been explored in previous studies to increase the limited cooling capacity of windcatchers. For example, Jafari et al. [37] showed that evaporative cooling can be incorporated in windcatchers to reduce interior space temperature by as much as 6-12°C. However, a high relative humidity in the supply air was observed which suggested that additional dehumidification is needed. The dehumidification of the windcatcher was addressed in a study performed by O'Connor et al. [39]. A novel electrically powered silica gel-coated desiccant rotary wheel was added to a multi-directional windcatcher. Although dehumidification was achieved, a significant amount of energy was required for the desiccant regeneration. In addition, the process raised the temperature of the air supply, which required additional energy to cool down. In regions with energy deficits like Sub-Saharan Africa, the increased consumption of energy by ancillary systems of a windcatcher limits its use. Furthermore, the climate of sub-Saharan Africa is

characterised by alternating periods of hot, dry, and humid weather conditions which lessens the need for dehumidification all year round.

Incorporating heat pipes into windcatchers was investigated in different types of [36], [40], [41]. A drop in the air temperature from 8.6K to 14.25K was achieved. Various heat pipe configurations with uni-directional (one-sided) windcatchers [42] or two-sided windcatchers [43] have been evaluated. All of them required additional cold-water storage. The cold-water storage tank acts as a heat sink for effective heat transfer. Although seamless, continuous water replacement of cold-water storage restricts the wider application in sub-Saharan Africa where there are areas with acute water shortages.

Improvements within the cooling and thermal storage capacity of windcatchers are necessary to achieve ideal temperature control, especially in the tropical savanna of sub-Saharan Africa with inconsistent outdoor temperatures. The daily outdoor temperatures can vary significantly from about 20 °C to 35 °C throughout the day [44]. Attempts to improve windcatcher cooling were made in various studies. However, the inability of windcatchers to stabilise air temperatures needs to be addressed to establish its use in sub-Saharan Africa.

TES technologies, such as PCMs are capable of lowering energy consumption and enhancing the thermal efficiency of windcatchers. For example, replacing heat pipes in windcatchers with PCMs can eliminate the need for additional cold-water storage and the continuous replacement of water in the storage. This is because PCM serves a dual function by acting as both a heat sink and a thermal storage material. In addition to stabilising air temperatures, there is the potential for implementing the PCM integrated system in a region with water shortage, such as sub-Saharan Africa [45].

PCMs are recognised for their substantial latent heat storage capacity [46] and isothermal behaviour with minimal variation in transition

temperature [47]. Hence, the integration of PCM with ventilation or free cooling systems better stabilises the temperature of incoming air in such systems [48]. During the PCM phase transition, the PCM absorbs heat from the heat transport fluid (air) and sustains a consistent PCM temperature while cooling the incoming air.

Integrating PCMs with windcatchers offers an efficient passive approach to cooling and enhancing TES [49]. The temperature of the supply air is reduced by the absorption ability of the PCM. Seidabadi et al. [49] and Abdo P. et al. [50] achieved substantial air temperature reductions of up to 9.85% or 2.78°C, respectively, in their windcatcher models by incorporating PCM. Although implementing PCMs to improve cooling and TES in windcatchers is viable, the low thermal conductivity of PCMs is still a limitation that impacts the effectiveness of the heat transfer process in PCMs. PCM encapsulation is a method that improves the low thermal conductivity limitation in PCMs [51], which also improves the heat transfer for efficient cooling and TES.

Some studies have also considered using forced ventilation or hybrid ventilation with the assistance of fans to enhance the heat transfer rates of PCM. In those studies, the continuous flow due to the fans enhanced the interaction of the air with the PCM. This further improved the charging and discharging rates of the PCM [50], [52]. However further investigation is required to understand the effect of encapsulated PCM in multi-directional windcatchers designed for hybrid ventilation. Additionally, it is imperative to determine how to maintain the cooling and TES performance of these systems without compromising ventilation capacity. Therefore, there is a need for further optimisation of the size and configurations of encapsulated PCMs within hybrid multi-directional windcatchers. Also, a configuration that will ensure efficient performance in daytime fluctuations of outdoor conditions under hot climates needs to be defined, such as in the tropical savannah climate of sub-Saharan Africa.

This study proposes the use of encapsulated PCMs to enhance the cooling and TES performance of hybrid multi-directional windcatchers in the hot, tropical savannah climate of sub-Saharan Africa.

1.3 The research aim

This study aims to develop a novel encapsulated PCM integrated hybrid multi-directional windcatcher (EPCM-HMW) system. The effectiveness of the PCM in cooling and stabilising air temperature without compromising the windcatcher's ventilation efficiency is assessed under the varied outdoor conditions of a sub-Saharan African tropical savannah climate.

1.4 The research objectives

The research aim was achieved through the following objectives:

1. Performed a comprehensive review of passive cooling and ventilation systems. Recent advancements in windcatcher systems, including windcatcher-integrated and hybrid systems, as well as TES technologies such as PCM were reviewed. System configurations, working principles, prospects, and limitations of integrated systems for enhancing ventilation, cooling, and thermal storage were reviewed.
2. Conceptualised and designed the EPCM-HMW system for use in the tropical savannah climate of sub-Saharan Africa.
3. Conducted preliminary geometric parametric numerical study on different E-PCMT samples to select the E-PCMT used in the EPCM-HMW system.
4. Developed numerical models of the EPCM-HMW system to investigate airflow (ventilation), temperature reduction (cooling), and stabilisation (thermal storage) based on different "encapsulated PCM tubes" (EPCM-T) arrangements under varied daytime conditions of the sub-Saharan African tropical savannah climate.

5. Validated models with experimental data from existing literature.
6. Conducted an economic feasibility of the EPCM-HMW System.

1.5 Novelty of research and contribution

The novelty of this research was the vertical integration of EPCM-T directly within the proposed integrated windcatcher's airstreams. Furthermore, the wall-mounted operation of the solar fan effectively reduced airflow resistance caused by the PCM within the windcatcher's airstreams while serving as a secondary airflow vent during low outdoor wind conditions. There was no prior research done which assessed the combined cooling, ventilation, and TES performance of hybrid multi-directional windcatchers with encapsulated PCM in the tropical savannah climate of sub-Saharan Africa.

This research has contributed to the advancement of integrated windcatcher technology by demonstrating the potential of incorporating TES to improve the cooling efficiency and temperature stabilisation in windcatchers. The modelling of the EPCM-HMW system presented practical ways for achieving a temperature reduction in indoor air temperature and the stabilisation of indoor air temperature. Consequently, the findings from this research have the potential to pave the way for the utilisation of PCM integrated hybrid windcatchers in the tropical savannah climate of sub-Saharan Africa and regions with similar climates. This study also expanded existing knowledge by providing valuable data on integrated hybrid windcatchers with PCM that can be used as a premise for future research endeavours.

1.6 Thesis structure

Chapter 2 presents the literature review, comprising two main sections.

The first section (Section A) provides an overview of passive cooling and ventilation systems and their performance limitations. It specifically

conducts an in-depth review of windcatcher systems. It emphasizes the potential enhancements to hybridise the ventilation and improve the cooling performance through integration with other systems. The review also identifies performance limitations in different climatic conditions. Furthermore, the section explores previous studies on hybrid windcatcher ventilation.

The second section (Section B) of this chapter provides an overview of TES and its classifications. Studies on TES performance in the context of integrating PCM TES in ventilation applications, with specific attention to windcatchers are also discussed. The chapter concludes by summarising gaps in the current literature.

Chapter 3 outlines the research approach adopted for this study, divided into two sections.

The first section (Section A) describes the proposed system: "Encapsulated PCM integrated hybrid multi-directional windcatcher" (EPCM-HMW), emphasising the technical characteristics of its components and the mechanism for operation.

The second section (Section B) details the methodology used to achieve the study's aims and objectives. It focuses on the CFD numerical modelling of the proposed EPCM-HMW system, including the E-PCMT geometric parametric numerical study. It specifies the software and theoretical models used to assess system performance. The chapter establishes the boundary conditions for analysing the system's ventilation (airflow), cooling (air temperature reduction), and thermal storage performance (air temperature stabilisation). It concludes by summarising key findings and addressing limitations in the CFD numerical approach used for the study.

Chapter 4 presents CFD results on airflow (ventilation), temperature reduction (cooling), and stabilisation (thermal storage) of the EPCM-

HMW system under different E-PCMT arrangements and varied daytime conditions typical of the sub-Saharan African tropical savannah climate. It also includes results for the preliminary geometric parametric study conducted on various E-PCMT samples to select the E-PCMT used in the EPCM-HMW system.

Chapter 5 presents the validation process of the CFD results in comparison to experimental data from the literature. An error analysis is conducted to substantiate the numerical findings of the current study.

Chapter 6 presents the economic feasibility of the EPCM-HMW system in comparison to traditional ACs, within the context of the selected climate.

Chapter 7 summarises key findings, acknowledges study limitations, and draws conclusions. This chapter also identifies achieved aims and objectives, the effects, and benefits of the integration of EPCM-T with hybrid windcatchers. The chapter also explores contributions to knowledge and potential areas where future research may be required.

References provide details for each of the sources cited in the work.

Chapter 2

2 Literature review

SECTION A:

2.1 Overview of passive cooling and ventilation systems

Passive cooling and ventilation systems are designed to utilise only natural forces to provide indoor comfort without active energy consumption [53], [54]. To differentiate between the two systems within buildings, passive cooling systems primarily reduce indoor temperatures [55] through natural processes such as convection, evaporation, and radiation [56]. In contrast, passive ventilation systems rely on wind and thermal buoyancy convective forces to facilitate indoor air exchange and circulation and promote natural airflow [57].

Buildings can benefit from the simultaneous use of passive cooling and passive ventilation systems, aiming to achieve optimal indoor environmental quality and thermal comfort. However, the perception of thermal comfort among building occupants varies depending on the climatic region and is subjectively assessed based on their level of satisfaction with the thermal environment relative to their expectations [58]. Therefore, the effectiveness of correctly combining the use of passive cooling and ventilation systems becomes crucial in lowering indoor temperatures and enhancing indoor air movement for indoor comfort.

For instance, in the tropical savannah climates of sub-Saharan Africa where the mean monthly temperatures can range from 24 °C to 36 °C [59] or occasionally exceed 40 °C on extremely hot days [60], in addition to the wind speeds that can be as low as 2 m/s [11], [12], the thermal comfort operative temperature perception of building occupants is slightly

higher, reaching up to 30 °C, according to Albatayneh et al.'s study [61]. This assumption is based on ASHRAE 55-2010 Standard, which recommends that indoor operative temperatures can fall within 80 % to 90 % acceptability limits, with a ±2 °C to 4 °C allowance on either side of the comfort limit as illustrated in Figure 2.1 [61].
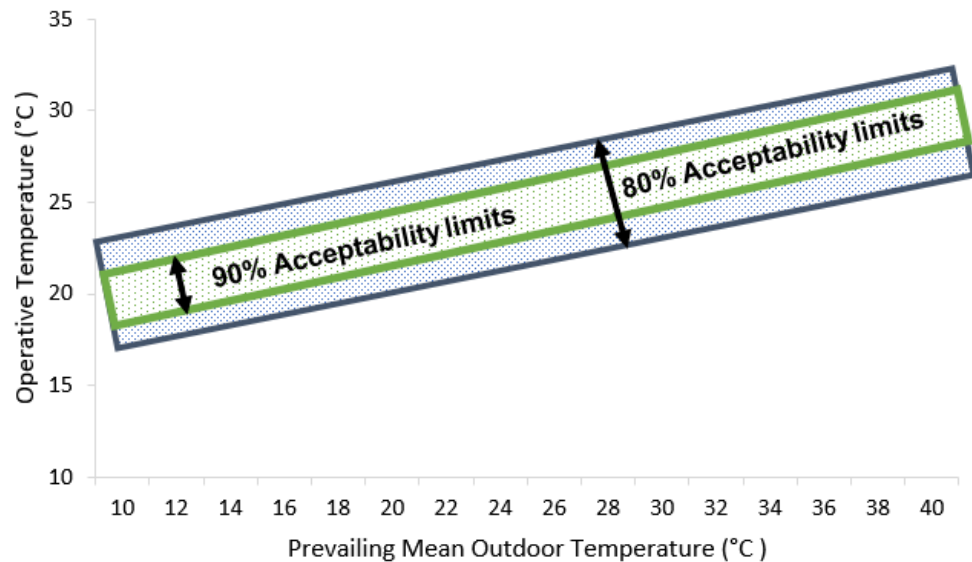
Figure 2.1. Indoor operative temperature's acceptability limits (90% and 80%) based on the prevailing mean outside temperature for tropical savannah climates [61].

The challenge remains to identify the appropriate passive cooling and ventilation system that can be adequately combined to achieve thermal comfort in such climates. This requires understanding the performance and limitations of different types of passive cooling and ventilation systems. Meanwhile, existing literature expands on several types of passive cooling and ventilation systems based on their heat transfer performance mechanisms.

2.1.1 Classification of passive cooling and ventilation systems

According to existing literature, most of the installable passive cooling and ventilation systems in buildings have been generally classified as heat dissipation systems [62], [63]. In contrast, thermal storage systems primarily operate based on heat modulation principles [64]. Particularly,

PCM-based TES systems modulate indoor heat to achieve simultaneous air temperature reduction and stabilisation, thereby shifting the cooling load from peak times to off-peak hours [65], [66]. The categorisation framework for passive cooling and ventilation systems is illustrated more explicitly in Figure 2.2, with in-depth discussions of studies on the systems' operations and performances in subsequent sections. Heat sinks play a significant role in the operation of these systems. For instance, systems that operate through heat dissipation, remove excess heat from a space into a heat sink with a lower temperature. A heat sink with a lower temperature can be ambient air, water, sky, or the ground.

Wind-driven ventilation systems like windcatchers, use air as a heat sink while evaporative cooling systems utilise air or water as the heat sink based on the classification framework of Bhamare et al. [62] and Samuel et al [67]. Conversely, ground cooling systems rely on the ground as the heat sink while radiative cooling systems utilise the sky as the heat sink. In the case of PCM-based TES systems, the PCM itself acts as the heat sink. This allows the PCM to be used in many passive cooling applications as well as a thermal storage material.
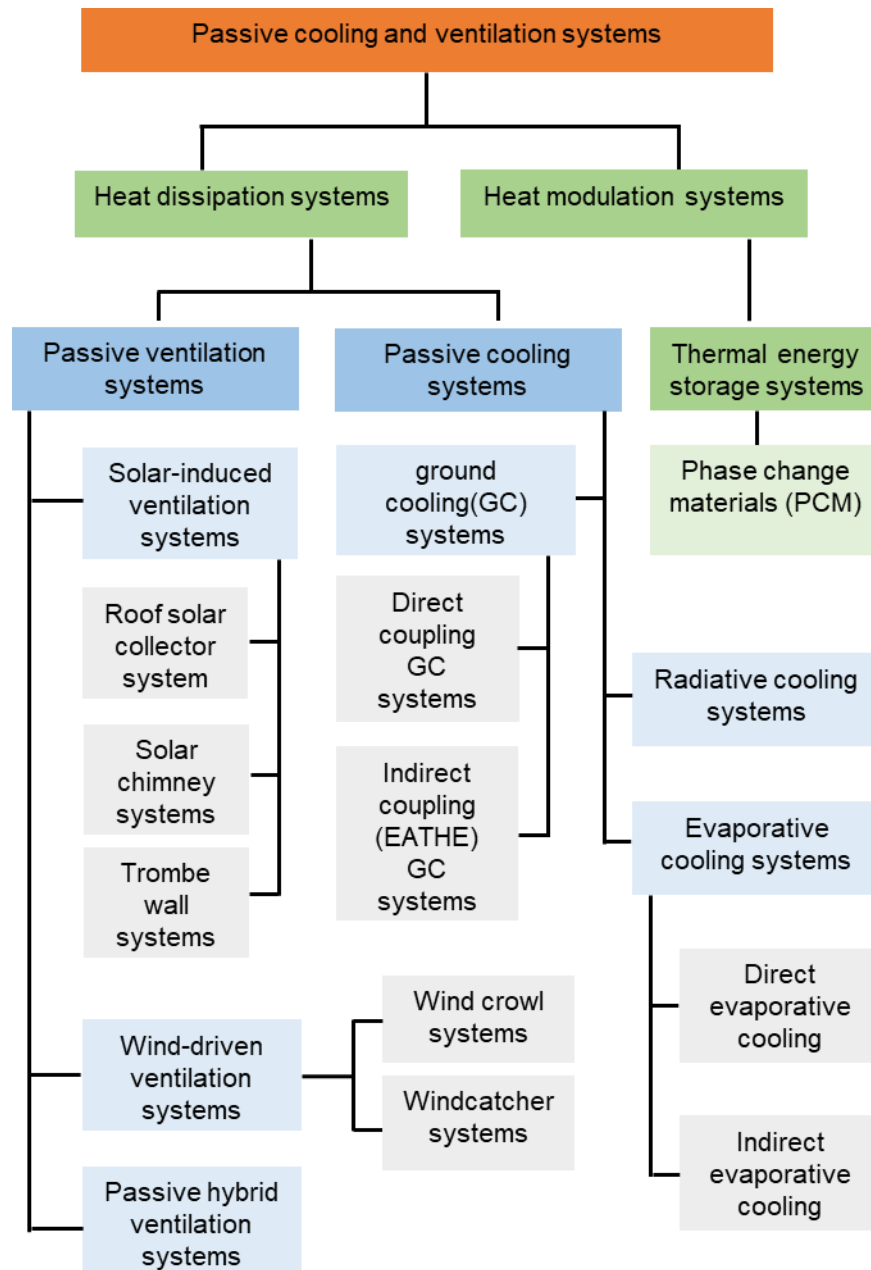
Figure 2.2. Categorisation of passive cooling and ventilation systems as heat dissipation and temperature modulation strategies

2.2 Passive cooling systems

Studies on various types of passive cooling systems including radiative cooling, evaporative cooling, and ground cooling, have been published. These studies have identified advantages and prospects based on the performance of each system.

2.2.1 Evaporative cooling system

Evaporative cooling systems can operate efficiently only under wet-bulb outdoor temperatures of < 25 °C [67]. There are two types of evaporative cooling systems: direct evaporative cooling (DEC) and indirect evaporative cooling (IEC) [68]. The evaporative cooling processes for different types of evaporative cooling systems are described through a psychometric chart in Figure 2.3 [69].

In direct evaporative cooling systems, a higher cooling capacity is offered by directly evaporating water into the air. One drawback of DEC system is its tendency to introduce excess moisture into the conditioned space. Consequently, these systems may not be suitable for use in sub-tropical climates like those found in tropical savannah regions of sub-Saharan Africa. Meanwhile, the IEC can overcome this additional humidity limitation. Its operation ensures that the incoming air does not come into direct contact with the water channel within the system. Instead, the air in the dry channel is utilised to condition the space [70].
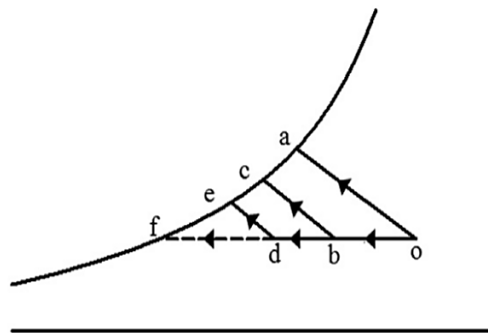
oa - Conventional evaporative cooling,   obc - DPEC with single state indirect cooling
ode - DPEC with two state indirect cooling, of   - Theoretical DPEC

DPEC- Dew point evaporative cooling

Figure 2.3. Different evaporative cooling processes in the psychometric chart [69]

According to Ma et al. [71], the finite volume method (FVM) and the finite difference method (FDM) CFD methods have been frequently used for investigating the performance of IEC. Previous theoretical and numerical

studies focused on the effect of outlet temperature and the efficiency of air humidity saturation [72], [73]. Bhamare et al. [62] performed studies on DEC that highlighted temperature reduction and energy savings outcomes. The resulting data suggested that the DEC achieved temperature reductions ranging from 3.5 to 14 °C. the study results also showed energy savings between 16 % and 75 %.

To decrease the humidity level in a DEC system, some researchers have proposed that the humid air inside the system should be passed through a desiccant membrane [74]. Apart from the obvious limitation of high indoor humidity caused by operating DEC in buildings, other concerns have been highlighted. For instance, a study by Hayden et al. [75] pointed out the disadvantages associated with evaporative cooling systems in buildings. Examples include increased risk of mosquito breeding, legionnaire bacteria and system corrosion. In contrast, a study conducted by Paschold et al. [76] concluded that evaporative coolers reduce particulate matter $PM_{2.5}$ by 10-40 % and PM_{10} by 50 %. The reduction in particulates indicated an improvement in indoor air pollution. However, DEC systems increase the humidity of indoor climate by adding moisture to the supply air. This poses as a problem in humid climates. Hence, DEC systems are less efficient in such climates.

Meanwhile, desiccant-based evaporative cooling systems provide an opportunity to enhance the dehumidification of incoming air. This can be an alternative system to mitigate the high humidity limitation of DEC in humid climates. Heidari et al. [77] proposed a novel solar-assisted desiccant-based evaporative cooling and water production system, illustrated in the block diagram in Figure 2.4.
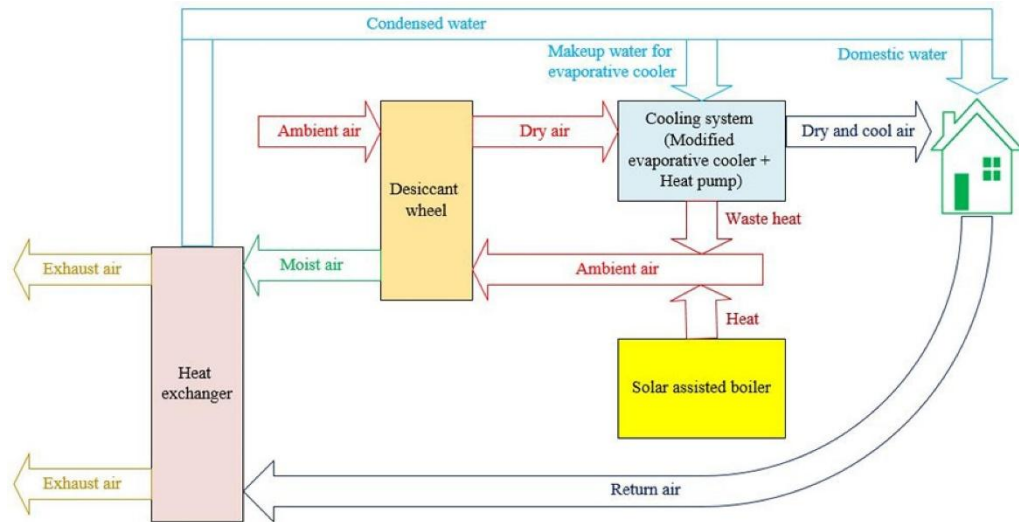
Figure 2.4. Block diagram showing the working mechanism of the solar-assisted desiccant-based evaporative cooling and water production system [77].

The system offered an additional advantage of moisture harvesting moisture. This served as makeup water for the evaporative cooler. However, there were certain drawbacks in its performance. This is related with system control difficulties and high energy consumption for desiccant regeneration. Additional limitations of the system included excessive water consumption by the evaporative cooler (up to 296 litres) and poor dynamic system performance. These factors led to a limited reduction in CO_2 emissions, at savings of only 18.71% [77].

A recent work by Aili et al. [78] deduced that radiative cooling outperforms the evaporative coolers, especially in high humidity and/or lower temperatures conditions. A comparative analysis between passive radiant cooling and evaporative coolers under similar conditions was also conducted in the study. This was to assess the impact of the relative humidity, convection, and outdoor temperatures on the performance of both systems. Results showed that the measured sub-ambient temperatures achieved by the evaporative cooler was -15 °C under conditions of low relative humidity of 13 % and a high ambient temperature of 26 °C. In contrast, the radiative cooling achieved sub-

ambient temperatures of -11.5 °C under a slightly higher relative humidity of 32 % and a slightly lower ambient temperature of 17 °C.

Additionally, Katramiz et al. [79] studied a hybrid crossflow dew-point indirect evaporative cooling (DPIEC) system that was equipped with a closed-cycle air-water harvesting (AWH) system, combined with radiative cooling (RC). The system operated in two modes: (a) as a DPIEC based on a combined operation with AWH and RC, and (b) as a standalone RC system, illustrated in Figure 2.5 (a) and (b).
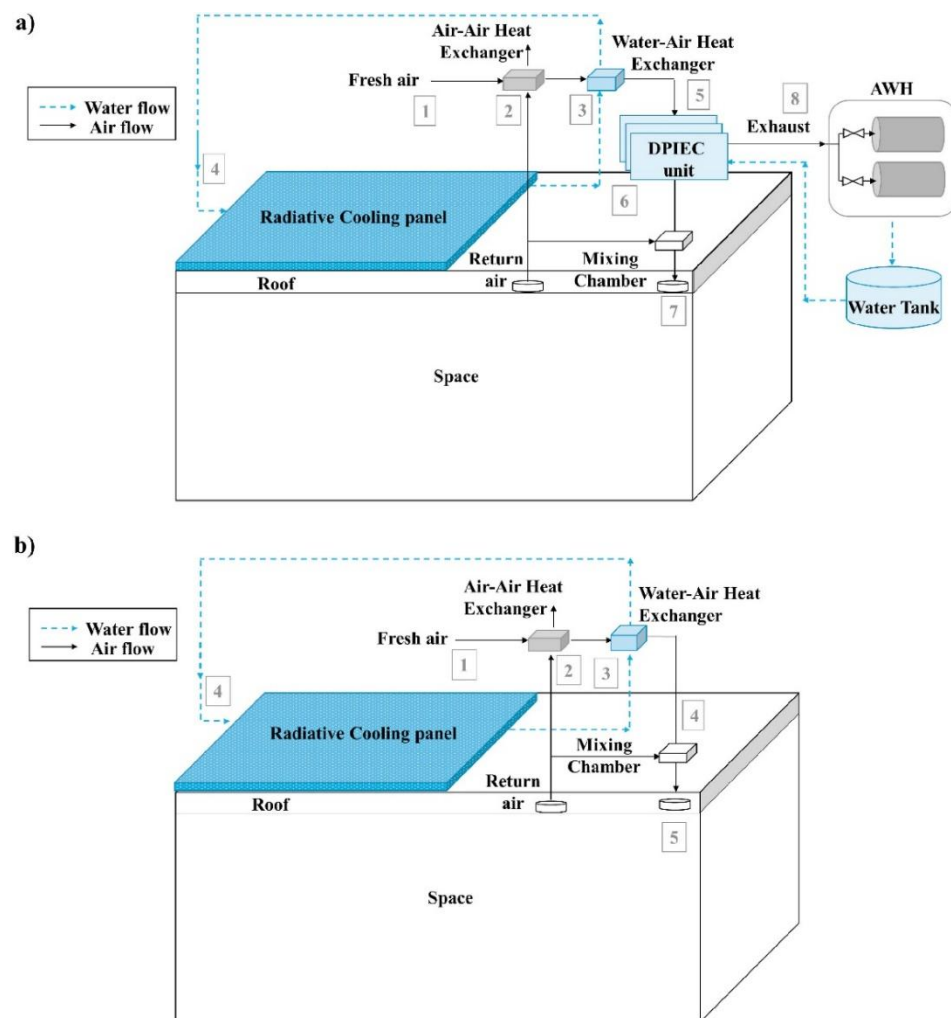
Figure 2.5. (a) RC with DPIEC and AWH operation mode; (b) RC-only operation mode [79].

The study compared the impact and performance of the RC in the hybrid system with a standalone DPIEC system under the hot and dry weather

conditions of Kuwait. The RC component met nighttime indoor cooling requirements. But the DPIEC allowed for pre-cooling of indoor air to fulfil daytime cooling needs, especially when outdoor temperatures exceeded 45 °C. Based on low-grade thermal energy usage, the AWH system regenerated the domestic water for the building.

The results demonstrated a 44.2% reduction in water consumption and 53.4% energy savings. These were attributed to the inclusion of radiative cooling in the hybrid system. The study also showed that there were cooling performance limitations in the hybrid DPIEC system when relative humidity exceeded 60%. This increased humidity also triggered a reduction in the performance of the radiative cooling system under these conditions. It compensates for performance if the system is operated under less dusty conditions. That applies to even outdoor operating conditions with high relative humidity. Even though it is widely used in residential buildings in hot climates, evaporative cooling is seen to have some critical limitations as far as its performance is concerned, at least in areas where there is higher humidity. It is indicated from literature that radiative cooling has been researched more for hot and humid climate conditions compared to evaporative cooling.

2.2.2 Radiative cooling system

Studies have shown that radiative cooling (RC) systems achieve cooling through heat loss and gains by conduction and radiation [80]. These systems operate based on radiation. This occurs as a result of the emission of energy, known as blackbody or thermal radiation. The exposed surface in the RC absorbs radiation energy from the sun and releases this radiation periodically. Essentially, electromagnetic waves are emitted when the temperature of the surface body is above absolute zero [81]. This is aided by an emitter installed inside an insulated transparent frame which also prevents convection heat loss. Generally,

the net heat transfer from the radiative surface defines the systems' cooling power [82].

RC systems' operation is governed by Stefan-Boltzmann law which defines thermal radiation as proportional to the fourth power of the absolute temperature of the body [83]. Emitted radiation from the atmosphere occurs at around 4 μm. The dominant solar radiation wavelength is shorter than 2.5 μm [84].

Typically, hotter bodies produce smaller peak wavelengths and sharper curves, with most of the emitted energy not falling within the visible light spectrum [83]. Figure 2.6 clearly illustrates Planck's law of blackbody radiation graph, which highlights emissive intensity against different wavelength spectrums.
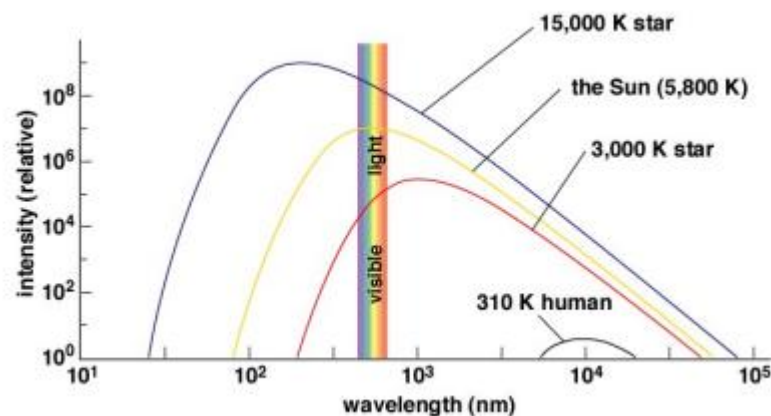
Figure 2.6. Thermal radiation emitted by several reference bodies [15]

RC is generally divided into two main categories: nocturnal RC and radiant cooling systems [85]. As highlighted in Panchabikesan et al.'s review [85], radiant cooling requires a continuous flow of cold water between 14 – 17 °C through the pipes to remove heat via heat transfer. This poses a disadvantage in areas where water is scarce. Additionally, the study identified that climates with high humidity present the lowest cooling potential (127 W m^{-2}) for nocturnal radiative cooling. Moreover, the radiative heat exchange rate in nocturnal RC performance reduces

when there is a high content of humidity and CO_2 in the supply air [86]. Accordingly, the radiative heat transfer rate in nocturnal RC is higher than the sky temperature (T_{sky}) in humid climates. As a result, the cooling performance efficiency of the RC is reduced.

For example, Zeyghami et al. [84], in their review of several aspects of clear-sky radiative cooling, have identified climatic conditions as a major factor affecting RC performance. On the other hand, the major drawback with the RC systems is that cool air cannot be stored by such systems, especially in hot climates wherein daytime temperature undergoes fluctuation. Suhendri et al. [80] reviewed the application of radiative cooling in buildings and explored some strategies of improvement from past studies. These conclusions showed that the cooling power of RC systems increase in when integrated with renewable energy systems. Improvements in insulation can reduce ambient temperature by up to 37 °C in a 24-hour cycle for diurnal radiative cooling. Additionally, design improvements in nanoparticle-based emitters can achieve sensible heat reduction up to 35 °C in the ambient temperature. The emission spectrum can be extended to 10 μm for the case of high-emissivity surfaces, like highly emissive paints. This provides a better enhancement in cooling [87]. Recently, Saber et al. [88] reviewed several previous performance studies of different radiative cooling systems, including radiant cooling panels (RCP) depicted in Figure 2.7, passive chilled beams (PCB) presented in Figure 2.8, and radiant slab cooling (RSC) displayed in Figure 2.9. The authors reviewed the cooling performances of these systems integrated into various mechanical cooling systems under hot and humid climate conditions. This review confirmed that such hybrid systems can reduce air temperatures as high as up to 25 °C. However, there was a disadvantage identified in the fact that pre-dehumidification with pre-ventilation was necessary as long as one hour prior to the operation of the radiant cooling panels. This is a major operational limitation in climates where humidity levels are higher. This can also result in increased energy consumption. Pre-dehumidification efforts may

also tend to raise the temperature of the incoming air, increasing the cooling load requirement thereafter. The major limitation of RC systems is that they cannot satisfactorily attain optimal daytime cooling, particularly when the intensity of solar radiation surpasses the system's cooling effect.
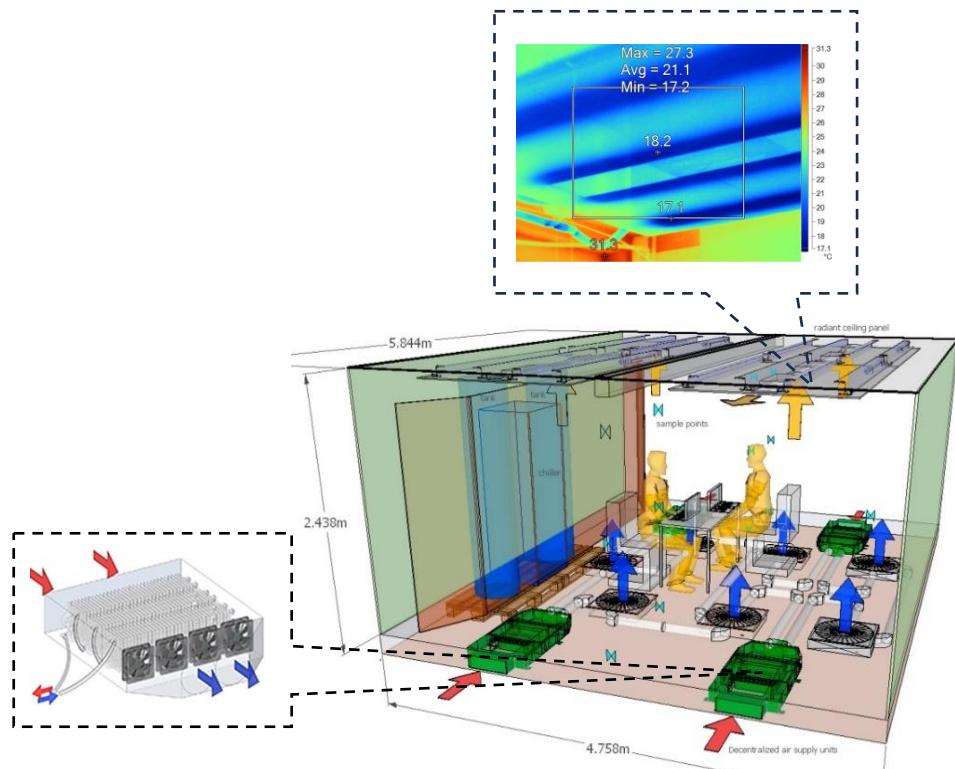
Figure 2.7. Combined decentralised dedicated outdoor air system and radiant cooling system (DDOAS-RCP) installed in BubbleZERO test bed building [89]
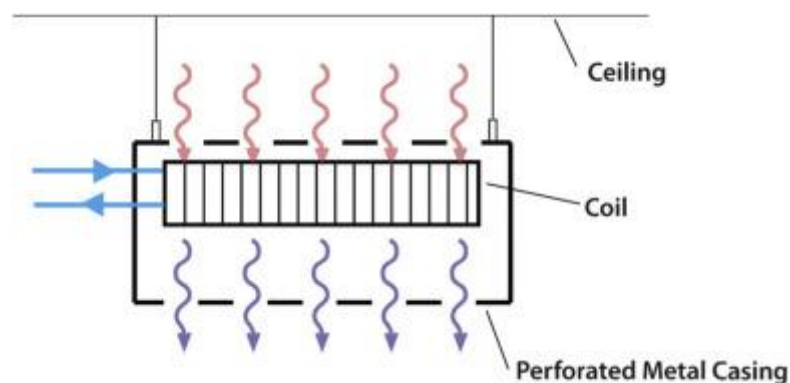
Figure 2.8. The operational mode of a passive chilled beam (PCB) [90]
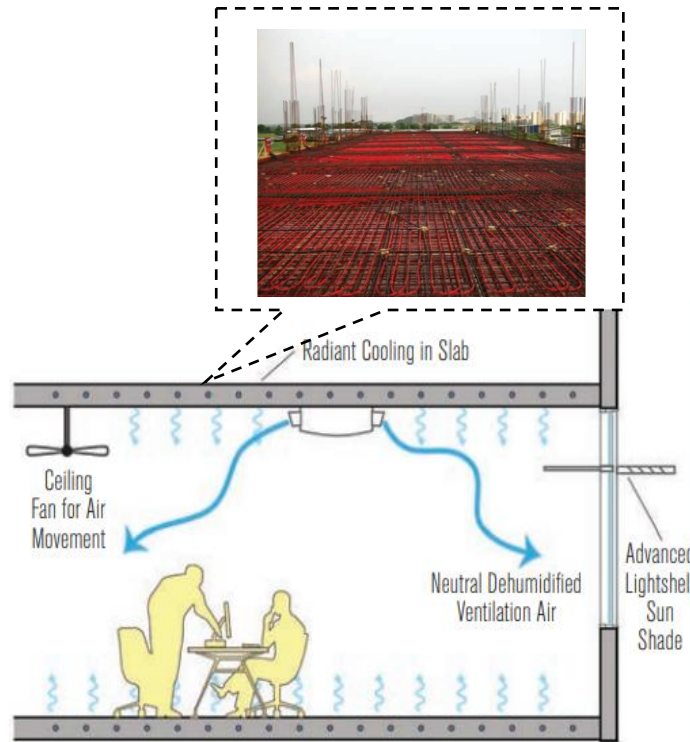
Figure 2.9. Schematic diagram of radiant slab cooling (RSC) building installation indicating its combined operation with VAV system assisted with ceiling fans [91]

According to the study by Santamouris [92], it was also noted that the radiant cooling capacity during nocturnal cooling cannot exceed 150 W/m². During hot humid climates, the net radiant heat loss is even lower at about 40-50 W/m², according to Givoni's study [93]. This is in contrast to the higher values of about 70 W/m² provided in hot arid climates. It is therefore evident that radiative cooling performs better in low humidity-level climates. Notwithstanding, the intermittency of cooling, influenced by changes in sky conditions, significantly impacts performance despite the outdoor conditions.

2.2.3 Ground cooling (geothermal) system

Ground cooling systems operate differently from radiative cooling systems. In ground cooling, heat transfer occurs underground rather than outdoors [94]. This allows it to overcome the intermittent cooling performance associated with radiative cooling. The more stable

underground temperature of the earth helps to minimise fluctuations in air temperature [95]. Moreover, research indicates that ground cooling systems do not always require integration with mechanical cooling systems, unlike radiative cooling systems. Ground cooling systems can function independently as the sole cooling system in buildings. However, previous studies have mainly focused on their application in commercial and office buildings rather than residential buildings [96].

As indicated in existing literature, ground cooling systems can be categorised as either direct or indirect [97]. According to Arghand [96], in direct ground cooling, only the ground is used as a cooling source. However, both direct and indirect ground cooling systems provide indoor comfort by connecting earth pipes underground with a building, allowing continuous airflow into the structure. A significant advantage of these systems is their ability to maintain a consistent indoor temperature by mitigating the temperature fluctuations of the supply air.
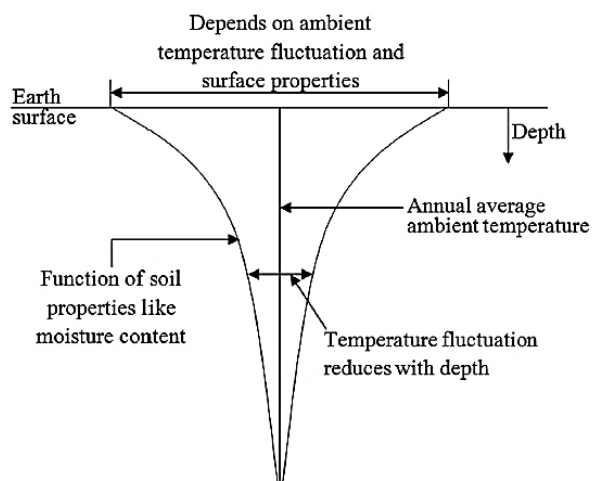
Figure 2.10. Earth's temperature fluctuation by depth [98]

Figure 2.10 illustrates that the earth's temperature fluctuation decreases with depth and becomes negligible at a depth of 4 m into the earth [98]. Existing ground cooling systems' thermal performance studies have been conducted using numerical [99], [100]; experimental [101] or both

methods [102], [103]. The performance of ground cooling systems was presented numerically by Hollmuller et al. [104] using equation 2.1. The equation indicates the direct proportionality of ground cooling system performance Q_a in relation to the undisturbed earth temperature. This direct proportionality is not dependent on time or outdoor air temperature.

$$Q_a = \dot{m}_a C_a (T_g - T_{ai}) \left(1 - e^{\frac{2\pi r h_{gf} L}{m_a C_a}} \right) \qquad \textit{Equation 2.1}$$

Furthermore, a pioneer study carried out by Wijk et al. [105] suggested that underground earth pipes in ground cooling systems should be placed at 1.5 – 3 m below the earth's surface. Over the years, the results derived from this study have led to the adoption of a standard depth for earth piping in several other ground cooling systems studies [106].

Gao et al. [107] investigated various ground cooling applications. However, a particular focus was on air-based ground heat exchanger systems integrated into building floors or walls. The study emphasised the use of both open and closed-loop ventilation modes when these exchangers are installed in the floor slab or within building walls.

(a) Open loop   (b) Close loop
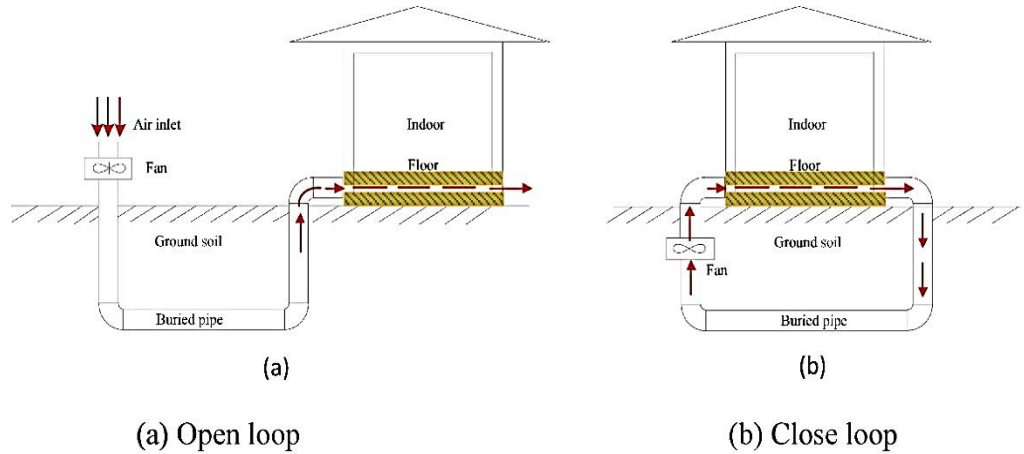
Figure 2.11. Air-based ground heat exchangers integration in building floor [107].

In the open-loop ventilation mode of the air-based ground heat exchanger (GHE) system installed on the floor (Figure 2.11), fresh air is precooled

and supplied directly to the hollow core slabs for indoor cooling. Alternatively, the system can operate in a closed-loop ventilation mode. In this mode, the air is recycled and resupplied into the ventilation space. However, when air-based ground heat exchangers are installed on the floor, meeting the cooling demand has proven to be difficult.

(a) Open loop   (b) Close loop
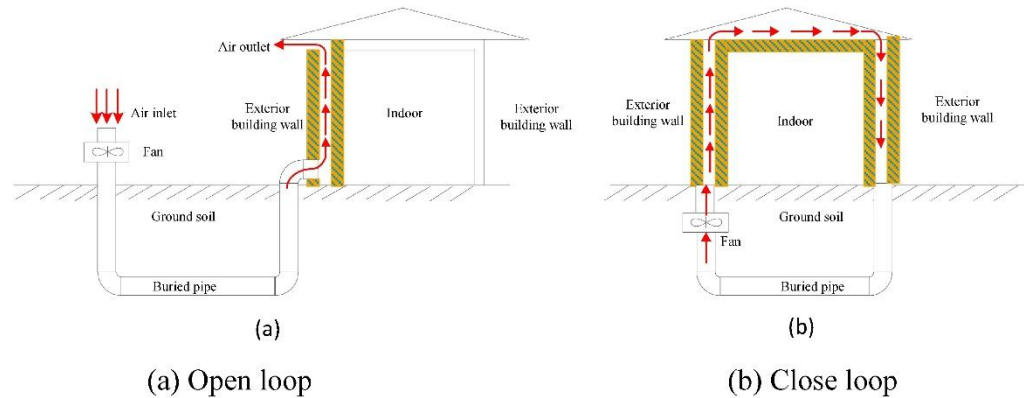
Figure 2.12. Air-based ground heat exchangers integration in building walls [107].

When air-based ground heat exchangers are installed within building walls, they can operate as either open-loop or closed-loop systems, similar to water-based GHEs. The cooled air circulates through a ventilated passage as illustrated in Figure 2.12.

Gao et al. [107] pointed out that most air-based ground heat exchangers cannot meet the average cooling demands of buildings. To make up for the weak points of this passive system, active heat pumps can be coupled with the passive system to boost the cold air circulation to increase the cooling effect. In this case, extra heat pumps consume energy and defeat the energy passiveness of the ventilation system. It is also believed that when the earth's temperature near the earth pipe tunnel is high, the performance of the system reduces significantly [108]. Effective ground cooling occurs only when the underground temperature is lower than the ambient air temperature [97]. This phenomenon is a limitation to ground cooling implementation in extremely hot climates. According to Man et al.'s study [109], the use of additional heat

dissipaters can improve the system's performance under hot conditions. The nocturnal radiative cooling system served as an auxiliary heat dissipater. This achieved energy savings of 10.22% and lowered the cooling load of the building. However, with the increase in airflow of the system, the energy consumption of the heat pump increased. The only other drawback or issue pointed out in the study was the high installation cost of the systems. The ability of the system to provide ventilation, the cost of installation, and the energy usage of the heat pump create a very complex trade-off, thus placing a strong limitation on its use.

Another main challenge with ground cooling systems is the humidity buildup within the underground earth pipes when employed in hot humid climates. Uddin et al. [110] evaluated an earth-air heat ground heat exchanger cooling system to assess its thermal comfort performance. Results indicated a decrease in airflow resistance and a reduction in air temperature by 6 °C. However, in the hot and humid climate conditions of Bangladesh, relative humidity increased by an additional 10 % during the summer period. Passive cooling systems deployed in regions with high humidity should not worsen indoor humidity levels.

While passive cooling systems present both performance constraints and advantages, some of the limitations highlighted can be reduced through their integration with various other passive cooling systems. For instance, Gao et al. [107] highlighted that ground heat exchangers can be integrated with other cooling systems such as solar thermal collecting systems, evaporative cooling, and nocturnal RC to balance the cooling load gap that the ground heat exchangers cannot fill.

Although dehumidification may not be necessary in some hot climates, but both cooling and ventilation are still quite essential for indoor comfort. In addition to the passive cooling systems discussed, various other passive ventilation systems have been explored in existing literature, including Trombe walls, solar chimneys, and windcatchers.

2.3 Passive ventilation systems

Passive ventilation systems assist the exchange of indoor and outdoor air by introducing fresh outdoor air into the building while simultaneously expelling stale indoor air. In past studies, passive ventilation systems have been grouped based on three distinct airflow mechanisms [111]. These include thermal buoyancy ventilation systems, also known as solar-induced ventilation systems, wind-driven ventilation systems, and hybrid ventilation systems [112], [113].

But in this study, passive ventilation systems have been broadly categorised into only two main types: solar-induced ventilation systems and wind-driven ventilation systems. The various systems within this framework are outlined in Figure 2.1.

2.3.1 Solar-induced ventilation systems

Solar-induced ventilation systems are mainly buoyancy-driven based on air density differential. The buoyancy phenomenon is based on indoor-outdoor air temperature differential. According to Awbi's study [114], solar-induced ventilation systems include Trombe walls, solar chimneys, and roof solar collector systems. Monghasemi et al. [115] also referred to the similarities between Trombe walls and solar chimneys. The study related these identified similarities to the introduction of open cavities in both their configurations. Both Trombe wall and solar chimney systems use solar absorbers to capture solar radiation. The absorption of solar radiation creates air temperature differences, thereby inducing airflow to drive their ventilation performance. Once the absorber is heated up by solar radiation, an induced stack effect is created. The heated air, now less dense, rises. This less dense is then replaced by cooler and denser air. The airflow pattern in the systems vary with respect to the outdoor temperature in relation to the indoor temperature.

2.3.1.1 Solar chimney system

The working principle of solar chimney systems is that when solar energy provides a natural draft, the in-and-outdoor temperature variations are produced. This temperature difference causes convective airflow between indoor and outdoor spaces to improve ventilation [116]. A solar chimney usually consists of a vertical shaft, cavity or chimney having a transparent cover or collector which captures the solar radiation. Model experiments and theoretical investigations have been the primary research methods used to explore the performance of solar chimney ventilation systems [115].

For instance, Maghrabie et al.'s review [116] identified that many theoretical studies on solar chimney ventilation performance in existing literature have primarily focused on solving momentum, mass, energy, and heat transfer equations. The results differed based on the parameters investigated. Other studies also emphasised the impact of solar chimney geometry design factors, such as height, width, absorber material, and absorber inclination angle orientation, on ventilation performance [117]. Jianliu et al. [118] developed a theoretical and experimental model to assess the effect of solar chimney inclination on its performance. Results showed that the ventilation rate was highest when the solar chimney angle of inclination was 45 °. This was in addition to the increase in the height-to-cavity ratio. Conversely, the study by Imran et al. [119] indicated that the best ventilation performance was at a power density of 750 W/m^2 when the solar chimney was at a 60 °angle inclination.

In terms of the impact of climate on the ventilation performance of solar chimney systems, Drori et al.'s study [120] demonstrated that the system effectively ventilated a small-sized building, even under low solar radiation levels of 50–60 W/m². This was achieved by expanding the absorber area and incorporating two inner partitions. According to Shi et

al. [121], solar chimneys with cavity widths between 0.2 and 0.3 m and a height-to-gap ratio of 10 provided the best ventilation performance in terms of airflow rates. The study further concluded that outdoor winds significantly influence solar chimney ventilation performance. Shi [122] conducted both theoretical and experimental studies to assess the impact of wind on the ventilation performance of solar chimneys. Results showed that as solar radiation increased from 100 to 1300 W/m2, a 0.65 to 1.55 m/s increase in critical wind velocity was achieved.

Neves et al. [123] highlighted the importance of considering the combined influence of wind and the buoyancy effect in solar chimney performance studies, especially under low outdoor wind speeds conditions. Results from the study specifically showed that aside from solar radiation, low outdoor wind speeds of 1-2 m/s and the indoor airflow pattern impacted negatively on the buoyancy ventilation performance of the solar chimney. When the incident wind angle was opposite the inlet opening at low wind speeds between 1-2 m/s, the airflow rate reduced by 47 %. This suggests that inefficiencies in the ventilation performance of solar chimney systems persist, especially in areas with low wind speeds.

2.3.1.2 Trombe wall system

Trombe wall systems are typically installed on the south-facing walls of buildings. The systems feature a high thermal mass wall that absorbs and stores heat during the day, releasing it gradually back into the space at night as ventilation occurs. Many studies have found that Trombe wall systems, whether ventilated or unvented, are more suited for cold climates rather than hot climates. This is because the systems naturally provide additional heating while ventilating spaces, rather than cooling [124]. Only very few studies have presented strategies to improve Trombe wall ventilation performance in hot conditions.

Blasco Lucas et al. [125] conducted a comparative experimental study on an integrated solar screening system combined with a non-ventilated

Trombe wall. The study examined two scenarios: one with low-energy measures for night/day ventilation and one without. These scenarios were tested across different climate conditions. Their findings revealed that the thermal performance of these systems varied across different climate conditions. However, all scenarios resulted in increased indoor temperatures, suggesting room for improvement in the systems' performance.

Gan [126] conducted a CFD parametric study on various Trombe wall configurations to assess their ventilative cooling performance during summer conditions. This study utilised the renormalization group (RNG) k-ε turbulence model. The results showed that increasing the size of the inlet and outlet openings in the Trombe wall system increased ventilation rates. Insulating the interior surface improved ventilative cooling during summer. Another study by Bevilacqua et al. [127], identified the risk of overheating in typical Trombe wall systems, especially in regions with abundant sunlight. This limitation highlights the reduced cooling capacity of Trombe walls. Omrany et al.'s study [128] provided a summary of the advantages and disadvantages of Trombe walls regarding their performance and limitations in hot climates. This summary is presented in Table 2.1.

Table 2.1. Advantages and disadvantages of the Trombe wall system [128].

	Performance of Trombe walls	Limitation of Trombe walls
1.	Integration Potential: Can be integrated with other building applications.	Indoor Overheating: This may lead to indoor overheating in hot conditions, as walls can act as heat sinks.
2.	Energy Efficiency: Exhibits high energy efficiency.	Low Thermal Resistance: Shows low thermal resistance at night, causing colder uncomfortable temperatures at night during prolonged cloudy days.
3.	Humidity Reduction:	Solar Intensity Susceptibility:

	Reduces humidity levels, making it suitable for high-humidity climates.	Highly susceptible to changes in solar intensity.
4.	TES: Possesses excellent TES properties due to thermal mass advantages.	High Installation Cost: Initial installation costs are relatively high.

Ghrab-Morcos et al. [129] conducted a study to address the issue of overheating associated with Trombe wall usage in hot conditions. The effectiveness of combining overhangs with cross ventilation to enhance the performance of Trombe walls was studied. The two Trombe wall models developed in the study are shown in Figure 2.13(a) and 2.13(b).
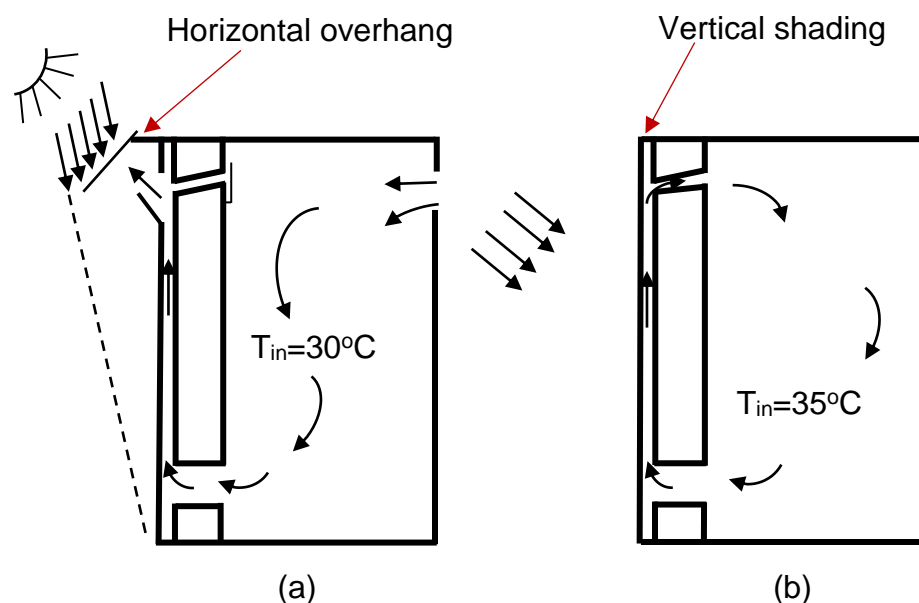
Figure 2.13. Trombe wall operation in summer (a) integration with an overhang (b) operation without overhang integration [129].

In both models, hot air was allowed to flow from the indoor space through the wall cavity and be expelled outside. When outward circulation was allowed, the room temperature exceeded 35 °C, surpassing the thermal comfort range, as shown in Figure 2.13(b). However, by incorporating a shading device into the Trombe wall system, along with the wall opening, as depicted in Figure 2.13(a), overheating in the cavity was mitigated. As a result, the indoor temperature dropped to around 30 °C, which falls within the acceptable thermal comfort range.

Raman et al. [130] studied the ventilative cooling performance of a metallic Trombe wall system based on two different passive model concepts. Model 1 combined two solar chimneys and an evaporative cooler in an insulated walled room. In Model 2, the roof duct was wetted by an evaporatively cooled surface and connected to a south wall collector on insulated walls. Observations of the performance over a year showed that Model 2 performed better thermally than Model 1, particularly during the summer months. Passive model I only achieved a 2-3 °C temperature drop. But when the ambient temperature was 42 °C, Model 2 was able to reduce the indoor temperature to 28-30 °C. It also maintained an indoor temperature of about 17 °C in winter.

Jaber et al. [131] studied the thermal and economic implications of utilising Trombe wall ventilation systems to reduce heat gains during periods of high outdoor temperatures in Mediterranean climates. The results suggested that while the Trombe wall did not reduce the maximum cooling load, it reduced the heat load by 32.1 %. The study recommended that to achieve optimal economic and thermal value, the Trombe wall-to-total wall area ratio should be at 37 %.

Stazi et al. [132] conducted an experimental study comparing the thermal performance of two types of Trombe walls: an unvented and a Trombe wall with solar protection; under varied screening, ventilation, and internal heat gain conditions. The introduction of the screening reduced the surface temperature of the Trombe wall by 1.4 °C. This resulted in reduced indoor heat gains. Compared to the unvented Trombe wall, cooling loads were reduced by 72.9% and 63.0%, respectively, when overhangs and roller shutters were incorporated alongside the cross ventilation provided by the Trombe wall system. Similarly, a CFD heat transfer study was conducted by Charqui et al. [133] on Trombe wall's thermal performance under unsteady conditions. The different wall types investigated showed that minimal incoming flux had low impact on indoor temperature. The heat transfer time lag in the walls ranged from 4 to 6

hours. The study also suggested that switching the position of the vents and replacing cavity air with materials like argon or xenon could improve the thermal performance of Trombe walls in hot conditions.

In a study by Song et al. [134], the influence of air velocity on acceptable indoor temperature for occupants' thermal comfort was studied. The study found that occupants were only able to tolerate indoor temperatures ranging from 25.5 to 27.3 °C when the air velocity was 0.6 m/s. However, at an air velocity of 1.2 m/s, tolerable indoor temperatures increased in the range between 27.5 and 30.9 °C. This therefore means that increased air velocities make higher indoor temperatures more tolerable upon the use of Trombe wall systems. It is believed that wind-driven ventilation systems may offer better thermal comfort compared to solar-induced ventilation systems. This is because they can generate higher indoor wind velocities.

2.3.2 Wind-driven ventilation systems

Generally, wind-driven ventilation is often more effective than buoyancy-driven (stack effect) ventilation in many scenarios because wind can create larger pressure differences across openings and primarily operates based on induced wind speeds and direction. In the study by Hughes et al. [135], which focused on a comparative CFD modelling of wind-driven and buoyancy forces on the ventilation performance of a commercial windcatcher, the results validated the conclusion that external wind provided 76 % more ventilation than buoyancy. Besides windcatchers, wind cowls are also examples of wind-driven ventilation systems.

2.3.2.1 Wind cowl

Wind cowls also referred to as chimney caps, are installed primarily to prevent downdrafts caused by airflow reversal. They are designed to improve chimney drafts by harnessing wind energy and redirecting

airflow into the building, which indirectly enhances indoor ventilation. Depending on the design and other environmental conditions, wind cowls also act as ventilation duct shields, preventing rain and debris from entering the building. Additionally, they may indirectly also reduce turbulence, thereby creating a wind suction effect to enhance ventilation in buildings [136]. Various designs of wind cowls exist, categorised as either static or rotating.

Static wind cowls remain unaffected by wind movement or direction while rotating wind cowls revolve according to the prevailing wind direction [137]. An example of an anti-down draught static wind cowl is depicted in Figure 2.14, while Figure 2.15 illustrates an exhaust-rotating wind cowl.
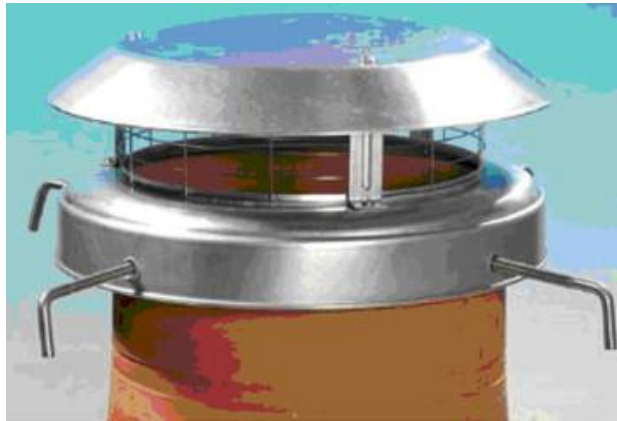
Figure 2.14. Anti-down draught static wind cowl [137]

Figure 2.15. Exhaust rotating wind cowl installed on the roof of a building

Rashid et al. [138] conducted a wind tunnel experiment to evaluate the airflow patterns facilitated by wind cowls and the operational effectiveness of rotating wind ventilators. Pfeiffer et al. [139] developed a new CFD modelling approach for wind cowl studies. The study also experimentally assessed the wind energy-to-wind pressure conversion performance of the exhaust cowl which was integrated with hybrid ventilation. The results denoted that the accuracy and performance of wind cowls and the suction effect models were significantly influenced by external climate conditions. The study also highlighted that for accurate representation, advanced CFD models such as the Reynolds Stress Model (RSM) should be employed rather than using the standard k-epsilon model.

He et al. [140] conducted a wind tunnel experiment on a scaled solar chimney to comparatively assess the effect of an elbow outlet and two wind cowls (a louvre type and a baffle type) on wind pressure distribution, ventilation rate, and exhaust flow performance in buildings. Both the louvre and baffle wind cowls prevented reverse flow from occurring. However, the baffle wind cowl offered 57% higher ventilation performance in the windward direction and 37% higher in the leeward direction compared to the ventilation rate provided by the elbow outlets. However, the roof-mounted elbow outlet, when facing the wind, presented reverse flow, thereby weakening the stack ventilation design. The study recommended the use of baffle wind cowls.

In another study, Adekoya [141] conducted a field study on a rotating wind cowl to analyse static pressures relative to varying airflow rates for a farm building. Results showed a good curvilinear relationship between airflow and static pressure values. Essentially, the wind cowl offered very low static pressure and airflow rates compared to what can be achieved by electrical drying fans. The low pressure and airflow rates observed in the study were found to be beneficial for 400mm depth of drying grains when moisture content is not excessive (below 20 % wetness). However,

low airflow offered may not be sufficient for residential buildings, where higher ventilation rates are typically required to maintain indoor air quality and comfort.

Monahan et al. [142] conducted a field test on a static cowl integrated with a wind-driven radon sump to evaluate the system's effectiveness in depressurising buildings under Irish climate conditions. Results indicated a notable 75 % reduction in radon levels. However, several wind cowls are required to be installed to achieve the desired indoor comfort. The use of wind cowls is limited primarily because the costs associated with the installation and maintenance often surpass the ventilation benefits it offers. Consequently, wind cowls are not as commonly adopted or studied as sole ventilation systems, especially for residential buildings where more effective alternatives such as windcatcher systems are available.

2.3.2.2 Windcatcher system

Windcatcher systems are sometimes referred to as "wind towers" or "natural air conditioning" [143]. The intrinsic appeal of windcatchers for ventilation lies in their zero-energy passive operation, which eliminates the need to use active energy [144]. Windcatchers require very low maintenance since they do not have any moving parts necessary for operation [145].

According to Hejazi et al. [146], traditional windcatchers were originally utilised as ventilators to supply fresh air in buildings, drawing air from outside or even from basements or courtyards to ventilate spaces in the absence of external wind. Additionally, these traditional systems served other societal functions. For instance, two-sided windcatchers, aside from their ventilation roles, also functioned as water storage units [147]. However, Aryan et al. [148] presented a contrasting submission, highlighting the predominant use of eight-sided multi-directional windcatchers rather than two-sided windcatchers for water storage in

those buildings. Some of the famous examples of these types of windcatchers include the Amirchakhmaq mosque windcatcher [149], Dowlat Abad garden windcatcher [150], and those found in the historical city of Alzubair [151]. In retrospect, the height of traditional windcatchers typically ranged from 5 to 33 m, towering above the building's rooftop.

These different heights were thought to have been influenced by the climate [96], [152]; a symbolic expression for the wealth of the owners of the building [153]; or an expression of the architectural style dominant in the region at the time [154]. Alsailani et al. [155] conducted a parametric study on 40 geometrical parameters of the windcatchers to investigate their effect on airflow performance through 3D steady RANS CFD simulations. The result showed that the straight and nozzle-shaped inlet windcatchers could enhance airflow up to 23%. The introduction of vanes to the straight and nozzle-shaped inlets resulted in increased airflow performance up to 29%. The result confirmed that shape, size, and the position of inlet-outlet vent are all effective parameters of windcatchers in their ventilation performance. As a matter of fact, this was proved through research proposed by Alsailani et al. [155]. In a separate study, Varela-Boydo et al. [156] used the CFD *SST k-ω* model to assess the impact of the outlet position of a traditional windcatcher. The study examined 33 alterations to both the position and size of the outlet vent. Results showed that a 3.65 % enhancement in mass flow was achieved with increased outlet size and when the outlet was positioned vertically. However, this study did not consider the effect of the windcatcher height.

Aside from the height of the windcatcher, other geometrical factors that impact the performance of windcatchers include the number of openings (vents), internal partitions, stories, and cross-sectional shapes [157]. Windcatchers have been classified based on such geometrical parameters. However, the most outstanding parameter used for classification is the direction that the vent of the windcatcher faces from the prevailing winds.

2.3.2.3 Types of windcatchers

Traditional or contemporary windcatchers can be classified as one-sided (uni-directional), two-sided, three-sided, or multidirectional. One-sided windcatchers are primarily designed to admit air only from the north-direction vent [157], which facilitates effective regulation of airflow, especially during severe storms [158]. Generally, a higher number of vents provides more opportunities for airflow.
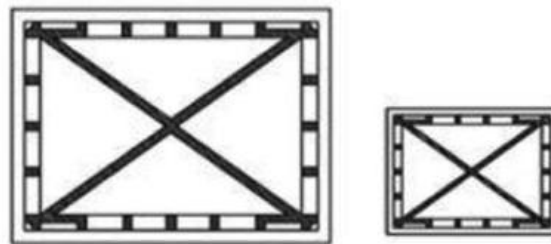
Figure 2.16. X-shaped internal partitions in windcatchers [106], [159]
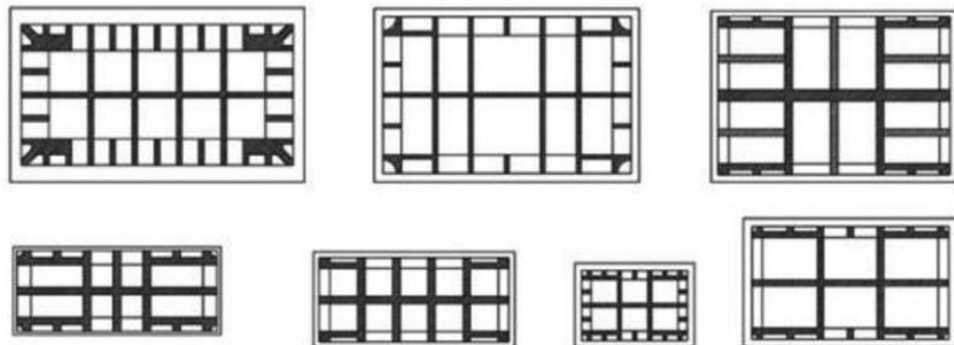
Figure 2.17. +-shaped internal partitions in windcatchers [106], [159]
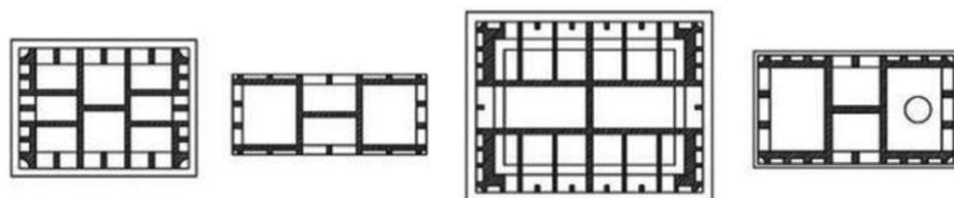
Figure 2.18. H-shaped internal partitions in windcatchers [106], [159]
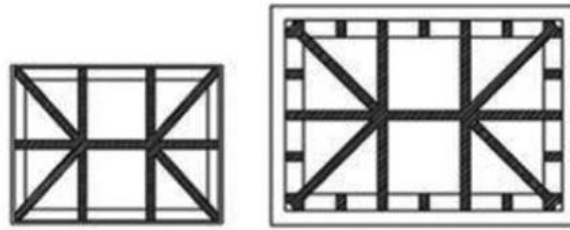
Figure 2.19. A combination of + and K-shaped internal partitions in windcatchers [106], [159].

Consequently, the multi-directional category is the most utilised and the most diverse, featuring four-sided, six-sided, eight-sided, and cylindrical windcatchers [160], each offering unique vent configurations and airflow characteristics. Mahmoudi's study [161] and Sahu [159] suggested that four-sided multi-directional windcatchers can have up to four distinct internal partition styles: "X" (Figure 2.16), "+" (Figure 2.17), "H" (Figure 2.18), or a combination of "+" and "K" shaped partitions as illustrated in Figure 2.19.

Figure 2.20 presents a comprehensive categorisation of windcatchers based on traditional designs sourced from various references [108], [162], [162]. This classification framework has also been found to be equally applicable to contemporary windcatchers. However, it is noteworthy that most contemporary windcatchers adopt the "X" internal windcatcher partition rather than the more complex ones.

Bahadori's study [163] was the first study that established the definition of windcatchers, exploring the various types, and their implementation in buildings. In a subsequent study, a flow and thermal network numerical analysis was conducted to assess the inclusion of water spray systems based on momentum, mass and energy analyses to enhance windcatcher cooling performance. Results showed higher air flow rates suitable for night cooling [164].
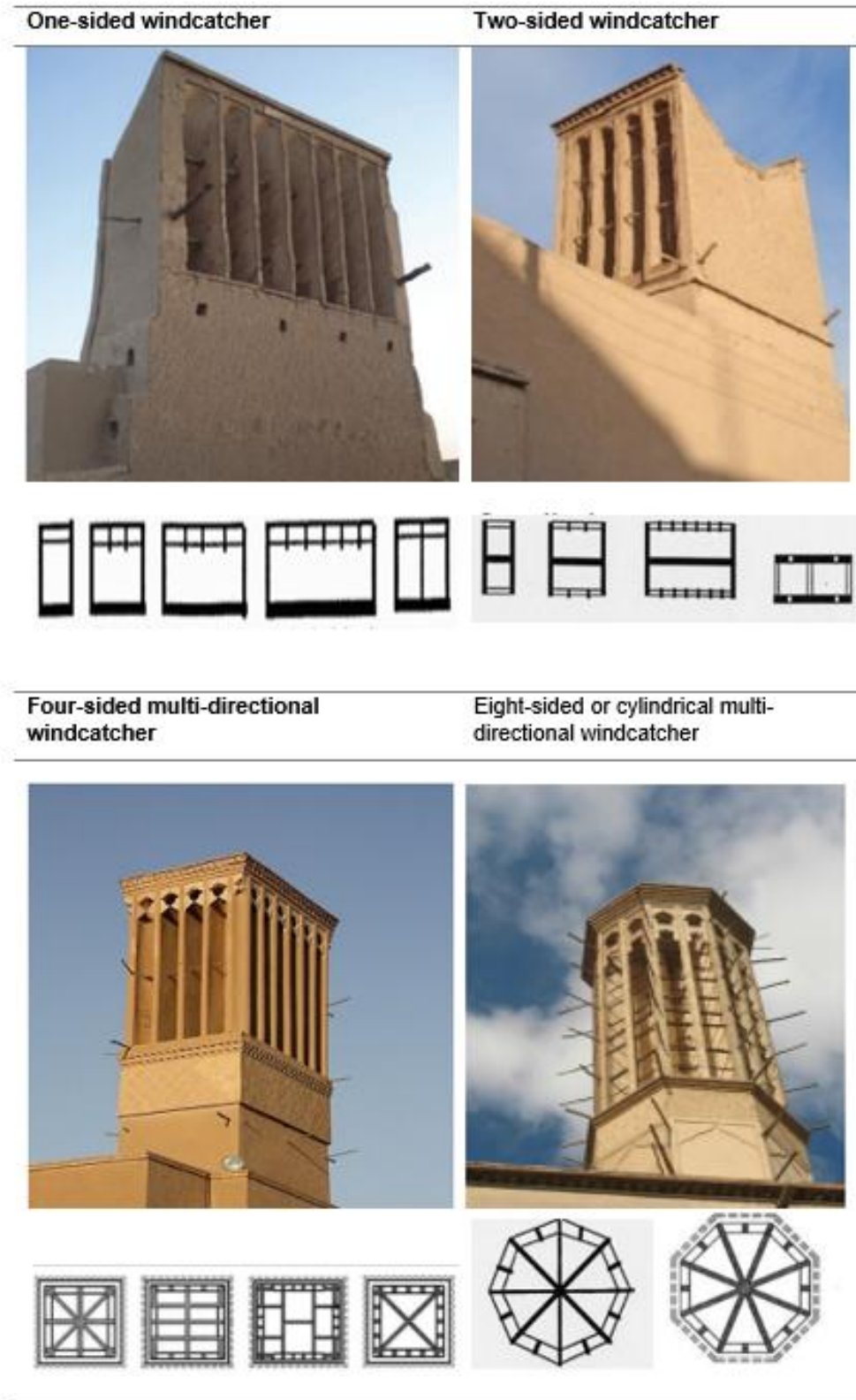
Figure 2.20. Classification of traditional windcatchers [108], [162], [162].

Further research, such as that by Karakatsanis et al. [165], investigated the impact of pressure coefficients, wind speed, and wind angles on windcatchers through wind tunnel experimentation. Results showed that the airflow rate was influenced by pressure coefficients, which increased with the wind angle. Other pioneering windcatcher performance studies [166] explored the integration of solar chimneys with windcatchers to enhance airflow suction

These early investigations demonstrated the potential to significantly enhance traditional windcatcher performance through system integration. However, the complexities of urban microclimates and ventilation requirements have spurred the evolution of traditional windcatcher designs into contemporary ones [167]. Contemporary windcatchers aim for reduced windcatcher height while still efficiently combining buoyancy and stack principles to enhance ventilation. Hence, research and innovations have emerged for contemporary one-sided, two-sided, and multi-directional windcatchers, aligning with the broader trend of enhancing windcatcher performance pioneered by researchers like Bahadori.

2.3.2.3.1 One-sided windcatchers

Hughes et al.'s study [168] reviewed the development trends of commercial windcatchers, highlighting that one-sided windcatchers are only able to effectively operate within the single wind direction the opening faces. However, if prevailing winds fall outside this range, the inlet vents must be elevated, either by design or through automation, to facilitate ventilation. This highlights a limitation in the utilisation of one-sided windcatchers in regions with low wind speeds or where wind directions are variable. Another study identified this limitation. A comparative study conducted by Heidari et al. [169] combined a one-sided windcatcher with evaporative coolers mounted on a contemporary two-story residential building in Iran (*Figure 2.21*).
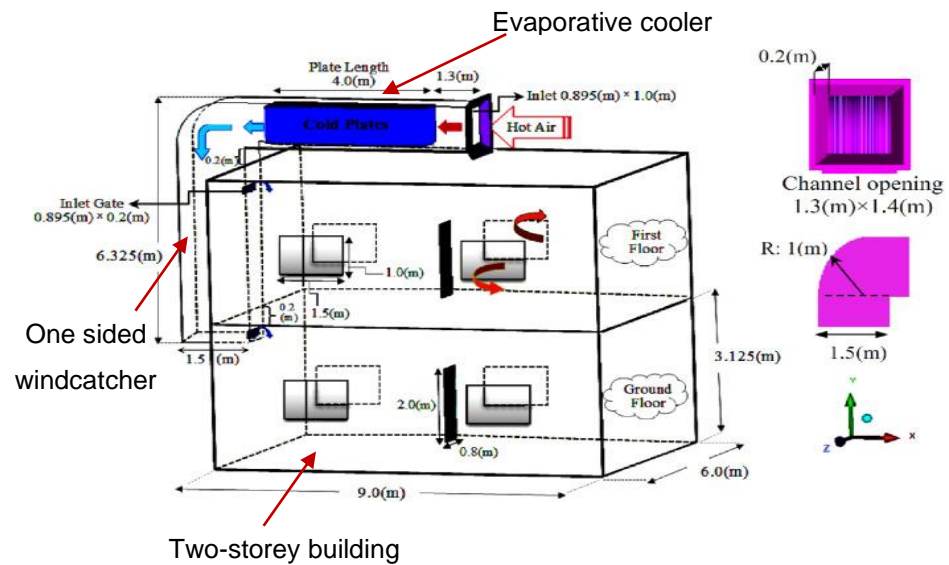
Figure 2.21. Schematic diagram of the evaporative cooling integrated one-sided windcatcher mounted on the two-storey building [169]

The study used Ansys and MATLAB to simulate the airflow ventilation behaviour of the model. Results showed that ventilation was only adequate when the wind speed reached 3.2 m/s. Although the inclusion of evaporative coolers reduced the cooling load by 50 %, adequate ventilation was not achieved when wind speed was below 3.2 m/s. There is a possibility of modifying the geometry of one-sided windcatchers to enhance ventilation in low wind conditions. However, as a general principle, increasing the number of vents and vent direction will enhance the potential for effective ventilation, especially when wind speeds are low. A numerical and experimental study was conducted on three designs of flat, inclined, and curved-roofed one-sided windcatchers by Dehghan et al. [170]. The study revealed that the geometrical design and incident wind direction significantly influenced the induced airflow and internal pressure. Specifically, higher supply airflow was observed with the curved-roofed one-directional windcatcher when the incident wind direction was at 0 º compared to the other designs. However, with other wind directions and roof designs, the ventilation performance was reduced significantly. In another study conducted by Esfeh et al. [171] on various scaled one-sided windcatcher models using smoke visualisation

experimentation, the results emphasised the necessity of separating airflow passages to enhance ventilation performance.

In all these studies, one notable limitation identified was the one-sided windcatcher's inability to effectively capture wind when the wind direction varies, hindering increased induced supply airflow. The suggested solution is to increase the number of windcatcher vents. This implies that a two-sided windcatcher would outperform a one-sided windcatcher in terms of achieving improved supply-induced airflow.

2.3.2.3.2 Two-sided windcatchers

Despite that two-sided windcatchers can provide ventilation more than one-sided windcatchers, studies show the need to combine their use with additional windows before effective ventilation performance can be achieved. For instance, Zaki et al. [172] utilised a combined approach, incorporating scaled wind tunnel experiments and Computational Fluid Dynamics (CFD) modelling, to assess the influence of turbulent flow on the ventilation of a two-sided windcatcher. The study captured both external and internal flow fields using installed pressure traps. The findings indicated the necessity of incorporating additional windows at lower regions of the building walls in addition to the use of a two-sided windcatcher, as this factor significantly influences the interior airflow pattern, hence achieving better indoor ventilation.

Additionally, unsteady, and limited airflow occurs when incident wind angles are not directly aligned with the two-sided windcatcher vents. This was confirmed by Afshin et al.'s experiment [173] to assess the effect of wind angels on a two-sided windcatcher ventilation performance. Results showed that the pressure coefficient was highest at zero wind angle. But ventilation decreased with increased wind angle. Ventilation ceased when the wind angle was 55 ° and at the window transition angle of 39 °, no air flow was observed through the window. Ghadiri et al. [174] conducted a numerical study on the ventilation performance of two-sided

windcatchers. The results highlighted the impact of wind-induced ventilation and how numerical equations influence this phenomenon.

Other studies have highlighted additional features such as wing walls to improve two-sided ventilation performance. Nejat et al. [175] studied the effect of wing walls on two-sided windcatcher ventilation performance in low wind conditions. Based on a varied wind wall between 5 – 70 °, the CFD results showed that when the wing wall was set between 15 – 30 °, improved supply airflow was achieved. Zaki et al. [176] conducted a wind tunnel experiment to assess the turbulent flow effects of integrating a two-sided windcatcher ventilation system on the roof of a single-zone building with a window opening. The study emphasised that windcatcher design should facilitate turbulent flows to ensure effective ventilation, especially when wind directions vary both directly and indirectly.

2.3.2.3.3 Three sided windcatchers

Three-sided windcatchers are characterised by the windward vent being larger than the other two vents [177], allowing optimal capture of prevailing winds from the windward vent only. Khan et al. [178] studied evaporative cooling in a three-sided windcatcher in hot, humid conditions using a realizable k-ε turbulence model with an Eulerian-Lagrangian CFD algorithm. Directing airflow downward to the exhaust vent increased density, water vapour mass fraction, and relative humidity while reducing air temperature from 323 K to 300 K. Higher airflow rates resulted in 100 % relative humidity, compared to about 70 % at a wind speed of 1 m/s. This suggests that windcatchers using evaporative cooling offer higher humidity under high wind conditions, which may affect their suitability in hot, humid climates with strong winds.

Montazeri [179] conducted a comparative analysis of cylindrical windcatchers with two, three, four, six, and twelve sides using wind tunnel experiments and CFD simulations based on the SIMPLE algorithm. The three-sided windcatcher achieved airflow rates of 0.026 and 0.030 m³/s

in experimental and CFD models at a 0 ° wind angle. The two-sided windcatcher had 13 % higher efficiency than the one-sided at the same angle. Both two- and three-sided windcatchers performed well at low wind angles, but their efficiency decreased with increasing wind angles due to airflow separation on the windward sides.

Soutullo et al. [180] developed a thermal model of a three-sided evaporative windcatcher with an integrated auxiliary fan and nozzles using TRNSYS. The model showed that the indoor air temperature could be reduced by 6 to 8 °C from the ambient temperature. Generally, existing literature reveals limited studies on three-sided windcatchers, as these are considered less efficient compared to multi-directional windcatchers in an urban environment context.

2.3.2.3.4 Multi-directional windcatchers

Existing literature establishes that the efficiency of four-sided multi-directional windcatchers supersedes cylindrical types in similar outdoor conditions. In a wind tunnel and CFD experiments conducted by Elmualim and Awbi [181], the ventilation performance of a four-sided and a circular windcatcher were compared. The results favoured the four-sided windcatcher, demonstrating higher ventilation performance. This was attributed to the higher pressure and flow separation occurring at the wall edges of the four-sided multi-directional windcatcher compared to the cylindrical one.

Unlike other windcatcher categories, the four-sided multi-directional type is the most prevalently used in urban environments and for commercial applications [182]. In general, four-sided multi-directional windcatchers are more commonly used in modern windcatcher designs [183]. Moreover, the four-sided multi-directional windcatcher's suitability is enhanced by its capacity to function effectively in low wind conditions.

Therefore, a four-sided multidirectional windcatcher can be particularly beneficial in numerous hot and humid climates [184], including subtropical climates like tropical savannah climates, which experience a blend of hot dry and hot humid conditions. Farouk [177] conducted a comparative study between a hexagonal windcatcher and a four-sided square windcatcher. But the most used windcatchers in modern times in urban contexts are the commercial four-sided multi-directional windcatchers.
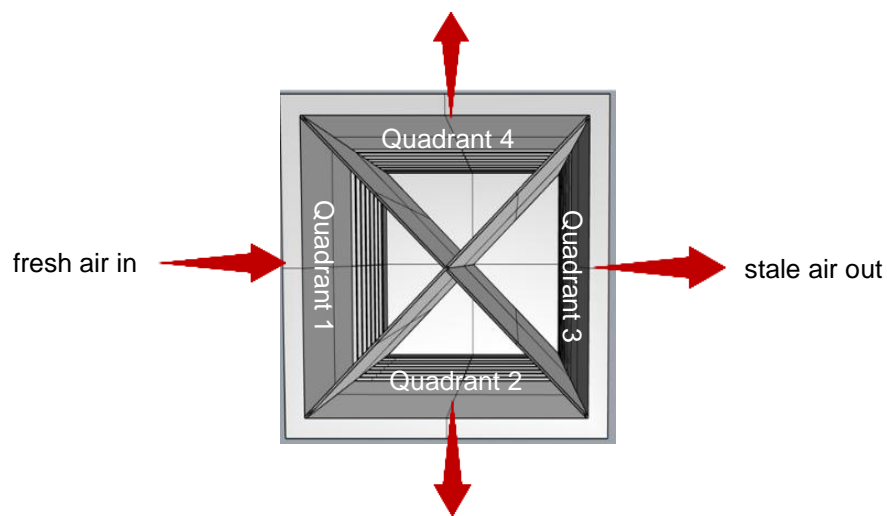
Figure 2.22. Cross-section of a four-sided multidirectional windcatcher showing airflow pattern through the X-shaped partitions / Quadrants.

As indicated in Figure 2.22, a four-sided multi-directional windcatcher is divided with an X-shaped partition to separate the movement of the inlet and outlet airflow as wind direction changes [33]. However, these quadrants play specific roles in the airflow ventilation operation, with one quadrant typically supplying fresh air, while the other three quadrants expel air out of the ventilated space [185]. However, the airflow dynamics can change slightly depending on the angle of the prevalent leeward wind incident to the windcatcher. Thus, the quadrants dedicated to inlet and outlet airflows can change depending on the wind direction changes [33].

The most widely accepted methodologies in windcatcher studies are small-scale and full-scale experiments, and theoretical assessments

based on analytical, empirical, and numerical modelling techniques [186]. For example, Elmualim [187] conducted both experimental wind tunnel tests and smoke visualisation tests in addition to developing a CFD κ–epsilon (κ–ε) CFX turbulence windcatcher model to assess the airflow performance of the windcatcher when heat source is introduced. Figure 2.23 shows the schematic of the windcatcher rig indicating the pressure measurement points during the wind tunnel experiment.
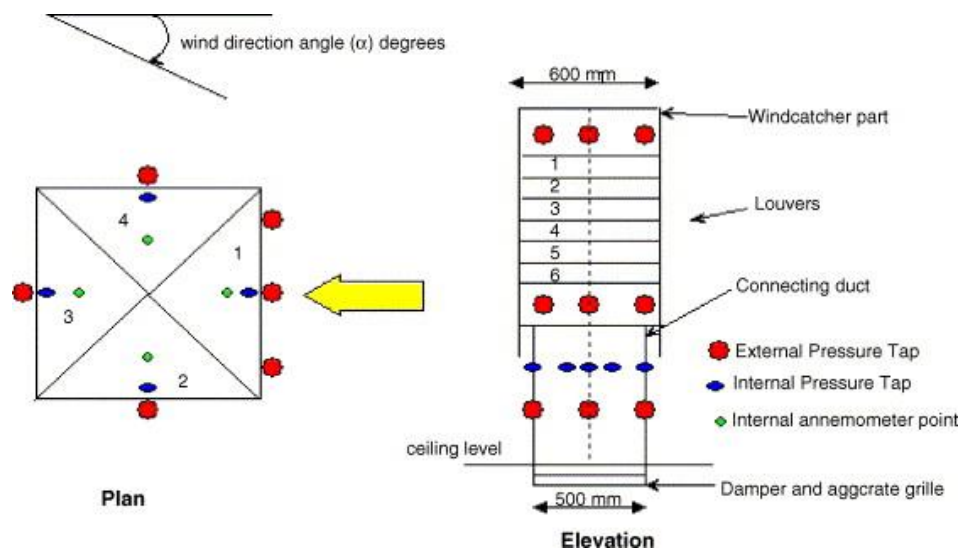
Figure 2.23. Schematic of the windcatcher model showing the pressure measurement points used during the wind tunnel experiment [187]
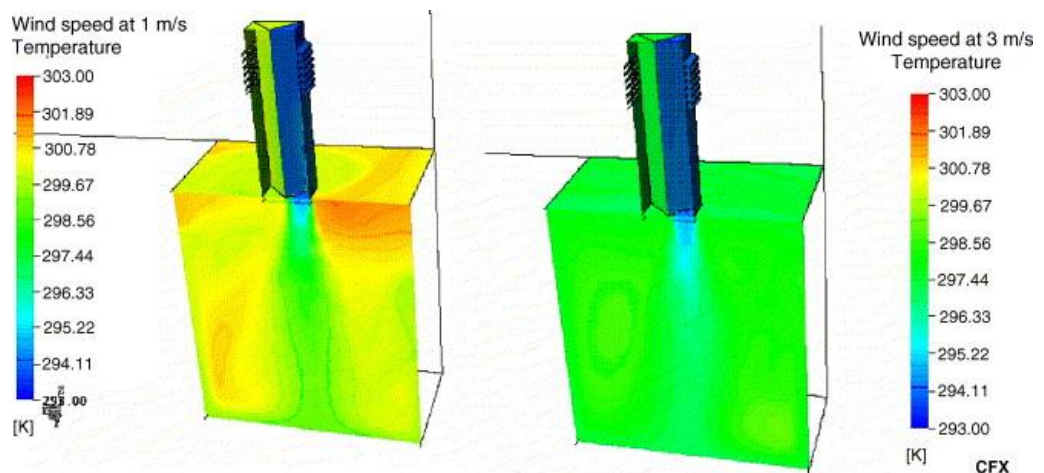
Figure 2.24. Comparison of temperature contours of the CFD windcatcher model at wind speeds of 1 m/s and 3 m/s [187].

The experimentation set-up mimicked windcatcher implementation in hot conditions. The results revealed that airflow increased by 7 % to 54 % as the wind speed rose from 1 to 3 m/s. Conversely, the extract flow increased by only 2 % at a wind speed of 3 m/s, while air extraction surged by 34 % at a wind speed of 1 m/s. The continuous airflow also improved the indoor temperature slightly as shown in the comparative temperature contour when wind speed was 1 and 3 m/s shown in Figure 2.24.

2.3.3 Studies on the impact of different climatic parameters on multi-directional windcatcher performance

In addition to wind speeds, indoor-outdoor air pressure differences, wind angles, and air temperature variances are critical factors influencing windcatcher airflow in hot climates. Consequently, these parameters have been fundamental in many previous studies on windcatcher performance [42].

2.3.3.1 Wind speeds

Typically, higher wind speeds result in superior ventilation rates in windcatchers [188]. However, excessively high wind speeds may not necessarily benefit windcatcher cooling performance. In general, multi-directional windcatchers offer more satisfactory ventilation in limited wind speed conditions than other types of windcatchers [26]. Gharakhani et al. [189] conducted wind tunnel experiments and CFD analysis to investigate windcatcher ventilation performance under low-wind hot conditions. The findings revealed that, in addition to the windcatcher height, increasing the number of vents improved the ventilation performance at nominal wind speeds of 5-7 m/s. Other studies by Calautit et al. [190] and O'Connor et al. [39] indicated the potential of four-sided multi-directional windcatchers to operate optimally even at low wind speeds as low as 2 m/s. This capability can be attributed to the efficient sizing and positioning of the vents in multi-directional windcatchers [191].

Dehghani-Sanij et al. [192] assessed the ventilation performance of a single-sided rotating cylindrical windcatcher with moistened pads. The windcatcher rotated in response to the highest wind speeds, typically falling within the range of 3-10 m/s. Their findings indicated that higher ventilation efficiency was achieved at greater wind speeds.

2.3.3.2 Wind angles

Wind angles significantly impact the pressure difference across openings in passive ventilation systems [193], such as multi-directional windcatchers, influencing ventilation performance. According to previous research, the highest ventilation performance and pressure coefficient are achieved when the wind flows into the multi-directional windcatcher vents at a 0° angle [33]. It is believed there is a strong relationship between wind speed, wind angles and the airflow performance of a windcatcher. According to Afshin et al. [173], zero-ventilation windcatcher performance occurs at a 55° wind angle. Li et al. [29] conducted a CFD numerical model assessment to evaluate the airflow performance of a windcatcher across wind speeds ranging from 0.5 to 6 m/s at various wind angles. Their findings revealed a correlation between inlet airflow and both wind speed and wind angle. However, other studies show that as wind angle changes incrementally, the airflow rate begins to reduce until ventilation is no longer feasible [27]. Meanwhile, wind angles exceeding 45° can also reduce windcatcher cooling effectiveness [194]. These studies illustrate how varying wind speeds and angles heavily impact the passive ventilation potential of four-sided multi-directional windcatchers. Meanwhile, hybrid ventilation via fans can reduce the impact of wind angle variation in multi-directional windcatcher ventilation operations. However, the extent of this effect is yet to be discussed in existing literature. Therefore, more research is needed in this context.

2.3.3.3 Air temperature

Davies Wykes et al. [195] found that wind-driven cross-ventilation can be significantly influenced by air temperature. Their study revealed a 6 % reduction in wind-driven ventilation rates, while buoyancy-driven airflow increased ventilation rates by 40 %. Moreover, the study also showed that an increase in wind speeds can further augment the buoyancy-driven indoor-outdoor airflow rates. This suggests that air temperature impacts windcatcher ventilation performance. Consequently, windcatchers are expected to perform better when there is a notable difference between indoor and outdoor temperatures. Combining both wind-driven and buoyancy-driven airflow operations can optimise performance, especially in hot climates.

Additionally, Ghoulem et al. [196] examined the impact of ambient temperatures ranging from 30–45 °C on windcatcher performance in greenhouses situated in hot climates. They observed higher flow rates compared to when crossflow ventilation was employed. However, the minimal difference between outdoor and indoor temperatures in hot climates could pose a drawback, particularly in regions with low wind speeds. While there has been extensive research on enhancing windcatchers to lower indoor temperatures, limited studies have focused on how external or ambient air temperature affects their cooling and ventilation performance.

2.3.3.4 Air pressure

Ventilation occurs when airflow is from a positive pressure point to a negative pressure point. As a result, the air or wind pressure is a very significant parameter that affects windcatcher ventilation. Accordingly, there must be a balance between positive air pressure and negative air pressure to facilitate adequate airflow within the space. If not effectively considered, under low wind conditions, air pressure imbalance may affect windcatcher ventilation. The relationship between air pressure difference,

wind speeds, air density and wind pressure coefficient can be derived from Equation 2.2 [197].

$$\triangle Pa = (Cp_i - Cp_e) \, {}^1\!/_2 \, \rho V_o 2 \qquad\qquad Equation \ 2.2$$

2.3.4 Windcatcher Hybrid Integrated Systems

The possibility of enhancing windcatchers with other passive systems is becoming a common trend in recent research. For instance, O'Connor [198] incorporated a heat recovery device with a windcatcher system, achieving an indoor-outdoor temperature variation of up to 0.68 °C. The pressure drop ranged from 10.02 to 10.31 Pa, considerably less than the average pressure drop in conventional windcatchers of 150 Pa. However, the airflow rate was measured at 140.86 L/s, which is sufficient for a room accommodating 17 occupants. The conclusion drawn from the study highlighted that the closeness of the inlet and outlet airstreams and vents allows for easy windcatcher integration of other passive cooling systems, particularly for air preconditioning purposes. In general, windcatchers can be combined with other passive systems to achieve enhanced performance without compromising energy efficiency attributes.

2.3.4.1 *Windcatcher integrated systems for enhanced ventilation*

There are studies on improving windcatcher ventilation by combining them with other low-energy ventilation systems. Ther studies have also introduced the use of fans, especially for low wind conditions.

2.3.4.1.1 *Windcatcher system integrated with solar chimney system*

Bansal et al. [199] conducted an analytical study on a solar chimney integrated with a windcatcher to examine its impact on induced ventilation. The results demonstrated that the solar chimney enhances ventilation performance, particularly in low-wind outdoor conditions. For instance, when the wind speed was 1.0 m/s and incident solar radiation

reached 700 W/m^2, the solar chimney effect induced airflow in the system up to 1.4 kg/s.

In another study, a simplified and validated windcatcher integrated with a solar chimney was numerically modelled by Nouanégué et al. [200], using the SIMPLE algorithm in CFD. The study incorporated variable parameters such as Rayleigh, Richardson, and Reynolds numbers. Ventilation improved notably when the Richardson number was at $R_i \leq 1$, alongside an increased aspect ratio and higher Rayleigh numbers. Interestingly, the tower functioned as an energy storage system, presenting a promising strategy for low wind periods, particularly when the aspect ratio was optimised. This concept was further illustrated by Jomehzadeh et al. [201]. This is shown in Figure 2.25.
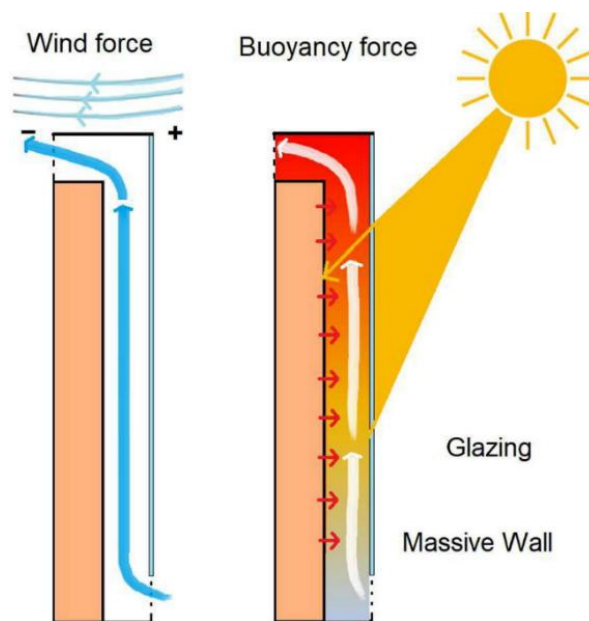
Figure 2.25. Illustration of the Windcatcher integrated solar chimney system developed by Nouanégué et al. [200], [201].

Li et al. [202] developed a novel chimney-integrated multidirectional dual-channel windcatcher integrated with a rotary wind scoop to provide more versatile wind-induced ventilation for hot climate buildings. Although results demonstrated better indoor ventilation compared to an 8-sided windcatcher under diverse wind directions, the research was based on high-wind conditions only and did not address low-wind scenarios. Thus,

it was recommended as a potential for future study. The authors also highlighted the necessity for more exploration into multidirectional windcatchers integrated with passive cooling.

2.3.4.1.2 Windcatcher system integrated with fans

A few studies have demonstrated the potential of integrating fans in windcatchers to improve ventilation performance. In the study by Elmualim [203], a mechanical fan system was combined with a windcatcher operation to increase indoor airflow. However, the windcatcher's contribution to the ventilation was not verified. Hughes and Ghani [204] developed a CFD model to evaluate the effect of different fan positions on the induced airflow of a windcatcher. Results presented a consistent ventilation rate of 370 L/s when the fan was at 20 Pa fan pressure and positioned at the top inside the windcatcher. The findings established the potential of the hybrid system to provide ventilation throughout the day, even under low wind conditions. Another study by Lavafpour and Surat [205] suggested the possibility of orienting wall-mounted fans parallel to the windcatcher's vents to reduce irregular ventilation flows. However, no data was presented to support this recommendation, highlighting the need for further research on fan-assisted windcatchers to better understand how to achieve windcatcher hybrid ventilation. Nonetheless, in line with the global focus on sustainable energy technologies, solar fans could be considered alternatives to mechanical fans for integration into windcatchers. While hybrid ventilation in multi-directional windcatcher systems shows promising results, other studies have emphasised the importance of achieving efficient windcatcher cooling to ensure widespread utilisation, even in hot conditions [35]. This can be achieved by combining windcatchers with additional passive cooling strategies.

2.3.4.2 Windcatcher integrated systems for enhanced cooling

Windcatcher systems cooling performance enhancement has been studied extensively [62]. Table 2.2. highlights a few windcatcher studies based on different types of buildings indicating the research method used, temperature reduction performance and energy savings under different climates. However, the most common passive cooling systems integrated with windcatchers are evaporative cooling systems and heat pipes.

Table 2.2. Windcatcher studies for buildings in different climates [62]

Climate	Building type	Study objective	Method	Findings	Ref.
Hot humid climate	Office buildings	Performance and energy saving potential of wind catchers in different Chinese cities	Numerical study - using energy plus simulation	17 % cooling energy savings. 2 $^{\circ}$C temperature reduction. Ventilation requirement achieved for 50 % of occupied hours. The most suitable city for the windcatcher was Harbin.	[206]
Hot humid climate	Public residential buildings	natural ventilation performance of wind wing wall	Numerical study using CFD for wind pressure prediction.	Hot humid climate	[207]
Hot humid climate	Residential buildings	Thermal performance of single-sided wind catchers	Experimental study	5 $^{\circ}$C temperature reduction	[208]

		in traditional residential buildings			
Hot dry climate	Residential buildings	Thermal behaviour of different square plan wind catcher geometry suitable for night-time ventilation	Numerical study using 3-D CFD model to compare indoor air temperature in different square wind catchers	Taller towers capture winds at higher wind speed capture is proportional to the height of the wind catchers.	[209]

Based on the inference from Table 2.2, there are minimal efforts in regions with hot dry-humid sub-tropical climate conditions. This requires further research efforts.

2.3.4.2.1 Windcatcher system integrated with evaporative cooling

Bahadori [210] and Bahadori [211] compared the effect of introducing wetted unglazed clay conduits columns and wetted surfaces into windcatcher air streams for evaporative cooling under a hot arid climate as illustrated in Figure 2.26 [183]. This was also reported in ref. [212]. Accordingly, the incorporation of wetted columns into the wind catcher facilitated the pre-cooling of ambient air. The study investigated parameters such as supply air temperature, relative humidity, and airflow. Findings indicated that while excess water was directed into a sump, the evaporative effect of the water-cooled the columns, thereby further cooling the supply air as it traversed through the windcatcher column. During peak conditions, the wetted columns exhibited a volumetric airflow rate of 1.39 m^3/s, while the wetted surface measured a volumetric airflow rate of 1.05 m^3/s. Both measurements were lower than the volumetric airflow rate of the conventional windcatcher, which stood at 1.5 m^3/s. The results revealed that the performance of the wetted columns in the windcatcher was significantly enhanced with high wind speeds, whereas

the wetted surface windcatcher demonstrated better performance in low wind speed conditions.
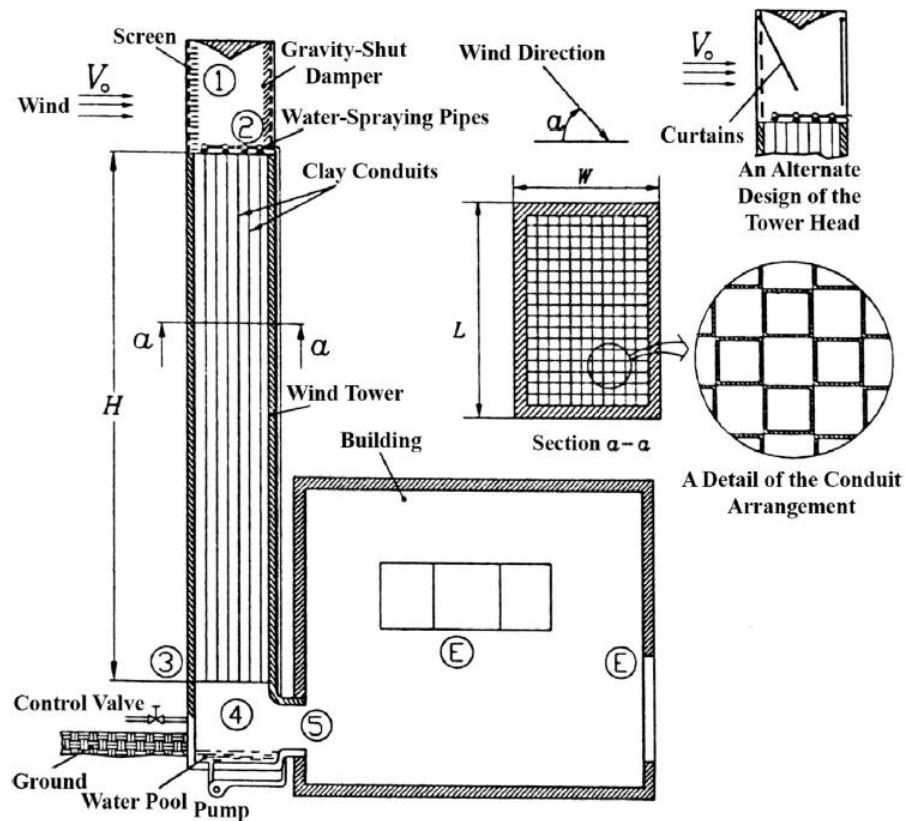
Figure 2.26. Cross-section of a wind tower with wetted conduits or columns [211], [212]

Hughes et al. [213] further demonstrated in their review the potential integration of wetted columns, and wetted cotton cloth, for evaporative cooling within windcatchers. The effect of these configurations on temperature reduction was compared with that of a conventional windcatcher, as depicted in Figure 2.27.
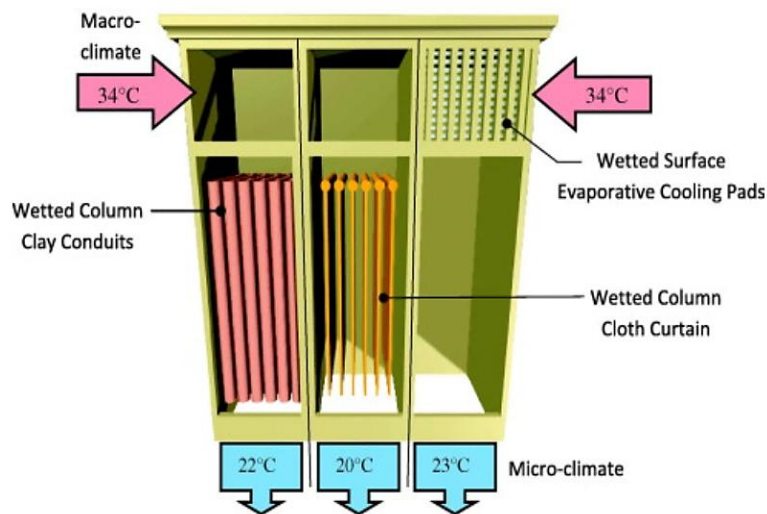
Figure 2.27. Comparison of conventional wind catcher and wind catcher integrated with wetted columns [168]

By maintaining a column spacing of 5-10 cm inside the windcatcher air streams, a temperature reduction from 34 °C to 20 °C can be achieved with the use of a wetted column cloth curtain. Wetted columns achieved a temperature reduction of 22 °C compared to the conventional windcatcher, which only reduced the temperature from 34 °C to 23 °C.

Issa et al. [214] used a thermodynamic mathematical model to predict the cooling performance of a multi-stage wind tower consisting of two interconnected venturi tubes with spray nozzles as evaporative cooling integrated within the windcatcher air stream. The three-stage evaporative cooling showed good cooling performance in low wind conditions. However, this is only suitable for hot dry climates where minimal humidity is experienced.

Consequently, all these studies highlight the high humidity content, suggesting their unsuitability for outdoor conditions with high humidity levels. However, the studies did not provide any recommendations for improving cooling performance without the added increase in humidity to adapt to climates with high humidity.

2.3.4.2.2 Windcatcher system integrated with heat pipes

Heat pipes are recognised as low-energy heat transfer devices that can adequately reduce incoming air temperature when integrated with windcatchers [215]. According to Calautit et al. [216], heat pipes have a 45-65 % sensible effectiveness. Calautit et al. [217] were the first to incorporate heat transfer devices in a uni-directional windcatcher system as illustrated in Figure 2.28.
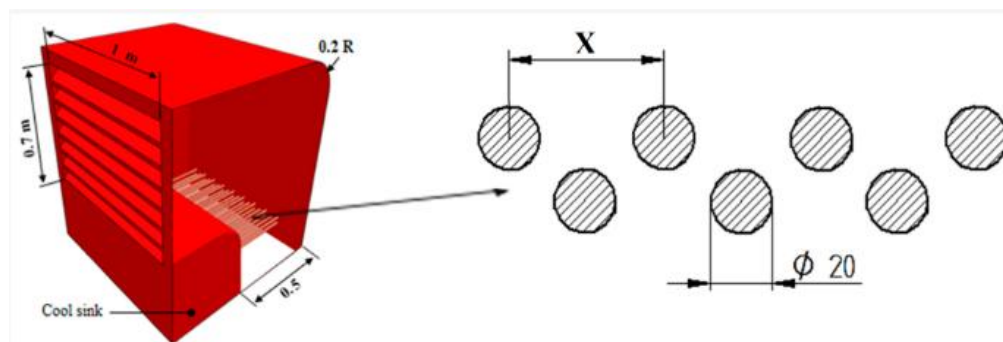
Figure 2.28. Heat pipes integrated into uni-directional windcatcher [217].

The study conducted both wind tunnel tests and CFD analysis to assess the cooling performance of the windcatcher model at varied wind speeds between 1-5 m/s. The results demonstrated a significant reduction in supply air temperature. According to the findings, when the ambient temperature was 318 K at 3 m/s, the indoor temperature achieved ranged between 309 – 312 K as shown in Figure 2.29. However, optimum cooling was achieved at wind speeds between 1-2 m/s, with the least cooling performance occurring at an ambient wind speed of 5 m/s.
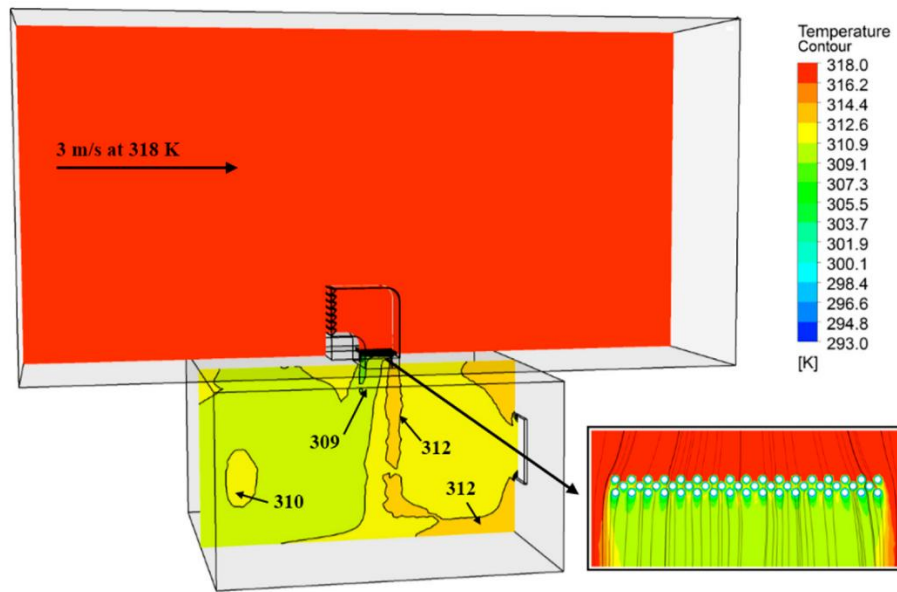
Figure 2.29. Temperature contour of CFD analysis at a wind speed of 3 m/s and an air temperature of 318K [217]

Calautit et al. [218] further conducted another similar study to investigate the external airflow, supply rate, and pressure coefficients when cylindrical heat pipes are integrated inside a similar uni-directional windcatcher at a 318 K external air temperature boundary condition. The heat pipe configuration led to a 12 K reduction in the temperature of the supply air. This time, the emphasis of the study was more on the impact of the heat pipe configuration on temperature reduction rather than the effect of outdoor wind speed on thermal performance. Despite a 20 - 35 % decrease in ventilation rate due to the heat pipe configuration inside the windcatcher, the system was able to maintain a supply airflow rate of up to 10 L/s per person. While the authors suggested the potential to further improve windcatcher ventilation rates with the use of fans, the study conclusively indicated that heat pipes exhibit effective cooling capabilities. Another numerical study by Calautit et al. [219] compared the impact of integrating evaporative cooling and heat pipes into a commercial windcatcher. Both approaches offered comparable temperature drops of up to 15 °C. However, the findings favoured the use of heat pipes over evaporative cooling, primarily due to water conservation considerations, even though both configurations required

working fluids (water or ethanol) to maintain a consistent cooling loop. Moreover, these studies did not address the windcatcher's inability to reduce and stabilise supply air temperature consistently. PCMs can offer streamlined integration, improving the TES performance of windcatchers.

<div align="center">

SECTION B:

</div>

2.4 Overview of thermal energy storage (TES)

TES is the thermal energy stored in a storage medium [220] in the form of sensible heat, latent heat, thermochemical energy, or a combination of these energies [221]. TES systems have wide-ranging applications in buildings, such as enhancing thermal comfort [46] and improving air-conditioning performance. Lin et al. [222] have also identified various defining factors that impact the selection of TES, such as heat loss during storage and transportation, phase cycle time, storage capacity, temperature, and cost. According to a review by Saha et al. [223], TES systems are not intermittent, making them a reliable option for cooling compared to other passive cooling systems, even in varied climates. TES stabilises indoor temperatures and helps minimise energy demand-supply imbalances in buildings [224].

2.5 Classification of thermal energy storage (TES)

Computational fluid dynamics (CFD) has been widely adopted to study TES in various engineering applications due to its cost efficiency [225]. However, to the appropriate TES system for building applications, it is essential to have a comprehensive understanding of the various types available. Generally, according to the type of storage reaction, TES can be divided into two major categories: chemical and thermal, as illustrated in Figure 2.30. Based on this, TES systems were further classified as sensible heat storage, latent heat storage, thermochemical energy storage, or in a combined form [226].
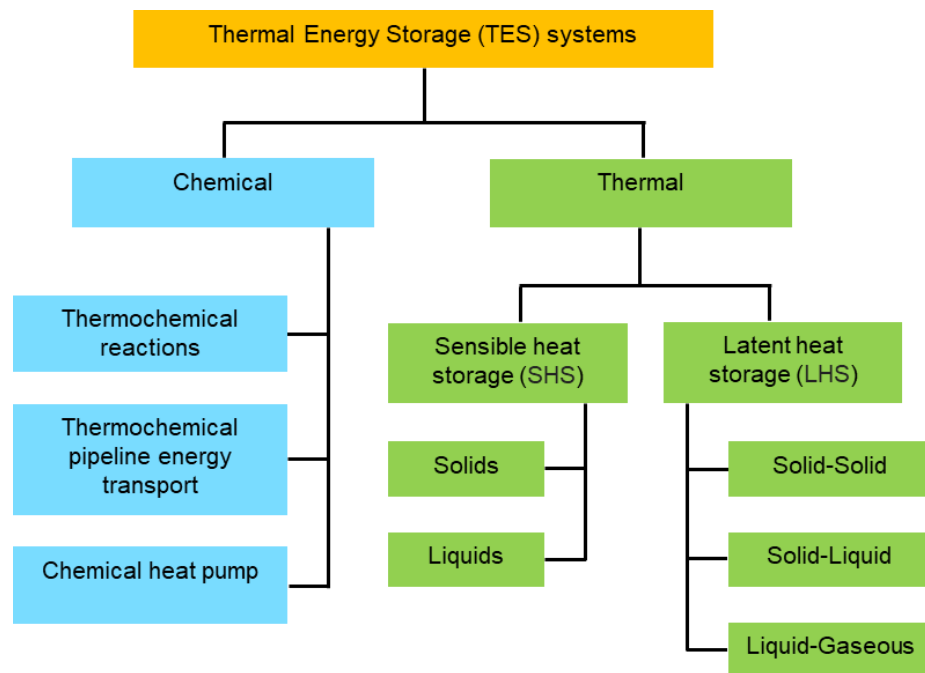
Figure 2.30. TES systems classification framework [226]

2.5.1 Thermochemical energy storage

Thermochemical energy storage (TCES) involves storing energy by breaking and the reformation of molecular bonds through reversible chemical reactions. This reaction can occur in three primary modes: thermochemical reversible reactions, thermochemical pipeline energy transport, and chemical heat pump storage [227].
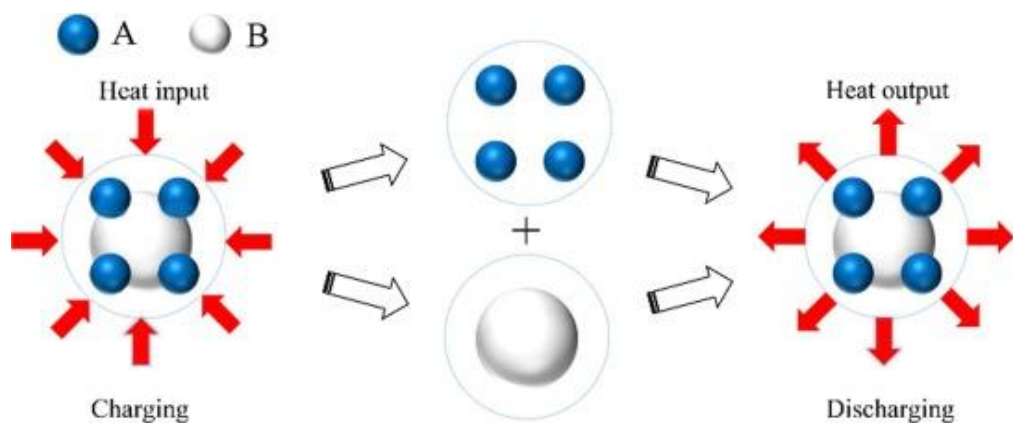
Figure 2.31. The heat sorption and storage process in a TCES [222].

Lin et al. [222] described the heat storage process that occurs in a typical TCES as indicated in Figure 2.31. A chemical reaction takes place, mixing A and B and pre-heated. Then a reversible reaction occurs that reforms this mixture of A and B into a reactant AB which then allows large amounts of heat to be released [222].

Compared to latent and sensible heat storage, TCES offers higher energy density and long-term stability across a broader temperature range [227]. But Faraj et al. [228] compared SHS and LHS and identified that LHS still offers five to fourteen times more heat storage per unit volume of material. Tatsidjodoung et al. [229] also compared the annual heat storage volumes required for latent heat storage, sensible heat storage, and TCES in a 6480 MJ energy passive house. It was reported that a 16 m³ sized latent heat storage medium is required for storing 300 - 500 MJ/m³. The sensible heat storage medium requires about 70 m³ to store 100 MJ/m³. In contrast, the TCES system requires only 7 m³ to store approximately 1000 MJ/m³, demonstrating its superior heat storage density, as shown in Figure 2.32.
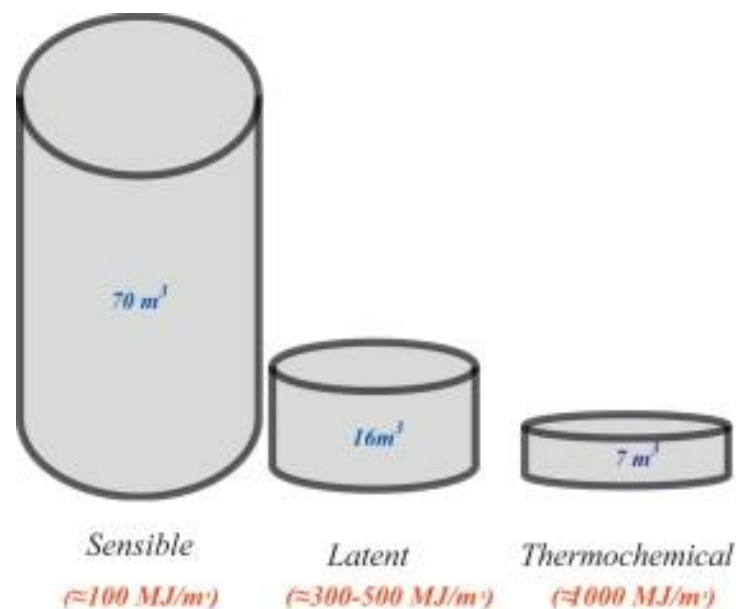
Figure 2.32. Comparison of sensible, latent, and TCES heat storage volume requirements for storing 6480 MJ for a passive house [229].

TCES reactants are usually a combination of sorbents and sorbates. There are recent research efforts on the suitability and application of various reactants as TCES [230]. Prieto et al. [230] performed a study on non-redox reactions in metal oxide species, focusing on sulphur-based cycles, metal oxide cycles, and perovskite-type hydrogen production mechanisms. Lefebvre et al. [231] pointed out that these reactions must be fully reversible, occur at temperatures above 500 °C, and be easily storable. Other studies focused on studying TCES material suitability [232], selection [233], and application as porous materials [234], salt hydrates [235], or composite sorbents [236].

According to the literature, TCES material characterisation is crucial for TCES optimal storage performance. Tatsidjodoung et al. [232] stated that TCES characterisation varies by scale: material scale is for quantities less than 10 mg. For the reactor scale, quantities must be greater than 10 mg. System-scale characterisation is adopted when heat storage capacity is the ratio of stored heat to the total volume of storage vessels, including pipes and heat exchange vessels.

While TCES theoretically offers better storage capacity and potential for long-term and seasonal storage compared to sensible and latent heat storage, practical application is still low. Barriers include high implementation costs and low thermal conductivity of some TCES materials, such as metal chlorides (0.1 - 0.5 W/(m K)) [237],[238] and metal hydrides (1 W/(m K)) [239]. Poor heat and mass transfer between reactants and heat exchanger walls further reduce performance, causing agglomeration phenomena [240].

Despite these limitations, Raam Dheep et al. [241] suggested TCES systems can improve energy storage performance by facilitating long-distance energy transport and heat pumping. However, limited information still exists on the long-term operation of TCES [242], and

more research is needed to support its viability for widespread building applications [243].

2.5.2 Sensible heat storage (SHS)

Sensible heat storage (SHS) stores heat through a heat exchange process that raises or lowers the temperature of the storage medium without changing its phase [244]. SHS can utilise either liquid or solid mediums to store sensible heat [245].

Liquid SHS mediums are generally more cost-effective but tend to be more thermally sensitive compared to solid SHS, which exhibits a superior ability to store heat [246]. Selection of SHS depends mainly on the intended application for which it is to be used [247]. Large volumes of SHS material are sometimes required for effective storage due to considerable heat loss to the surroundings during storage [247]. Achieving a high volumetric storage capacity (MJ/m³) requires materials with high specific heat and density. However, SHS typically demonstrates low energy densities ranging between 10 - 50 KWh/m^3 [248]. Since most SHS materials possess low heat capacity and storage efficiency, their attractiveness as effective long-term TES systems is reduced [249]. Moreover, substantial heat loss occurs during the heat storage process due to the significant swing in temperature that occurs, thereby diminishing the SHS storage capacity. This thermodynamic drawback undermines the long-term storage effectiveness of SHS [250].

The amount of energy stored as sensible heat (Q) in an SHS medium (m) is represented by Equation 2.3 below, as it depends on the temperature change (ΔT), between the initial t_i and the final temperature t_f, during the storage process [251], [252], [253]:

$$Q = \int_{t_i}^{t_f} mC_p \Delta T = mC_p \left(t_f - t_i \right) \qquad\qquad \textit{Equation 2.3}$$

Deeper insights into the application of SHS in building applications have been addressed extensively in the work of Lizana et al. [254], further discussing the prospects and limitations. Table 2.3 showcases a few examples of SHS materials, along with their corresponding thermophysical properties [253].

Table 2.3. Some examples of SHS materials [253]

SHS materials		Maximum operational temperature °C	Specific heat capacity KJ / (J/kg.K)	Thermal conductivity W / (m K)
Liquids	Water	0 -100	4.190	0.598 – 0.670
	Molten Salt (K-NaNO₃)	≤ 230	1.570	0.500
	Transformer Oil	≤ 60	2.090	0.122
	Engine oil	≤ 160	1.880	0.150
	Liquid Sodium	≤ 100	1.385	85.840
Solids	Aluminium	≤ 660	0.945	238.400
	Iron	≤ 1550	0.440	80.200
	Copper	≤ 1500	0.419	372.000
	Lead	20	0.131	35.250
	Limestone	≤ 825	0.740	2.200
	Cast Iron	≤ 1100	0.465	59.300
	Brick	≤1000	0.840	0.500
	Wood	25	1.600	0.120
	Slag	20	0.840	0.570
	Concrete (aggregates)	≤1000	0.720	1.450
	Graphite	≤ 2000	0.610	155.000

2.5.3 Latent heat storage (LHS)

Latent heat storage (LHS) operates by absorbing heat through the process of heat transfer. This heat absorption occurs as the LHS changes phase from one physical state to another within a specific operational temperature range. The phase change process can involve transitions from solid to solid, solid to liquid, solid to gas, liquid to gas or vice-versa [223].

Not many LHS systems are suitable for residential applications. However, the utilisation of LHS in residential buildings primarily aims to reduce temperature rise and fluctuations indoors [232]. Solid-to-solid and solid-to-liquid transition materials are more attractive for residential building applications due to their lower heat of fusion [225]. According to Hasnain [255], the high latent heat of fusion during solid-to-gas and liquid-to-gas phase changes makes LHS systems in this category unsuitable for building applications due to the significant volume change over a large temperature range, necessitating large container requirements. Among the most prevalent materials used in LHS are ice, paraffin wax, and molten salts [256]. PCM are the primary materials used in LHS. Table 2.4 below identifies the range of thermophysical values for organic and inorganic latent heat storage (LHS) materials [228].

Table 2.4. Range of thermophysical values for organic and inorganic LHS materials [228]

	Organic LHS	Inorganic LHS
Density (kg/m^3)	800 - 1200	1500 - 3500
Thermal Conductivity (W/m.K)	0.2 - 0.4	0.5 - 2.0
Specific heat (J/kg.K)	1500 - 2500	1000 - 2000
Latent heat of fusion (kJ/kg)	150 - 250	100 - 300
Latent heat (kJ/m^3)	152	368
Storage mass for 10^6J	5300	4350
Storage volume for 10^6J	6.6	2.7

2.5.3.1 Phase change material (PCM)

PCMs are characterised by their ability to undergo phase changes from one crystalline state to another at a consistent temperature, allowing for significant TES [257]. Moreover, PCMs are commonly used in building applications to shift peak cooling loads to off-peak times [258]. PCM materials are typically classified into organic, inorganic, and eutectics. This classification is based on their molecular composition,

thermophysical properties and structure, as illustrated in Figure 2.33 [259], [260]. The stored heat in PCM transits from sensible heat to latent heat and then back to sensible heat. This process is characterised by high heat of fusion occurrence as the PCM charges and discharges within a certain phase change temperature range [261].
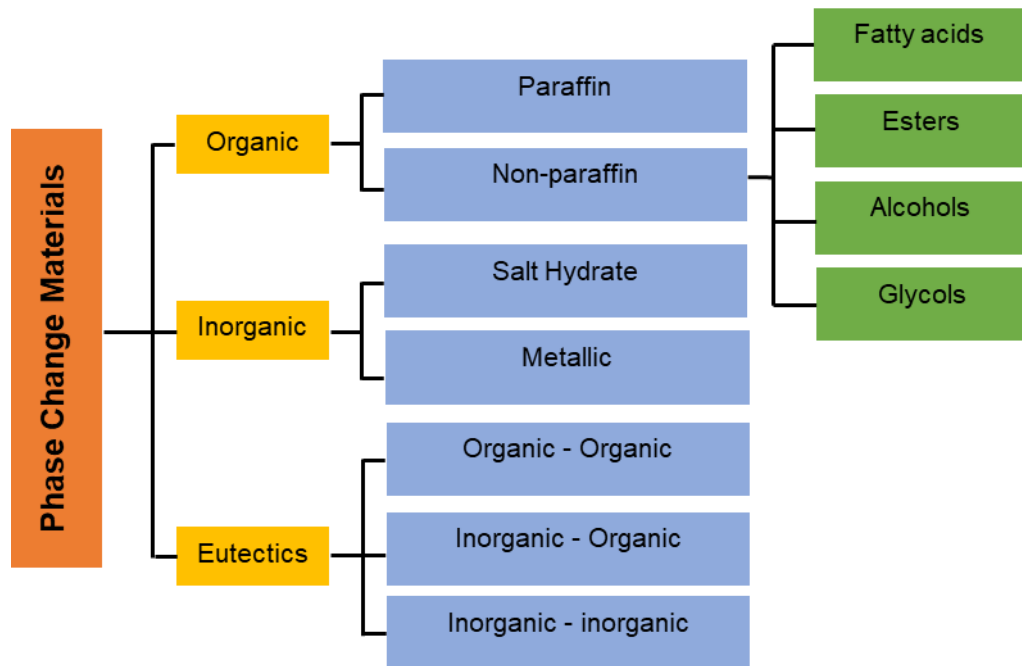
Figure 2.33. Categorisation of PCMs [259], [260]
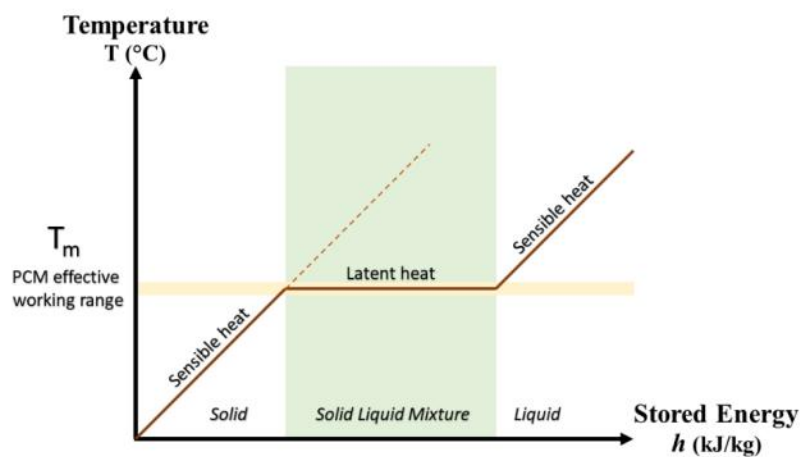
Figure 2.34. Typical sensible and latent heat storage behaviour over time in a PCM [261]

This phase change process is characterised by a decrease or rise in air temperature which occurs as the PCM changes phase from liquid-gas, solid-gas, solid-liquid or solid-solid. Figure 2.34 illustrates PCM's sensible-latent heat storage behaviour.

2.5.3.1.1 PCM selection criteria

It is crucial that during PCM selection, the PCM's kinetic, chemical, thermophysical, environmental, and economic properties are considered, as outlined in references [260], [262], [263]. These properties determine PCM behaviour as summarised in Table 2.5. Hence, regulates the selection of PCMs for various applications.

Table 2.5. Properties that govern the selection of PCMs [260], [262], [263].

Thermophysical properties	
i.	Phase change temperature suitable for building application
ii.	High latent heat of fusion per unit volume so that smaller size of container can be used
iii.	High thermal conductivity to assist in charging and discharging of PCM within the limited time frame
iv.	High specific heat so that additional energy in the form of sensible heat is available to the TES system
v.	Small volume change during phase transition and small vapour pressure at operating temperature to avoid the containment problem
vi.	PCM should melt completely (i.e. congruent melting) during phase transition so that the solid and liquid phases are homogenous
vii.	Thermally reliable (i.e. cycling stability) so that PCM is stable in terms of phase change temperature and latent heat of fusion and can be used in the long run
Kinetic properties	
i.	High rate of nucleation to avoid supercooling of the PCM in the liquid phase
ii.	High rate of crystal growth so that heat recovery from the storage system is optimum
Chemical properties	
i.	Chemically compatible with construction/encapsulated materials
ii.	No degradation after a large number of thermal (freeze/melt) cycles to ensure long operation life
iii.	Non-toxic, non-flammable and non-explosive to assure safety

	iv.	Corrosion resistant to construction/encapsulated materials
Economic properties		
	i.	Cost-effective
	ii.	Commercially available
	iii.	Environmental properties
	iv.	Low environmental impact and non-polluting during service life
	v.	Having recycling potential

While other properties are important criteria, studies have shown that the PCM melting temperature and enthalpy temperature are crucial factors for optimising thermal storage performance. As seen in Figure 2.35 melting temperature and enthalpy temperatures impact how PCMs are grouped range [261], [264].
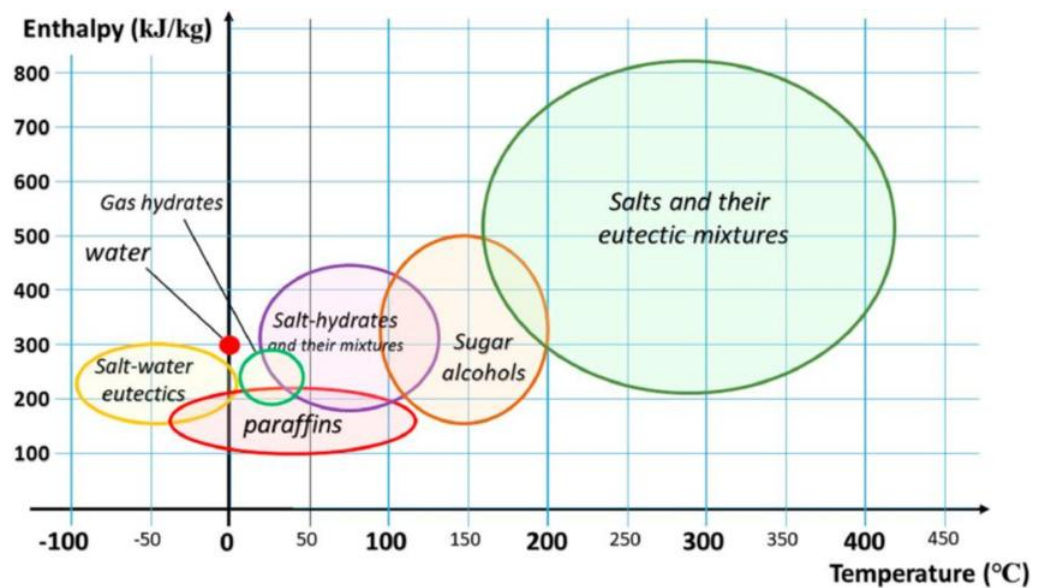
Figure 2.35. PCM grouping based on melting temperature and enthalpy temperature range [261], [264]

Xiao et al. [265] developed a simplified analytic model for PCM optimisation for energy storage by examining the optimal melting temperature and latent heat capacity benefits under Beijing's humid continental climate conditions. Equation 2.4 is derived based on their results.

$$T_m = T_a + \frac{(Q_r + Q_{r,in})}{h_{in.} \Delta T_a . A}$$ *Equation 2.4*

Accordingly, the optimal PCM melting temperature T_m is related to the amount of radiant energy Q_r absorbed by the PCM through the radiation heat transfer rate from indoor heat sources $Q_{r,in}$ and the average indoor air temperature T_a. Where h_{in} is the heat transfer coefficient of the interior surface A.

As outlined in the study conducted by Mehling et al. [266], two main principles influence the effective utilisation of PCM for temperature reduction. Xu et al. [267] developed a simulation model to assess the thermal performance of a PCM floor. Based on the results, it is observed that temperature swings reduce. This occurs when the PCM melting temperature aligns with the average indoor air temperature. However, for this temperature stabilisation to occur, it is important that the thermal conductivity of the selected PCM be more than 0.5 W/(m K), with the heat of fusion exceeding 120 kJ kg.

Furthermore, if the PCM melting temperature exceeds the room temperature, it reduces temperature peaks because the temperature drops, or rise cannot surpass a specific temperature threshold. Consequently, selecting a PCM with a melting temperature higher than the indoor temperature is advantageous to prevent temperature peaks, especially in hot climates. Essentially, PCM is generally applicable in locations with diurnal temperatures ranging between 12 – 15 K. Tropical savannah climates exhibit diurnal temperatures with the range of 15 – 20 °C or more. This provides substantial fluctuations between daytime highs and nighttime lows, which is suitable for PCM performance.

Furthermore, Barreneche et al. [268] developed a novel PCM selection criteria database system for choosing PCM for building applications based on their thermo-properties. The "PCM for comfort" database is categorised into different PCM groupings based on various PCM

formulations, establishing a thermal comfort range of 18 °C to 29 °C as shown in Figure 2.36.

Furthermore, several studies have emphasised the suitability of organic PCM and paraffins for passive cooling applications. This preference is because of their eco-friendliness and low toxicity properties. This category of PCMs also offer other advantages. These include recyclability, ease of use, chemical stability, non-corrosiveness, high heat of fusion, compatibility with building materials, and minimal volume change during melting [269].
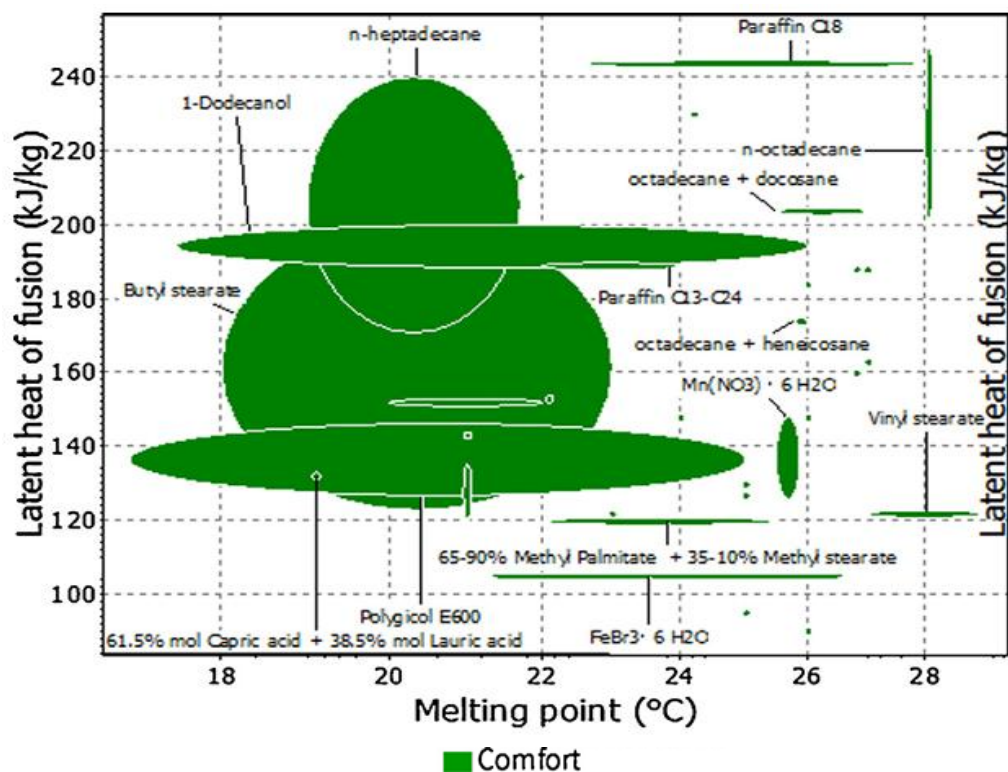
Figure 2.36. "PCM for comfort" selection database for different building applications

Moreover, numerous organic PCMs within the melting temperature range of 25°C to 29°C have undergone extensive investigation [270]. Amongst which the PCM performance study conducted by Bimaganbetova et al. [271] highlighted the potential of utilising PCMs within this range for passive cooling in tropical savannah climates. Bimaganbetova et al. [271]

conducted a series of numerical simulations on PCM performance in HVAC systems across various cities in tropical savannah climates. The results from the study showed that when PCM 25 - PCM 29 were integrated into the HVAC system, a 2.76 °C indoor temperature drop and a 68.63 % reduction in cooling energy consumption were achieved. This implies that PCMs within this melting temperature range between 25 - 29 °C can potentially be utilised for hot climates characterised by low wind conditions, such as sub-Saharan tropical savannah climates. However, a careful PCM selection remains crucial.

Kuznik et al. [269] and Memon [260] also presented a detailed analysis of the thermophysical properties of several organic PCMs and paraffins with different melting temperatures falling within this specified range as presented in Table 2.6. Accordingly, it has been identified that vinyl stearate, RT 27, and RT 28 HC paraffins offer a melting temperature range between 27 - 29 °C, encompassing three distinct temperature points within this range. These findings are consistent with the study by Bimaganbetova et al. [271], which supports the use of PCMs with melting temperature ranges of 27 – 29 °C for effective passive cooling and thermal storage in climates with significant daily temperature variations, such as tropical savannah climates.

Table 2.6. Organic PCMs in the literature [260], [269].

PCM type	Temp of Fusion, T_f	Latent Heat of Fusion, H_f	Heat Capacity (Solid), C_{ps}	Heat Capacity (Solid), C_{pl}	Thermal Conductivity (Solid), K_s	Thermal Conductivity (liquid), K_l
N-Octadecane	27	243.5	1.934	2.196	0.358	0.148
Octadecane	28-28.1	244 – 250.7				
RT27	26-28	179	1.8	2.4	0.2	0.2
RT 28 HC	27-29	245	1.65	2.2	0.2	0.2

MICRONAL26	26	110	-	-	-	-
GR27	28	72	-	-	0.15	0.15
MICRONAL 5001	26	110	-	-	-	-
MPCM28-D	28	180-195	-	-	-	-
U3	28	244	-	-	0.28	0.22
Octadecyl thioglycolate	26	90				
Lactic acid	26	184				
1-Dodecanol	26	200				
Vinyl stearate	27-29	122				
Paraffin C18	28	244				
Methyl palmitate	29	205				

2.5.3.1.2 Encapsulation of PCM

Based on the review by Faraj et al. [228], paraffins exhibit lower enthalpy compared to other types of PCMs. In their study, Souayfane et al. [272] identified other limitations of paraffins associated with low thermal conductivity (about 0.2 W/mK) and low density (less than 103 kg/m³). However, these shortcomings can be effectively addressed through encapsulation techniques. Significant progress has been made in improving PCM thermal conductivity through impregnation and encapsulation.

Cabeza et al. [273] compared the energy density of an 8.8 cm × 31.5 cm encapsulated cylindrical aluminium container with three types of sodium acetate trihydrate PCM modules. At a 1 K temperature difference, energy density increased by 40 %, 57.2 %, and 66.7 % for PCM types 2, 4, and 6, respectively. At an 8 K temperature difference, the increases were 6 %, 12 %, and 16.4 %. This implies that the impact of encapsulation diminishes as the temperature change increases. The findings also established a thermal storage duration of 10 - 12 hours due to the implementation of the encapsulated cylindrical aluminium containers with the PCMs.

According to Salunkhe et al. [274], outcomes from many studies suggest that, in addition to enhancing thermal conductivity, PCM encapsulation can reduce reactivity, improve physical and chemical stability during thermal cycling, enhance phase transition performance, and prevent leakages. The morphology of different encapsulated PCM was presented in the review by Ghasemi et al. [275] and Alva et al. [276]. They identified that simple encapsulated PCMs (EPCMs) usually have spherical, tubular, or oval shapes, while irregular EPCMs are mononuclear. Other types include EPCMs with multiple distinct cores inside a shell and EPCMs with particles embedded in a continuous matrix, as shown in Figure 2.37.
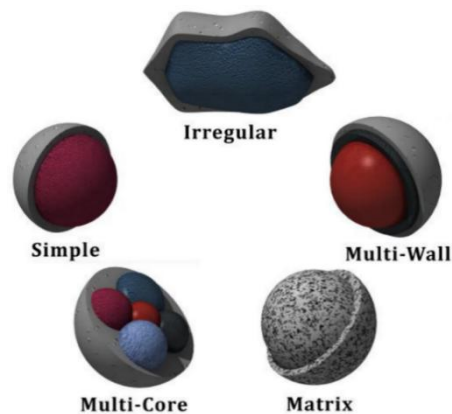
Figure 2.37. Different EPCM morphologies [275]

Alva et al. [276] suggested some other viable forms of micro-encapsulation as mononuclear spheres, polynuclear structures, multi-layered walls, matrices, and multi-shell slurries as shown in Figure 2.38.
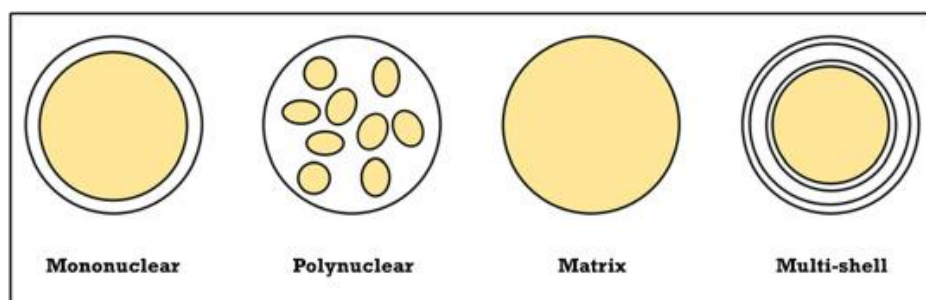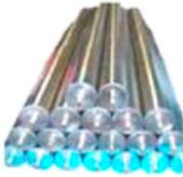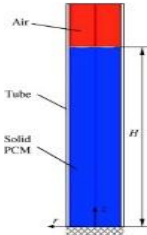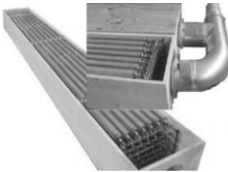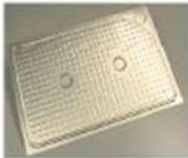
Figure 2.38. Forms of PCM shell encapsulation [276]
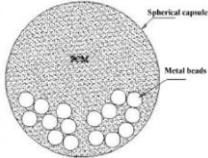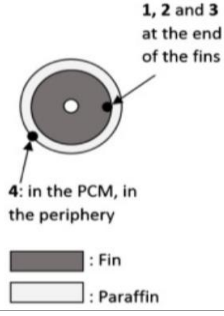
It concluded that while the shell exhibited a higher temperature than the PCM, encapsulation had an insignificant impact on the PCM's thermal stability. However, shell porosity negatively affected performance, especially in high-temperature applications. Therefore, the choice of shell composition, whether organic, inorganic, or hybrid, is crucial before the encapsulation process.
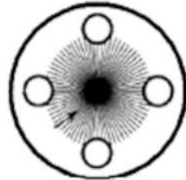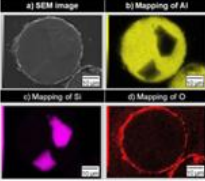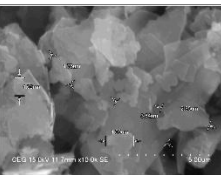
Meanwhile, in the experiment conducted by Farid et al. [277], it was found that impregnating PCMs in flat aluminium panels was found to increase heat flow by 2%, although it decreased the interfacial bond. Fiedler et al. [278] conducted a numerical study on PCM-impregnated cellular porous matrix metals (copper, aluminium, and diamond-coated copper) using Lattice Monte Carlo analyses. According to the results, thermal conductivity increased by up to 80%, with the diamond-coated matrix performing the best. Liu et al. [279] conducted experiments on the impact of nanocarbon aerogel-based bead encapsulation on PCM thermal conductivity and shape stability. The results indicated that heat conduction was 25 times faster with the encapsulation than when pure paraffin was at a phase transition enthalpy of 187-188 $J \cdot g^{-1}$. Table 2.7 summarises the outcomes of several studies that explored PCM encapsulation and impregnation techniques. These studies primarily investigated the application of these techniques to enhance PCM thermal conductivity and their overall performance.
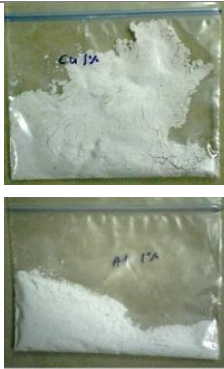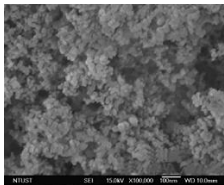
Table 2.7. Different techniques used in studies to improve PCM thermal conductivity

Ref.	Study method	PCM encapsulation and impregnation techniques	Examples of PCM studied	Outcomes of the studies

[278]	Numerical study / Lattice Monte Carlo analyses	Impregnation of high conductivity cellular porous matrix metals (copper, aluminium and diamond-coated copper)		80% increase in PCM thermal conductivity with copper matrix in comparison to aluminium matrix. Diamond-coated matrix performed best.
[280]	Numerical (PISO vs. SIMPLE and PRESTO! vs. Body-Force-Weighted schemes) and Experiment	Impregnating PCM in module cylindrical beams		Natural convection improved during PCM melting due to heat transfer enhancement from the encapsulation. As the PCM melted. The mushy zone constant $C=10^8$ best simulated the melting in the vertical circular tube which also reduced the PCM volume. Variations in pressure discretization schemes further influence the heat transfer dynamics and melt fraction accuracy.
[281]	Experiment / Numerical	Impregnating PCM in module cylindrical/rectangular beams		The results determined the impact of encapsulation shape and tube arrangements on the efficiency of the heat exchanger and provided suggestions for future design improvements.
[277]	Experiment	Impregnating PCM in flat panels		Aluminium flat panel encapsulation increased heat flow by 2% but also decreased the interfacial bond.

				Increasing the amount of aluminium foam further reduced the heat storage time.
[282]	Experiment	Placing metal structures – lesser copper rings in PCM (copper rings of sizes 0.5 cm and 1 cm, with volumetric percentages of 3%, 6%, and 10%)		Using 1 cm copper rings at 3% and 6% volumetric percentages reduced PCM melting rates compared to 0.5 cm rings, while a 10 % volumetric percentage increased the melting rate.
[279]	Experiment	Placing metal beads in PCM	PCM beads	The nanocarbon aerogel-based bead encapsulation significantly improves the PCM thermal conductivity and shape stability. This achieves phase transition enthalpies of 187-188 J·g^{-1}, with 25 times faster heat conduction than in neat paraffin.
[283]	Experiment / Numerical	Placing metal fins in PCM		The encapsulation of PCM in an ENG matrix significantly enhanced the thermal performance, resulting in an Overall Heat Transfer Coefficient (OHTC) of about 3000 W m^{-2} K^{-1}. The composite material's thermal conductivity became approximately 100

				times greater than that of the PCM without encapsulation.
[284]	Experiment / Numerical	Using low density highly conductive materials (carbon fibres) in PCM		The encapsulation of the tube with fibres significantly enhanced the heat exchange rate during both the charge and discharge processes. The fibres reduced the time required to reach a heat exchange rate of 0.1 kW by 10-20% during charging and about 30% during discharging.
[285]	Experiment	Microencapsulating PCM (Al-Si alloy microspheres with α-Al$_2$O$_3$ balls or beads) to improve heat transfer surface.		Al-Si alloy microspheres with α-Al$_2$O$_3$ encapsulated shells significantly improved the thermal stability and durability. At high temperatures up to 573°C latent heat reached 247 J g^{-1}. This shows great promise for future energy and chemical processes.
[286]	Experiment / T method	Dispersing graphite flakes in PCM (molten salt)		The natural graphite flakes (NGF) significantly shortened the solidification duration and reduced the enthalpy by 13 % at 3 wt.%.
[287]	Experiment	Dispersing aluminium/coppe		TES performance improved with the

		r particles in PCM		inclusion of the D-Mannitol (DM) with 2% micron-sized copper particles. Total phase change time by 22% during charging and 16% during discharging compared to plain DM. Improved enthalpy of fusion, phase transition temperature, and thermal stability.
[288]	Experiment	Dispersing silver nanoparticles in PCM		The melting temperature was reduced based on silver nanoparticles of 0.05% and 0.1% mass fraction.

Despite that encapsulation and impregnation increases PCM thermal conductivity, it is noted that these enhancements may come at the expense of reducing the PCM's heat storage capacity. Therefore, it is recommended that the mass/volume fraction of such encapsulated or impregnated PCMs be carefully examined [260].

Paraffins PCM have been proposed in various studies as suitable for building cooling applications due to their chemical stability, non-corrosive and non-toxic properties, and minimal supercooling during solidification [289]. Meanwhile, research indicates that paraffin encapsulation with either aluminium, stainless steel, or copper exhibits the best thermal conductivity enhancement and material compatibility. Detailed in Table 2.8 is the comparative analysis conducted by Kahwaji et al. [290] to evaluate the chemical compatibilities of PCMs with different materials. Corrosion rates were examined at 75 $^{\circ}$C except for Al laminate foil. Aluminium and copper were identified to have had good chemical compatibility with paraffin PCM. The encapsulation compatibility of other metals with paraffin PCM was also assessed. But among all the plastic

encapsulation materials tested, only polycarbonate, Type I PVC, and ABS plastic demonstrated superior compatibility with paraffin PCM. Encapsulation of paraffin suggests a greater opportunity for use as TES or combined with other passive cooling systems.

Table 2.8. Chemical compatibility chart for six paraffin PCM (Kahwaji et al., 2018)

*	Recommended for long term use (|C&|< 10mg cm-2 yr-1)
!	Recommended with caution (10≤|C&|< 50mg cm-2 yr-1)
x	Not recommended for use (|C&|≥ 50mg cm-2 yr-1)

	6061 Aluminium	6063 Aluminium	5052 Aluminium	304 stainless Steel	316 stainless Steel	101 Copper	110 Copper	Ni C7521	Mg AZ91D	Polycarbonate Film	Polypropylene	Cast Acrylic	Type 1 PVC	Silicone Rubber	ABS Plastic	Nylon
Nonadecane	*	*	*	*	*	*	*	*	*	*	x	!	*	x	!	!
Eicosane	*	*	*	*	*	*	!	*	*	*	x	!	*	x	*	x
Docosane	*	*	*	*	*	*	!	*	*	*	x	!	*	x	*	x
Paraffin Wax 48	*	*	*	*	*	*	*	*	*	*	x	!	*	x	*	!
Paraffin Wax 52	*	*	*	*	*	*	*	*	!	*	x	!	*	x	!	!
Paraffin Wax 58	*	*	*	*	*	*	*	*	!	*	x	*	*	x	*	!

2.5.3.2 PCM-integrated passive cooling systems

Several studies have investigated the TES impact of PCM integration with passive cooling systems. Osterman et al. [291] identified that PCM integration with cooling systems can be categorised into four groups: PCM in free cooling applications, encapsulated PCM systems, PCM in air-conditioning (AC) systems, and PCM in sorption cooling systems. Other studies have also explored PCM integration in building envelopes [292], PCM in free cooling applications [293] and PCM as heat storage

units in cooling systems [291]. Table 2.9 provides an additional summary of reviews conducted studies on PCM integration in various building applications for passive cooling [62]. Furthermore, PCM integration with passive ventilation systems has been extensively studied, although less research conducted on passive ventilation systems such as the windcatcher.

Table 2.9. Reviews carried out on PCM integration in different building applications [62]

Review focus	Study Outcomes	Gaps in literature/limitations/recommendations	Ref.
Commercial PCM in building applications	Possibility to use most commercial PCM in buildings. PCM require little or no structural modification for integration in passive cooling systems and buildings	Overcoming the limitation caused by lowering latent heat storage per unit weight to realise increased PCM thermal conductivity.	[270]
Types of PCM used in energy storage applications in buildings	Thermo-physical properties affect PCM selection for building cooling applications	Future studies to focus on finding solutions to PCM sub-cooling, segregation and PCM compatibility with other materials	[294]
PCM selection for building applications and encapsulation methods	Encapsulation improves PCM cooling performance	Future studies should focus on the selection criteria of active and passive PCM-based cooling systems	[295]
Experimental and numerical studies of the effect of PCM on building energy performance.	PCM is good for buildings where shifting peak loads is needed. PCM decreases indoor temperature fluctuation	The problem of incomplete PCM solidification during the discharging phase. PCM low convective heat transfer	[272]
Passive cooling simulation tools such as Energy	Possibility to Implement PCM passive cooling in different climatic conditions	Insufficient studies towards more advanced numerical modelling for	[296]

Plus, TRNSYS,	PCM-based ventilation
ESP-r	cooling performance

2.5.3.3 PCM-integrated passive ventilation systems

The ability of PCMs to absorb and release substantial amounts of latent heat while exhibiting minimal temperature variation [297] particularly offers the opportunity to reduce and stabilise air temperature for effective passive cooling [298]. The study conducted by Lizana et al. [299] highlighted the advantages of integrating PCM into ventilation systems to enhance PCM-air heat transfer and reduce the required amount of PCM for cooling in buildings. However, determining the size and arrangement of PCM is crucial for enhancing the efficiency of TES in a ventilation system. Additionally, the arrangement of PCM impacts the energy charging rate in any system, making an appropriate PCM arrangement beneficial for improving the overall performance of the ventilation system. For example, in a numerical study conducted by Liang et al. [300], the impact of PCM plate configuration relative to airflow rates on the rate of heat flow was examined. The study observed that a 36.34% and 55.97% increase in the charging/discharging process was achieved with optimised PCM flat plate arrangements.

Likewise, appropriate sizing of PCM is crucial for achieving optimal thermal performance when integrated into passive ventilation systems. Hu et al. [301] conducted a performance analysis on a PCM heat exchanger integrated into a window, which pre-cooled the supply air into the building. The study revealed that increasing the thickness of the PCM heat exchanger to 5 mm enhanced overall thermal performance and improved indoor cooling. Hence, a ventilation air temperature reduction of 6.5 °C was achieved at 3.9 hours of pre-cooling effective time. In an experiment by Weinläder et al. [302], a PCM integrated into a ventilated ceiling demonstrated improved heat transfer at an airflow rate of 300 m3/h, resulting in a 2 K drop in operative temperature. These findings

underscore the practicality of incorporating PCM into passive ventilation systems. However, according to O'Connor et al. [303], there have been limited efforts in utilising PCMs in passive ventilation systems, indicating significant study potential for PCM integration in passive ventilation systems such as windcatchers.

2.5.3.4 PCM integrated with windcatcher system

Seidabadi et al. [49] conducted a heat transfer study on an integrated two-sided windcatcher with PCM using MATLAB software. As indicated in Figure 2.39, the PCM was placed on the interior of the 35 cm thick Styrofoam-insulated brick windcatcher wall. As ambient air passed over the PCM, the results demonstrated a 15 K reduction in air temperature, maintaining a 36 °C air temperature for 7 hours between 12:00 P.M. and 7:00 P.M. However, reduced air-PCM heat transfer was still observed due to the PCM's location inside the windcatcher wall.
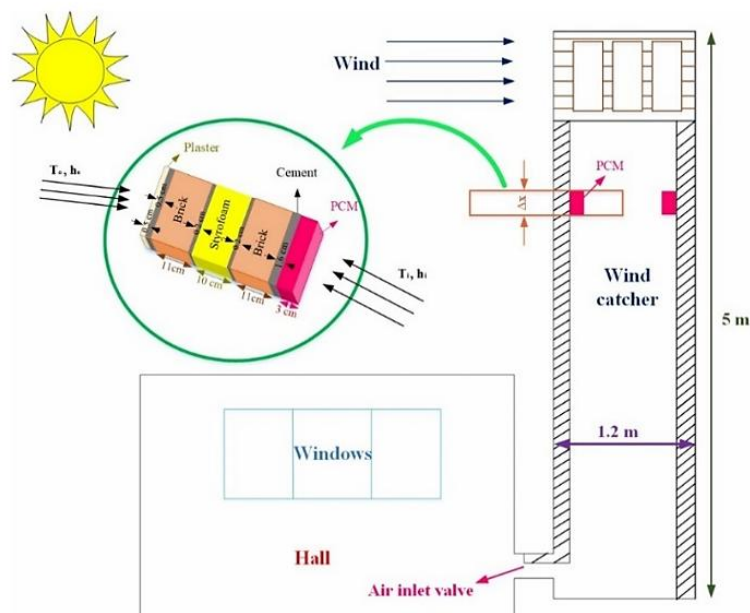
Figure 2.39. PCM placed on the windcatcher interior wall [49]

In a study by Lizana et al. [299], an improved air-PCM heat transfer rate was achieved when the PCM was directly integrated into the airstream of a ventilated cooling ceiling. Rouault et al. [281] conducted a numerical study on a latent heat TES (LHTES) ventilation system, which revealed

a strong correlation between the shape of the PCM profiles, the arrangement of PCM within the system, the air-PCM heat transfer rate, and the performance of close contact melting. Abdo et al. [50] studied the cooling performance of an integrated two-sided windcatcher with PCM and achieved a temperature reduction of 9.85 % (2.78 °C) when PCM was placed directly in the airstream.

Despite the positive outcomes from previous studies that investigated different windcatcher types, there is a lack of research specifically examining the TES performance of multi-directional windcatcher systems. Moreover, a notable absence of studies focusing on the cooling and TES performance of solar-fan-assisted multi-directional windcatchers integrated with PCMs is evident. Additionally, the impact of wind speed on the TES performance of multi-directional windcatcher hybrid ventilation systems remain poorly understood and has not received sufficient attention in research endeavours.

2.6 Chapter's concluding remarks

Passive cooling and ventilation systems represent promising solutions for achieving indoor comfort in hot climates. While the need for dehumidification may not be necessary for some hot climates, it is crucial to acknowledge both cooling and ventilation as fundamental to building occupants' indoor comfort in many hot climates. Hence, buildings can optimise indoor environmental quality and thermal comfort by combining the use of passive cooling and ventilation systems. However, the most critical parameter that affects the effectiveness of passive cooling systems in tropical savannah climates is the ability to stabilise fluctuating indoor temperatures. While passive ventilation systems that can function under minimal outdoor winds are desirable. The review explored studies on ground cooling, radiative cooling, and evaporative cooling systems, highlighting their advantages and potential based on various

performance scenarios in hot climates. Meanwhile, in terms of indoor ventilation, the literature reviewed passive ventilation systems as categorised into two broad categories either solar-induced ventilation systems or wind-driven ventilation systems.

2.6.1 Performance and limitations in the passive cooling systems discussed in literature

- Evaporative cooling systems can reduce PM2.5 by 10-40 % and PM10 by 50 % but are effective only under < 25 °C wet-bulb outdoor temperatures, introducing unwanted humidity. In climates with more than 25 °C wet-bulb temperatures like tropical savannah climates, evaporative cooling may promote mosquito breeding, legionnaire bacteria, and system corrosion.

- Radiative cooling past research has focused mainly on the impact of radiative surfaces and solar radiation on radiative cooling system performance. In low-humidity climates, radiative cooling performs better. However, in hot humid climates, radiant heat loss is lower, reducing efficiency to 40-50 W/m^2. Changes in sky conditions affect performance, impacting cool air storage, especially during intense solar radiation.

- Ground cooling relies on underground temperatures lower than ambient air. In extremely hot climates, achieving low enough underground cooling may pose a challenge impacting on effectiveness of ground cooling in such extreme climatic conditions. Heat dissipaters can enhance ground cooling performance to overcome this limitation. However, humidity buildup in earth pipes in hot, humid climates limits effectiveness. Notwithstanding balancing ventilation, installation costs, and energy consumption still pose a challenge to ground cooling system utilisation.

2.6.2 Performance and limitations in the passive ventilation systems discussed in the literature

- Passive ventilation systems can be categorised into solar-induced (e.g., Trombe wall, solar chimney) and wind-driven (e.g., wind cowls, windcatchers).

- Solar-induced systems rely on temperature differences to facilitate ventilation, while wind-driven systems use induced wind speeds, contributing 76% more effectively to ventilation.

- Four-sided multi-directional windcatchers can be used in low wind conditions, and urban areas and are the most common types used as commercial windcatchers.

- Windcatcher performance has been mainly assessed through experiments, numerical studies, field tests, and wind tunnels.
  The performance of windcatcher ventilation is based on winds, wind angles, air temperature and pressure. Accordingly, optimal windcatcher ventilation can be achieved at a 0° wind angle. In low wind conditions, the utilisation of a fan can help address pressure imbalances and irregular air flow, improving windcatcher ventilation.

- Windcatchers can only achieve minimal temperature drops in hot climates. To improve on this cooling deficiency, other passive cooling systems such as evaporative cooling, and heat pipes can be employed. However, heat pipes are favoured over evaporative cooling for water conservation and in climates with high humidity.

- Windcatchers even if cooling deficiency is improved, are still limited in their ability to stabilise indoor temperatures in climates with fluctuating outdoor conditions such as that of sub-Saharan African tropical savannah climates.

2.6.3 Performance and limitations of TES discussed in the literature

- TES are either sensible heat storage, latent heat storage, thermochemical energy storage, or in a combined form.
- The thermal heat energy of PCM makes them advantageous for integration in ventilation systems like the wind catcher to pre-cool and post-cool air.
- PCM melting temperature and enthalpy temperature are a crucial factor for optimising thermal storage performance.
- PCM with melting temperatures between 25-29°C (PCM 25 – PCM 29) is the most suitable for passive cooling applications in buildings located in the sub-Saharan Africa tropical savannah climate.
- Paraffin PCM fall within the range of "PCM for comfort" and are mostly used for passive cooling in buildings and their thermal conductivity properties can be improved by encapsulation with aluminium, stainless steel and copper without experiencing corrosion.
- Aluminium and copper have good chemical compatibility with paraffin PCM. While polycarbonate, Type I PVC, and ABS plastic can also be used as encapsulation materials.
- Both RT27 and RT28HC paraffin PCM were studied and have been identified to be the PCM having the closest melting temperature which is within the comfort range target for buildings in tropical savannah climates. However, the latter, RT28HC is the higher-performing paraffin in comparison with RT27 and is preferred.
- The arrangement and sizing of PCM in the air channel of a ventilation system affect the PCM energy charging rate. Hence, the PCM efficiency improves with the right sizing and arrangement.

- PCMs can offer streamlined integration that can improve the TES performance of windcatchers.

2.7 Research gaps

- Tropical savannah climates have been largely overlooked in windcatcher research, particularly those adaptable to residential buildings.
- While windcatcher cooling performance studies exist, studies focusing on improving windcatchers' ability to consistently reduce and stabilise supply air temperature are scarce.
- Few windcatcher studies integrating PCM focus on indoor temperature reduction and air stabilisation, with limited discussion on the role of external air temperature in enhancing or limiting performance.
- Research on the TES performance of multi-directional windcatcher systems is lacking despite previous studies on different windcatcher types.
- While a few CFD studies have investigated windcatcher thermal storage improvement, the impact of PCM arrangement in a multi-directional windcatcher still requires further studies.
- Particularly, there is a notable absence of studies on the combined ventilation, cooling, and TES performance of solar-fan-assisted multi-directional windcatchers integrated with encapsulated PCMs under typical sub-Saharan African tropical savannah climates in the existing literature.

Chapter 3

3 The proposed EPCM-HMW system

3.1 Overview of chapter

Chapter 2 (section 2.7) identified research gaps in existing studies, highlighting the need for new research on solar-fan-assisted multi-directional windcatchers integrated with encapsulated PCMs. These gaps emphasised the importance of improving windcatcher ventilation, cooling, and thermal storage performance in sub-Saharan African tropical savannah climates. To address these gaps, this chapter introduces and describes the novel EPCM-HMW system.

The methodological approach adopted to develop and assess the EPCM-HMW is detailed in this chapter. Firstly, the conceptual physical model development of the system is highlighted, followed by the theoretical model formulation, and concluding with the specific computational fluid dynamics (CFD) simulation approach utilised in the study, within the context of other CFD numerical methods. To maintain a logical flow, the contents presented in this chapter are organised in line with these three distinct sub-sections as illustrated in Figure 3.1. The chapter provides insights into the rationale behind the EPCM-HMW system design choice, and the methods adopted for its investigation.
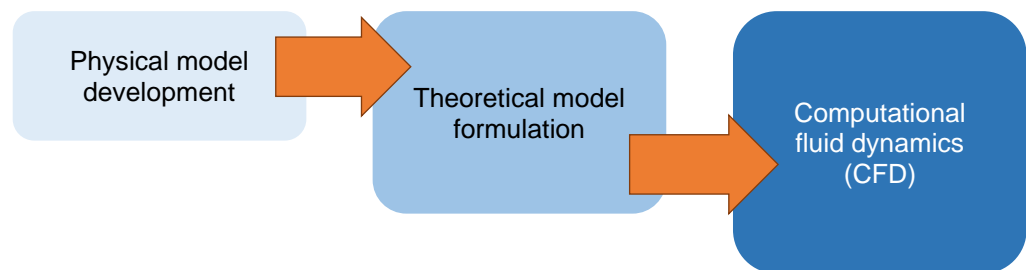
Figure 3.1. Sequential flow of Chapter 3 discussions

3.2 Physical model development

The physical model development of the EPCM-HMW system involved defining and conceptualising the overall system. This entailed specifying the technical characteristics and operational mechanisms of each system component and ensuring seamless integration with the overall operational concept of the entire system. Additionally, this phase explored the rationale behind the system design for its effective operation within the intended climatic environment.

3.2.1 System description and components definition

The EPCM-HMW system integrates a solar fan-assisted multi-directional windcatcher with EPCM-Ts. Hence, the EPCM-HMW system comprises of three main components:

   i. A multi-directional windcatcher
   ii. A wall-mounted solar axial fan
   iii. EPCM-Ts

The multi-directional windcatcher component is divided by an X-shaped partition into four quadrants as shown in Figure 3.2. This partitioning prevents crossflow within the airstreams, ensuring that incoming and outgoing air remain separated. One quadrant is designated for supply airflow, while the others are for exhaust airflows. The airflow patterns within each quadrant may vary based on the incident wind direction and the positions of the EPCM-Ts within the airstreams. Additionally, as shown in Figure 3.2, the windcatcher louvres are angled at 45 $^{\circ}$, aligning with the standard louvre angles used in commercial windcatchers [304]. This angle is also consistent with previous windcatcher studies conducted by Calautit et al. [305].
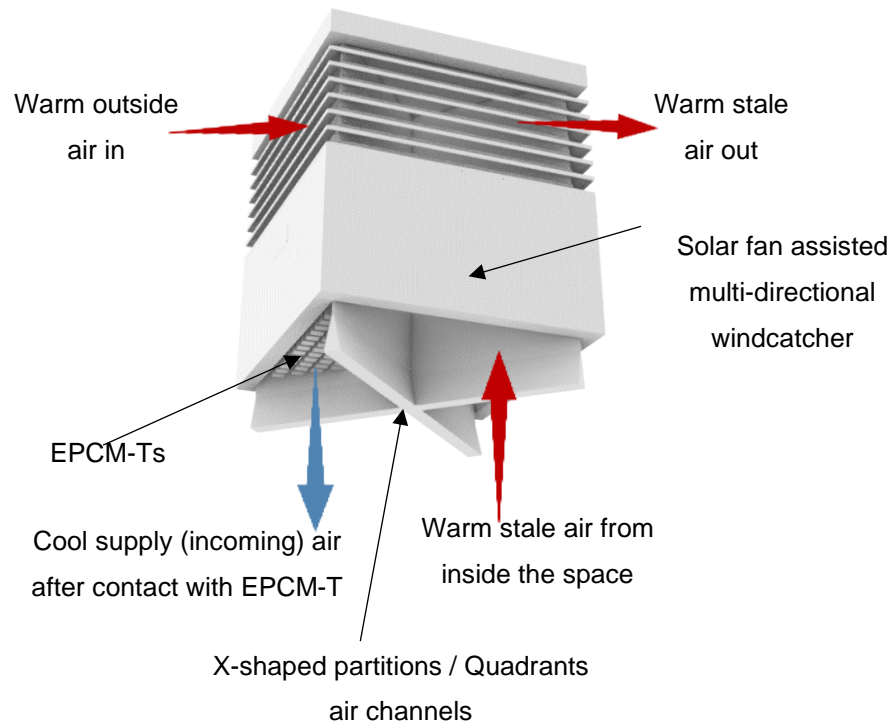
Figure 3.2. The EPCM-HMW System

The EPCM-Ts are vertically positioned within the airstreams of the EPCM-HMW system to enhance the PCM-air contact surface area. Mounted on the windward side of the system, directly above the EPCM-Ts, is a wall-mounted solar axial fan. Operating in hybrid ventilation mode, the fan's static pressure capacity effectively mitigates airflow resistance and fluctuations caused by the presence of the EPCM-Ts within the airstreams. Additionally, the fan's operation enhances air movement, thereby improving PCM-air heat transfer. Table 3.1 shows the dimension details of the windcatcher and EPCM-T components base case models. The conceptual coupling of all the components to form the EPCM-HMW system is graphically shown in Figure 3.3.

Table 3.1. Detailed dimensions of the windcatcher and the EPCM-T components base case models.

component	dimension type		value	unit
Windcatcher base model	length of windcatcher	l_w	1.4	m

	width of windcatcher	w_w	1.4	m
	height of windcatcher	h_w	1.7	m
	the thickness of the windcatcher wall	D_w	0.2	m
	number of windcatcher air vents/side	W_{vents}	7	nos.
Selected EPCM-T base model	length of EPCM-T	l_p	0.500	m
	width of EPCM-T	w_p	0.050	m
	breadth of EPCM-T	b_p	0.060	m
	EPCM-T profile thickness	T_p	0.001	m
Solar wall-mounted axial fan	solar fan opening measured on windcatcher wall	$D_{s\text{-}w}$	0.110	m
	ventilation capacity (m³/ h)	V_c	60	m³/ h
	pressure jump (Pa)	P	10	Pa
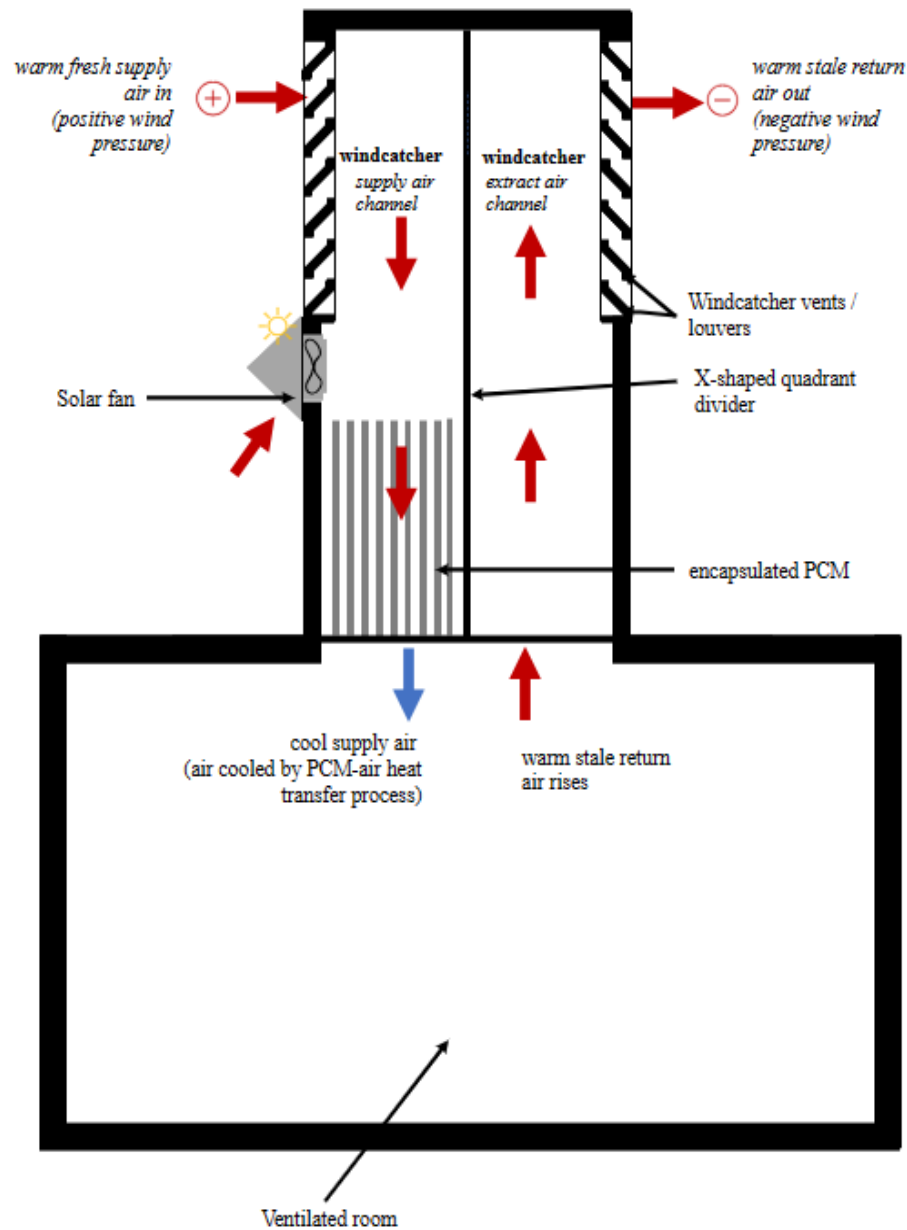
Figure 3.3. Main components within the EPCM-HMW system including the system's airflow and cooling operational concept.

3.2.2 Conceptualisation and development of the EPCM-HMW system

The EPCM-HMW system was developed in two stages. First, EPCM-T profiles were conceptualised and designed as the basis for the initial

EPCM-T parametric study, leading to the selection of the EPCM-T profile used in the system.

3.2.2.1 EPCM-T geometry designs

Four different EPCM-T designs were developed: shell-tube rectangular EPCM-T (model 1A), and shell-tube cylindrical EPCM-T (model 2A), rectangular EPCM-T (model 1B), cylindrical EPCM-T (model 2B). These designs were evaluated for integration into the EPCM-HMW system. Figures 3.4 to 3.7 depict graphical representations of each design, while Tables 3.2 to 3.5 provide detailed specifications and dimensions.

(a)

(b)
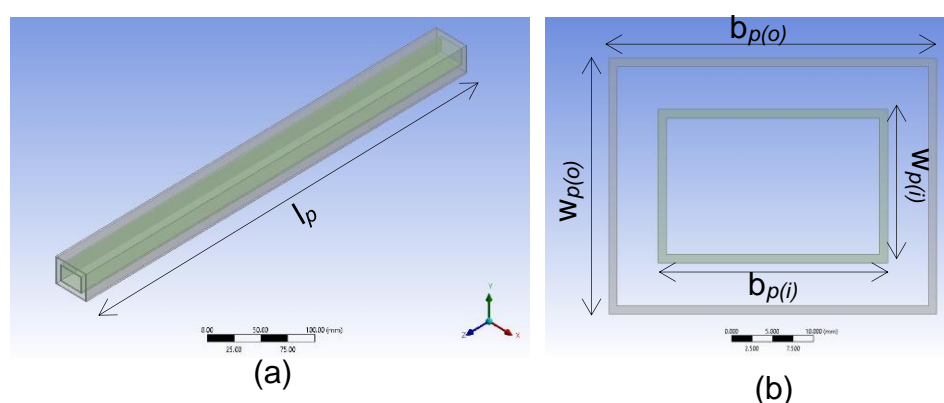
Figure 3.4. EPCM-T shell-tube rectangular EPCM-T (model 1A): (a) 3D-view (b) plan view

Table 3.2. Dimension specifications of the EPCM-T shell-tube rectangular EPCM-T (model 1A).

EPCM-T sample		dimension type		value	unit
EPCM-T	length of EPCM-T		l_p	0.500	m
shell-tube	outer tube	width	$w_{p(o)}$	0.050	m
rectangular		breadth	$b_{p(o)}$	0.060	m
EPCM-T	inner tube	width	$w_{p(i)}$	0.040	m
(model 1A)		breadth	$b_{p(i)}$	0.050	m
	encapsulation thickness		T_p	0.001	m
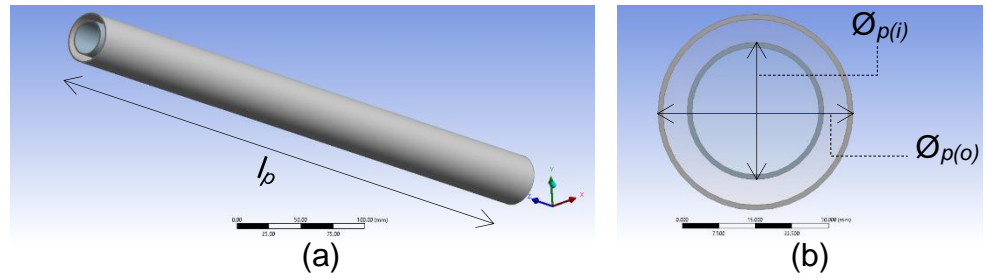
Figure 3.5. EPCM-T shell-tube cylindrical EPCM-T (model 2A): (a) 3D- view (b) plan view

Table 3.3. Dimension specifications of the EPCM-T shell-tube cylindrical EPCM-T (model 2A).

EPCM-T sample	dimension type			value	unit
EPCM-T shell-tube cylindrical EPCM-T (model 2A)	length of EPCM-T		l_p	0.500	m
	outer tube	diameter	$\varnothing_{p(o)}$	0.100	m
		radius	$r_{p(o)}$	0.050	m
	inner tube	diameter	$\varnothing_{p(i)}$	0.080	m
		radius	$r_{p(i)}$	0.040	m
	encapsulation thickness		T_p	0.001	m
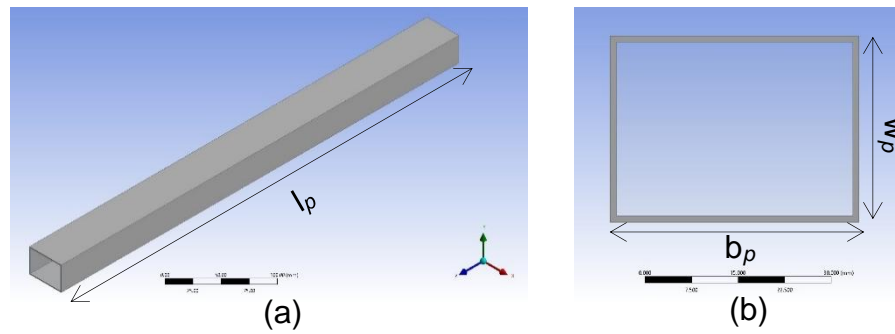
Figure 3.6. EPCM-T rectangular EPCM-T (model 1B): (a) 3D- view (b) plan view

Table 3.4. Dimension specifications of the EPCM-T rectangular EPCM-T (model 1B).

EPCM-T sample	Dimension type		value	unit
EPCM-T rectangular	length of EPCM-T	l_p	0.500	m
	width	w_p	0.050	m
	breadth	b_p	0.060	m

| EPCM-T (model 1B) | encapsulation thickness | T_p | 0.001 | m |

(a)   (b)
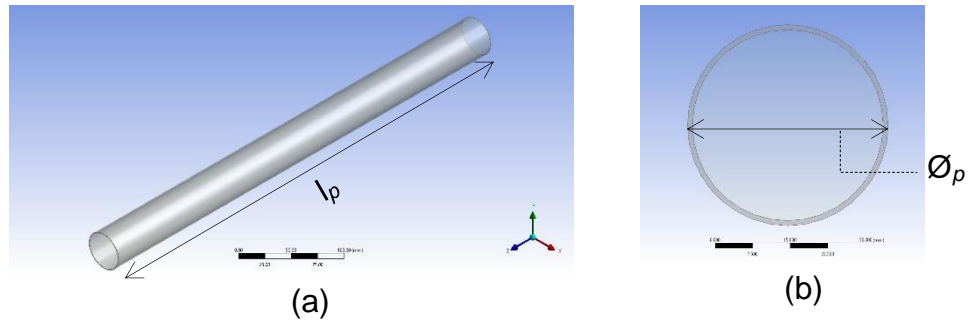
Figure 3.7. EPCM-T cylindrical EPCM-T (model 2B): (a) 3D-view (b) plan view

Table 3.5. Dimension specifications of the EPCM-T cylindrical profile sample.

EPCM-T sample	dimension type		value	unit
EPCM-T cylindrical EPCM-T (model 2B)	length of EPCM-T	l_p	0.500	m
	diameter	$Ø_p$	0.100	m
	radius	r_p	0.050	m
	encapsulation thickness	T_p	0.001	m

3.2.2.1.1 Factors considered in the EPCM-T parametric design study

The primary goal of the EPCM-T parametric designs was to identify the most effective geometry capable of achieving a prolonged, stabilised, and reduced supply air temperature over time. Key factors considered in the parametric study included:

i.   Impact of ambient airflow on the heat transfer rate between the PCM and encapsulated tube materials, and its effect on temperature variations within each EPCM-T design over time.

ii. Impact of different encapsulated tube materials on the thermal storage performance of each EPCM-T design over time.

The findings from the EPCM-T parametric design study guided the determination of the number of EPCM-T units required for integration into the main EPCM-HMW system.

3.2.2.2 EPCM-HMW system design based on different EPCM-T arrangements

The geometry of the EPCM-HMW system was first developed as a three-dimensional (3D) geometry using Rhinoceros 6 CAD software. It was then refined into a simplified computational physical model in ANSYS 18.0 Design Modeler. To further understand the impact of EPCM-T inclusion in the system, two distinct EPCM-T arrangements within the airstreams were incorporated in the EPCM-HMW system, represented as Case 1 and Case 2.

Figure 3.8. Two different arrangements of the EPCM-Ts within the airstreams of the EPCM-HMW system

EPCM-HMW Case 1: As indicated in Figure 3.8, Case 1 represents the model when integrated with 48 EPCM-Ts placed within the supply airstream.

EPCM-HMW Case 2: In Case 2, 48 EPCM-Ts were placed in each of the system's airstreams (supply and exhaust), resulting in a total of 197 EPCM-Ts evenly distributed across all four airstreams.

3.2.2.3 Justification for the EPCM-HMW system's novel integrated design

The multi-directional windcatcher component of the EPCM-HMW system shares similarities with the windcatcher design by Calautit et al. [305]. The decision to incorporate EPCM-Ts stemmed from the necessity to address both the thermal storage and cooling limitations observed in traditional multi-directional windcatchers. The vertical placement of the EPCM-Ts directly inside the airstreams improves the PCM-air close contact melting process, addressing limitations identified in previous studies by Seidabadi et al. [49] and Abdo et al. [306]. Additionally, in Sub-Saharan Africa's tropical savannah climates characterised by low wind conditions, the wall-mounted solar axial fan component augments airflow during reduced wind speed periods without additional energy from the grid.

Designing two different EPCM-T configurations within the EPCM-HMW system for investigation allows for a deeper understanding of how different EPCM-T integration modes influence airflow patterns, temperature distribution, and the system's potential for temperature stabilisation, to optimising the overall system performance.

3.2.3 Operational and working principles

The typical operation of the EPCM-HMW system is based on three key simultaneous processes: airflow, thermal storage, and air cooling. These modes of operation collectively define the system's performance.

3.2.3.1 The cooling operation of the EPCM-HMW system

The cooling operation primarily occurs due to the inclusion of EPCM-Ts within the system's airstreams. Warm outside air enters through the windward vents into the supply airstream, passing directly over the EPCM-Ts and into the indoor space. This EPCM-T-to-air interaction facilitates an efficient heat transfer process, absorbing heat from the incoming air before it enters the indoor space as cooled air.

Simultaneously, warm, used, and stale air from the indoor space is expelled through the exhaust vents on the leeward side, creating a vacuum that allows fresh air to replace the stale air, causing the warm air to rise out of the space. Additionally, the temperature difference between incoming and outgoing air further promotes buoyancy, aiding indoor-outdoor air exchange. This entire process helps achieve a balanced cooling effect within the indoor space.

3.2.3.2 The thermal storage operation of the EPCM-HMW system

The EPCM-Ts are responsible for the thermal storage operation of the system, acting as thermal batteries. While cooling the incoming air, the heat absorbed from it is stored inside the PCM as latent heat. The encapsulation of the PCM further improves the effectiveness of this PCM-air heat transfer. During absorption, the PCM begins transitioning from a solid to a liquid state, storing the heat over time until complete PCM melting occurs. Consequently, not only does the temperature of the incoming air reduce, but it also achieves a stabilised state throughout the phase change process until the PCM completely melts. This enables the

incoming air to maintain a reduced temperature state for an extended period.

3.2.3.3 *The passive ventilation operation of the EPCM-HMW system*

The system primarily relies on passive ventilation with a secondary reliance on hybrid ventilation. As air flows from the windward vents, positive pressure is generated, pushing air into the system. Conversely, negative pressure occurs at the leeward side, drawing stale air out of the indoor space. The passive ventilation operation is facilitated by buoyancy resulting from the temperature difference between indoor and outdoor air, which is further enhanced by natural convection. Warm indoor air rises, creating a vacuum that allows cooler incoming air, already cooled by the EPCM-Ts, to enter the indoor space. The placement of the system on top of the indoor space encourages vertical airflow, facilitating the easy escape of warm stale air and promoting better indoor air circulation.

3.2.3.4 *The hybrid ventilation operation of the EPCM-HMW system*

Since wind speeds in the target region can drop as low as 2 m/s, the system incorporates a hybrid ventilation mode alongside passive ventilation. This is achieved through the use of a low-speed, wall-mounted solar axial fan, which serves as a secondary vent to enhance airflow and complement the system's overall ventilation performance. Essentially, the fan operates concurrently with passive ventilation, ensuring consistent airflow throughout the ventilation process.

3.3 Theoretical model formulation

The EPCM-HMW system theoretically exhibits two main phenomena: turbulent airflow and PCM heat transfer, both crucial for understanding its ventilation, cooling, and thermal storage performance. A theoretical modular approach combining two key sub-models is adopted: a turbulent

airflow model for ventilation and a PCM heat transfer model for thermal storage and cooling.

3.3.1 Theoretical sub-models

The two theoretical sub-models discussed in this section are essential to the analytical framework adopted for understanding turbulent airflow for ventilation performance and PCM heat transfer for thermal storage and cooling performance. These sub-models combined output variables predict the overall operational behaviour of the EPCM-HMW system and form the foundation for the CFD numerical code and algorithm's solution.

3.3.1.1 Turbulent airflow models for ventilation

Turbulence models are primary computational approaches for predicting convection in indoor airflows [307]. According to the "Best Practice: RANS Turbulence Modelling in Ansys CFD" guideline, a turbulence model is chosen based on its ability to accurately represent a given flow or class of flows [308]. However, the accuracy is dependent on the complexity of the turbulent flow phenomena being replicated [309] These models solve time-averaged governing fluid flow equations while determining Reynolds stress factors in the flow fields. However, their complexity varies, from simple eddy viscosity formulas to more complicated algebraic stress models and Reynolds-stress differential equations, which provide exact flow and transport solutions.

For example, standard turbulence models for incompressible fluids determine eddy viscosity values, emphasising the relationship of viscous stresses to the rate of fluid deformation elements, as indicated in equations 3.1 and 3.2, which are analogous [309]. This addresses the internal friction, or barrier to flow, between adjacent fluid layers moving at different velocities [309].

$$\tau_{ij} = \mu e_{ij} = \mu \left(\frac{\partial u_i}{\partial x_j} + \frac{\partial u_j}{\partial x_i} \right) \qquad \text{Equation 3.1}$$

$$\tau_{ij} = \rho \overline{u_i' u_j'} = \mu_t \left(\frac{\partial u_i}{\partial x_j} + \frac{\partial u_j}{\partial x_i} \right) \qquad \text{Equation 3.2}$$

Where μ is the dynamic viscosity, μ_t is the eddy viscosity. τ_{ij} is the Reynolds stress component in the fluid flow in directions i and j., which can be linked to the shear stress tensor. ρ is the fluid density. The terms $\overline{u_i' u_j'}$ represent the fluctuating velocity components in directions i and j. While $\frac{\partial u_i}{\partial x_j}$ represents how the fluid flow velocity changes in directions i and j.

Zhai et al. [310] emphasised the importance of using different turbulent modelling approaches for indoor airflow assessment, especially when the influence of external wind conditions on internal airflow phenomena is considered. Cook [311] outlined various methods for solving turbulent airflow models, including analytical, numerical, semi-empirical, and empirical models. While empirical models are widely seen as the most accurate but quite complex, numerical models, particularly those using pre-simulated computer-based databases, are less complex and can solve mathematical equations that cannot be solved using analytical methods. There are three widely accepted CFD turbulent airflow models found in the existing literature: RANS (Reynolds-Averaged Navier–Stokes) equations simulation, LES (Large-Eddy Simulation), and DNS (Direct Numerical Simulation) [312].

Zhai et al. [312] noted that DNS solves Navier-Stokes equations without approximations, while LES characterises turbulent flows with macroscopic structures of three-dimensional time-dependent large eddies and small eddies. Another study by Zhang et al. [313] assessed eight different turbulent airflow models for four geometries. It was concluded that LES eliminates the need for fine grids or small-time steps but offers a more detailed airflow solution and requires less

computational resources compared to DNS. However, both the DNS and LES required more computational resources than RANS. In another study by Diarce et al. [314], it was concluded that RANS is more widely accepted than DNS and LES methods because RANS has the advantage of being able to calculate averaged flow quantities that represent several turbulence scales. Accordingly, the time-averaged general RANS equation for stationary incompressible turbulent flow is given by:

$$\rho \bar{u}_j \frac{\overline{\partial u_i}}{\partial x_j} = \rho \bar{f}_i + \frac{\partial}{\partial x_j}\left[-\bar{p}\delta_{ij} + \mu\left(\frac{\partial \bar{u}_i}{\partial x_j} + \frac{\partial \bar{u}_j}{\partial x_i}\right) - \overline{\rho u_i' u_j'}\right] \quad \textit{Equation 3.3}$$

ρ represents the density of the fluid; $\bar{u}_j$ and $\bar{u}_i$ are the velocity components in the j and i directions. But the unsteady mean momentum and fluid flow convection represented by $\rho\bar{u}_j\frac{\overline{\partial u_i}}{\partial x_j}$ is achieved when the average body force per unit mass $\rho\bar{f}_i$ in the i direction; and isotropic stress $\frac{\partial}{\partial x_j}$ due to Reynolds' stress $\overline{\rho u_i' u_j'}$ which includes pressure field isotropic stress, viscous stress, and apparent stress from velocity field fluctuations are balanced.

To complete the RANS equation, especially in nonlinear Reynolds scenarios, further modelling is required which necessitates adjustments to various types of RANS turbulence models. In this light, several two-equation turbulence models, including the RNG k-ε, standard k-ε, realizable k-ε, standard k-ω and SST k-ω and SST k-ω models, have been discussed in the context of turbulent airflow and temperature distribution simulations in existing studies [315]. However, the selection of a turbulence model for CFD simulations is a critical aspect influenced by various factors such as computational time and accuracy needed to be achieved for the model solution [313]. Nonetheless, amongst all the turbulence models, the standard k-ε turbulence model was selected. The rationale behind this selection is discussed in section 3.3.1.1.1.

3.3.1.1.1 Justification for the selected turbulent model

The selection of the turbulence model for this study was guided by established advantages and limitations highlighted in previous studies. Zhai et al. [312] provided insights into different RANS turbulence models, highlighting their characteristics and applicability in indoor airflow modelling. In a subsequent study by Zhang et al. [313], comparing turbulent model results of four geometries with experimental data from existing literature, the RNG k-ε and a modified V_{2-f} model were identified as offering superior model performance.

The RNG k-ε model is a semi-empirical model, similar to the standard k-ε model. However, it combines empirical correlations with physical principles derived from the turbulence kinetic energy (k) and dissipation rate (ε) transport equations [316] to provide accurate predictions for flows with turbulent shear layers, separated flows, and recirculation zones. However, it has limitations in predicting complex, buoyancy-driven flows, especially at low airflow conditions and near walls.

The standard k-ε model is suitable for various flow regimes, including free shear flows, boundary layer flows, and internal flows. Walsh et al. [317] found that this model effectively captures near-wall turbulence behaviour by employing wall functions influenced by viscous effects and boundary layer dynamics. Their study concluded that the standard k-ε model was the most effective for indoor airflow in thermal environments. Similarly, many windcatcher studies have utilised this model, highlighting its acceptance and suitability in this domain [29], [175], [176], [318], [319], [320], [321], [322], [323].

While the SST k-ω model is another option for turbulent airflow cases involving free shear and wall-bounded flows, it is a fully empirical model. This results in additional computational time caused by the interaction between near-wall k-ε, far-field k-ω components, and refinements in the computational domain [309].

Considering these established advantages and limitations of the various turbulent models discussed, the need to balance between accuracy and computational efficiency is of high importance. Tailored to this specific study's requirements and its relevance in solving the free shear and wall-bounded internal flows, the standard k-ε model was chosen for this study.

3.3.1.1.2 Governing equations for turbulent airflow in the EPCM-HMW system

The standard k-ε turbulence model selected for this study generally combines two transport equations: turbulent kinetic energy (k) and turbulent dissipation rate (ε). The equations are derived from the general RANs equations as discussed in established studies of Mumovic et al. [324] and Teodosiu et al. [325]. The governing equations were therefore adopted without any further changes.

The turbulent kinetic energy (k) is governed by:

$$\frac{\partial(\rho k)}{\partial t} + \nabla \cdot (\rho k u) = \nabla \cdot \left[\alpha_k k_{eff} \nabla k \right] + G_k + G_b - \rho_\epsilon \qquad \text{Equation 3.4}$$

G_k is the TKE source caused by average velocity gradient; G_b represents the TKE source based on buoyancy force; the Turbulent Prandtl's are represented by constants α_k and α_ε; while vectors $C_{1\varepsilon}$, $C_{2\varepsilon}$ and $C_{3\varepsilon}$ are the empirical model constants.

The energy dissipation rate (ε) is governed by:

$$\frac{\partial}{\partial t}(\rho Y_i) + \nabla \cdot (\rho u Y_i) = -\nabla \cdot \vec{J_i} + R_i + S_i \qquad \text{Equation 3.5}$$

where $\vec{J_i}$ represents fusion flux of species i, R_i represents the net rate of production of species i; S_i is the rate of creating species by addition from the dispersed phase and any user-defined sources.

The conservation equations for mass, momentum, and energy, which are fundamental in describing all transport phenomena in fluid dynamics, were solved using the CFD codes alongside the turbulence model equations.

Accordingly, the conservation of mass (continuity equation) in the turbulent airflow was given in Chen et al.'s study [326] as:

$$\frac{\partial \rho}{\partial t_j} + \frac{\partial}{\partial t}(\rho u_i) = 0 \qquad \textit{Equation 3.6}$$

Where the fluid velocity in the model is represented by u; the density of air is represented by ρ; and time is t.

The momentum conservation (Navier-Stokes equations) in the model is governed by:

$$\frac{\partial(\rho u)}{\partial t} + \nabla \cdot (\rho u u) = -\nabla p + \rho g + \nabla \cdot (\mu \nabla u) - \nabla \cdot \tau_t \qquad \textit{Equation 3.7}$$

The vectors in the equations are represented as p pressure, and g as the gravitational acceleration. The molecular dynamic viscosity μ; τ_t represents the turbulence stress divergence that occurs due to the velocity fluctuations caused by the auxiliary stresses in the model .

The energy conservation in the model is solved by:

$$\frac{\partial(\rho e)}{\partial t} + \nabla \cdot (\rho e u) = \nabla \cdot \left(k_{eff} \nabla T\right) - \nabla \cdot \left(\sum_i h_i j_i\right) \qquad \textit{Equation 3.8}$$

e represents specific internal energy and effective heat conductivity is k_{eff}; the temperature of the air is represented by T; h_i represents the fluid-specific enthalpy, while j_i is the mass flux.

3.3.1.2 PCM heat transfer models for thermal storage and cooling

PCM isothermal heat transfer problems generally often involve solving moving boundary problems, known as the "Stefan problem". Stefan's study [327] described the heat transfer mechanism that occurs during PCM melting, identifying two distinct phases. The solid phase Ω_s, and the liquid phase Ω_l, are separated by a moving interface with a temperature field corresponding to the melting temperature T_m [328]. However, assessing PCM thermal storage requires a thorough understanding of the transient performance of the isothermal phase change process based on different PCM heat transfer models [329]. The enthalpy technique, heat capacity method, and temperature method are the most commonly accepted numerical methodologies for PCM heat transfer prediction, each with its own set of advantages and complexity [330], [331], [332]. Moreover, the intrinsic challenge of solving nonlinear PCM temperature variations requires a careful selection of the right PCM heat transfer method. Nonetheless, amongst all the PCM heat transfer prediction numerical approaches, the temperature method was selected as the PCM heat transfer method adopted for this study. The rationale behind this selection is discussed in section 3.3.1.2.1.

3.3.1.2.1 Justification for the selected PCM heat transfer model

The selection of the specific PCM heat transfer model was based on established methodologies discussed in the literature. As highlighted in the literature by Voller [330], the enthalpy method provides a rapid implicit solution for phase change problems without explicitly tracking the phase change boundary, making it indispensable in applications where such transitions play a crucial role [330]. On the other hand, the heat capacity method offers a direct understanding of PCM thermal behaviour based on material property variations, simplifying phase change problems into single-phase equations as shown in equations 3.9 and 3.10 [331].

However, the complexity of gathering data across various PCM temperatures can complicate modelling efforts.

$$\rho C_p \frac{\partial T}{\partial t} = \frac{dH}{dT}$$ *Equation 3.9*

where $C_p = \frac{dH}{dT}$ *Equation 3.10*

C_p is heat capacity; dT is the temperature change, while dH is the enthalpy change.

Studies employing the enthalpy and heat capacity methods can be found in Raj et al. [333]. However, Alvarez-Rodriguez et al. [334] concluded that these methods and equations do not account for the phase change front, but instead, assess explicitly the interface condition of the PCM.

On the other hand, the temperature method provides a straightforward yet effective means to model and monitor the temperature variation of PCM during the phase change process. This simplified approach is suitable for studies that specifically target PCM temperature changes without the need to account for the latent heat effects of the process. Despite its simplicity, the temperature method maintains a balance between accuracy and computational complexity [332].

Cui [332] further suggested the suitability of the temperature method to assess either 2-dimensional (2D) or 3-dimensional (3D) PCM models using finite difference or finite element methods based on temperature variation in the PCM solid, liquid and interface zones. By tracking the temperature distributions, and important heat transfer characteristics, the phase change and overall PCM thermal behaviour can also be inferred, without delving into intricate fluid dynamics details, phase change interfaces, or complex multi-physics interactions within the PCM, which would consume more computational resources. Based on Cui's recommendation [332] and in line with the specific objectives of this study, the temperature method was chosen as the theoretical model for

analysing the PCM heat transfer phenomena within the EPCM-HMW system. This model was selected to effectively capture essential heat transfer by monitoring temperature variations while maintaining computational simplicity.

3.3.1.2.2 Governing equations for phase transition heat transfer interfaces in the EPCM-HMW system

All governing equations for the phase transition heat transfer interfaces utilise a simplistic method which ignores the volume expansion of the temperature variation in the PCM. Accordingly, for the transient heat transfer in PCM using the temperature method, particularly when considering the solid state in 3D cases, the governing equation can be expressed based on reference [332] as follows:

$$\rho_s C_s \frac{\partial T_s}{\partial t} = \nabla \bullet (k_s \ \nabla T_s) + q_s \qquad\qquad Equation\ 3.11$$

The equation 3.11 describes the transient heat transfer in the PCM relative to time t which is connoted by $\frac{\delta T_s}{\delta t}$ and equals the heat conduction $\nabla \bullet (k_s \ \nabla T_s)$ that occurs in the PCM in addition to the internal heat source generated within the solid PCM q_s.

where C_s is heat capacity of PCM at solid state; ρ_s is the density of PCM at solid state. T_s is the PCM solidus temperature; k_s is the thermal conductivity of the PCM at solid state. ∇ is the nabla operator (gradient).

During PCM liquid state, the transient heat transfer in the PCM over time t is given by:

$$\rho_l C_l \frac{\partial T_l}{\partial t} = \nabla \bullet (k_l \ \nabla T_l) + q_l \qquad\qquad Equation\ 3.12$$

Where ρ_l is the density of PCM in liquid state, C_l is the specific heat capacity of the PCM in its liquid state and $\frac{\delta T_l}{\delta t}$ represents the transient heat transfer that occurs in the PCM in its liquid state, taking into

consideration the heat generation or absorption q_l that occurs in the PCM when in its liquid state. C_l is heat capacity of PCM in liquid state; ρ_l is the density of PCM at liquid state. T_l is the PCM liquidus temperature; k_l is the thermal conductivity of the PCM at solid state.

The transient heat transfer that occurs during the solid-liquid phase interface in the PCM can be expressed in equation 3.13 [335]:

$$\frac{\partial T}{\partial t} = \nabla \bullet (\propto \nabla T) + \frac{H}{\rho.C} \frac{\partial \emptyset}{\partial t} \qquad\qquad Equation\ 3.13$$

Where the thermal diffusivity is $\propto = \frac{k}{\rho.C}$; with k representing the thermal conductivity, ρ is density and C is the specific heat capacity.

$\nabla \bullet (\propto \nabla T)$ in the equation represents the PCM heat transfer that occurs in spatial coordinates x, y, z. T is temperature as a function of time t in x, y, and z coordinates.

$\frac{H}{\rho.C} \frac{\partial \emptyset}{\partial t}$ is the rate at which the PCM changes its phase in relation to the latent heat of phase change H. Meanwhile, the $\emptyset$ represents the phase fraction at 0 in the solid phase and 1 in the liquid phase. H is the latent heat of phase change.

Equation 3.14 further defines the liquid-solid transition during the PCM melting process as introduced in the study by Lin et al. [336]:

$$\beta = \begin{cases} 0 & for & T \leq T_s \\ \frac{T-T_s}{T_l-T_s} & for & T_s < T < T_l \\ 1 & for & T_l \leq T \end{cases} \qquad\qquad Equation\ 3.14$$

Where T_s and T_l is the solidification and melting temperature, respectively.

When $\beta = 0$, $T < T_s$; when $\beta = 0$, $T < T_s$; when $0 < \beta < 1$, solid-liquid PCM phase co-existence occurs; when $T = T_s$, only liquid and solid separate phases exist in the PCM.

The effective heat capacity of the PCM depends on the volume fraction β, the phase change interface or the mushy zone A_{mush} and the relative velocity between the surrounding fluid (air) and the PCM $(\vec{V} - \vec{V}_p)$ [337].

This dynamic relationship of all factors is given by:

$$S_{pcm} = \frac{(1-\beta)^2}{\beta^3 + \varepsilon} A_{mush}(\vec{V} - \vec{V}_p) \qquad\qquad \textit{Equation 3.15}$$

Where S_{PCM} represents the PCM's specific heat capacity during the phase change. β is the PCM volume fraction at constant ε with a value of 0, <0.0001. A_{mush}, represents the PCM mushy zone or effective contact area during the phase change process at a value of 10^4 ~10^7. $\vec{V}$ and $\vec{V}_p$ are velocity vector quantities of fluid around the PCM and the PCM itself.

Furthermore, the PCM heat transfer behaviour H in the system is influenced by the PCM volume fraction β, the effective contact area A_{mush}, and the phase change effectiveness Φ, which is defined in equation 3.16 as identified in the study by Liu et al. [338].

$$H = \frac{(1-\beta)^2}{\beta^3 + \varepsilon} A_{mush}{}^{\Phi} \qquad\qquad \textit{Equation 3.16}$$

The same governing equations used for modelling turbulent airflow, including the continuity equation for mass, the Navier-Stokes equations for momentum, and the energy equations, were also applied to the PCM model integrated within the EPCM-HMW system. All these governing equations were solved computationally in CFD.

3.4 Computational fluid dynamics (CFD)

Computational fluid dynamics (CFD) is a simulation modelling method widely used by researchers to solve numerical fluid flow problems related

to heat transfer, temperature distribution, and airflow within various spaces [339]. CFD achieves this by interpreting codes through steady-state and/or dynamic time-averaged simulations for incompressible turbulent flows, by solving the Navier-Stokes fundamental fluid dynamics equations for energy, mass, and momentum, along with other additional transport equations for turbulent velocity, as discussed in the studies by Awbi [340] and Awbi [341]. More importantly, the utilisation of unstructured grids and a variety of boundary condition options is advantageous for the widespread acceptance of CFD simulations in predicting turbulent airflow, heat transfer, and temperature distribution.

Amidst other CFD software, the ANSYS Fluent CFD commercial software is most common in many CFD research, particularly for airflow and heat transfer fluid problems. The ANSYS Fluent CFD software has two solvers. They are the density-based and pressure-based solvers [342]. Density-based solvers are suited for high-speed compressive flows, solving nonlinear equations of continuity, momentum, coupled energy and species transport. Pressure-based solvers, on the other hand, are ideal for low-speed incompressible flows. Convergence in density-based solvers typically requires multiple iterations due to the complexity of the equations. But pressure-based solvers employ algorithms such as the projection method, with options like segregated and coupled algorithms. However, the pressure-based segregated algorithm increases convergence time, but it is a more memory-efficient algorithm compared to coupled algorithms, making it preferable for efficient simulations [342].

Although ANSYS FLUENT offers four pressure-based segregated algorithm solvers: semi-implicit methods for pressure-linked equations (SIMPLE), SIMPLE–consistent (SIMPLEC), pressure-implicit with splitting operators (PISO), and fractional step method (FSM), the semi-implicit methods for pressure-linked equations (SIMPLE) being a commonly used choice and was adopted for this study. A typical pressure-based segregated algorithm is illustrated in Figure 3.9 [343].
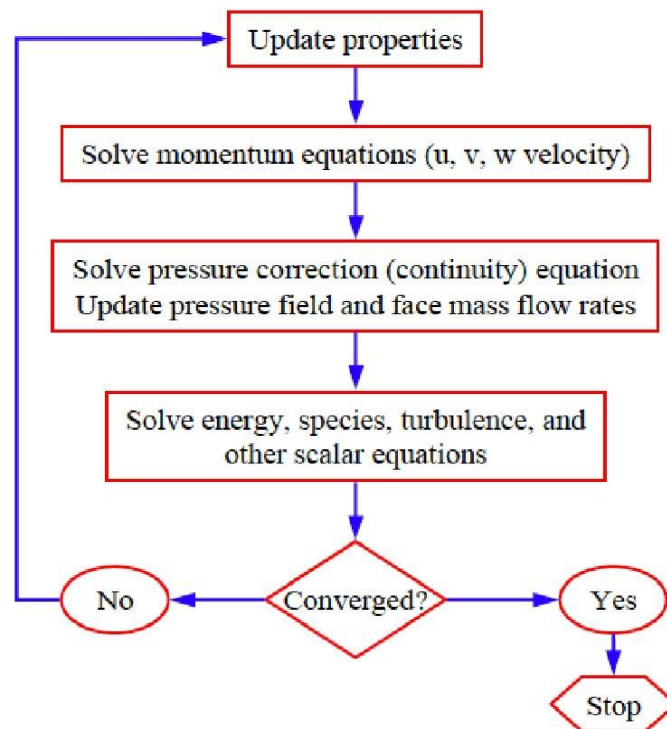
Figure 3.9. pressure-based segregated algorithm [343]

3.4.1 Fundamental steps in CFD simulations

Vardoulakis et al. [344] highlighted that commercial CFD packages typically operate in three main stages: pre-processing, solving, and post-processing. Another study by Coleman et al. [345] identified CFD simulation steps based on modelling physics and error analysis solved, which aids in thorough verification and validation of the CFD models.

According to "The Best Practise Guideline for the CFD Simulation of Flows in the Urban Environment: An Outcome of COST 732" [346], a systematic 10-step procedure is frequently followed when conducting CFD simulations. This allows for the CFD solution to accommodate minor errors. The 10-step procedure for CFD code entails defining target variables, selecting approximation equations, simplifying geometry, determining computational domains, setting boundary and initial conditions, creating the computational grid, choosing the time step size, managing numerical round-up, and establishing convergence criteria. All

these steps are widely grouped under the 3 stages in the CFD code as pre-processing, solving and post-processing, as identified in Vardoulakis et al.'s study [344].

i. **Pre-Processing:** As discussed, during pre-processing, geometric modelling is developed alongside defining mesh characteristics, fluid properties, and boundary conditions.

ii. **Solving:** On the other hand, the solving stage focuses on simulating the fluid flow or heat transfer while refining solution accuracy by solving the governing equations till convergence is attained.

iii. **Post Processing:** In the post-processing stage, quantitative assessments such as residual plots, mass flow rates, forces and other qualitative analyses including contour lines, and vectors are developed to comprehensively evaluate the simulation results.

3.4.2 Adopted CFD code for the study

The numerical study utilised the commercially available Ansys Fluent software (version 18.1) for all CFD simulations. The computational equipment used was an X64-based Windows 10 PC with an AMD Ryzen 5 3600 6-Core Processor, operating at 3600 MHz, with 6 cores and 12 logical processors.

The system's 3D models were created in Rhinoceros software and further refined in the Ansys Workbench Design Modeler interface, except for the EPCM-T samples, which were developed directly in the Ansys Workbench Design Modeler interface. The flow regime is assumed to exhibit turbulent and transient behaviour. The CFD transient flow modelling was three phases: first, preliminary EPCM-T parametric heat transfer modelling; second, computational modelling of the entire system; and lastly, validation of the EPCM-T temperature distribution and PCM liquid fraction alongside the windcatcher airflow validation. This comprehensive modelling encompassed turbulent airflow, simulated

using the Standard k–ε model. The EPCM-T parametric study was initially based on laminar flow assumptions, while the PCM melting process was simulated using the temperature heat transfer method, which was activated in the turbulent and transient modelling of the EPCM-HMW model.

3.4.2.1 EPCM-T parametric CFD study

The EPCM-T geometric parametric CFD study focused on assessing the PCM melting performance, following the methodology outlined in Cui's study [332]. This was based on the impact of the effect of the tube encapsulation on the different EPCM-T heat transfer and thermal storage performance.

The PCM geometry from Rouault et al. [281] served as the baseline for the four distinct EPCM-T geometries used in the parametric study. The selected PCM for this study is the commercial RT28HC paraffin manufactured by Rubitherm-GmbH [347]. Although not a pure PCM, RT28HC paraffin demonstrates a gradual phase change process with an inverse relationship with enthalpy due to its composition [348]. With a narrow transition temperature range between 27°C and 29°C [349], [350], it also exhibits favourable organic composition and thermo-physical properties such as high latent heat and chemical inertness [348]. These attributes align well with its suitability for achieving the Abuja comfort temperature range for building applications, as substantiated by Batagarawa Amina's work [351], further justifying its selection for the study.

Two EPCM-T encapsulation tube materials: aluminium, and copper, varied across all the four EPCM-T geometries. The detail of the tube encapsulation variation is shown in Table 3.6 and identified as EPCM-T Case 1 to 8.

Table 3.6. Aluminium and copper encapsulation variation for the four EPCM-T geometries samples

tube encapsulation material	EPCM-T geometry samples			
	rectangular EPCM-T samples		cylindrical EPCM-T samples	
	EPCM-T rectangular profile	EPCM-T shell-tube rectangular profile	EPCM-T cylindrical profile	EPCM-T shell-tube cylindrical profile
aluminium	EPCM-T Case 1	EPCM-T Case 3	EPCM-T Case 5	EPCM-T Case 7
copper	EPCM-T Case 2	EPCM-T Case 4	EPCM-T Case 6	EPCM-T Case 8

For each EPCM-T physical model, four distinct physical domains were established in the CFD modelling process. These domains depend on defined fluid and solid material assignments and represent different parts of the EPCM-T. The fluid domains were classified as the air domain (fluid) and the PCM domain (fluid), while the solid domains represented the shell-tube domain (solid) and the solid tube domain.
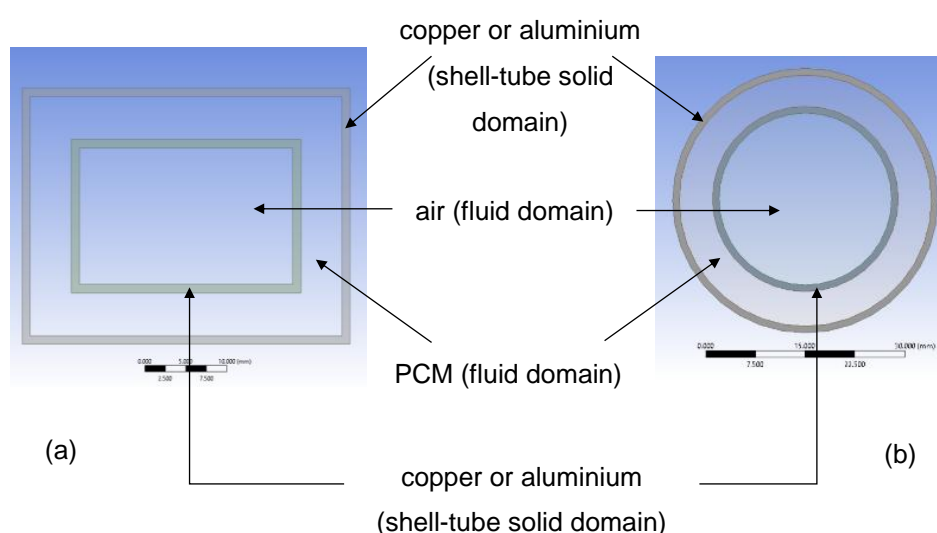
Figure 3.10. Physical domain identification for (a) EPCM-T shell-tube rectangular profile, (b) EPCM-T shell-tube cylindrical profile

The shell-tube domain (solid) and solid tube domain represent the aluminium or copper tube structures that encase the PCM material in the
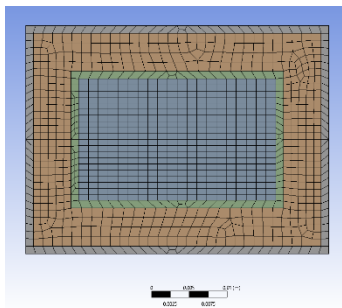
models. The air domain functions as the heat transfer fluid (HTF) during PCM melting simulations. The domain assignment is illustrated in Figures 3.10 and 3.11.
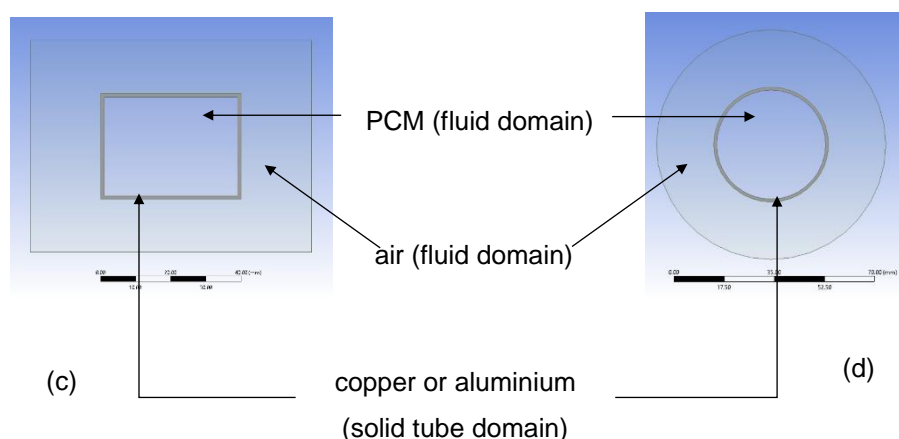
Figure 3.11. Physical domain identification for (c) EPCM-T rectangular profile, (d) EPCM-T cylindrical profile

The model was meshed using non-uniform hybrid computational meshes, employing additional edge-sizing properties to refine the mesh within each assigned domain. Table 3.7 provides details on the mesh sizes utilised during meshing, specifying the number of nodes and elements for each type of EPCM-T geometry investigated.

Table 3.7. Type of meshing used and mesh size data

geometry	meshing type	nodes	elements
EPCM-T shell-tube rectangular profile	non-uniform hybrid	51345	47652
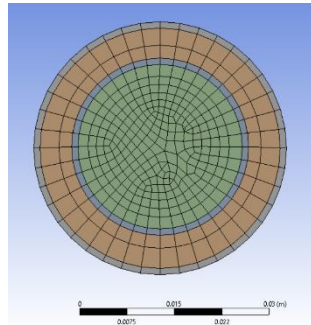
EPCM-T shell-tube cylindrical profile	non-uniform hybrid	98550	93958
EPCM-T rectangular profile	non-uniform hybrid	49296	45904
EPCM-T cylindrical profile	non-uniform hybrid	77625	74772
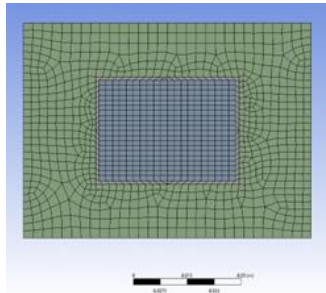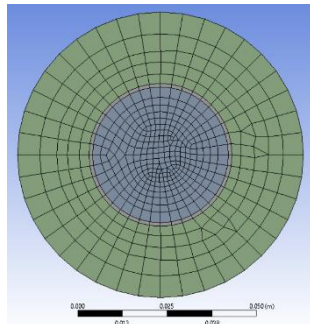
Table 3.8 further provides detailed information on the thermophysical properties of RT28HC paraffin, along with those of the encapsulation tube materials (aluminium and copper) and the HTF (air) [281], [347]. A comprehensive overview of the CFD simulation physical domain specifications, operating conditions, boundary conditions, and solution methods used for the EPCM-T parametric study, are outlined in Table 3.9.

Table 3.8 Thermo-physical properties of RT28HC, air, copper and aluminium [281], [347].

	properties	values	units
RT28HC paraffin	melting temperature	28	°C
	solidus temperature	27	°C
	liquidous temperature	29	°C
	latent heat	245000	J/kg
	heat capacity of the solid phase	1650	J/kg K^{-1}
	heat capacity of the liquid phase	2200	J/kg K^{-1}
	thermal conductivity	0.2	W/m K^{-1}
	density of the solid phase	880	kg/m^3
	density of the liquid phase	768	kg/m^3
	melting volume expansion	14	%
	kinematic viscosity	3.1×10^{-6}	mm/s
	dynamic viscosity	0.002.38	kg/m s
aluminium	shell conduction thickness	0.001	mm
	density	2719	kg/m^3
copper	shell conduction thickness	0.001	mm
	density	8850	kg/m^3
air	density	1.225	kg/m^3
	dynamic viscosity	0.000017894	kg/m s

Table 3.9. Input and boundary conditions for the EPCM-T parametric CFD simulation

input	details
model	energy, standard k-omega viscous laminar flow model with standardised wall functions and species transport
physical domain specification	fluid domain – air
	fluid domain - RT28 HC paraffin
	solid domain – aluminium or copper
boundary conditions	initial gauge air pressure set at 500 Pa
	inlet air temperature set at 308.15K (35 ºC)
	inlet air velocity magnitude set between 1.88 - 3 m/s
	initial temperature value set at 298.15K (25 ºC)
	turbulent intensity set at a default value of 5 %
	turbulent viscosity ratio at a default value of 10
	Semi-Implicit Method for Pressure-Linked Equations (SIMPLE) pressure-velocity coupled algorithm

solution methods	intensity and viscosity ratio turbulence specification method is adopted
	square-based cell-based gradient option
	second-order upwind momentum and energy and liquid fraction equations are calculated
	under-relaxation factors were set at the default values
	standard initialisation is adopted
	number of steps time is 38600
	time size steps is 1
	simulation set at 1 maximum iteration per time steps

After analysing the thermal storage performance of the various EPCM-T geometries as individual components, the EPCM-T rectangular profile emerged as the most suitable choice for integration into the EPCM-HMW system based on the results obtained. Results and analysis obtained from the parametric study are discussed in detail in Chapter 4.

3.4.2.1.1 Assumptions for EPCM-T parametric study

To overcome the complexity of the PCM heat transfer modelling during the parametric study, the following assumptions are taken into consideration:

i. The PCM initial temperature is set at 298.15K (25 °C), and 275.15K (2 °C) below the PCM melting temperature.
ii. Air temperature on the inlet side is steady at the average ambient temperature of Abuja at 308.15K (35 °C).
iii. The physical properties of the PCM, air and aluminium are assumed to be at constant value independent of temperature variation.
iv. The modelling is 3-dimensional (3D).
v. The volume changes of the PCM and air are neglected.
vi. The PCM system is assumed to the isotropic.
vii. It is assumed that the transient convection is in a series of steady-state steps.

The parametric study of the EPCM-T was the premise with which the preferred EPCM-T geometry was selected for integration into the EPCM-HMW system. Details of EPCM-HMW CFD modelling is discussed in the next section 3.4.2.2.

3.4.2.2 The EPCM-HMW system CFD modelling

In section 3.4.2, it was noted that the CFD modelling of the EPCM-HMW system was performed using the commercially available Ansys Fluent software (version 18.1). The simulation employed the RANS (Reynolds-Averaged Navier-Stokes) transient 3D algorithm with the standard k-ε turbulence modelling approach. A turbulence intensity of 5% at the windward inlet and a turbulent viscosity ratio of 10 were assumed, aligning with the CFD methodology outlined in a similar windcatcher study by Hughes et al. [213]. The Finite Volume Method (FVM) based on the Semi-Implicit Method for Pressure-Linked Equations (SIMPLE) was used to solve the airflow governing equations stated in section 3.3.1.1.2, and consistent with the methodology described by Rodríguez-Vázquez et al. [352].

While the overall CFD modelling of the EPCM-HMW system utilised the SIMPLE solver, addressing the EPCM-T CFD heat transfer computational problem within the model required specific consideration of the melting and solidification processes of PCM, as recommended by Groulx et al. [353]. This complexity stems from accurately predicting PCM behaviour during phase transitions, influenced by the solid-liquid interface between PCM, encapsulation material, and heat transfer fluid [354]. Consequently, the PCM phase transition and heat transfer problem was solved using an additional numerical algorithm based on the "Stefan problem", as discussed in Prakash et al.'s study [355]. Hence, the CFD code activated solidification/melting equations in the SIMPLE solver to address the PCM computational modelling aspect based on the single-

phase temperature method of variable density, with all governing equations detailed in section 3.3.1.2.2.

3.4.2.2.1 Assumptions for EPCM-HMW system CFD modelling

The basic assumptions adopted during the numerical simulation exercise to make the model computationally tractable are as follows:

i. Airflow within the model was assumed to be 3D, incompressible, transient, and turbulent.

ii. Convective heat losses around the EPCM-HMW model and indoor space walls were neglected and treated as adiabatic.

iii. All equations were per the specifications outlined in the Ansys Fluent theory guide [356], without any modifications made.

iv. The expansion of PCM volume due to density differences between solid and liquid phases was not considered.

v. The initial temperature of the PCM inside the EPCM-Ts in the EPCM-HMW model was assumed to be 293 K (20 °C).

vi. The PCM was treated as isotropic, assuming uniform thermal conductivity throughout.

vii. All material thermophysical properties across phases were assumed homogeneous at constant values, independent of temperature variations.

viii. The indoor room housing the EPCM-HMW system on its roof is assumed to be windowless, enabling a focused assessment of the system's performance under worst-case room conditions.

3.4.2.3 Models' validation

While recognising the inherent uncertainties and approximations in CFD results, consistency and reliability were established by verifying and validating the results with experimental data from literature. Due to the absence of an exact model, the airflow field was verified independently from the integrated EPCM-T temperature variation and liquid fraction

performance. Consequently, the performance of the windcatcher and EPCM-T components of the EPCM-HMW system were verified individually. These models were compared with the experimental data from Calautit et al. [357] and Rouault et al. [281], respectively.

3.4.2.3.1 EPCM-T heat transfer model validation

To validate the accuracy and performance of sample of the EPCM-T rectangular profiles placed inside the EPCM-HMW system, the study monitored the CFD predictions C_p for the PCM spatial average liquid fraction per-flow rate f_l and the temperature variation ΔT in the encapsulation material (aluminium tube) during PCM phase change over 600 minutes of simulation time. These CFD predictions were compared with Rouault et al.'s study [281] experimental data observations $C_{o(E)}$ and CFD predictions $C_{o(N)}$ model simulation results.

The confidence limits of the model's accuracy were assessed using three widely accepted statistical performance models: normalised mean square error (NMSE), Fractional Bias (FB), and the fraction of predictions within a factor of two of observations (FAC2). These were determined by solving the equations 3.17, 3.18, and 3.19, respectively [358].

$$NMSE \ = \frac{\overline{(C_o - C_p)^2}}{\overline{C_o}\ \overline{C_p}} \qquad\qquad Equation\ 3.17$$

$$FB \ = \frac{(\overline{C_o} - \overline{C_p})}{0.5(\overline{C_o} + \overline{C_p})} \qquad\qquad Equation\ 3.18$$

$$FAC2 = Fraction\ of\ data\ that\ satisfies\ 0.5\ \le\ \frac{C_p}{C_o} \le 2.0 \quad Equation\ 3.19$$

Where 'C_o' represents the experiment observations; the data set average is represented by '$\overline{C}$' and 'C_p' represents the model predictions.

3.4.2.3.2 Airflow model validation

The airflow performance validation was conducted on the windcatcher component of the EPCM-HMW system. The airflow performance validation was initially carried out on a 1:10 scale model version of the windcatcher component to ensure alignment of model dimensions, boundary conditions, and grids with the experimental model studied in Calautit et al.'s research [357]. Upon successful verification of the model's airflow performance, it was scaled up to a full 1:1 ratio to align with the real-life scale of the EPCM-HMW system. This scaling was necessary to ensure accuracy in the PCM heat transfer and thermal storage investigations, which require real-life scaling rather than a reduced scale.

The validation exercise involved estimating the confidence limits for the average weighted indoor air velocity data in the CFD predictions (C_p model) against the experimental data observations (C_o) and CFD predictions (C_{pL}) in Calautit et al.'s research [357] at 12 monitoring points. However, the model was assumed to be in steady state and the model simplified in accordance with specification in Calautit et al.'s research [357].

Similar to the approach adopted for the EPCM-T heat transfer model validation statistical predictions [359], the NMSE statistical model [360] governed by equation 3.17, the FB statistical model governed by equation 3.18, and the FAC2 statistical model governed by equation 3.19 [358] were utilised.

3.4.3 Parameters and data used in the CFD code

The CFD code utilised a range of parameters and data for the EPCM-HMW model simulation. These included criteria such as Abuja climatic data representative of a typical sub-tropical savannah climate in Africa,

which informed the selection of boundary conditions in the CFD simulation.

Additionally, parameters such as the physical domain, and initial conditions were clearly defined in addition to the modelling assumptions mentioned in sections 3.4.2.1.1 and 3.4.2.3.1. Also, mesh generation and adaptation, the selection of fluid and thermophysical properties, as well as conducting a time step independence study, and ensuring that solution convergence is achieved were all integral parts of the CFD simulation process as discussed in this section.

3.4.3.1 *Climatic data and comfort target adopted for the study*

Understanding the characteristics of a typical sub-Saharan African tropical savannah climate was crucial in establishing the target system design comfort temperature for the EPCM-HMW system in line with the study's objectives. To achieve this, the historical weather data for the year 2019 in Abuja, a city in Nigeria located at a longitude of 7.48 °E and a latitude of 9.07 °N, with a tropical savannah climate known for experiencing a mix of hot, humid, and dry outdoor conditions, was analysed.

3.4.3.1.1 Abuja weather data analysis

The Abuja weather data was obtained directly from the Nnamdi Azikiwe weather station, sourced from the National Centers for Environmental Information (NCEI) databank [361]. Literature establishes that Abuja experiences two distinct seasons: a dry season from November to March and a rainy season from April to October [10], [362]. Furthermore, the analysis of the weather data conducted using Rhinocerosvidsit6-ladybug software [363] also aligns with the predictions in the study by Abubakar [364], indicating that the highest outdoor dry-bulb temperatures occurred in May, reaching up to 40 °C (313.15 K), while temperatures were at their lowest point at approximately 12 °C (285.15 K) [365].

The accuracy of the Abuja weather data in CSV (comma-separated values) format was verified by converting it into an EPW (Energy Plus Weather Format) file using the Rhino-ladybug software interface. This EPW file was then analysed and interpreted graphically. However, the relative humidity data was omitted from the analysis as it falls outside the scope of the objectives of this study.

3.4.3.1.2 Outdoor air temperature analysis

On average, the annual cooling degree days based on the Abuja weather data were calculated to be 1132.14 hours, with no heating required throughout the year. Analysis of the data presented in Figure 3.12 indicates that during seven months – January, February, March, April, May, November, and December – daytime temperatures ranged between 35 °C (308.15 K) and 40 °C (313.15 K).
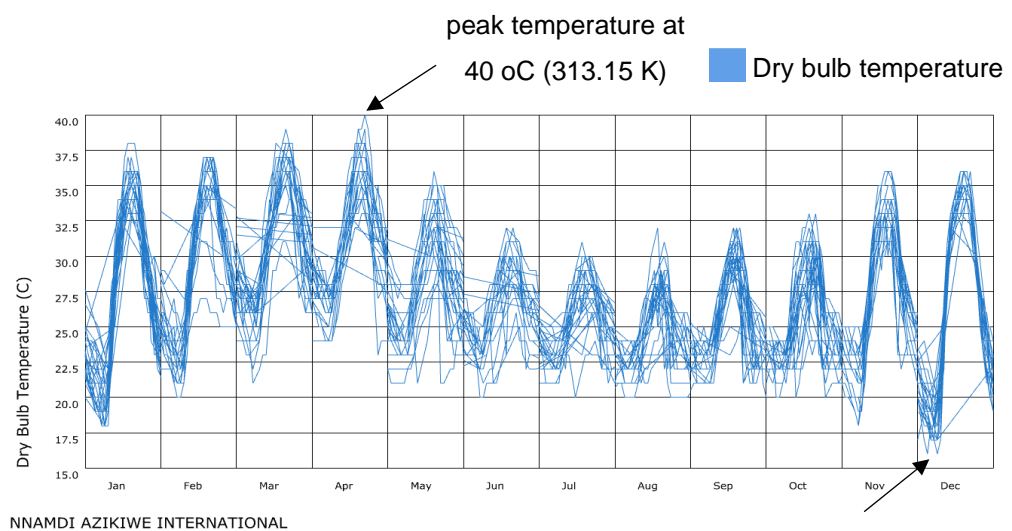
Figure 3.12. Abuja weather data: hourly dry bulb temperatures gradient for Abuja from January 2019 to December 2019 [365], [366].

Each line in the graph represents the temperature variation for each month, highlighting the peaks and low points. The x-axis shows the months of the year, while the y-axis indicates dry-bulb temperature values. The graph is segmented by month for easy identification of the temperature trends within each month. Despite the mono-colour scheme,

the temperature trends are clear, with peaks and lowest temperatures labelled accordingly.

During these months, the lowest hourly temperatures were observed to range from 16 °C to 23 °C (289.15 K to 296.15 K). On the contrary, in the remaining five months – June, July, August, September, and October – the highest daytime temperatures peaked at approximately 30.5 °C to 32 °C (303.65 K to 305.15 K), with the lowest hourly temperatures at approximately 20 °C (293.15 K). The highest hourly temperature occurred in April, reaching about 40 °C (313.15 K), while the lowest hourly temperature was recorded in December at around 16 °C (289.15 K).

Dry Bulb Temperature (C) - Hourly
NNAMDI AZIKIWE INTERNATIONAL
1 JAN 1:00 - 31 DEC 24:00
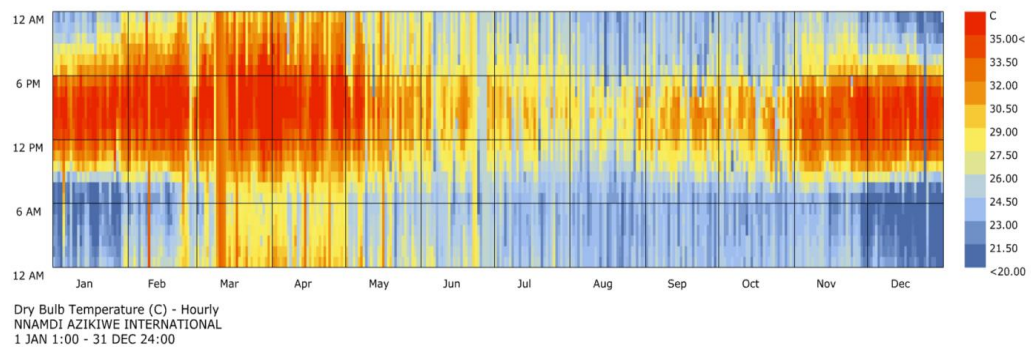
Figure 3.13. Abuja weather data: dry bulb temperature showing monthly temperature gradient for Abuja from January 2019 to December 2019 [365], [366]

As graphically shown in Figure 3.13, heat stress levels peaked in January, February, March, April, November, and December; 6 months of the year, recording an overall 37.3 % annual value. However, in general, the daytime outdoor temperature values throughout the year suggest a need for cooling for up to 8 hours in a typical day, from 12:00 pm to 7:00 pm, but temperatures drop between 7:00 pm to 11:00 am (16 hours). On average, a daily temperature swing of approximately 10.5 °C to 20 °C (283.65 K to 293.15 K) was observed, indicating suitability for PCM use.

This temperature range aligns with recommendations for PCM operational temperature swings found in existing literature [367].

3.4.3.1.3 Wind speed and direction analysis

To further analyse the wind speed and direction of the wind, a wind rose analysis was conducted as shown in Figure 3.14. This revealed an average wind speed measuring 2.2 m/s. Prevailing winds in Abuja primarily come from the south to west, ranging from 2 to 4 m/s.
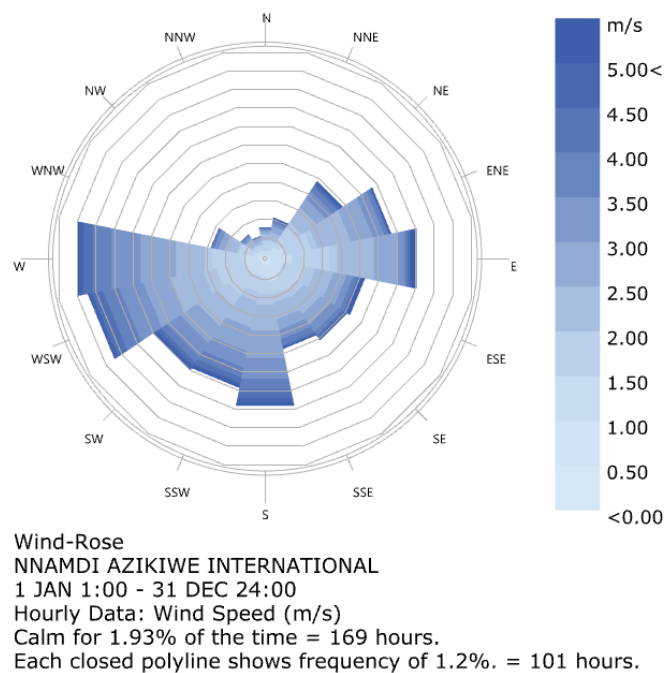
Figure 3.14. Abuja weather data: Prevailing winds between January 2019 to December 2019 [365], [366]
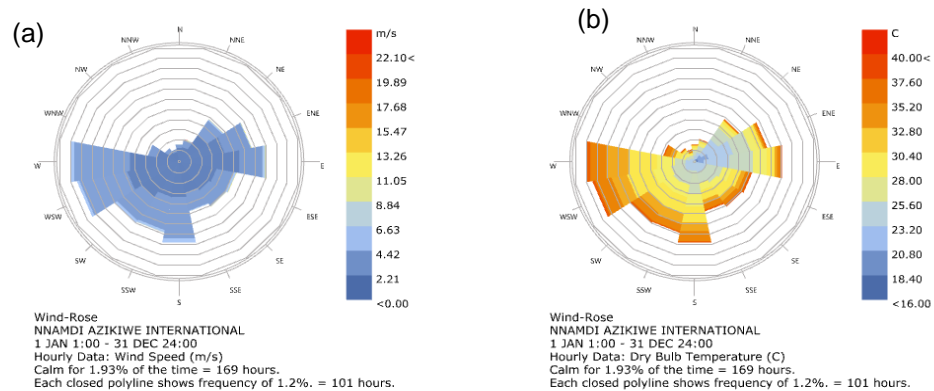
Figure 3.15. Abuja weather data from January 2019 to December 2019: Comparison between (a) prevailing winds and (b) ambient dry bulb air temperature [365], [366].

It was also noted as indicated in Figure 3.15 (a) and (b), that there is a correlation between wind speeds and ambient temperatures. When wind speed increased from approximately 2 m/s to 4 m/s, the ambient dry bulb air temperature was observed to have also increased from approximately 30.4 °C (303.55 K) and 35.2 °C (308.35 K). However, wind calmness occurred only 1.93 % of the time, necessitating that hybrid or assisted ventilation may be required for indoor thermal comfort.

3.4.3.1.4 Indoor thermal comfort temperature target

To predict the indoor thermal comfort target for the proposed EPCM-HMW system, the Grasshopper Ladybug psychometric chart based on the "Adaptive Predicted Mean Vote" (PMV) thermal comfort model was utilised.
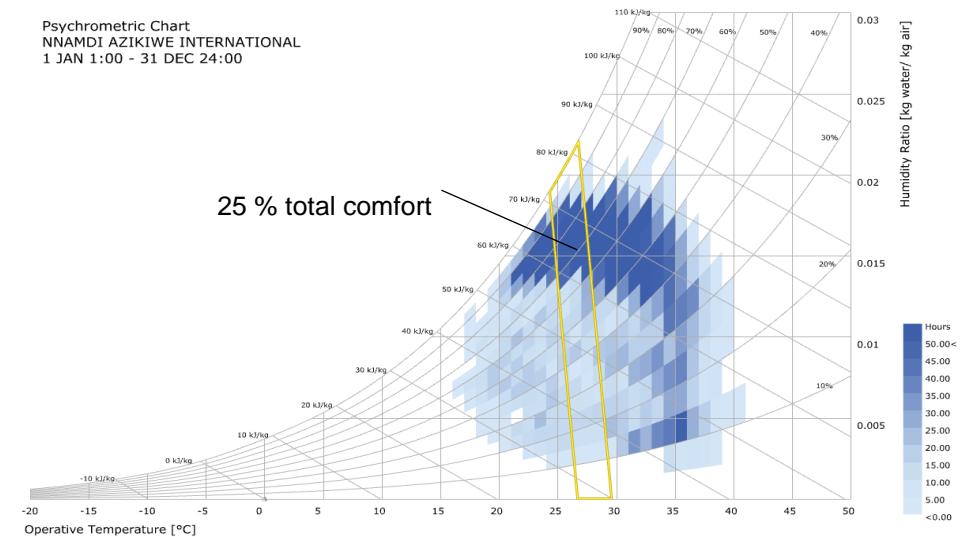
Figure 3.16. Thermal comfort prediction at the lowest wind speed limit of 0.2 m/s without any additional intervention [365], [366].

The analysis of the thermal comfort predicted target using psychometric charts in Figure 3.16 revealed a thermal comfort operative temperature band of 27.5 °C to 29.5 °C (300.65 K to 302.65 K), achieving only a 25 % comfort level. With hybrid ventilation, the operative temperature band expanded from 27.5 °C to 33.5 °C (300.65 K to 306.65 K), predicting a 44 % indoor comfort level (Figure 3.17). However, thermal storage intervention widened this comfort band further, predicting a 52 % comfort level as indicated in Figure 3.18.
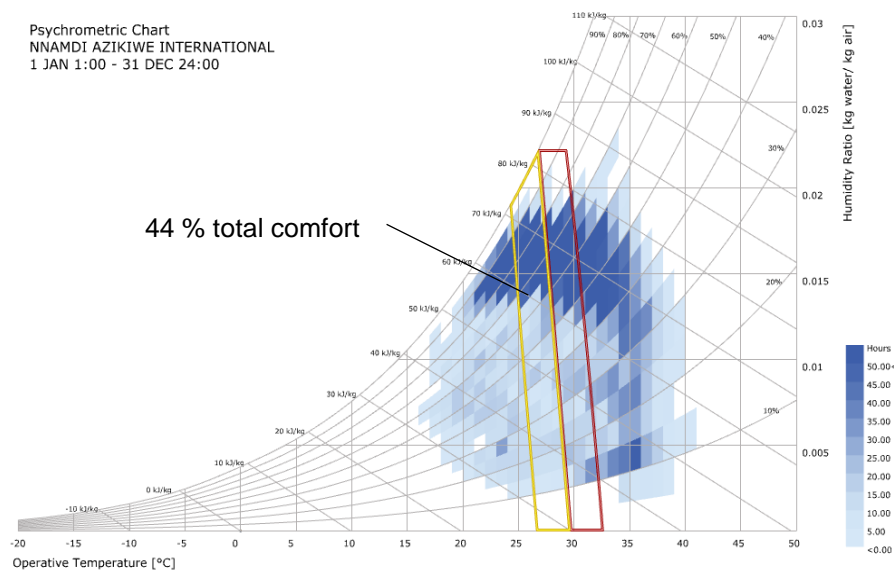
Figure 3.17. Thermal comfort prediction at the lowest wind speed limit of 0.2 m/s with the inclusion of hybrid ventilation strategy only [365], [366].
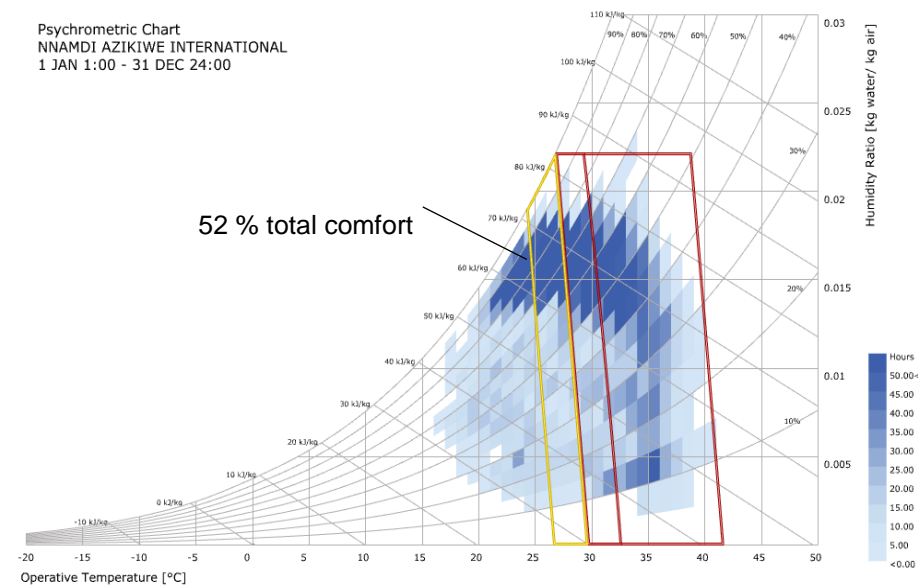
Figure 3.18. Thermal comfort prediction at the lowest wind speed limit of 0.2 m/s with the inclusion of hybrid ventilation strategy and thermal storage [365], [366].

Based on the thorough analysis conducted to evaluate temperature ranges, wind speed variations, and thermal comfort parameters within the chosen climate, Table 3.10 provides a summary of the derived data set used as input for the computational study of the EPCM-HMW system.

However, due to computational time constraints, simplified and averaged data sets were utilised instead of instead of inputting detailed daily weather data into the simulation code.

Table 3.10. Inferred climate input data for the computational study of the "EPCM-HMW system"

	wind speed	outdoor air temperature		thermal comfort temperature	
	m/s	°C	K	°C	K
Climatic daily data range Highest range		40	313.15		
Lowest range		16 - 23	289.15 - 296.15		
Average daily range	2.2	35	308.15		
Average daily temperature swing		10.5 - 20	283.65 - 293.15		
Operative temperature band with no intervention				27.5 - 29.5	300.65 - 302.65
Operative temperature band with hybrid ventilation				27.5 - 33.5	300.65 - 306.65
Adopted data for computational study	1.88, 3	30, 35	303.15, 308.15		

3.4.3.2 Establishment of the model's boundary conditions

Defining the boundary conditions of the CFD model was crucial to understanding how the model interacts with its surroundings. To determine this, the fluid volume of the model was first extracted from the solid model to simplify the computational domain. After this, the

microclimate and macroclimate domains were defined. According to Figure 3.19, the macroclimate represents the outdoor airflow domain around the EPCM-HMW system, while the microclimate represents the single-zone indoor room with wich the EPCM-HMW system provides ventilation.
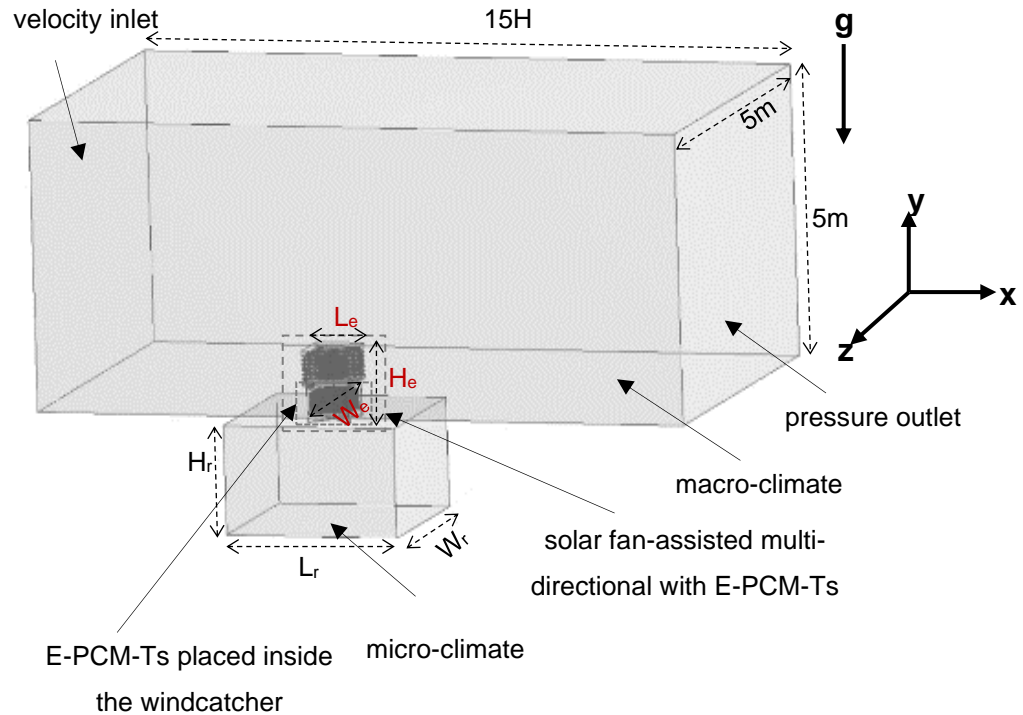
Figure 3.19. Interaction of the EPCM-HMW system with the macro-climate and micro-climate domains.

The size of the macro-climate was based on literature recommendations that specified that the upstream macroclimate should generally be extended by upto 5 times the height (5H) of the model [368], while downstream should extend 15 times the height (15H) to ensure adequate modelling and reduce venturi effects, reverse flow or wind-blocking effect [369]. To meet this criteria, the far-field pressure outlet of the macro-climate domain was extended by a 20 m extension from the inlet boundary.

The microclimate, dimensioned as $W_r \times L_r \times H_r$, measuring 5 x 5 x 3 m, represents a typical living room size in a 4-bedroom residential dwelling

unit, with occupancy of 4.5 people per household, representing a typical household size in Nigeria according to the 2023 data of the average household size in Nigeria [370], [371]. The living room space is chosen as the test room since it is one of the most utilised and largest single-zone spaces in a typical residential building (insert ref), which should meet ventilation rates of 2.5 L/s per person (11.25 L/s for 4.5 people) and 0.3 L/s per square meter (7.5 L/s per 25 square meter) based on "ASHRAE Standard 62.1-2013, Ventilation for Acceptable Indoor Air Quality Standard" [372].

The EPCM-HMW system mounted on top of the indoor space is dimensioned as represented by W_e x L_e x H_e, measuring 1.4 x 1.4 x 1.87 m. Additionally, the same twelve (12) monitoring points created in the CFD validation model were retained to monitor all properties throughout the numerical modelling for the EPCM-HMW system. Figure 3.20 shows the monitoring points created within the test room which are consistent with the vector points utilised in Calautit et al.'s experimental model [357].
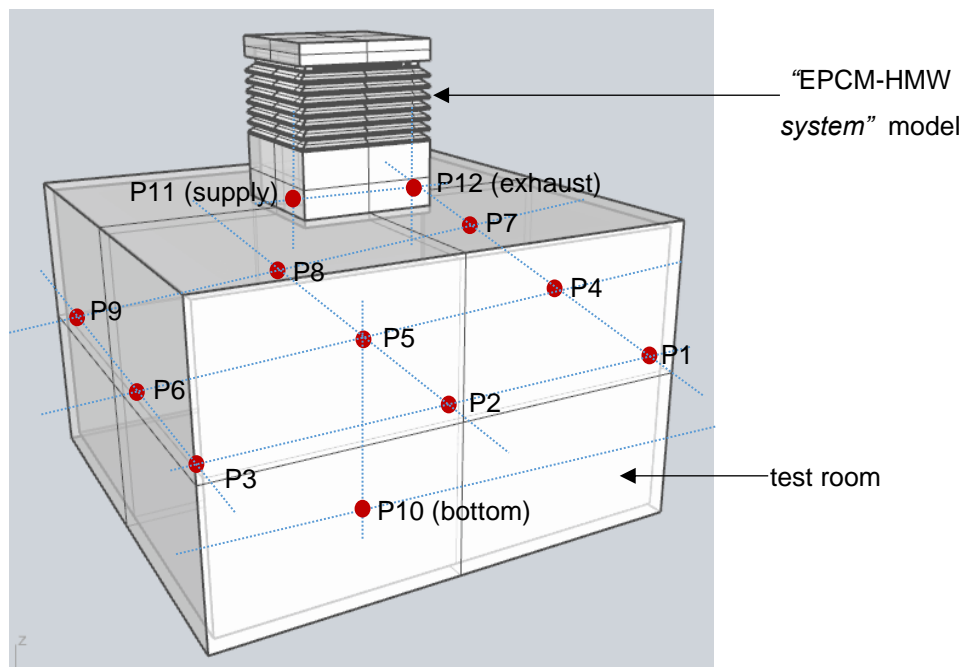
Figure 3.20. The twelve (12) monitored points where readings were taken throughout the "EPCM-HMW system" simulation study.

A uniform outdoor air velocity and temperature were applied at the inlet boundary during the CFD model simulations. However, for the different simulated cases, the inlet air temperature (T_{in}) at the macro-climate boundary varied, ranging between 303.15 K (30 °C) and 308.15 K (35 °C). This variation represents a typical outdoor temperature range (T_{out}) in extremely hot conditions.

The CFD model utilised inlet velocities ranging from 1.88 m/s to 3 m/s at incident wind angles of 0° and 45°. The incident wind angles of 0° (a), 30° (b), and 45° (c) to the air vents of the "EPCM-HMW system" are illustrated in Figure 3.21.
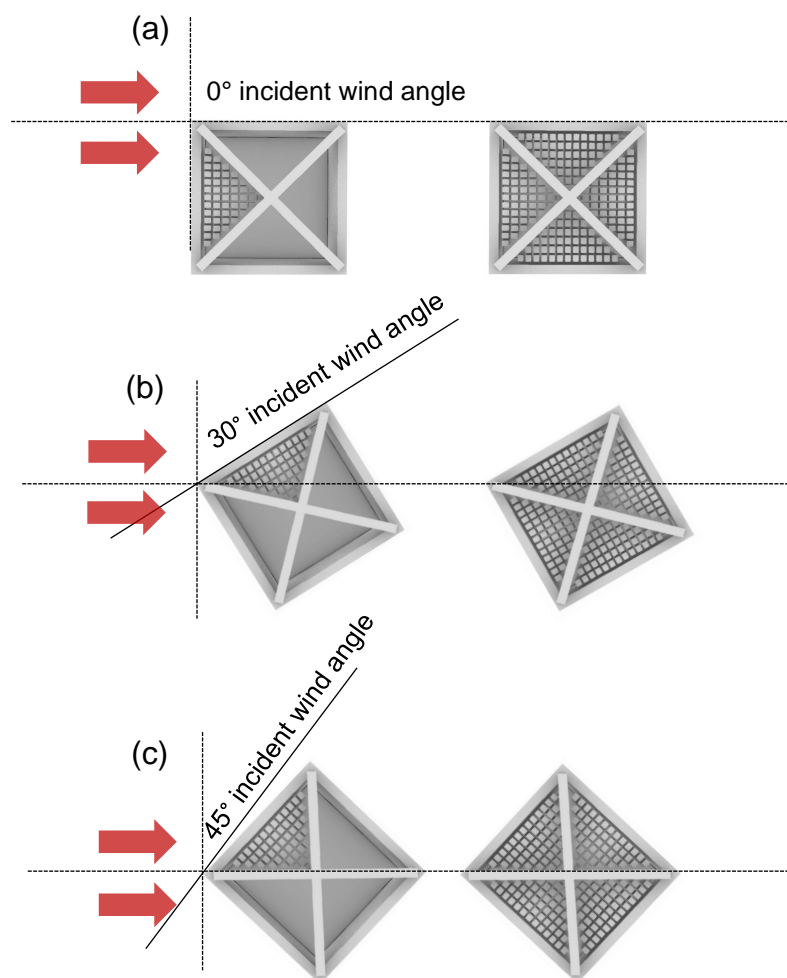
Figure 3.21. The incident wind angles of 0° (a), 30° (b), and 45° (c) to the "EPCM-HMW system"

The pressure outlet was positioned at the extended macro-climate domain to prevent reverse flow during all the simulation processes. The model incorporated a gravitational force of -9.81 m/s², and the domain walls were assigned a roughness height of 0.001 Ks. Throughout the simulation, atmospheric pressure was assumed, and outlet pressure was set at 0Pa. Relaxation factors were set at 0.3 for pressure, 0.7 for momentum, and 1 for energy.

In addition to the initial simulation setup, the EPCM-T's initial temperature was maintained at 293.15 K (20 °C). This initial PCM temperature was chosen because it represents the lowest temperature achievable in the system's operating climate at night or in the morning. Also, initialising the PCM at lower temperature extends the PCM's melting duration/ This can help the PCM to potentially stabilise the indoor temperature for a longer period. A solar fan static pressure jump of 10 Pa was defined. Table 3.11 further summarises the boundary conditions for the EPCM-HMW model.

Table 3.11. Parameters for boundary conditions for the "EPCM-HMW system" CFD Model

boundary condition parameters	values
inlet air temperatures	303.15 K (30 °C), 308.15 K (35 °C)
inlet air velocities	1.88 m/s, 3 m/s
inlet wind angles	0 °, 30 °, 45 °
non-slip wall roughness height	0.001 Ks.
gravitational force	-9.81 m/s²
pressure outlet	0Pa
EPCM-T's initial temperature	293.15 K (20 °C)
solar fan static pressure jump	10 Pa
relaxation factors	0.3 pressure, 0.7 momentum, and 1 energy

To collect relevant data during the simulation exercise, monitoring points were established along the micro-climate ZY plane, enabling the observation of supply airflow rates, pressure, and temperature. Thermal storage heat transfer of the PCM was analysed through the assessment of the liquid fraction f_l, at 120-flow time intervals.

3.4.3.3 Thermo-physical properties

The optimal PCM melting temperature $T_{m,r}$ for the set average room temperature $\overline{T}_r$ was derived from equations 3.22 and 3.23, based on the studies by Peippo et al. [373] and Nazir et al. [374]. This process justified the selection of RT28HC paraffin, a commercially available Rubitherm-GmbH PCM product, with a melting temperature of 28 °C (301.15 K) and a solid-state specific heat capacity of 1650 J/kg K^{-1} [281], which also aligns with the EPCM-T parametric study [281].

$$T_{m,r} = \overline{T}_r + \frac{Q}{h \times t_s} \qquad\qquad \text{Equation 3.20}$$

as Q represents the absorbed heat in a room per unit area surface in Jm^{-2}, stored based on a diurnal storage cycle $t_s = t_c + t_d$. The wall surface heat transfer coefficient is given as h in Wm^{-2} K^{-1}.

$$Where \; \overline{T}_r = \frac{t_c T_d + t_d T_n}{t_c + t_d} \qquad\qquad \text{Equation 3.21}$$

T_d represents the daytime room temperature and T_n represents the nighttime room temperature based on the PCM charging t_c and discharging t_d times.

This choice aligns with the recommended thermo-properties for PCMs suitable for hot outdoor conditions, as specified in the studies by Sheriyev et al. [375] and Lei et al. [376]. For this study and based on the outcomes of the EPCM-T parametric study conducted, the selected PCM was encapsulated in rectangular aluminium tubes measuring 40 x 30 x 500 mm, with a conduction thickness of 0.001 mm.

3.4.3.4 Mesh generation and adaptation

Two separate non-uniform hybrid computational meshes were generated based on Case 1 and 2 models, each featuring distinct EPCM-T arrangements within the EPCM-HMW system.
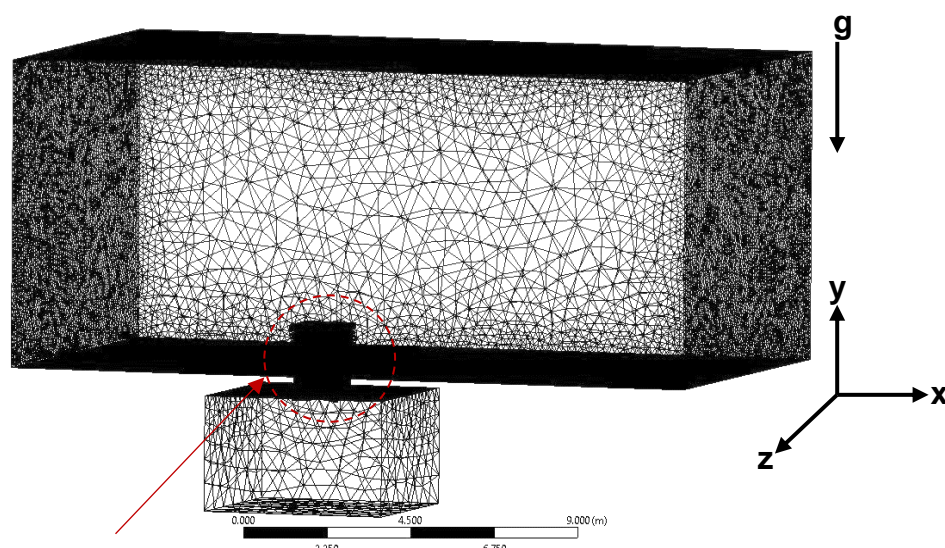
The mesh size was refined at the location where
the E-PCM-Ts were placed within the
computational domain.

Figure 3.22. The Computation domain is based on a non-uniform hybrid mesh.

As seen in Figure 3.22, the mesh region circled, was refined at a specific location where the E-PCM-Ts were within the windcatcher component of the model. This refinement process involved applying face meshing techniques in those areas of interest, aiming to enhance the precision of the simulation results. However, to ensure the accuracy of the CFD results, the meshing exercise was conducted based on a posterior estimate.

3.4.3.5 Grid sensitivity and time step sizing analysis

In CFD simulations, the grid sensitivity of the model as well as the appropriate time step size both influence the convergence of the CFD simulation. Hence, it is important to select an appropriate time step size

as well as conduct grid sensitivity testing of the CFD model to achieve an accurate and stable numerical solution.

The grid sensitivity of the model was performed until an insignificant posterior estimate error was achieved by varying the mesh size from coarse to fine grids [369].

Table 3.12. Meshing data used for the grid independence study.

Mesh grading	E-PCM-T face element size [mm]	Case 1 model (E-PCM-Ts placed only in the supply airstream)		Case 2 model (E-PCM-Ts placed in all four airstreams)	
		Nodes	Elements	Nodes	Elements
Fine	10	2207331	11684429	2899882	14512606
Medium	12	1276807	7141564	1969358	9969741
Coarse	15	822564	4683093	1515115	7511270

As shown in Table 3.12, the mesh sizes varied from 4.6 million to 14.5 million elements. The fine mesh sizing for the Case 1 model, with 11.6 million elements and 2.2 million nodes, and the Case 2 model with fine mesh consisting of 14.5 million elements with 2.8 million nodes, exhibited the minimum discretisation error and were chosen for further analysis.

Figures 3.23 and 3.24 present the results of the grid sensitivity study, comparing supply velocity (V_{supply}) and indoor velocity (V_{indoor}) for Case 1 and Case 2 using coarse, medium, and fine meshes, respectively. Both Figures 3.23 and 3.24 showed that the coarse mesh deviated more significantly from the medium and fine meshes at the earlier time steps. The deviation of the coarse mesh results from the other mesh models was approximately 1.6% for Case 1 and 1% for Case 2, respectively. On the other hand, there was only about a 0.05% deviation between the medium and fine mesh results for both Cases 1 and 2. As a result, the fine mesh size was selected, as no significant changes were observed beyond this level of refinement.
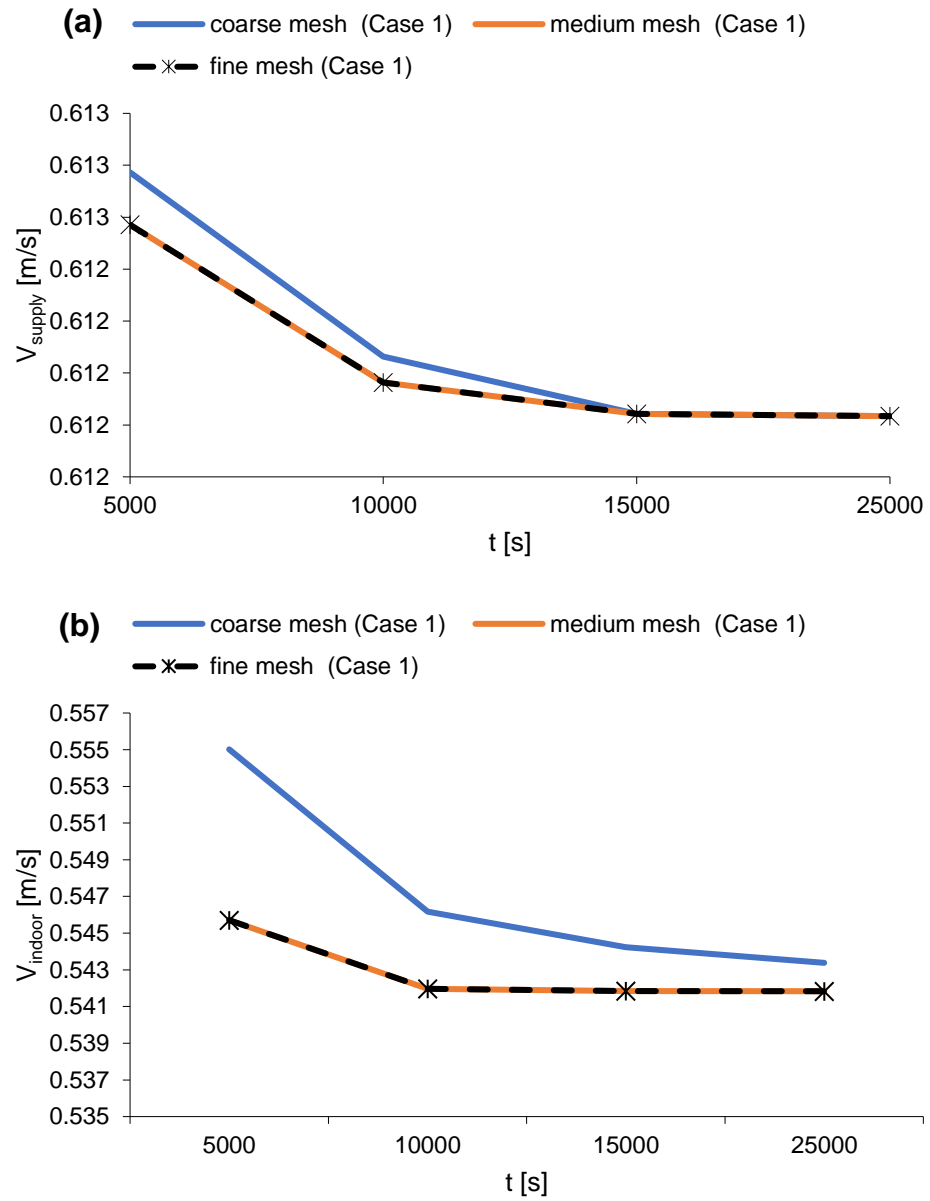
Figure 3.23. Comparison of (a) supply velocity (Vsupply) and (b) indoor velocity (Vindoor) for EPCM-HMW Case 1 model across different grid resolutions (coarse, medium, and fine meshes)
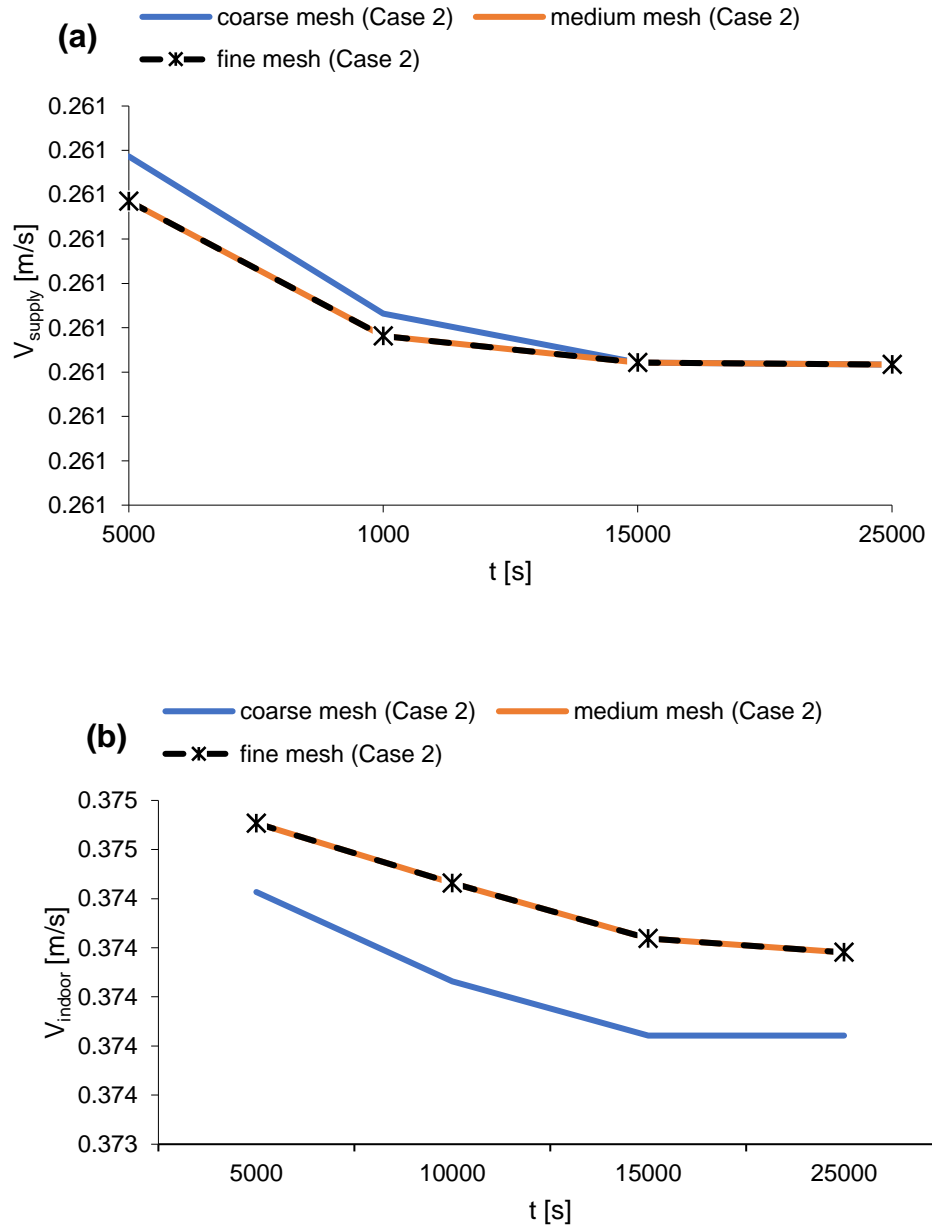
Figure 3.24. Comparison of (a) supply velocity (V_{supply})and (b) indoor velocity (V_{indoor}) for EPCM-HMW Case 2 model across different grid resolutions (coarse, medium, and fine meshes)

The time step size analysis was conducted by evaluating the liquid fraction performance of the selected mesh model Case 1 and 2 based on 60, 40, 10, and 5 timesteps. The solution iterated at each time step and was monitored until no further variations were observed in the residuals for velocity components, continuity, and energy. The smallest average error occurred at a 5-timestep for velocity outputs. Hence, a 5-timestep was adopted for the study.

3.4.3.6 Solution convergence

According to the Fluent User Guide [377], a residual error of 10^{-4} is acceptable to show that a CFD solution has converged. However, true convergence occurs when the CFD solution vectors no longer experience any changes. To assess this adequately, it is important to monitor parameters relevant to the CFD problem. Hence, for all simulation cases, which were based on varied boundary conditions with uniform inlet air velocities ranging from 1.88 m/s to 3 m/s at wind angles of 0 °, 30 °, and 45 °, the supply airflow rate, pressure, and temperature profiles were monitored at the specified twelve points ($P_1 - P_{12}$) to ascertain solution convergence.

Furthermore, the PCM heat transfer rate during the model solution also was closely monitored every 120 seconds of flow time, specifically focusing on the liquid fraction and PCM average weighted temperature profiles. The solution was allowed to converge without setting predetermined convergence criteria in the solver. As a result, convergence occurred when all the monitored residuals and properties showed no further changes, and the energy conservation property showed no error.

3.5 Limitations in CFD simulation studies

The study's computational resource constraints necessitated a focus on a limited number of CFD cases to achieve the study objectives. Simplifications were also made to the model geometry and boundary conditions to enhance computational speed due to this limitation, which could potentially limit result accuracy. Nevertheless, a strong correlation was observed during results validation against existing experimental data in the literature. This validation revealed minimal errors, well within the acceptable threshold according to established best practices.

3.6 Chapter's concluding remarks

This chapter presented the design, operational mechanisms and method of assessment used for the proposed EPCM-HMW system, aimed at addressing thermal storage and cooling limitations found in traditional windcatchers for Sub-Saharan Africa's tropical savannah climates. The system comprises a multi-directional windcatcher, a wall-mounted solar axial fan, and EPCM-Ts. The introduction of different EPCM-T configurations for parametric study allowed for a detailed investigation into the impact of various integration modes on airflow patterns, temperature distribution, and overall system performance.

It can be inferred from the discussions that the standard k-ε model was selected for turbulent airflow and the temperature-based method for PCM heat transfer to provide the theoretical foundation for this study. These models were chosen for their effectiveness in solving relevant flow and heat transfer problems while maintaining computational simplicity. RANS transient 3D standard k-ε turbulence Finite Volume Method (FVM) based on SIMPLE algorithm in Ansys software was adopted to assess the system's ventilation, thermal storage, and cooling performance in CFD based on pre-defined parameters. This approach enabled a detailed

analysis of the system's functionality within the constraints of the limitation of high computational resource requirements.

The validation method for the model was based on determining the confidence limits of the model's accuracy using three widely accepted statistical performance models: normalised mean square error (NMSE), Fractional Bias (FB), and the fraction of predictions within a factor of two of observations (FAC2).

Chapter 4

4 CFD results and discussions

4.1 Overview of chapter

This chapter discusses the results obtained from the CFD assessment of the EPCM-HMW system's ventilation, cooling, and thermal storage performance. It also covers the results from the EPCM-T parametric design study, which was used to select the exact EPCM-T employed in the EPCM-HMW system.

4.2 Results and discussions of the EPCM-T parametric design analysis

Models for shell-tube rectangular, shell-tube cylindrical, and cylindrical EPCM-T designs were simulated. A total of 28 simulations were conducted, with all parameters initially set to 20°C. The simulations were run under varying inlet air velocities (V_{inlet}) of 1.88 m/s and 3 m/s, with a constant ambient inlet temperature (T_{inlet}) of 35°C as the boundary condition. The objective was to assess the heat transfer and storage capacity of the EPCM-T samples based only on the charging cycle of the PCM. This represents the PCM heat absorption cycle for cooling the incoming air under these conditions. The results discussed in this section include variations in PCM temperature (T_{PCM}), air temperature (T_{air}), and PCM liquid fraction (f_l).

4.2.1 Impact of ambient airflow on heat transfer and temperature in the EPCM-T models.

This test aimed to understand how ambient airflow will influence heat transfer and temperature regulation within the EPCM-T models.

4.2.1.1 Shell-tube rectangular EPCM-T - model 1A

The temperature variations that occurred in the shell-tube rectangular EPCM-T model 1A during the simulation are represented by the temperature contours shown in Figures 4.1 to 4.4.

*Figure 4.1. Temperature contour for shell-tube rectangular EPCM-T **model 1A** when **aluminium encapsulation** is utilised at **1.88 m/s** inlet velocity and 35 ^{o}C inlet temperature.*
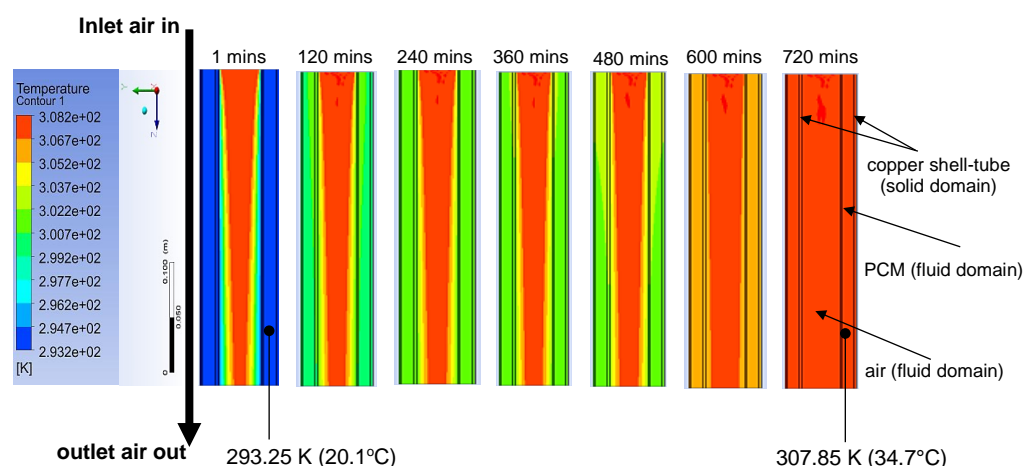
*Figure 4.2. Temperature contour for shell-tube rectangular EPCM-T **model 1A** when **copper encapsulation** is utilised at **1.88 m/s** inlet velocity and 35 oC inlet temperature.*

Accordingly, Figures 4.1 and 4.2 Illustrate that at a V_{inlet} of 1.88 m/s, the aluminium and copper shell-tube rectangular EPCM-T models exhibited a gradual temperature rise. The PCM temperature increased from

approximately 20.1°C (293.25 K) to around 34.7°C (307.85 K) in the copper model (Figure 4.2) as PCM charging was taking place, and 34.9°C (308.05 K) in the aluminium-encapsulated EPCM-T - model 1A (Figure 4.1) by the 720-minute mark. In this case, the aluminium model achieved approximately 0.6% higher final temperature than the copper model at 1.88 m/s. This indicates the completion of the heat transfer process across all components.

When the V_{inlet} was increased to 3 m/s, the heat transfer process accelerated, with temperatures stabilising around 600 minutes, as seen in Figures 4.3 and 4.4.
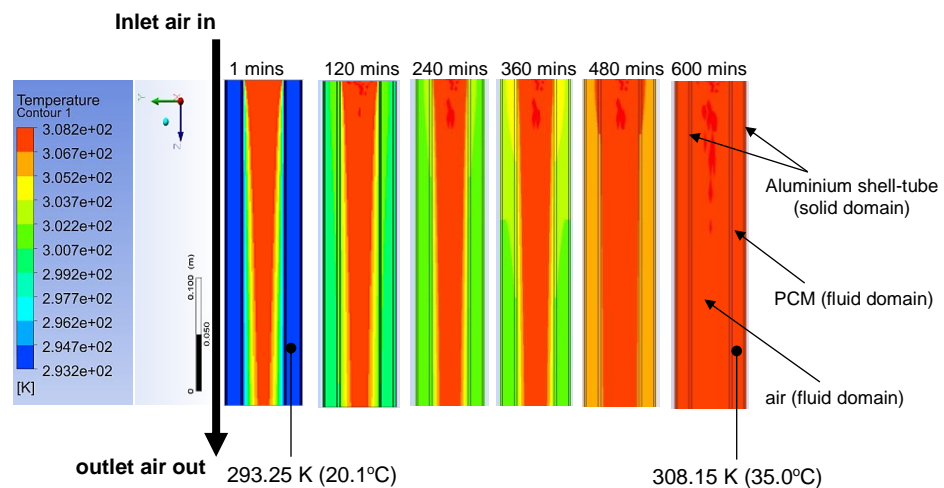
*Figure 4.3. Temperature contour for shell-tube rectangular EPCM-T **model 1A** when **aluminium encapsulation** is utilised at **3 m/s** inlet velocity and 35 °C inlet temperature.*

By 600 minutes, the final PCM temperature in the aluminium-encapsulated EPCM-T - model 1A had reached 35.0°C (308.15 K) (Figure 4.3), and 34.7°C (307.85 K) in the copper-encapsulated EPCM-T model 1A (Figure 4.4). This indicates that with higher airflow, the copper and aluminium-encapsulated EPCM-T models converged more rapidly, with the aluminium model achieving 0.9% higher PCM temperature than the copper model by 600 minutes.
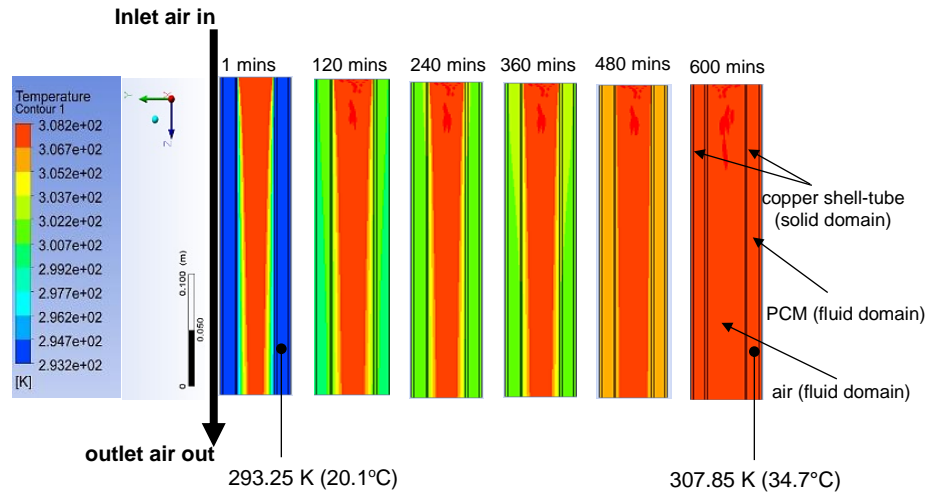
*Figure 4.4. Temperature contour for shell-tube rectangular EPCM-T **model 1A** when **copper encapsulation** is utilised at **3 m/s** inlet velocity and 35 °C inlet temperature.*

These observations reveal that the temperature of the PCM, air, and encapsulation tubes in Model 1A converged more rapidly at higher airflow speeds, indicating that higher velocities significantly enhance heat transfer rates.

Figures 4.5 and 4.6 provide the graphical comparative analysis of the PCM and air temperature changes in Model 1A at different V_{inlet} speeds.
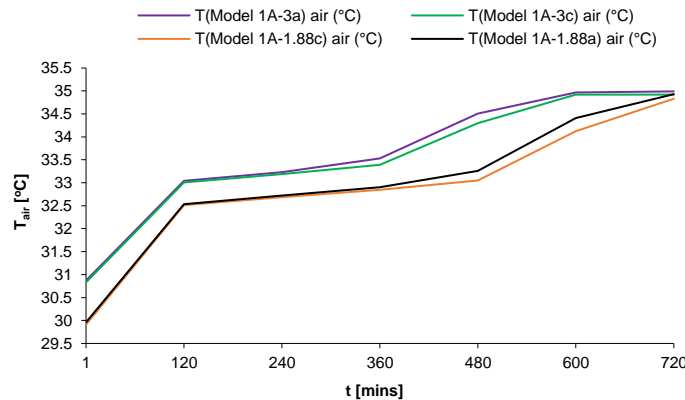
*Figure 4.5. T_{air} in shell-tube rectangular EPCM-T **model 1A** with **aluminium** and **copper encapsulation** at V_{inlet} of 1.88 m/s and 3 m/s.*

When the V_{inlet} increased to 3 m/s, T_{air} rose from 30.0°C (303.15 K) to 34.6°C (307.75 K) as indicated in Figure 4.5. However, the final T_{PCM} and T_{air} values were marginally lower in the copper model compared to the

aluminium models (Model 1A-1.88a and Model 1A-3a). Specifically, the T_{air} in the aluminium-encapsulated EPCM-T - model 1A was approximately 0.3% higher than in the copper-encapsulated EPCM-T - model 1A at 3 m/s. Though small, these percentage differences show that copper and aluminium-encapsulated EPCM-T models performed similarly. However, the aluminium models reached slightly higher final temperatures, particularly at higher airflow velocities.

In Figure 4.6, V_{inlet} significantly impacts temperature variation in both models. For example, between 360 and 720 minutes, Model 1A-1.88a (aluminium, 1.88 m/s) showed a 10.48% increase in T_{PCM}, while Model 1A-1.88c (copper, 1.88 m/s) exhibited an 11.29% increase. When V_{inlet} was increased to 3 m/s, T_{PCM} reached a slightly higher value of 34.7°C (307.85 K) after 720 minutes, compared to 34.5°C (307.65 K) at V_{inlet} of 1.88 m/s.
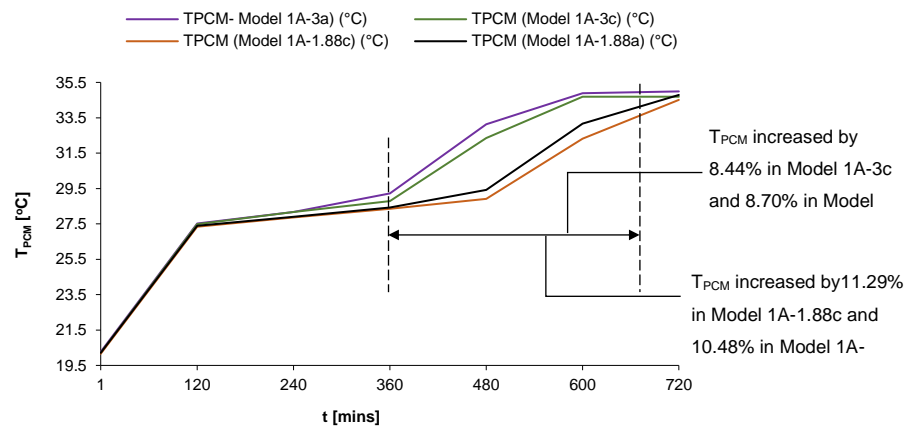
Figure 4.6. T_{PCM} *in Shell-tube rectangular EPCM-T* **model 1A** *with* **aluminium** *and* **copper encapsulation** *at* V_{inlet} *of 1.88 m/s and 3 m/s.*

The graph in Figure 4.7 shows the temperature variation of inner and outer tubes ($T_{inner\text{-}tube}$ and $T_{outer\text{-}tube}$) in the shell-tube rectangular aluminium and copper-encapsulated EPCM-T model 1A at V_{inlet} of 1.88 m/s and 3 m/s. There was a sharp initial temperature rise within the first 120 minutes, where the $T_{inner\text{-}tube}$ and $T_{outer\text{-}tube}$ across all models reached about 28.5°C (301.65 K). After this, the $T_{inner\text{-}tube}$ gradually increased

between 120 and 360 minutes, reflecting the phase change of the PCM absorbing heat. By 720 minutes, the $T_{outer-tube}$ in Models 1A-1.88c and 1A-3c reached around 34.9°C (308.05 K) and 35.0°C (308.15 K). Meanwhile, Models 1A-1.88a and 1A-3a exhibited a slower heat transfer. In these cases, the final $T_{outer-tube}$ and $T_{inner-tube}$ stabilised at about 34.7°C (307.85 K) and 34.8°C (307.95 K), respectively, by 720 minutes.
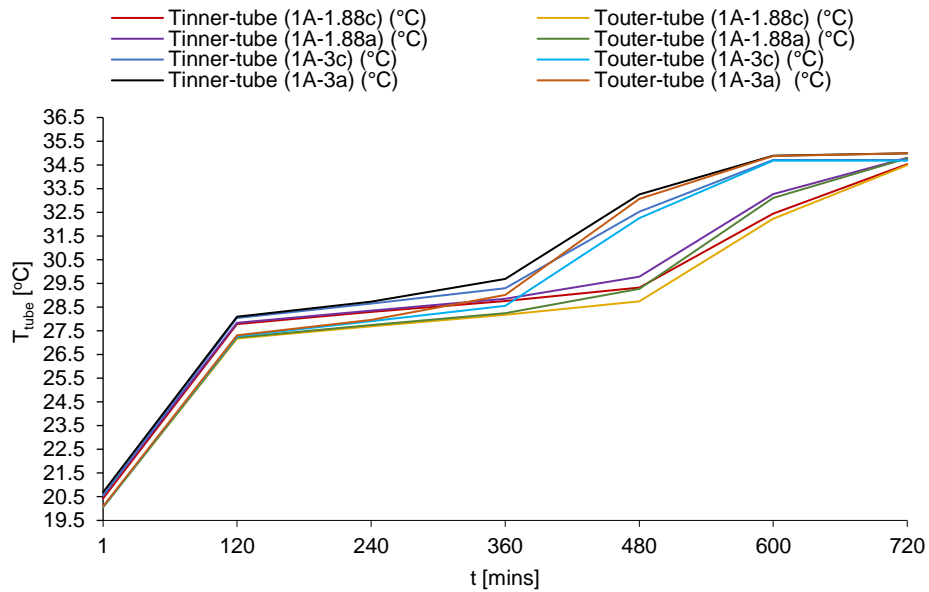
*Figure 4.7. T_{tube} in shell-tube rectangular EPCM-T **model 1A** when **aluminium** and **copper encapsulation** are adopted at V_{inlet} of 1.88 m/s and 3 m/s.*

It is clear from the results that the copper encapsulation model responds more quickly to heat transfer due to copper's higher thermal conductivity. In contrast, the aluminium-encapsulated EPCM-T models (1A-1.88a and 1A-3a) exhibited a slower, more controlled temperature rise, particularly at lower inlet velocities. In addition, higher airflow velocities (3 m/s) and copper encapsulation improve the heat transfer rate. Therefore, if the goal is to achieve slower temperature stabilisation and maintain a more controlled thermal profile, aluminium encapsulation is the more suitable choice for the Model 1A EPCM-T design.

4.2.1.2 Shell-tube cylindrical EPCM-T - model 2A

The temperature variations that occurred in the shell-tube cylindrical EPCM-T model 2A during the simulation are represented by the temperature contours shown in Figures 4.8 to 4.11. These results were compared under different encapsulations (aluminium and copper) at 1.88 m/s and 3 m/s inlet velocities with an inlet temperature of 35°C.

*Figure 4.8. Temperature contour for shell-tube cylindrical EPCM-T **model 2A** when **aluminium encapsulation** is utilised at **1.88 m/s** inlet velocity and 35 °C inlet temperature.*

In Figure 4.8, the aluminium encapsulated EPCM-T model 2A at 1.88 m/s showed a gradual temperature rise. The T_{PCM} stabilised for the first 240 minutes, at around 301.62 K (28.47°C) before it rose to 307.62 K (34.47°C) by 600 minutes. However, thermal equilibrium was achieved in 720 minutes.

From the temperature contour in Figure 4.9, the copper-encapsulated version showed a similar trend. However, the heat transfer between the EPCM-T and air was faster, achieving 308.08 K (34.93°C) by 600 minutes.

*Figure 4.9. Temperature contour for shell-tube cylindrical EPCM-T **model 2A** when **copper encapsulation** is utilised at **1.88 m/s** inlet velocity and 35 ᵒC inlet temperature.*
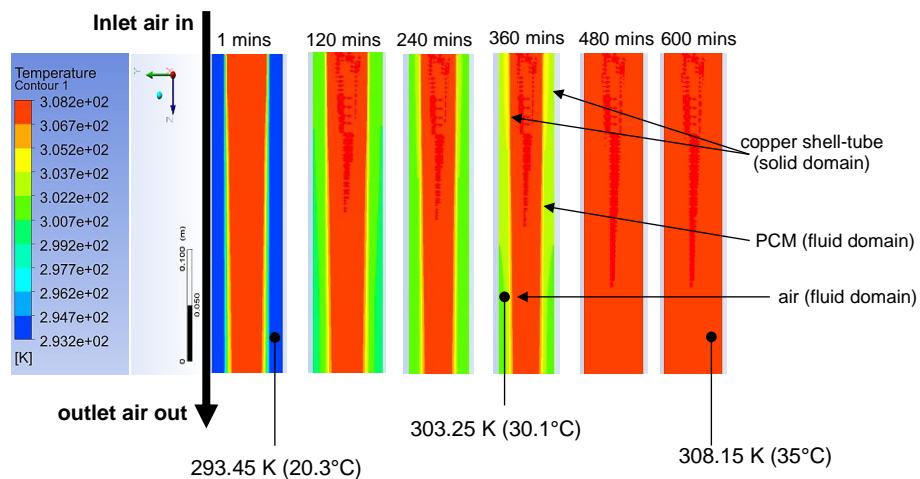
*Figure 4.10. Temperature contour for shell-tube cylindrical EPCM-T **model 2A** when **aluminium encapsulation** is utilised at **3 m/s** inlet velocity and 35 ᵒC inlet temperature.*

At a higher inlet velocity of 3 m/s, Figure 4.10 highlights more rapid heat transfer. In the shell-tube cylindrical EPCM-T model 2A, with aluminium encapsulation, a T_{PCM} and T of 308.15 K (35°C) were reached at 600 minutes. This indicated that thermal equilibrium was achieved earlier than at V_{inlet} of 1.88 m/s. This shows that less efficient cooling occurred, as the heat was transferred more quickly through the material.
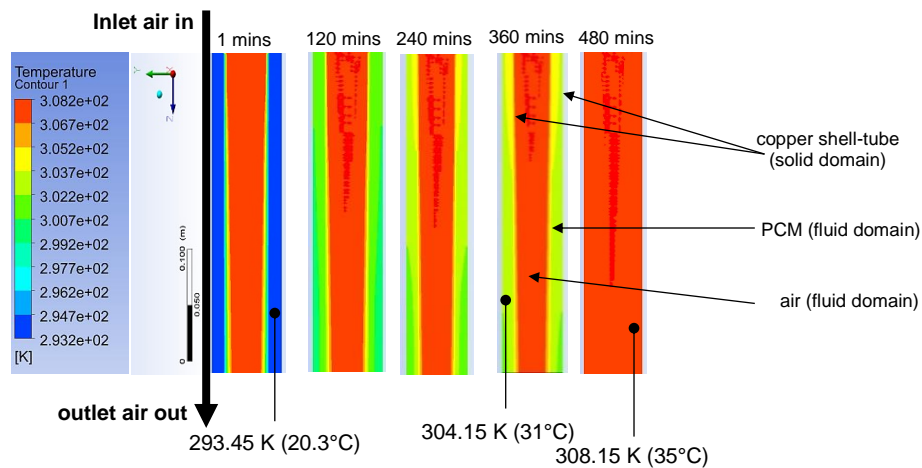
*Figure 4.11. Temperature contour for shell-tube cylindrical EPCM-T **model 2A** when **copper encapsulation** is utilised at **3 m/s** inlet velocity and 35 °C inlet temperature.*

In the case of the temperature variation in the copper-encapsulated model at 3 m/s, illustrated in Figure 4.11, faster heat transfer occurred. In this case, the PCM temperature quickly rose to 308.15 K (35°C) by 480 minutes by which time thermal equilibrium was achieved. Based on the results, copper encapsulation at 3 m/s offered faster heat transfer, implying that its prolonged temperature stabilisation capacity was less effective compared to the aluminium-encapsulated model. Additionally, it is clear that higher velocity reduced cooling, even though heat transfer was enhanced. Overall, copper achieved equilibrium 20% faster than aluminium. While the temperature differences were minimal, there was a significant difference in the rate of heat transfer based on the time equilibrium was achieved in the models.

4.2.1.3 Rectangular EPCM-T – model 1B

The temperature variations that occurred in the rectangular EPCM-T model 1B during the simulation are represented by the temperature contours shown in Figures 4.12 to 4.15.
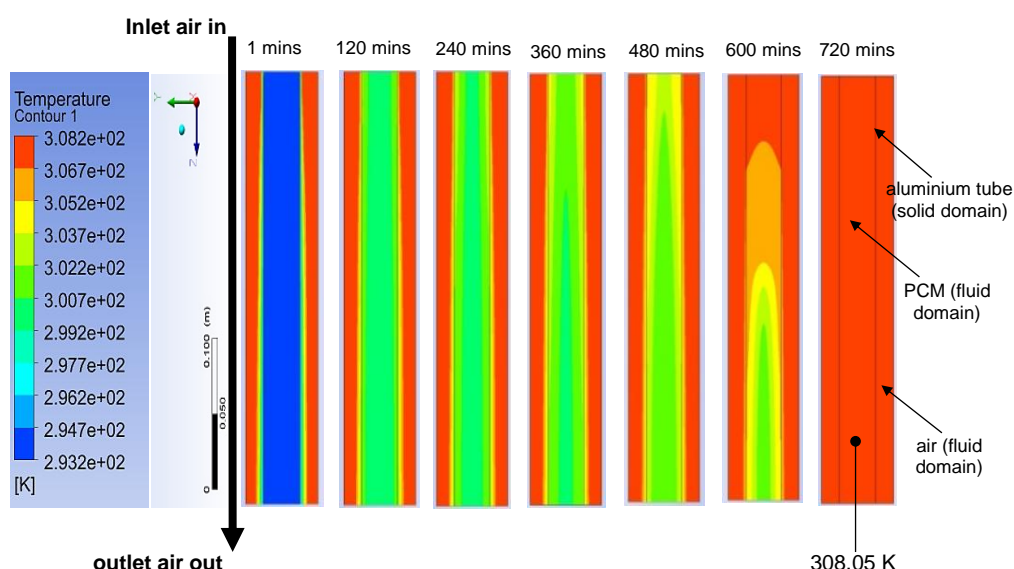
*Figure 4.12. Temperature contour for rectangular EPCM-T **model 1B** when **aluminium encapsulation** at **1.88 m/s** inlet velocity and 35 °C inlet temperature.*

At a V_{inlet} of 1.88 m/s, as seen in Figure 4.12, the PCM temperatures in the rectangular aluminium EPCM-T – model 1B rose gradually, with full heat transfer achieved at around 720 minutes. This slower heat transfer reflected the controlled nature of aluminium encapsulation, as the PCM temperature increased to approximately 34.9°C (308.05 K).
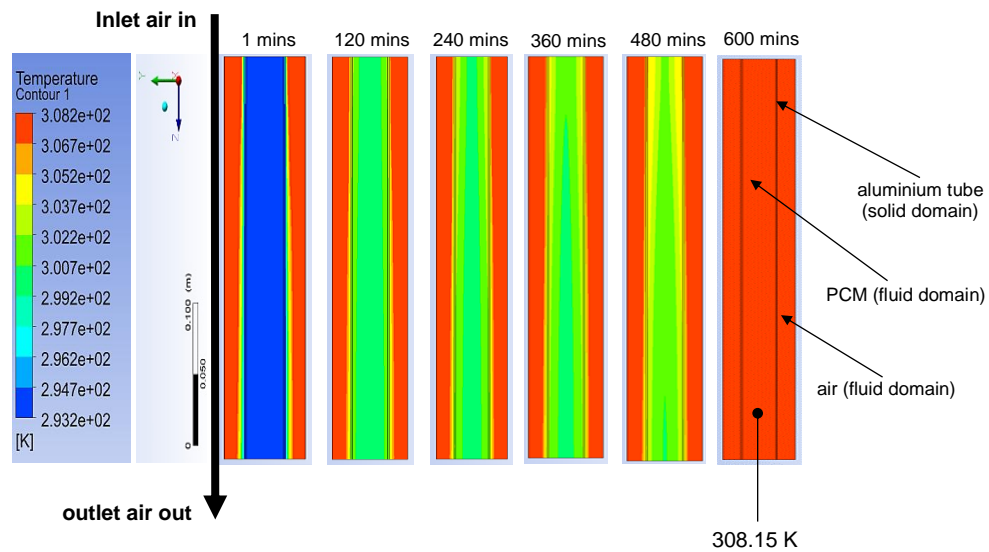
*Figure 4.13. Temperature contour for rectangular EPCM-T **model 1B** when **aluminium encapsulation** is utilised at **3 m/s** inlet velocity and 35 ᵒC inlet temperature.*

When V_{inlet} increased to 3 m/s (Figure 4.13), the heat transfer process accelerated. The PCM reached 35.0°C (308.15 K) by 600 minutes, demonstrating 0.29% faster heat transfer due to the increase in airflow. In contrast, the copper encapsulation in the rectangular copper EPCM-T – model 1B sample showed a slightly faster temperature increase compared to that of aluminium encapsulation, even at a low V_{inlet} of 1.88m/s (Figure 4.14). PCM temperatures rose to 34.7°C (307.85 K) by 720 minutes, indicating approximately 0.57% faster stabilisation than what was obtained with the use of aluminium.
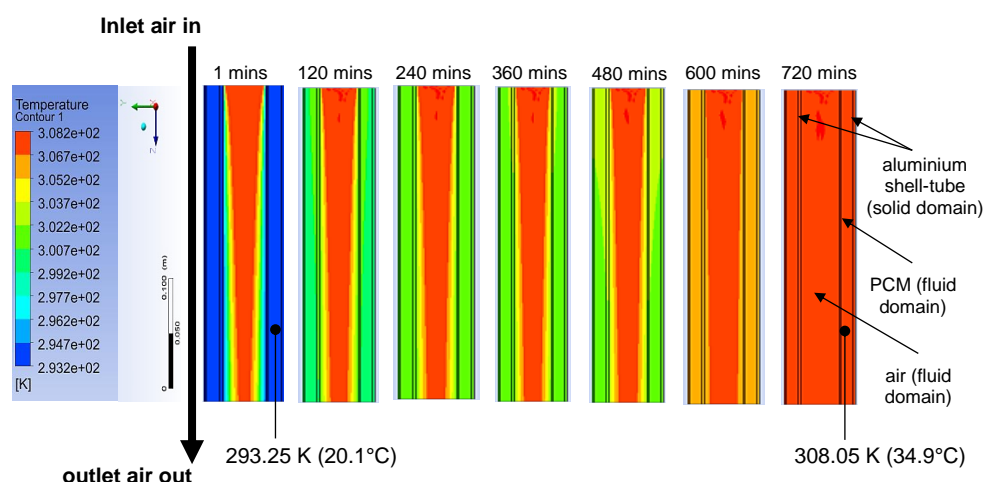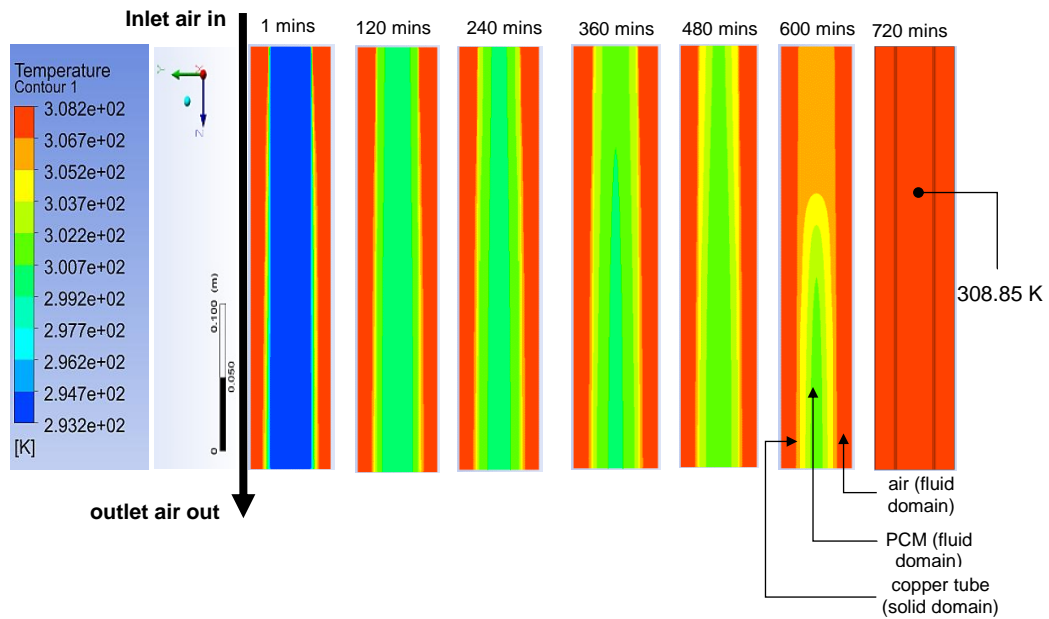
*Figure 4.14. Temperature contour for rectangular EPCM-T **model 1B** when **copper encapsulation** is utilised at **1.88 m/s** inlet velocity and 35 ºC inlet temperature.*

The results suggest that copper encapsulation leads to slightly more efficient heat transfer than aluminium in lower airflow conditions. However, the overall temperature difference between copper and rectangular aluminium EPCM-T – model 1B remain small.

As seen in Figure 4.15, when the V_{inlet} increased to 3 m/s, copper achieved rapid heat transfer, stabilising around 600 minutes with the PCM reaching a temperature of 34.7°C (307.85 K). Copper's faster heat transfer, though beneficial for rapid stabilisation, could result in less sustained thermal performance over extended periods. This indicates that copper facilitates quicker heat transfer in EPCM-T – model 1B designs.
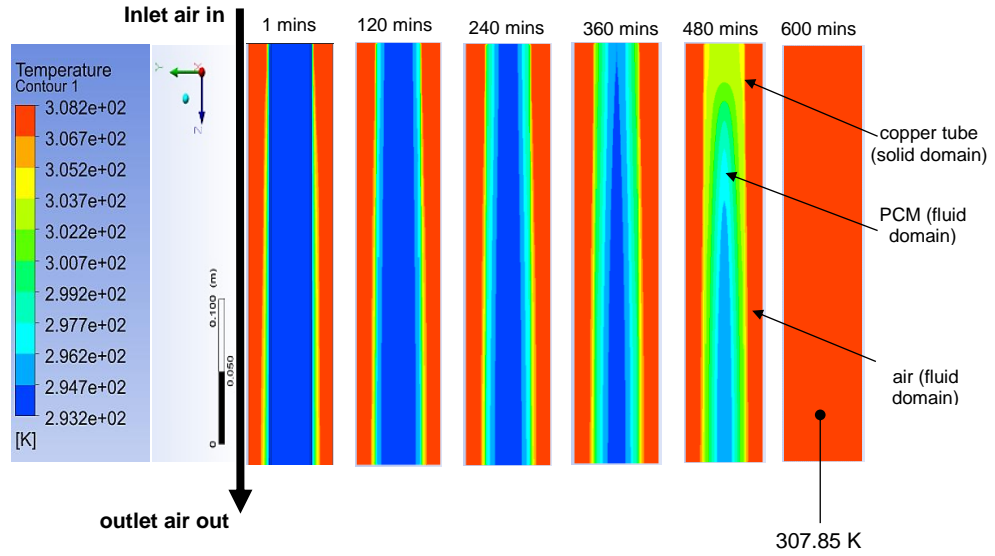
*Figure 4.15. Temperature variation contour for rectangular EPCM-T **model 1B** when **copper encapsulation** is utilised at **3 m/s** inlet velocity and 35 ᵒC inlet temperature.*
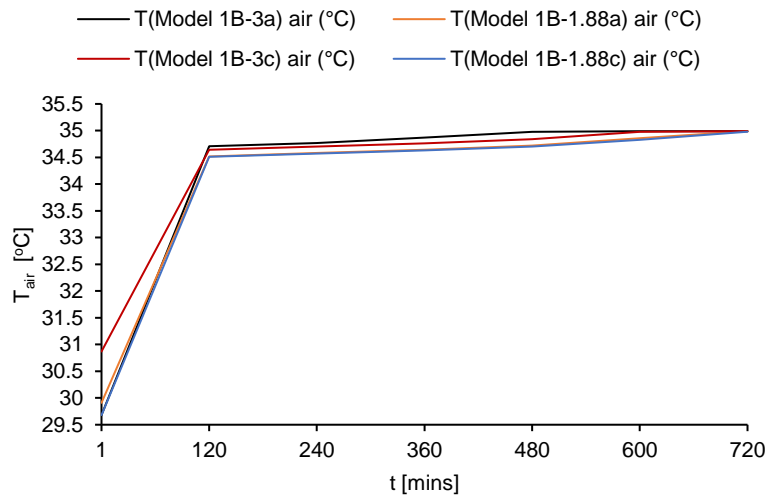
*Figure 4.16. T_{air} in rectangular EPCM-T **model 1B** with **aluminium and copper encapsulation** at V_{inlet} of 1.88 m/s and 3 m/s.*

However, the airflow velocity and the encapsulation material still have a limited impact on the long-term air temperature behaviour in the rectangular EPCM-T. It was observed in the graph shown in Figure 4.16 that airflow velocity mainly impacted the speed of the initial heat transfer process. Accordingly, in Figure 4.16, all models (1B-3a, 1B-3c, 1B-1.88a, and 1B-1.88c), with aluminium and copper encapsulation at V_{inlet} velocities of 1.88 m/s and 3 m/s, initially exhibited a sharp temperature

increase. T_{air} increased from around 30°C (303.15 K) to approximately 34.5°C (307.65 K) within the first 120 minutes. After this initial rise, the temperature stabilized, with only a slight increase over the remaining simulation time, reaching about 34.9°C (308.05 K) by 720 minutes. The copper-encapsulated models (1B-3c and 1B-1.88c) showed only a slightly faster initial temperature rise compared to the aluminium models.

Figure 4.17 and Figure 4.18 show the T_{tube} and T_{PCM} fluctuations in the rectangular EPCM-T model 1B with aluminium and copper encapsulation, respectively, at Vinlet of 1.88 m/s and 3 m/s.
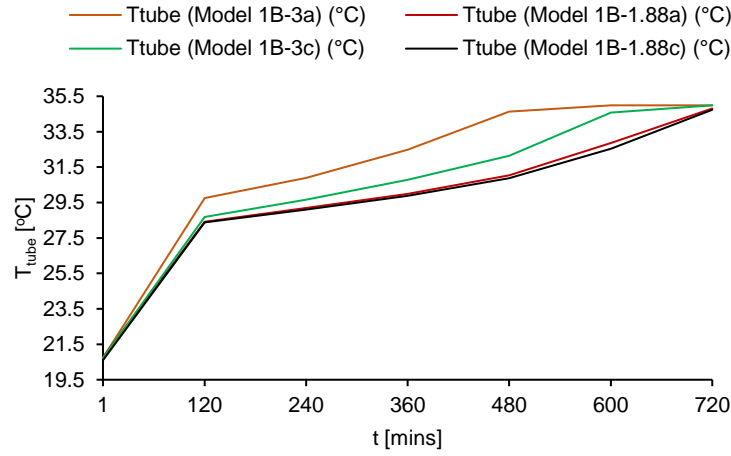
*Figure 4.17. T_{tube} in rectangular EPCM-T **model 1B** with **aluminium** and **copper encapsulation** at V_{inlet} of 1.88 m/s and 3 m/s.*

All the models compared in Figure 4.17 show a sharp T_{tube} rise between 0-120 minutes. The T_{tube} eventually converged at about 27.5°C (300.65 K) after 120 minutes. Between 120 and 360 minutes, T_{tube} in copper increased more rapidly than in the aluminium models. For instance, by 240 minutes, the copper model was approximately 5-6% ahead of the aluminium model in terms of temperature rise. By the final phase (360-720 minutes), the T_{tube} in all models reached between 34.9°C (308.05 K) and 35°C (308.15 K), with copper showing approximately 0.3% faster heat transfer compared to aluminium. It is indicative that during the 120-360-minute period, the thermal performance of the rectangular copper EPCM-T – model 1B was 5-6% more efficient than that of aluminium.
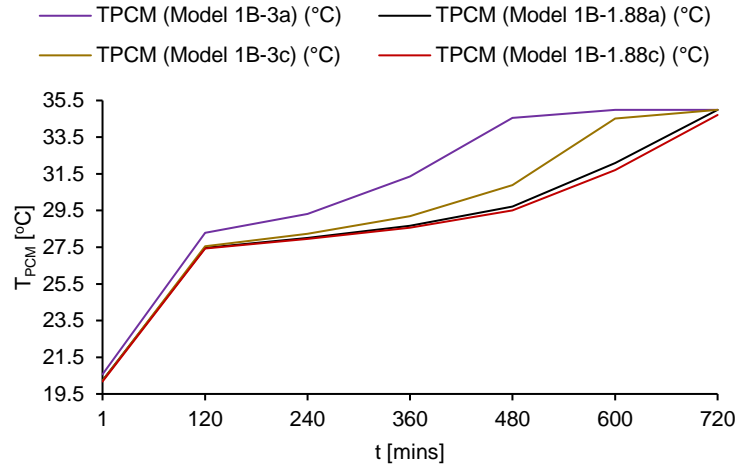
Figure 4.18. T_{PCM} in rectangular EPCM-T **model 1B** *with* **aluminium and copper encapsulation** *at V_{inlet} of 1.88 m/s and 3 m/s.*

In Figure 4.18, as the PCM charging commenced, T_{PCM} for all models reached approximately 27°C (300.15 K) by 120 minutes. During the mid-phase (120-360 minutes), the TPCM for copper increased more rapidly than for the EPCM-T – model 1B with aluminium encapsulation. As V_{inlet} increased to 3 m/s, by the final phase (360-720 minutes), T_{PCM} in the copper models reached 34.9°C (308.05 K). The effect of the increased V_{inlet} at 3 m/s was more pronounced across all models, with T_{PCM} reaching higher temperatures faster compared to lower V_{inlet}. The rectangular copper-encapsulated EPCM-T- model 1B stabilised more quickly than the aluminium-encapsulated ones. Despite copper's 4-5% faster heat transfer during the initial and mid-phases, both T_{tube} and T_{PCM} in copper and aluminium models converged by 720 minutes, especially at higher V_{inlet}. This indicates that while copper and increased airflow primarily impact the rate of heat transfer, they have little effect on the final temperature. Both copper and aluminium-encapsulated models achieve similar final temperatures (approximately 34.9°C or 308.05 K) by the end of the simulation.

4.2.1.4 Cylindrical EPCM-T - model 2B

The temperature variations that occurred in the cylindrical EPCM-T model 2B during the simulation are represented by the temperature contours shown in Figures 4.19 to 4.22.
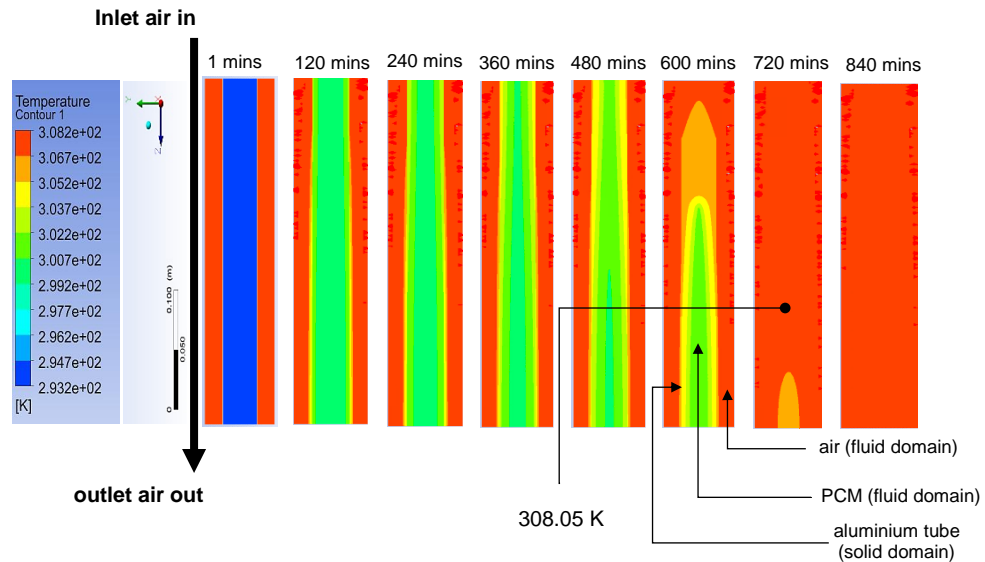
Figure 4.19. Temperature contour for cylindrical EPCM-T **model 2B** when **aluminium encapsulation** is utilised at **1.88 m/s** inlet velocity and 35 °C inlet temperature.

At 1.88 m/s, as shown in Figure 4.19, the temperature rise is similar to the rectangular EPCM-T – model 1B. Stabilisation began around 720 minutes, with T_{PCM} reaching 34.9°C (308.05 K). However, full equilibrium was only achieved by the 840-minute mark, at which point the temperature reached 35.0°C (308.15 K). The cylindrical shape, however, slightly slowed down the heat distribution by approximately 2.86%. At 3 m/s (Figure 4.20), the temperature stabilised earlier at around 600 minutes, with T_{PCM} reaching 35.0°C (308.15 K). The performance based on the EPCM-T cylindrical shape is comparable to the rectangular version but showed marginally slower heat transfer due to shape-induced airflow differences.
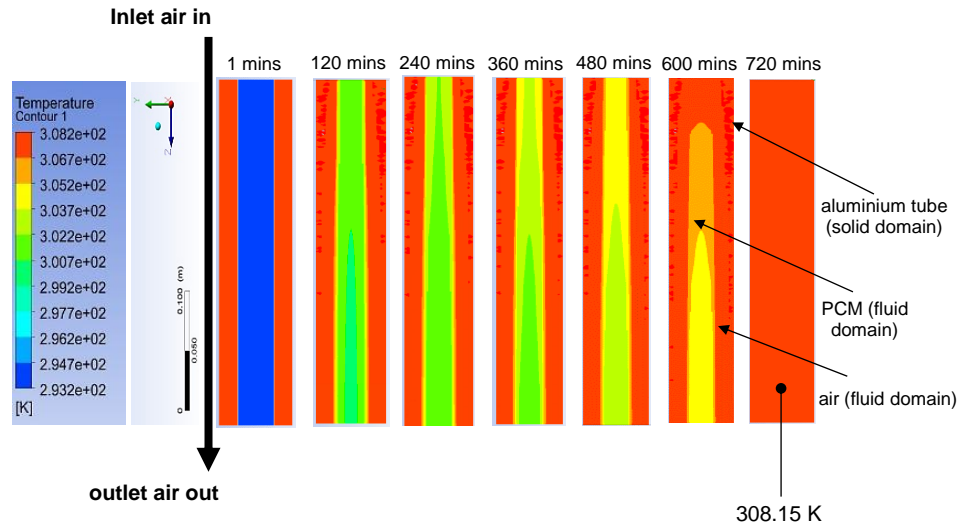
*Figure 4.20. Temperature contour for cylindrical EPCM-T **model 2B** when **aluminium encapsulation** is utilised at **3 m/s** inlet velocity and 35 ºC inlet temperature.*
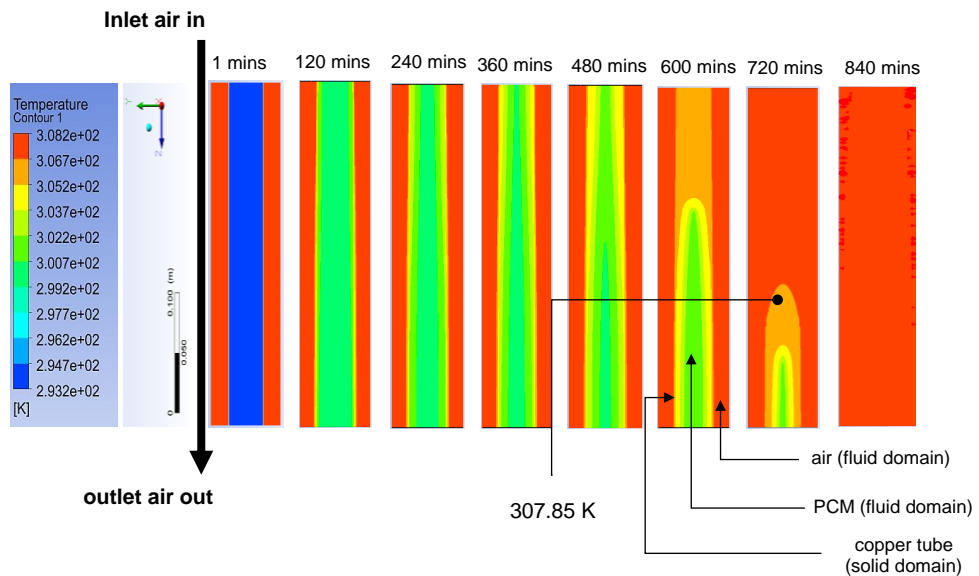
*Figure 4.21. Temperature contour for cylindrical EPCM-T **model 2B** when **copper encapsulation** is utilised at **1.88 m/s** inlet velocity and 35 ºC inlet temperature.*

At a V_{inlet} of 1.88 m/s (Figure 4.21), the copper-encapsulated cylindrical model 2B showed faster heat transfer compared to the aluminium-encapsulated version. The PCM reached 34.7°C (307.85 K) in 720 minutes, similar to the rectangular EPCM-T- model1B. At 3 m/s, the heat transfer accelerated, stabilising around 600 minutes (Figure 4.22), with

the PCM achieving 34.7°C (307.85 K). Copper in this model displayed faster heat conduction, allowing for rapid heat distribution, similar to the rectangular model.
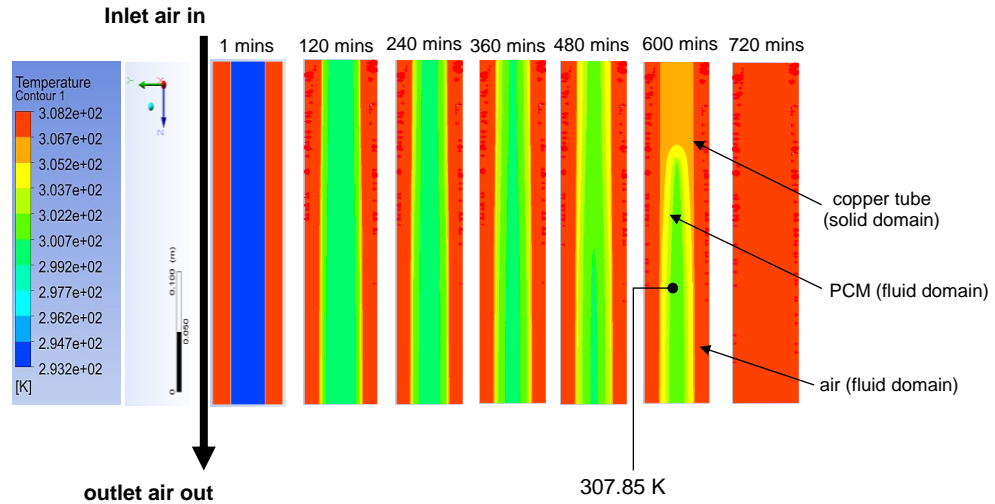
Figure 4.22. Temperature contour for cylindrical EPCM-T **model 2B** when **copper encapsulation** is utilised at **3 m/s** inlet velocity and 35 °C inlet temperature.
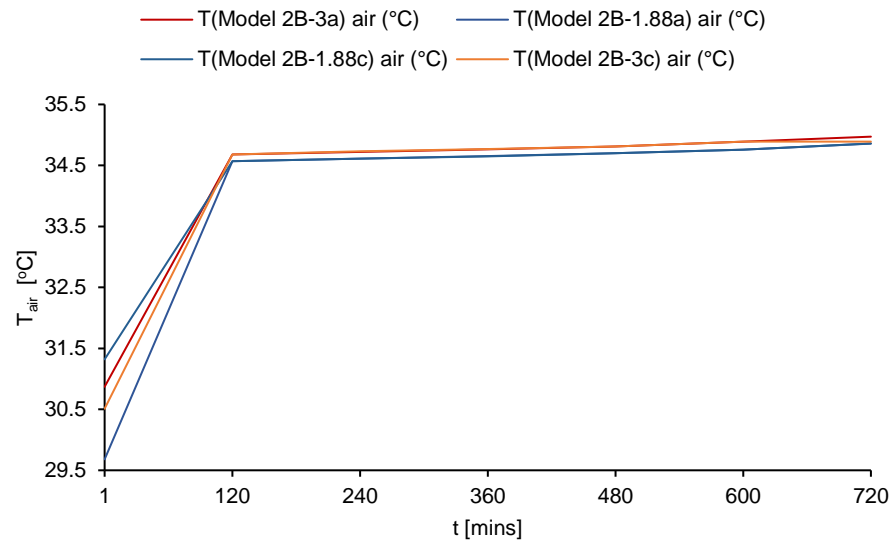
Figure 4.23. T_{air} in cylindrical EPCM-T **model 2B** with **aluminium** and **copper encapsulation** at V_{inlet} of 1.88 m/s and 3 m/s.

In Figure 4.23, T_{air} in all the cylindrical EPCM-T models rose sharply within 120 minutes but stabilised after this, 34.5°C (307.65 K). There was hardly any difference between the thermal behaviour of the copper and aluminium-encapsulated EPCM-T cylindrical models after stabilisation

when the V_{inlet} was 1.88 or 3 m/s. All models similarly converged near 34.9°C (308.05 K) at 720 minutes, indicating that the airflow and encapsulation materials had little effect on air temperature. This could be as a result of the EPCM-T design.
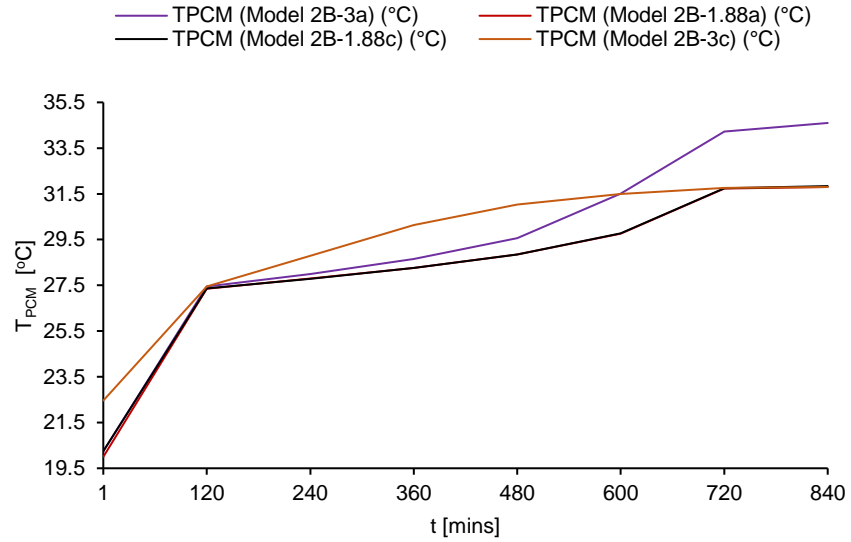
*Figure 4.24. T_{PCM} in cylindrical EPCM-T **model 2B** with **aluminium** and **copper encapsulation** at V_{inlet} of 1.88 m/s and 3 m/s.*

Increased airflow had a greater effect on T_{PCM} in Figure 4.24. T_{PCM} increased faster in the copper-encapsulated cylindrical EPCM-T (1B-3c and 1B-1.88c), reaching 34.5°C (307.65 K) before the end of the simulation. However, in the aluminium-encapsulated cylindrical EPCM-T (1B-3a and 1B-1.88a), T_{PCM} increased more slowly and stabilised around 34°C (307.15 K). The copper-encapsulated cylindrical EPCM-T exhibited faster heat transfer, especially at 3 m/s airflow, indicating that airflow greatly improved the PCM heat transmission.

As shown in Figure 4.25, a quicker T_{tube} increase was observed in the copper-encapsulated cylindrical EPCM-T than in the aluminium models at 3 m/s airflow. The aluminium-encapsulated cylindrical EPCM-T stabilised at 34°C (307.15 K), while copper-encapsulated models reached 34.5°C (307.65 K) by the end of the phase at 840 minutes.

Results generally indicate that higher airflow velocities improved heat transfer in copper models, accelerating T_{PCM} and T_{tube} temperature rises.
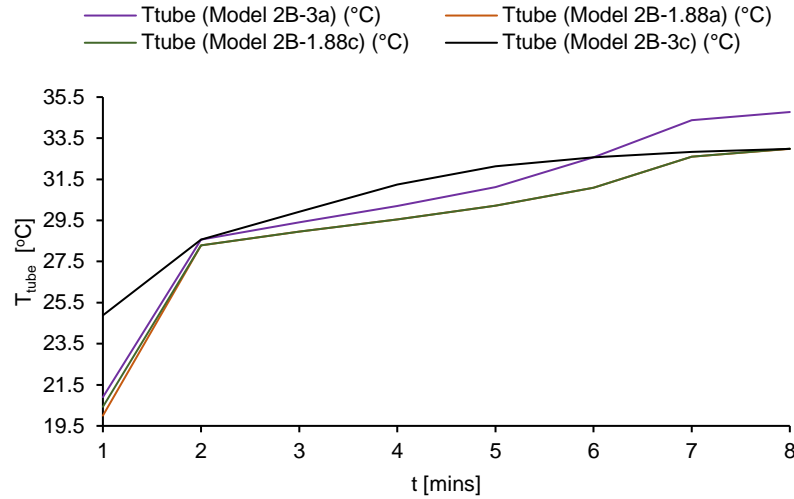
Figure 4.25. T_{tube} in cylindrical EPCM-T **model 2B** with **aluminium** and **copper encapsulation** at V_{inlet} of 1.88 m/s and 3 m/s.

4.2.2 Impact of encapsulation material on EPCM-T thermal storage performance.

The performance of aluminium and copper encapsulations in EPCM-T Models 1A, 2A, 1B, and 2B during the PCM charging process was assessed based on variations in airflow velocity. To fully understand this relationship, the PCM liquid fraction was assessed. The liquid fraction represents the degree to which the PCM has melted or transitioned into a liquid state, providing insight into how effectively the material absorbs and stores thermal energy over time. The analysis aimed to determine how the two selected encapsulation materials (copper and aluminium) and airflow velocities influenced the PCM charging in each of the EPCM-T models.

4.2.2.1 PCM charging in shell-tube rectangular EPCM-T - model 1A

Figures 4.26 and 4.27 illustrate how airflow velocity and encapsulation material (aluminium and copper) affected the phase change process in EPCM-T Model 1A.

At 1.88 m/s (Figure 4.26 (a)), the PCM in the aluminium-encapsulated EPCM-T - model 1A reached liquid fractions of 0.19 at 120 minutes and 0.46 at 240 minutes. Full melting was achieved at 600 minutes. According to Figure 4.26(c), the PCM in the copper-encapsulated EPCM-T - model 1A showed a marginally slower melting rate, with liquid fractions of 0.17 and 0.43 at 120 and 240 minutes, respectively. By 600 minutes, both had commenced their full melting phase which concluded with a 2-3% melting rate difference as shown in Figure 4.26(b).

At 3 m/s as shown in Figure 4.27, the melting process accelerated. Copper reached a liquid fraction of 0.27 at 120 minutes and 0.56 at 240 minutes. Full melting was achieved by 480 minutes (Figure 4.27(a) and (b)). According to Figure 4.27(c), the aluminium-encapsulated EPCM-T model 1A was slightly slower, with liquid fractions of 0.21 and 0.49 at 120 and 240 minutes, reaching 96% melting by 480 minutes and full melting at 600 minutes. At this velocity, it can be implied that the liquid fraction in the copper-encapsulated EPCM-T - model 1A, outperformed the aluminium-encapsulated version by 7% by the 240-minute mark. However, a 1% reduction in the liquid fraction value was observed when it was 480 minutes into the simulation. From the results, it can be inferred that both materials exhibited a faster PCM charging when the V_{inlet} was at 3 m/s. The copper-encapsulated EPCM-T - model 1A initially outperformed the aluminium-encapsulated versions. However, the difference became negligible as the simulation progressed.
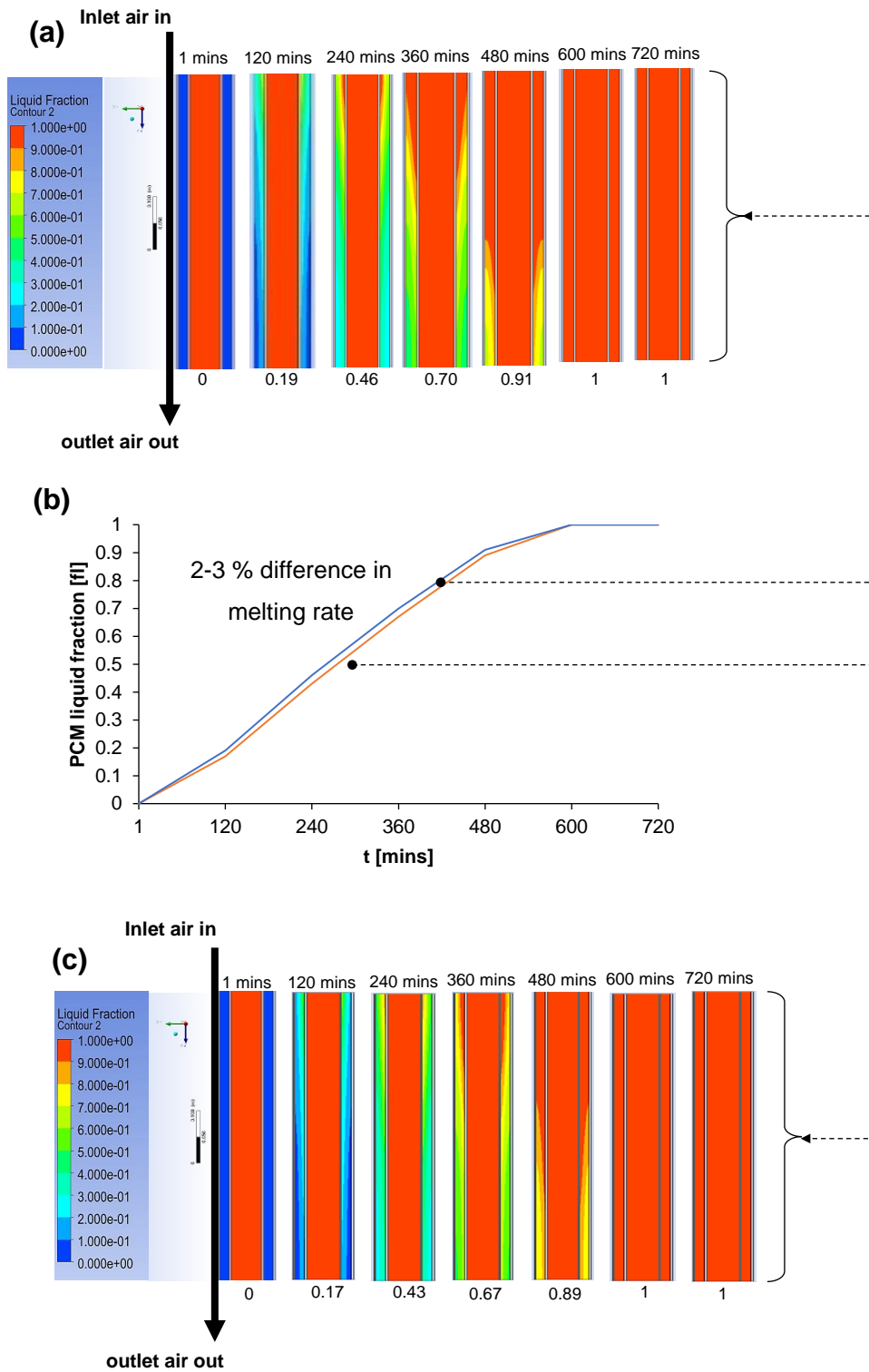
Figure 4.26. PCM liquid fraction contours for (a) aluminium and (c) copper encapsulated **rectangular EPCM-T Model 1A** at 1.88 m/s, and (b) liquid fraction variation between aluminium and copper in Model 1A.
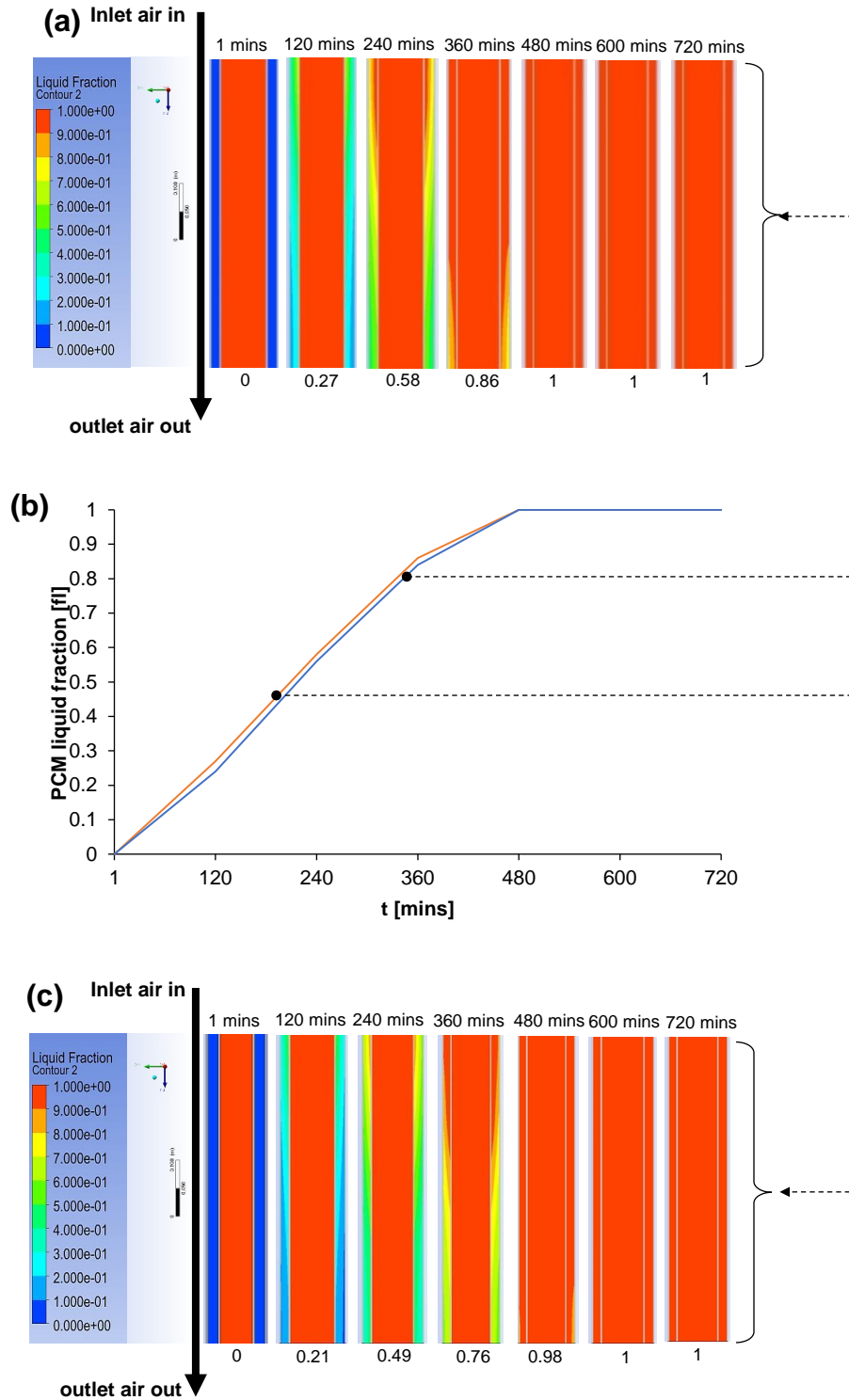
Figure 4.27. **(a)** *PCM liquid fraction contour for* **copper-encapsulated** *rectangular EPCM-T Model 1A at 3 m/s* **(b)** *Graph showing PCM liquid fraction variation between* **aluminium and copper Model 1A**, *and* **(c)** *PCM liquid fraction contour for* **aluminium-encapsulated** *rectangular EPCM-T Model 1A at 3 m/s.*

4.2.2.2 PCM charging in shell-tube cylindrical EPCM-T - model 2A

The graph in Figure 4.28 illustrates the PCM liquid fraction as a function of time (t) for four models: two variations of Model 2A-3 (3a and 3c) and two variations of Model 2A-1.88 (1.88a and 1.88c), with V_{inlet} of 3 m/s and 1.88 m/s, respectively. At the start of the simulation, all models showed.
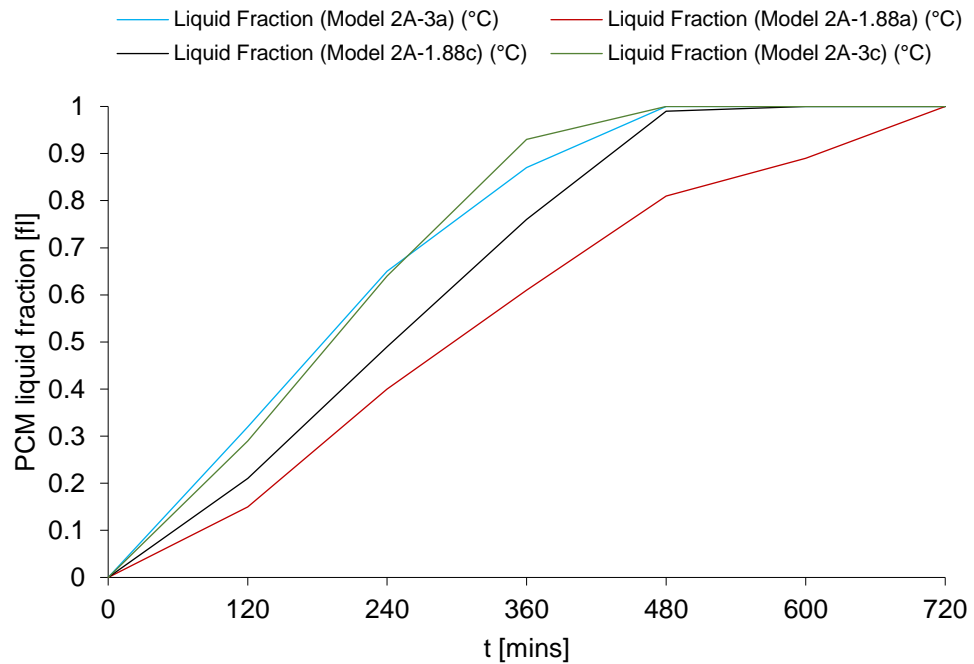
Figure 4.28. Comparison of PCM liquid fraction for for shell-tube cylindrical Aluminium EPCM-T - model 2A at 1.88 m/s and 3m/s.

All models showed a gradual PCM liquid fraction increase at the beginning of the simulation. But, by 240 minutes, both Model 2A-3a and 2A-3c (3 m/s) exhibited higher liquid fractions compared to Model 2A-1.88a and 2A-1.88c. Model 2A-3a displayed a slightly faster PCM melting rate than Model 2A-3c between 0 and 360 minutes. This was due to a faster rate of heat absorption that occurred. In contrast, both Model 2A-1.88a and Model 2A-1.88c took longer to reach full melting. Incomplete melting was still observed in Model 2A-1.88a by the 480-minute mark. But Model 2A-1.88c showed slightly better heat absorption but only began full melting by 720 minutes.

The difference in PCM charging times between these models has highlighted that lower airflow velocities, such as 1.88 m/s, resulted in slower heat transfer. This increases the length of time for PCM to melt. In contrast, higher airflow velocities, as seen in Model 2A-3a (3 m/s), improved the PCM's ability to absorb and store thermal energy more rapidly. However, a quicker PCM melting may not sustain thermal absorption over extended periods. This faster charging could lead to reduced long-term cooling performance.

4.2.2.3 PCM charging in rectangular EPCM-T - model 1B

The PCM liquid fraction behaviour for both aluminium and copper-encapsulated rectangular EPCM-T Model 1B at V_{inlet} of 1.88 m/s and 3 m/s is shown in Figures 4.29 to 4.31. The graphs and contours offer a comprehensive view of how airflow and encapsulation material affect the phase change process of the PCM.
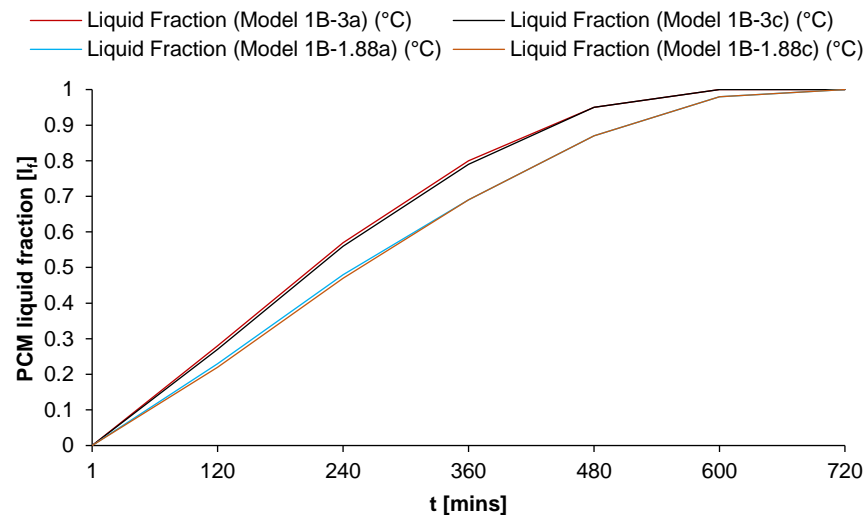
*Figure 4.29. Comparison of PCM liquid fraction for the **aluminium and copper-encapsulated** rectangular **EPCM-T Model 1B** at 1.88 m/s and 3m/s.*

As shown in Figure 4.29, the liquid fraction for the aluminium and copper-encapsulated rectangular EPCM-T Model 1B are compared at V_{inlet} of 1.88 m/s and 3 m/s. The PCM in the copper-encapsulated rectangular models (1B-3c and 1B-1.88c) melted up to 10-12% faster than in the

aluminium ones (1B-3a and 1B-1.88a) by the 240-minute mark. In this case, the liquid fraction reached a value of 1 at 720 minutes indicating the completion of a full PCM charging cycle. Copper-encapsulated rectangular EPCM-T models also showed a faster PCM charging cycle, particularly at the higher airflow rate of 3 m/s.
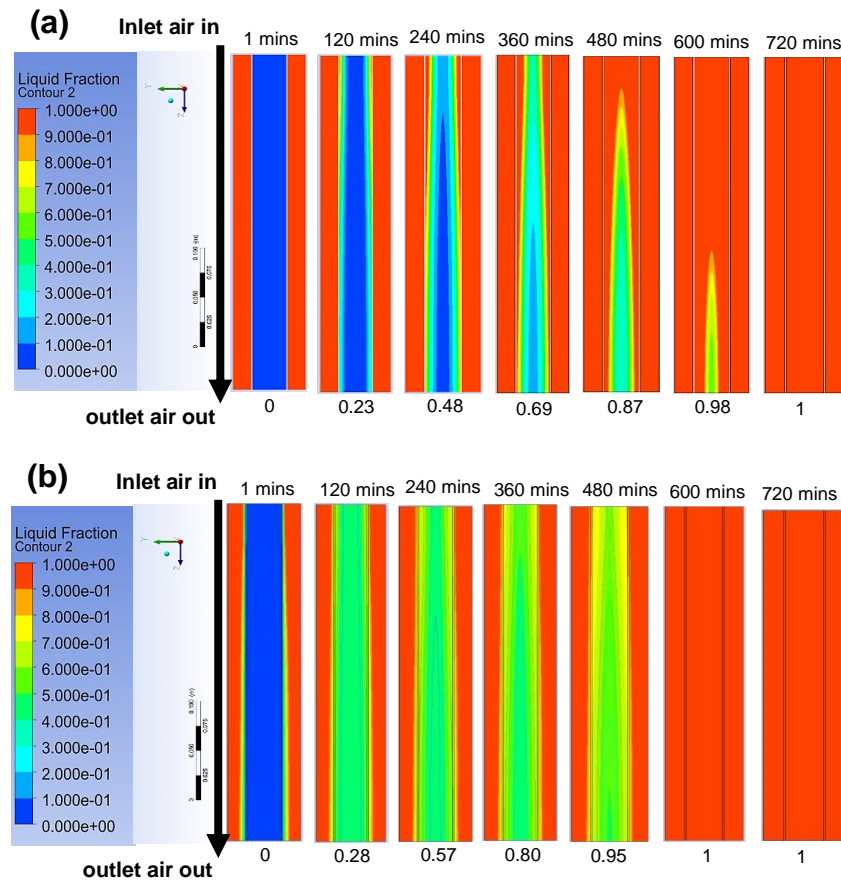
*Figure 4.30. PCM liquid fraction contour for (a) **aluminium-encapsulated rectangular EPCM-T Model 1B at (a) 1.88 m/s and (b) 3m/s.***

The results from Figures 4.30 and 4.31 compare the phase change performance of aluminium and copper-encapsulated rectangular EPCM-T Model 1B at airflow velocities of 1.88 m/s and 3 m/s. As observed in Figure 4.30 (a), the aluminium-encapsulated model reached a liquid fraction of 0.23 by 120 minutes when V_{inlet} was at 1.88m/s. It progressed steadily to 0.48 by 240 minutes and reached 0.87 by 480 minutes. Full melting occurred by 720 minutes into the simulation. At the higher airflow velocity of 3 m/s, Figure 4.30(b) indicates that the aluminium-

encapsulated model performed better. PCM liquid fraction reached 0.28 by 120 minutes, and 0.57 by 240 minutes, with full melting achieved by 600 minutes.
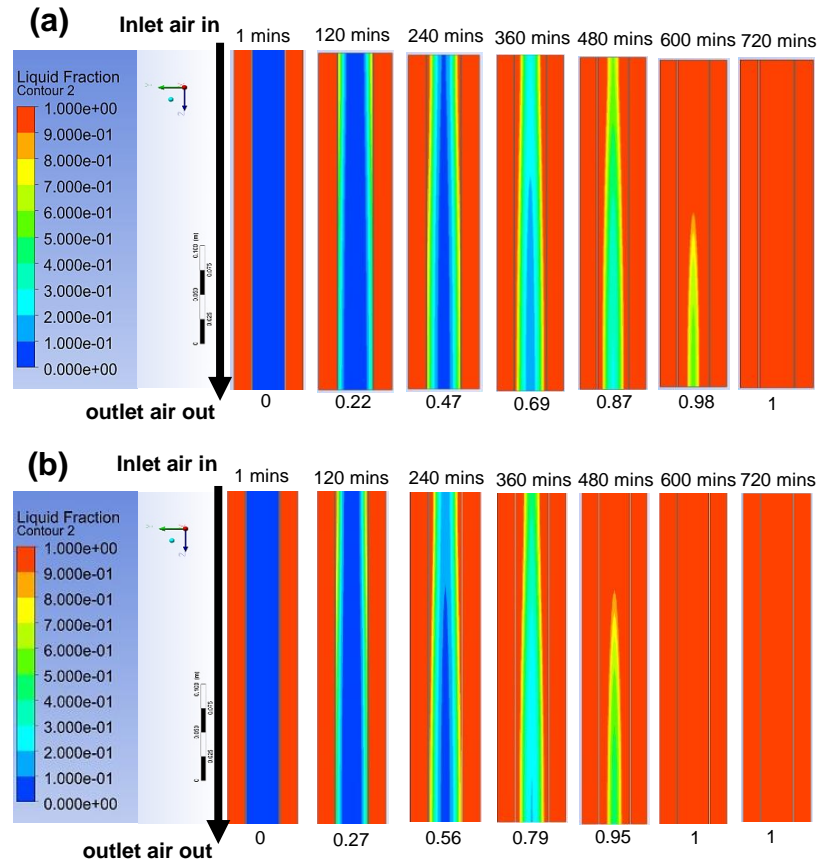
Figure 4.31. PCM liquid fraction contour for **copper-encapsulated** *rectangular* **EPCM-T Model 1B** *at (a) 1.88 m/s and (b) 3m/s.*

The copper-encapsulated model as indicated in Figure 4.31(a), shows that there was an initial rise in the PCM liquid fraction to 0.22 by 120 minutes when V_{inlet} was at 1.88m/s. This implies a faster change process. The PCM liquid fraction reached 0.87 by 480 minutes and full melting was achieved by 720 minutes, similar to that of the aluminium version. The copper-encapsulated rectangular EPCM-T Model 1B also exhibited a similar phase change rate to that of the aluminium model as V_{inlet} increased to 3m/s, as shown in Figure 4.31(b). The copper-encapsulated rectangular EPCM-T Model 1B also achieved full melting in 720 minutes.

The PCM liquid fraction increased from 0.56 to 0.95 from 240 minutes to 480 minutes. Only a very minimal difference was observed in the performance of both models.

4.2.2.4 PCM charging cylindrical EPCM-T - model 2B

Figure 4.32 shows the comparison of the PCM liquid fraction for aluminium and copper-encapsulated cylindrical EPCM-T Model 2B at V_{inlet} of 1.88 m/s and 3 m/s. The copper-encapsulated cylindrical models generally exhibited a faster PCM charging rate compared to the aluminium-encapsulated ones.
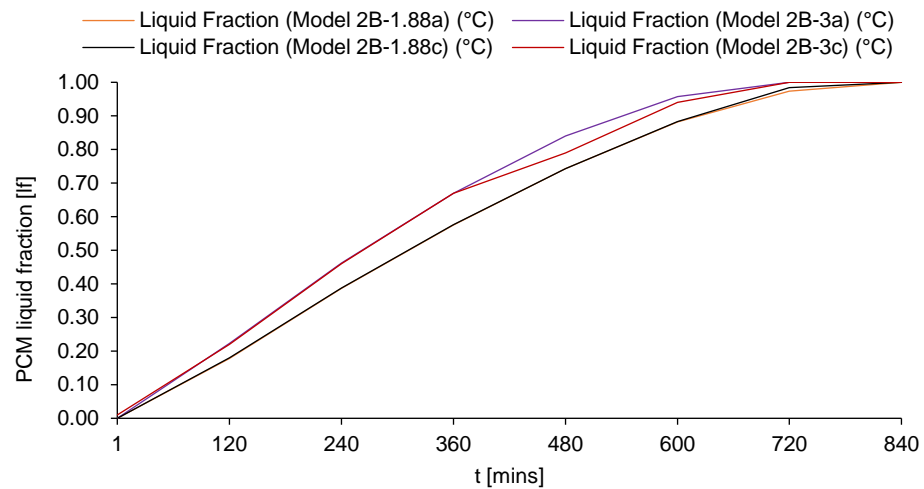
*Figure 4.32. Comparison of PCM liquid fraction for **aluminium and copper-encapsulated EPCM-T Model 2B** at 1.88 m/s and 3m/s.*

At a V_{inlet} of 1.88 m/s, the copper-encapsulated cylindrical EPCM-T Model 2B (Model 2B-1.88c) reached a liquid fraction of 0.18 at 120 minutes, while the aluminium-encapsulated version (Model 2B-3c) reached 0.16. This indicated a 6% faster melting rate for the copper-encapsulated model. By 240 minutes, the Model 2B-1.88c achieved a liquid fraction of 0.46, compared to the 0.39 for the aluminium-encapsulated model (Model 2B-1.88a). This highlights a 7% difference in phase change rate. Both models reached full melting of the liquid fraction of 1 by 720 minutes, with copper demonstrating a marginally faster charging rate during the

mid-phase. When the airflow velocity was increased to 3 m/s, the difference between model 2B-3c and model 2B-3a became more pronounced. The PCM in Model 2B-3c reached a liquid fraction of 0.22 at 120 minutes. However, the PCM melting rate in Model 2B-3c was 10% faster than that of Model 2B-3a. By 600 minutes, there was a 6% difference in their PCM melting rates. The PCM liquid fraction for Model 2B-3c and Model 2B-3a reached 0.94 and 0.96 respectively. However, full PCM melting occurred around 720 minutes for both models. The copper-encapsulated models generally showed consistently faster melting, particularly in the mid-phase of the process.
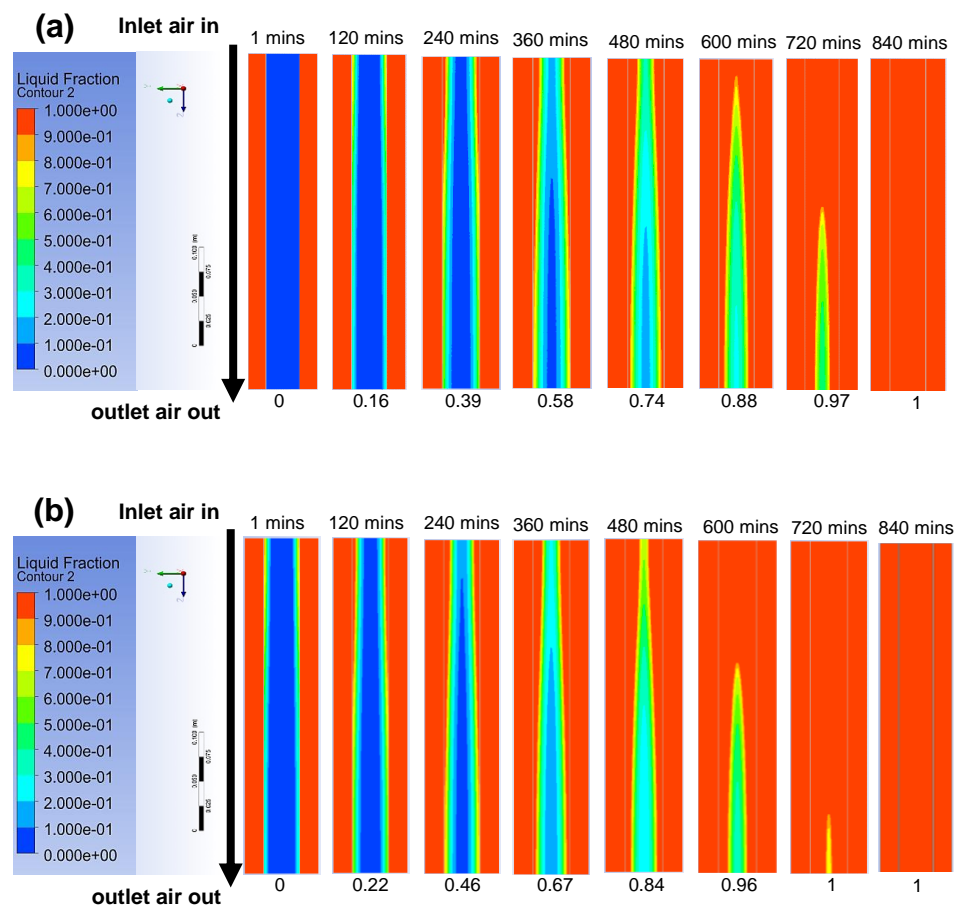
*Figure 4.33. PCM liquid fraction contour for **aluminium-encapsulated** cylindrical **EPCM-T Model 2B** at (a) 1.88 m/s and (b) 3m/s.*

Figure 4.33 illustrates the PCM liquid fraction contour for aluminium-encapsulated EPCM-T Model 2B at both 1.88 m/s and 3 m/s. At 1.88 m/s,

the aluminium-encapsulated cylindrical EPCM-T Model 2B exhibited a slower phase change, with a liquid fraction of 0.16 by 240 minutes and 0.74 by 480 minutes. The PCM eventually reached full melting at 840 minutes. When V_{inlet} increased to 3 m/s, the model showed a faster phase change process. In this case, the PCM liquid fraction reached 0.46 at 240 minutes and 0.84 by 480 minutes, achieving full melting by 720 minutes.
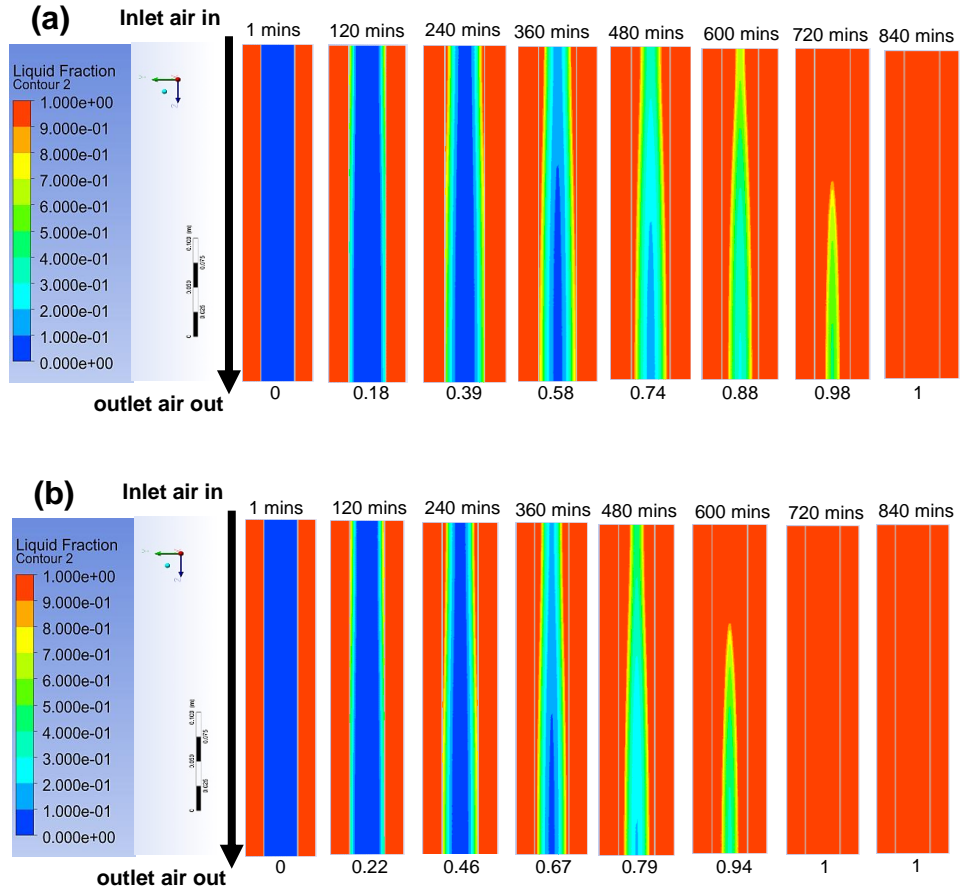
Figure 4.34. PCM liquid fraction contour for **copper-encapsulated cylindrical EPCM-T Model 2B** at (a) 1.88 m/s and (b) 3m/s.

The contour data for the copper-encapsulated cylindrical EPCM-T Model 2B at the respective V_{inlet} rates is depicted in Figure 4.34. With a velocity of 1.88 m/s, the PCM in the copper model exhibited a 2% faster phase transition than that of the aluminium model. A PCM liquid fraction of 0.39 was observed at 240 minutes and 0.74 at 480 minutes. At a V_{inlet} of 3 m/s, the copper model exhibited a 6% improvement compared to the aluminium-encapsulated cylindrical EPCM-T Model 2B, obtaining a value

of 0.46 after 240 minutes and 0.79 after 480 minutes. This indicates a 5.3% improvement in the melting process.

4.2.3 Optimal EPCM-T design: summary of key findings from the parametric study.

The most important conclusion of the evaluation of the parametric study indicated that Model 1B which is the rectangular EPCM-T samples achieved better temperature stabilisation for a longer period in comparison to other EPCM-T designs. With the aluminium encapsulation, Model 1B showed more uniform heat transfer and a prolonged thermal storage capacity across the different V_{inlet} conditions tested. The heat transfer in the aluminium-encapsulated EPCM-T was 10-12% slower than that of the copper versions for both V_{inlet} of 1.88m/s and 3m/s. This indicated a more prolonged retainment of temperature stability by the aluminium-encapsulated versions. Thus, the Model 1B is more effective at reducing incoming air temperature for extended periods compared to the copper-encapsulated versions. Since the EPCM-T's most important performance is for it to be able to achieve stabilised and reduced supply air temperature for an extended period, Model 1B with aluminium encapsulation was identified as the optimal EPCM-T design. Consequently, this model was selected for integration into the overall system for further performance analysis.

4.3 Results and discussions of the overall performance of the EPCM-HMW system

The EPCM-HMW system was assessed based on the two different EPCM-T configuration cases detailed in Chapter 3 (Figure 3.20). As identified, Case 1 is the EPCM-HMW system with 48 EPCM-T units placed within a single supply airstream. Case 2 features 197 EPCM-T units evenly distributed across all four EPCM-HMW system's airstreams.

The key factors influencing system performance such as ventilation, cooling, and thermal storage were thoroughly assessed. The results of these assessments are discussed in the following sections.

4.3.1 Ventilation performance assessment of the EPCM-HMW system

The impact of varying outdoor wind speeds, wind angle and air pressure distribution within the EPCM-HMW model was assessed to investigate the ventilation performance. The results discussed here are based on V_{inlet} of 1.88 m/s and 3 m/s at V_{angle} ranging between 0° and 45°, with solar fan static pressure set at 10 Pa. Based on this, the fan provided an additional 370L/s airflow.

4.3.1.1 Impact of varying outdoor wind speeds on ventilation performance

Fluctuations in wind speed can cause variations in airflow rates, affecting how much air passes over the EPCM-T within the EPCM-HMW system. This indirectly impacts how consistently the ventilation performance is maintained. To fully understand this, the analysis examined how airflow was distributed within the EPCM-HMW system. This led to the assessment of how efficiently the EPCM-HMW system performed at wind speeds of 1.88 m/s and 3 m/s, with a consistent V_{angle} of 0°. Hence, the velocity contour plots for the EPCM-HMW Case 1 model as shown in Figure 4.35(a) are compared with the air velocity profiles in Figure 4.35 (b).

According to the contour plot in Figure 4.35(a), when the inlet air speed was 1.88 m/s at 2500s, the airflow at $P_{11-supply}$, near the inlet vent, was around 0.47 m/s. As air moved further into the space, the velocity decreased to 0.34 m/s at $P_{10-bottom}$ 9 (Figure 4.35(b)). At the midpoint of the room height, P_5 recorded a 33% decrease in air velocity, measuring 0.18 m/s. Further reductions were noted near the walls, with P_2

measuring 0.07 m/s (Figure 4.35(b)). Even after 25,000, the decrease persisted, with P_3 showing a 33% to 50% reduction in air velocity compared to P_1. This indicates that at a low wind speed of 1.88 m/s, even with the solar fan providing a 10 Pa pressure jump, the ventilation performance was less effective, though still within acceptable thermal comfort limits of 140.86 L/s. This is sufficient airflow rate for 14 to 17 occupants.
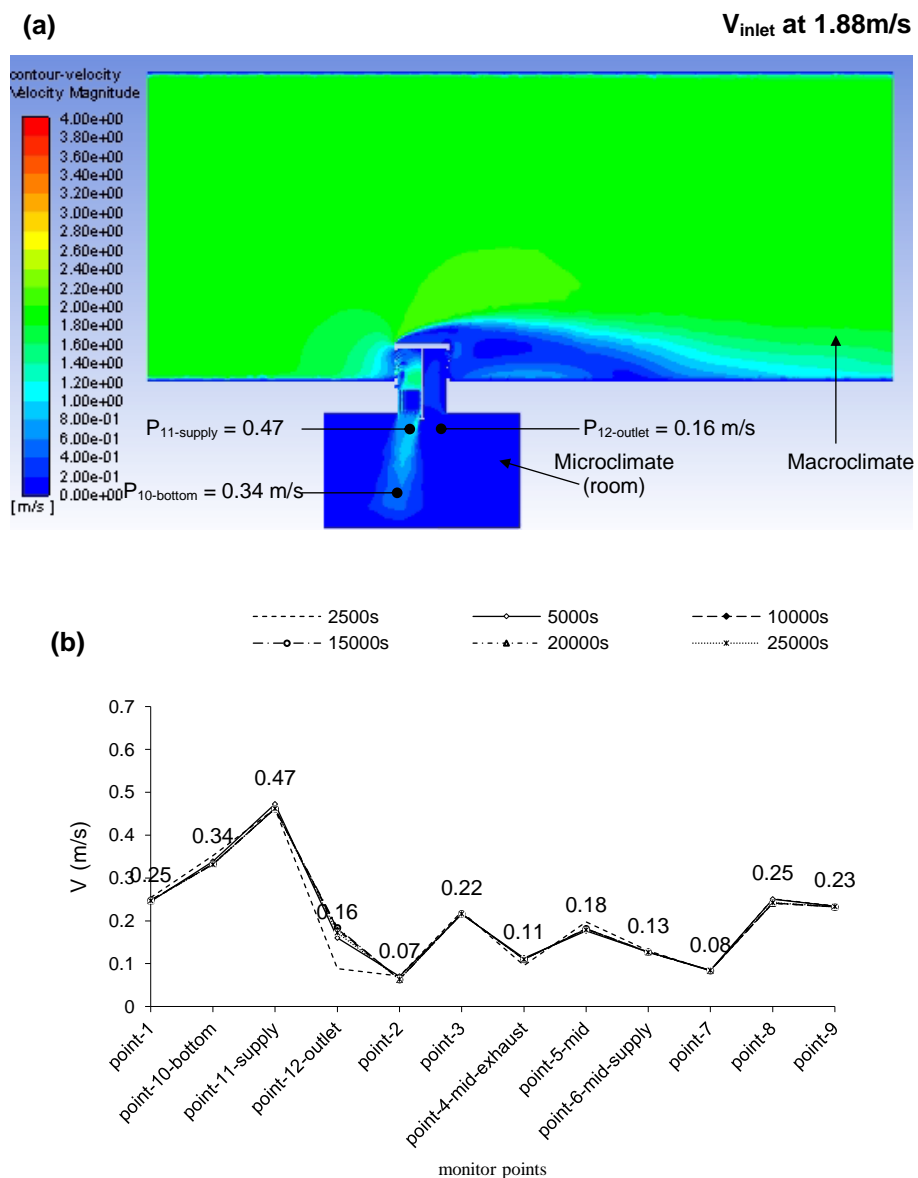
Figure 4.35. (a) Contour showing the variation in the air velocity magnitude (b) Air velocity profiles for Case 1 when V_{angle} is $0°$ at V_{inlet} 1.88m/s.

As shown in Figure 4.36(a) and (b), when the V_{inlet} increased to 3 m/s, a similar trend was also observed between P_1-P_{12}. The air velocity at $P_{11-supply}$ rose to 0.80 m/s, representing a 72% increase. The lowest airflow was at P_2, near the room wall. This shows that there was insufficient air circulation in that area. Results indicate that the solar fan at 10Pa pressure jump may not have fully compensated for the low wind speeds, the airflow remained within thermal comfort limits.
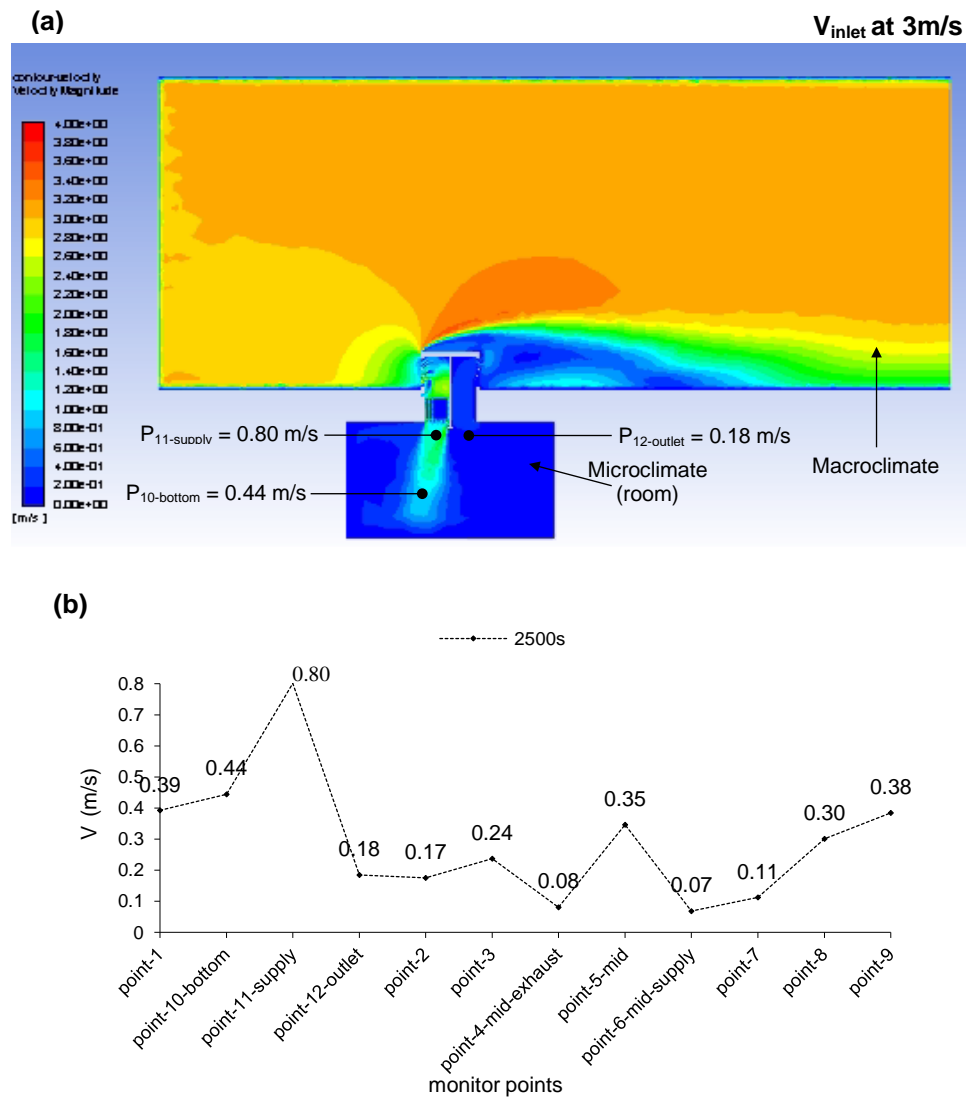
Figure 4.36. (a) Contour showing the variation in the air velocity magnitude (b) Air velocity profiles for Case 1 when V_{angle} is 0° at V_{inlet} 3m/s.

*Figure 4.37. (a) Contour showing the variation in the air velocity magnitude
(b) Air velocity profiles for Case 2 when **V_{angle} is 0°** at **V_{inlet} 1.88m/s.***

According to Figure 4.37(a) and (b), a similar air velocity distribution trend was observed in EPCM-HMW Case 2 when V_{inlet} was 1.88 m/s. However, there was slightly lower velocities at $P_{11\text{-supply}}$ for both wind speeds of 1.88m/s and 3m/s. $P_{11\text{-supply}}$ recorded air velocities of 0.37m/s when V_{inlet} was 1.88m/s (Figure 4.37(b)). This increased to 0.65 m/s when V_{inlet} reached 3 m/s (Figure 4.38(a) and (b)), indicating a 69% increase. These

results confirm that the higher inlet velocity improves airflow distribution, but air circulation near the walls, such as at P_2, remained insufficient.
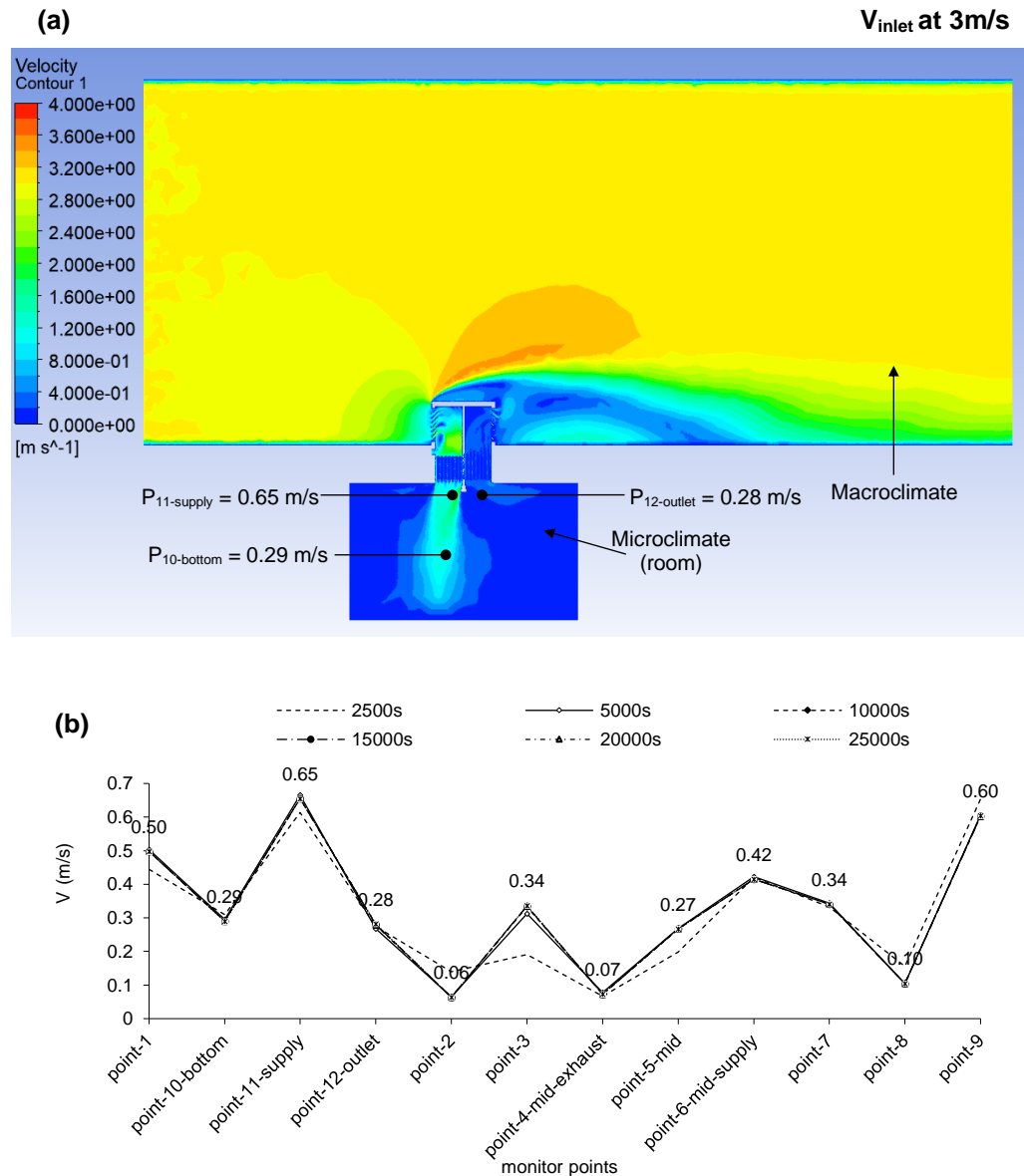
Figure 4.38. (a) Contour showing the variation in the air velocity magnitude (b) Air velocity profiles for Case 2 when V_{angle} is 0° at V_{inlet} 3m/s.

4.3.1.2 Impact of varying outdoor wind angles on ventilation performance

Figure 4.39 compares three scenarios based on different wind angles (V_{angle}) of 0°, 30°, and 45°, all at a constant V_{inlet} of 1.88 m/s.

The supply air velocity (V_{supply}) at $P_{11-supply}$ was highest at 0.61 m/s when V_{angle} was 30°, with an exit velocity of 0.28 m/s at $P_{12-outlet}$.
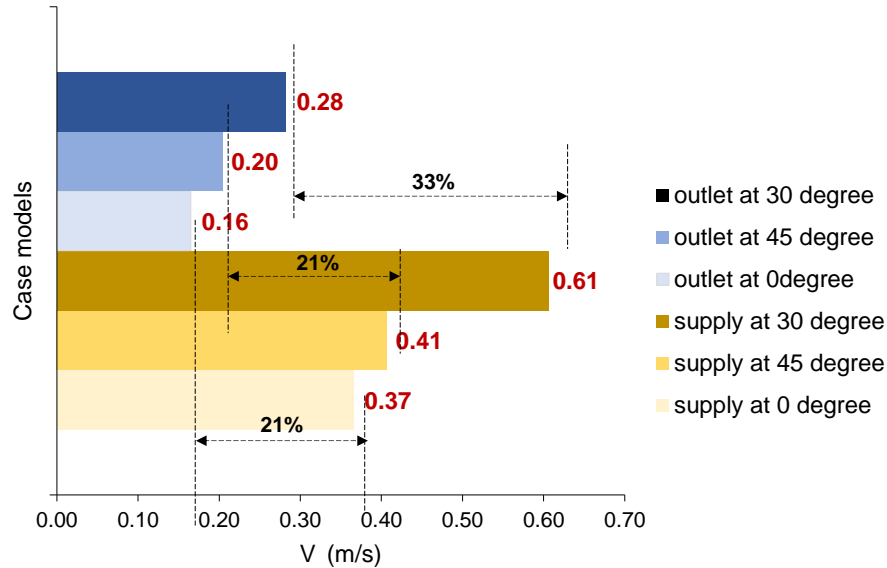
Figure 4.39. Comparison of the effect of different wind angles V_{angle} on the supply and exhaust air velocities in the EPCM-HMW model.

A close correlation was noted between V_{supply} at V_{angles} of 0° and 45°, where the system supplied air at 0.37 m/s and 0.41 m/s, respectively, showing a 21% reduction between the supply and exhaust velocities in both cases. Reverse airflow occurred at 45° and 30° V_{angle} compared to 0°, although 45° and 30° produced higher V_{supply} than 0°. The drop between supply and exhaust air velocities was most significant at 30°, despite it recording the highest V_{supply}. The effect of wind angle on ventilation performance was more pronounced at 30°. Hence, a 33% difference between supply and exhaust velocities was observed.

4.3.1.3 Air pressure distribution on ventilation performance

In this analysis, Case 1a, 1b, and 1c represent EPCM-HMW Case 1 with wind angles of 0°, 30°, and 45°, respectively. Similarly, EPCM-HMW Case 2 with wind angles of 0°, 30°, and 45° are represented by Case 2a, 2b, and 2c. The graph in Figure 4.40 presents a comparative analysis of

air pressure drops between supply and exhaust over a 20,000-second simulation period for Cases 1 and 2, with V_{inlet} set at 1.88 m/s at a 0° V_{angle}. In Case 1, supply air pressure decreased from approximately 3.11 Pa to between -0.66 and -0.54 Pa, while exhaust air pressure dropped from -26.4 Pa to between -0.65 and -0.76 Pa. In Case 2, exhaust air pressure fell sharply from -30.61 Pa to between 8.4 and 8.53 Pa. The supply air pressure decreased from 5.41 Pa to about -8.40 Pa. The percentage difference in exhaust air pressure between Case 1 and Case 2 was 15.9%. For supply air, the difference was approximately 87.6%. Both cases reached an equilibrium between supply and exhaust air pressures after 2,500 s (0.7 hours).
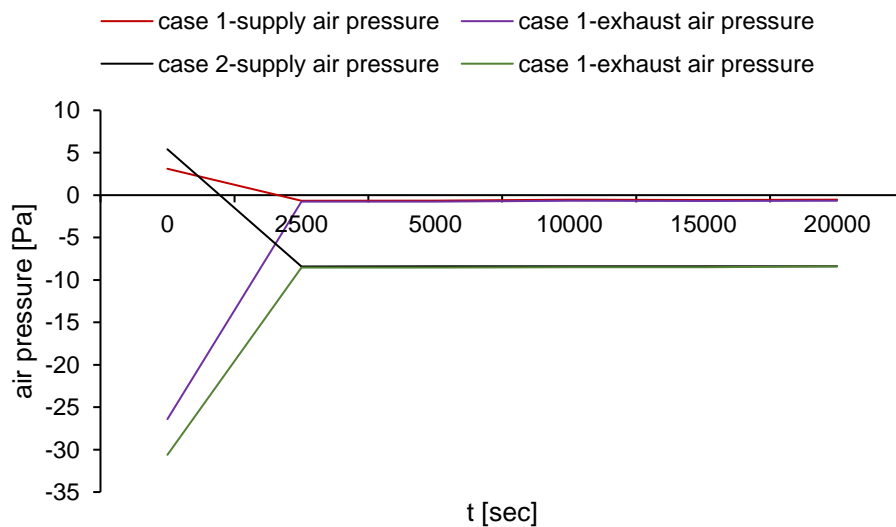
*Figure 4.40. Air pressure P drops between supply and exhaust over 20,000 s simulation time in cases 1 and 2 when V_{inlet} is **1.88m/s at 0° V_{angle}.***

Figure 4.41 compares the air pressure at $P_{11\text{-supply}}$ and $P_{12\text{-outlet}}$ when Vinlet was 1.88 m/s under varying V_{angles} of 0°, 30°, and 45°. In Cases 1a and 2a, there were minimal pressure drops at 0.11 Pa. This indicates restricted ventilation efficiency. Slight improvements were seen in Cases 1b and 2b, but negative pressures persisted. This suggests suboptimal airflow. The most significant improvements occurred in Cases 1c and 2c. The supply pressures increased by 1704% and 196%, respectively. The

polynomial trendline clearly showed this sharp improvement. This demonstrates that higher wind angles of 45° significantly enhance system performance, especially in Case 1.
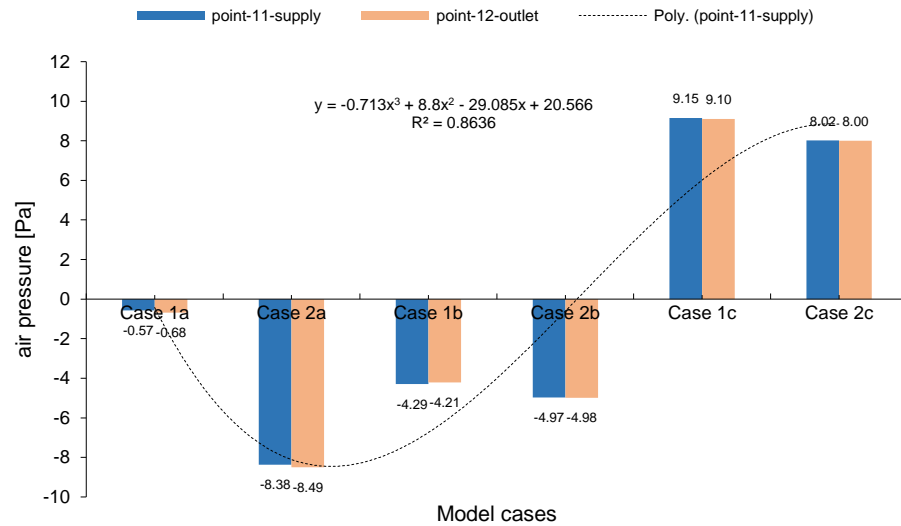
Figure 4.41. Air pressure comparison between six different EPCM-HMW model cases (cases 1a, 1b, 1c, 2a, 2b and 2c) at V_{angle} at 0°, 30° and 45°.

Figure 4.42 compares air pressure distribution across Cases 2a, 2b, and 2c at varying wind angles. A more uniform and symmetrical pressure distribution was observed in Case 2c as shown in Figure 4.42(c). The pressure values at $P_{1-supply}$ and $P_{2-exhaust}$ were at 8.02 Pa and 8.00 Pa, respectively. This indicates a near-equilibrium pressure and improved airflow. Comparing pressure contours in Figure 4.42(a) and Figure 4.42(b), this balance was less pronounced in Cases 2a and 2b.

(a) Case 2a with V_{inlet} at 1.88m/s at V_{angle} of 0°

Pressure
Contour 2
-2.000e+00
-2.800e+00
-3.600e+00
-4.400e+00
-5.200e+00
-6.000e+00
-6.800e+00
-7.600e+00
-8.400e+00
-9.200e+00
-1.000e+01
[Pa]

$P_{11\text{-supply}}$ = -8.38 pa $P_{12\text{-outlet}}$ = -8.49 pa

Microclimate (room)   Macroclimate

(b) Case 2b with V_{inlet} at 1.88m/s at V_{angle} of 30°

Pressure
Contour 2
2.000e+01
1.700e+01
1.400e+01
1.100e+01
8.000e+00
5.000e+00
2.000e+00
-1.000e+00
-4.000e+00
-7.000e+00
-1.000e+01
[Pa]

$P_{11\text{-supply}}$ = -4.97 pa $P_{12\text{-outlet}}$ = -4.98 pa

Microclimate (room)   Macroclimate

(c) Case 2c with V_{inlet} at 1.88m/s at V_{angle} of 45°

Pressure
Contour 2
2.000e+01
1.900e+01
1.800e+01
1.700e+01
1.600e+01
1.500e+01
1.400e+01
1.300e+01
1.200e+01
1.100e+01
1.000e+01
[Pa]

$P_{11\text{-supply}}$ = 8.02 pa $P_{12\text{-outlet}}$ = 8.00pa

Microclimate (room)   Macroclimate

Figure 4.42. Air pressure contour across three different EPCM-HMW model cases (cases 2a, 2b and 2c) at V_{angle} at (a) 0°, (b) 30° and (c) 45°.

To further analyse the optimal air pressure distribution at a 45° V_{angle}, Case 1c and Case 2c were compared when V_{inlet} was increased to 3 m/s

as shown in Figure 4.43(a) and Figure 4.43(b), respectively. In Case 1c, $P_{1\text{-supply}}$ was 8.34 Pa and $P_{2\text{-exhaust}}$ was 9.08 Pa.

In contrast, Case 2c showed a more balanced distribution, with $P_{1\text{-supply}}$ at 4.60 Pa and $P_{2\text{-exhaust}}$ at 7.70 Pa. The results implied that air pressure was more effectively distributed across Case 2c. This could be a result of the even distribution of EPCM-T in all the air streams.
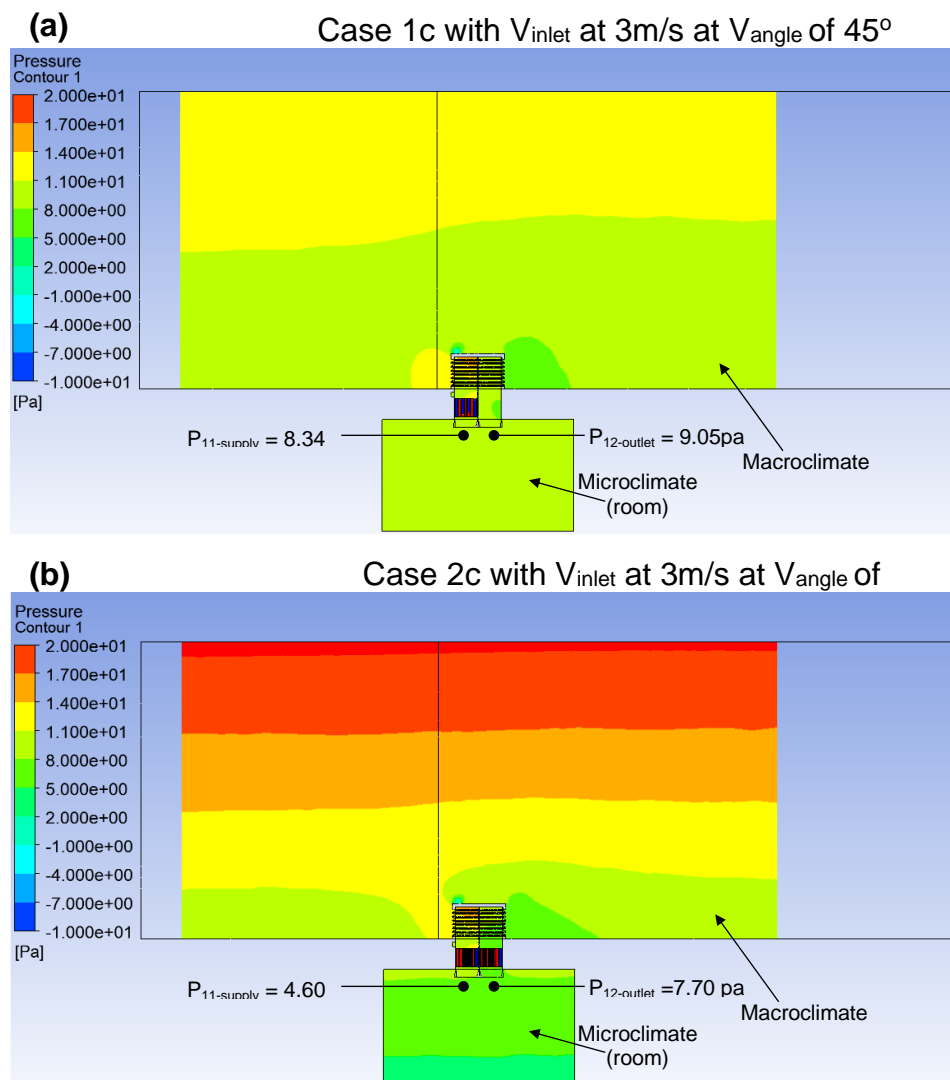
Figure 4.43. Air pressure contours showing a comparison of the air pressure distribution comparison across a ventilated room in (a) Case 1c and (b) Case 2c with V_{inlet} at 3m/s at V_{angle} of 45°

4.3.2 Cooling performance assessment of the EPCM-HMW system

The results of the cooling performance assessment of the model, based on varied V_{inlet} between 1.88 m/s and 3 m/s, are presented. Furthermore, the effect of different E-PCMT arrangements on the system's cooling performance, when the inlet air temperature T_{inlet} is at 308.15 K (35°C), is also presented.

4.3.2.1 Impact of varying outdoor wind speeds on cooling performance

The cooling performance of the EPCM-HMW system was investigated based on how different wind speeds impact the lowering and stabilisation of the air temperature. In both figures (Figure 4.44 and Figure 4.45), the temperature variation across different points was compared for the two wind speeds, 1.88 m/s and 3 m/s. In Case 1 with a wind speed of 1.88 m/s (Figure 4.44(a)), temperatures T ranged between 306.97 K (33.82 °C) to 307.07 K (33.92 °C) at 0s – 20,000 s (0.5 - 5 hours) flow time across all points. There was minimal temperature variation throughout the simulation time, indicating steady cooling.

In Case 2 with the same wind speed (Figure 4.44(b)), T_{supply} showed a sharper 0.65% decrease from the baseline of 307 K. Temperature reached as low as 305 K (31.85 °C), around 5,000 s (1.4 hours). However, temperatures remained stable for the rest of the simulation. The lower wind speeds led to a more significant temperature reduction in Case 2, particularly at $P_{11\text{-}supply}$. But overall, the model was able to provide cooling between 0 s to 20,000 s (5.5 hours).
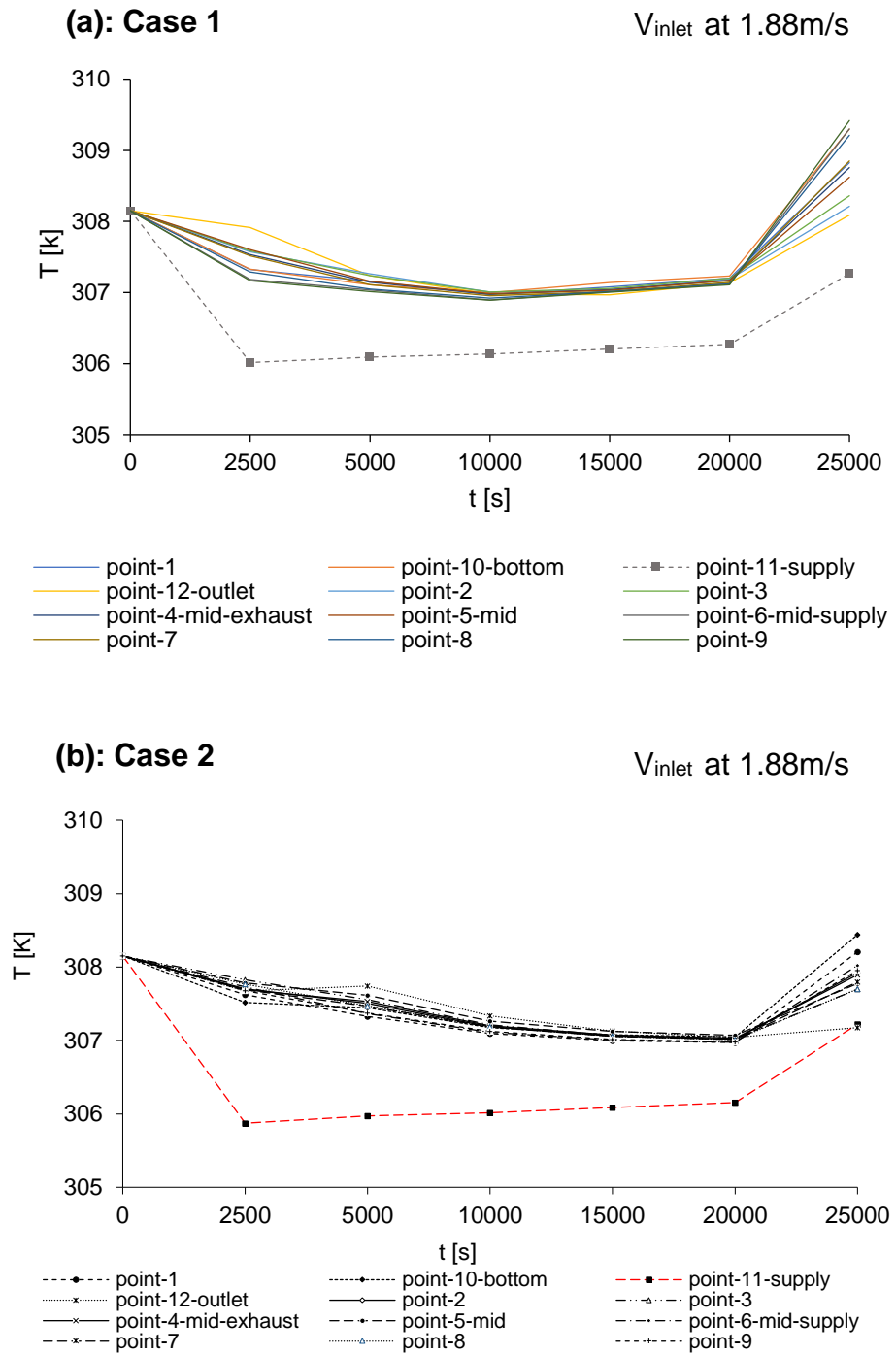
Figure 4.44. Comparison of air temperature T across (a) Cases 1 and (b) Case 2 between 0 s – 25,000 s simulation time at V_{inlet} is 1.88 m/s and V_{angle} of 0°.

(a): Case 1 V_{inlet} at 3m/s

(b): Case 2 V_{inlet} at 3m/s
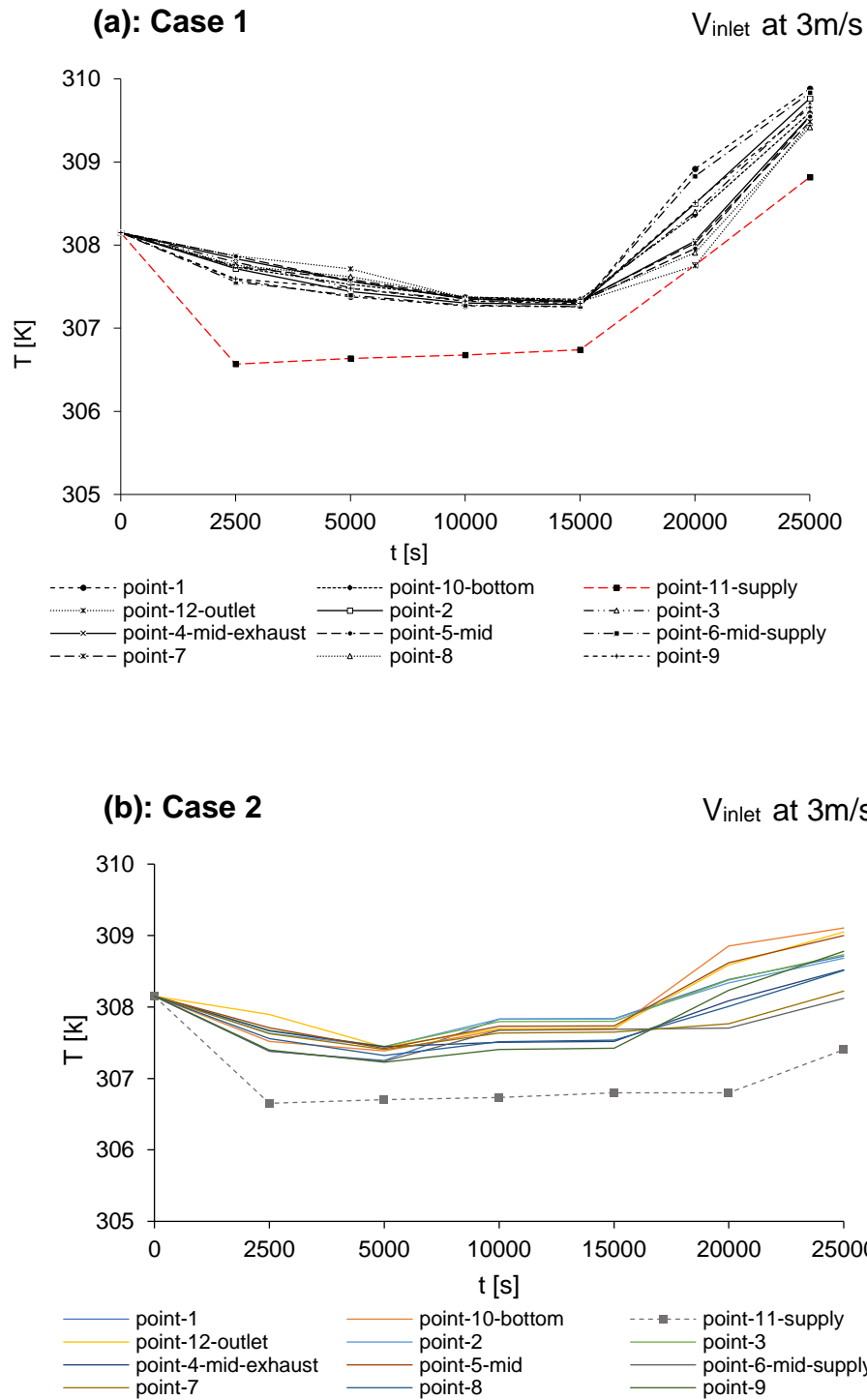
Figure 4.45. Comparison of air temperature T across (a) Cases 1 and (b) Case 2 between 0 s – 25,000 s simulation time at Vinlet is 3 m/s and V_{angle} of 0º.

According to Figure 4.45, higher temperatures across all monitored points, with less drastic drops were observed, for both Case 1 and Case

2 when the wind speed increased to 3 m/s. At 3 m/s Case 2 showed better stabilisation in cooling, maintaining T_{supply} at about 307 K from 2500 to 20,000 s (0.7 to 5.5 hours). But Case 2 at 1.88 m/s demonstrated the best performance in terms of cooling efficiency, with a temperature drop of approximately 0.65% at $P_{11-supply}$. Accordingly, wind speed had the most significant impact on the cooling performance and temperature variation in the EPCM-HMW Case 2 model.
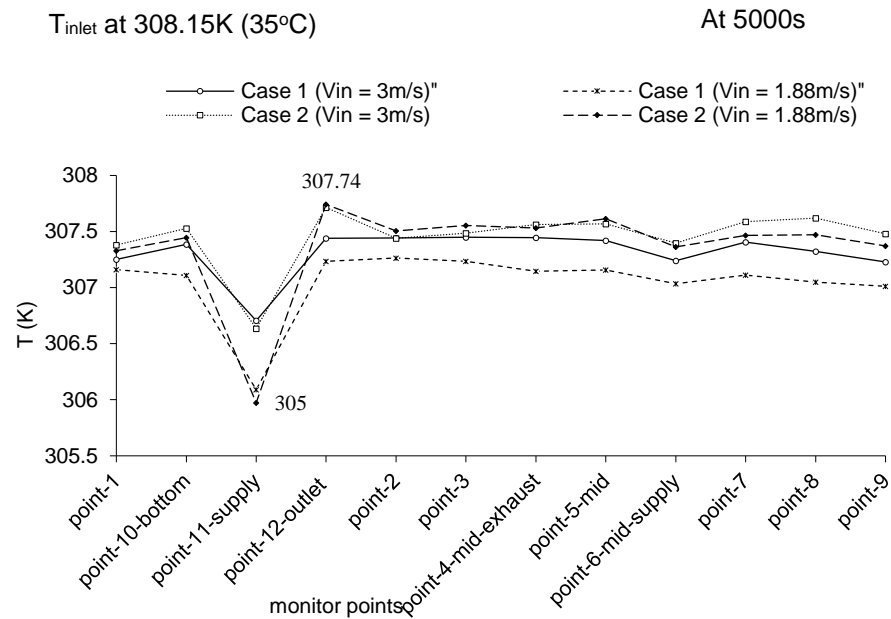
Figure 4.46. Comparison of air temperature T monitored at $P_1 – P_{12}$ for Cases 1 and 2 at V_{inlet} of 1.88 m/s and 3 m/s after 5000s (1.4 hours) of simulation.

It is noticeable from Figure 4.46 that T_{supply} in Case 2 reached 305 K (31.85 °C) when V_{inlet} was at 3m/s. On the other hand, at the same velocity, Case 1 maintained the highest temperature at P_3, peaking at 307.74 K. Across all points, higher temperatures were observed for both cases at 3 m/s when monitored at 5000s (1.4 hours). Higher airflow velocities resulted in more stable temperatures, though with less cooling efficiency compared to lower velocities. This highlights that while higher velocities stabilise the temperature distribution, lower wind speeds enhance cooling at specific points, such as the $P_{11-supply}$.

4.3.2.2 Impact of wind angle on cooling performance

Since the direction and angle of the wind impacts airflow efficiency in the EPCM-HMW system. This effect was further studied based on how this affects temperature variation and cooling performance. Figure 4.47 illustrates the effect of different V_{angles} on temperature variation for Case 1 and Case 2 after 3,000 s (0.8 hours) of simulation.

T_{inlet} at 308.15K (35°C)   At 3000s
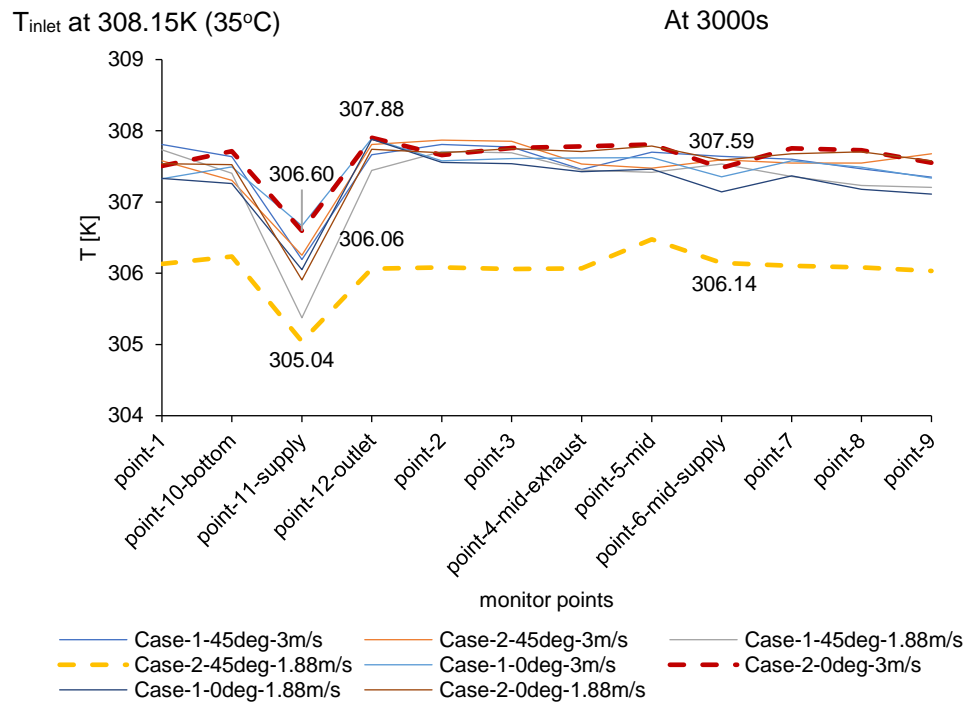
Figure 4.47. Comparison of T distribution at P1 – P12 for Case 1 and Case 2, at different Vangles of 0° and 45° of V$_{inlet}$ of 1.88 m/s and 3 m/s at 3000s.

With a lower wind speed of 1.88 m/s, there were more significant temperature drops than at a higher wind speed, particularly at $P_{11\text{-supply}}$. But Case 2 with 45° and 1.88 m/s showed the lowest temperature of 305.04 K. Conversely, at higher wind speeds (3 m/s), the temperature distribution across all points became more stable, with only smaller variations. When V_{angle} was at 0° at 3m/s, the model exhibited less cooling efficiency compared to lower wind speeds and wind angles. Hence, Case 2 with 0° and 3 m/s exhibited the highest temperature, peaking at 307.88 K (34.73^{o}C).

4.3.2.3 Impact of E-PCMT arrangement on cooling performance

The placement and distribution of E-PCMT within the airflow pathways were studied to understand its impact on temperature variation and the ability to maintain stable temperatures within the system. Based on this, Cases 1 and 2 were assessed at V_{inlet} of 1.88m/s and V_{angle} of 0° at a constant T_{inlet} of 308.15 K (35°C).

The bar chart (Figure 4.48) and the contour graphs (Figures 4.49 to 4.52) provide insights into the effects of the E-PCM-T arrangement on the cooling performance of the system under different time steps and operational conditions. As shown in Figure 4.48(a), there is seen a noticeable difference between the T_{supply} for Case 1 and Case 2. Case 2 exhibited a more significant reduction in supply air temperature T_{supply}, with an approximate 7 % decrease. This reduction was from an initial T_{inlet} of 308.15 K (35 °C) to the lowest measured air temperature of 305.87 K (32.72 °C). In comparison, in Case 1, the drop in T_{supply} was slightly less pronounced than in Case 2 but cooling was achieved at a faster rate. The T_{supply} for Case 1 averaged 306.02 K (32.87 °C), reflecting only a 6 % reduction. However, Case 2 consistently maintained lower temperatures across all time intervals. This indicates better thermal regulation and less temperature fluctuation provided by the E-PCM-T arrangement in Case 2. The data implied that there is an enhanced cooling performance. This is a result of the E-PCM-T configuration which has helped to absorb heat more effectively and maintain the air temperature at a lower level.

In Figure 4.48(b), the exhaust air temperature in Case 2 also demonstrates more stable and controlled behaviour compared to Case 1. In Case 1, a sharp decline was observed, with T starting at 308.15 K (35 °C) and reaching 306.98 K (33.83 °C) by 10,000 s into the simulation. A gradual increase was also observed, reaching 308.09 K (34.94 °C) by the end of the 25,000 s simulation period. Active temperature stabilisation occurred between 2500 s to 20,000 s (approximately for 5 hours).

(a)

(b)
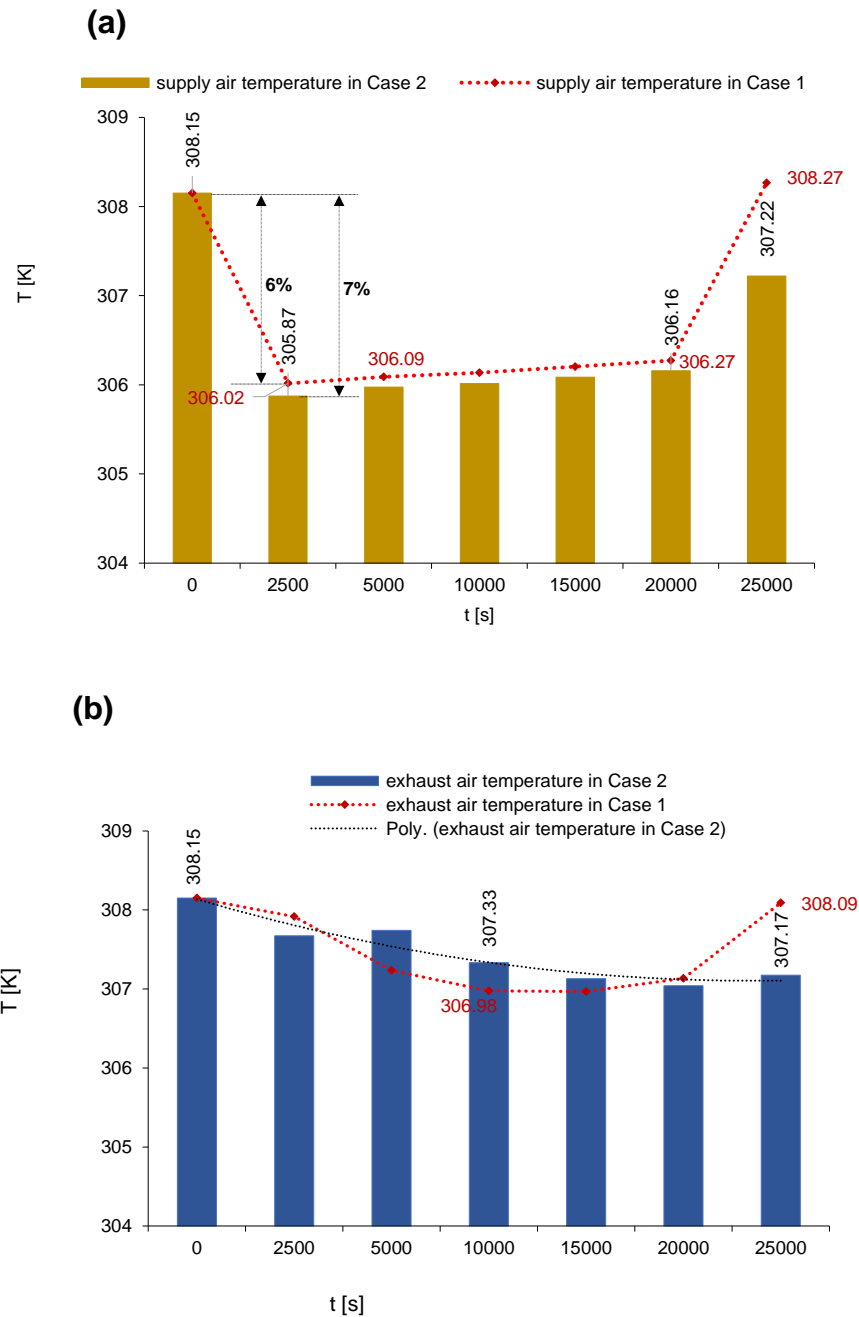
Figure 4.48. E-PCM-T arrangements' impact on temperatures—(a) Variation in supply air temperatures T_supply for Case 1 and Case 2, and (b) Variation in exhaust air temperatures T_exhaust for Case 1 and Case 2

The contour graphs further support the observations highlighted in the bar chart. Across the various time steps, Case 2 consistently demonstrated a more stable temperature distribution. It also maintained lower temperatures around critical areas than what was observed in Case 1.

Paying close attention to the comparison of Figures 4.50 to 4.52, a more uniform temperature distribution was observed in Case 2 (Figure 4.49(a)). This demonstrated better temperature regulation throughout the system compared to Case 1. It was observed that there were fewer hot spots and more balanced cooling in Case 2 than in Case 1. While Case 2 showed better stability and fewer fluctuations in temperature over time, Case 1 maintained a larger cool zone near the inlet in the earlier timesteps, which could suggest more immediate cooling at the source (Figures 4.50 to 4.52). This indicated more immediate cooling at the source.

However, this initial advantage of Case 1 is offset by the consistent temperature regulation in the micro-climate domain of Case 2, which persisted throughout the simulation cycle. From the 1000-timestep mark (Figure 4.50(b)), through 2500 timesteps (Figure 4.51(b)), until the cooling effect diminished at 5000 timesteps (Figure 4.52(b)), Case 2 maintained better overall temperature stability. Since long-term temperature reduction and stabilisation are the key performance objectives, Case 2 provides a more favourable cooling solution due to its ability to maintain more uniform and sustained cooling over time.

Overall, the results suggest that the E-PCM-T arrangements within the airstreams of the model substantially influenced the behaviour of both supply and exhaust air temperatures.

Case 1 at 500 timesteps
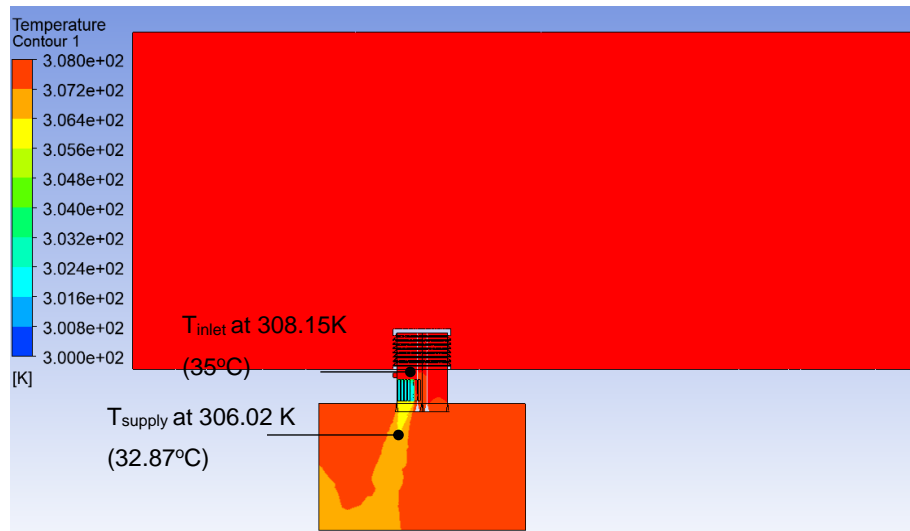
Case 2 at 500 timesteps
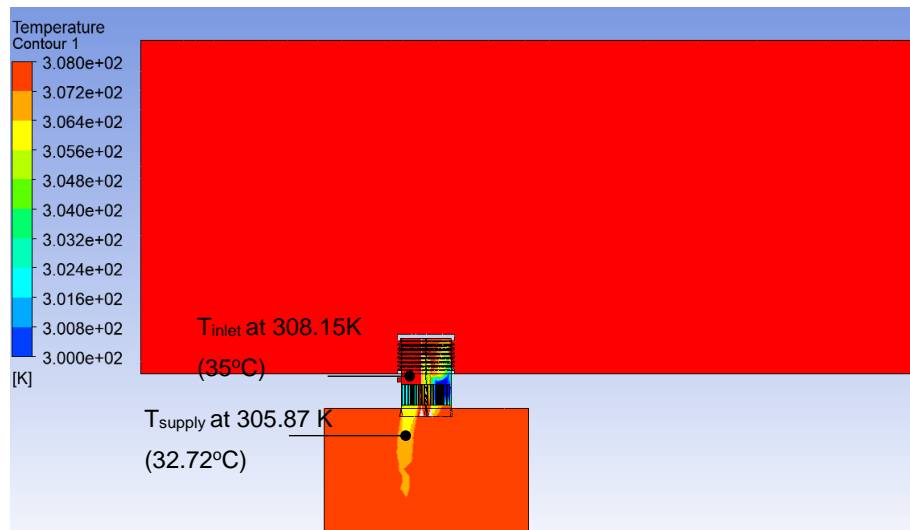
Figure 4.49. Comparison of temperature contour for cases 1 and 2 at V_{inlet} 1.88m/s at 500 timesteps

Case 1 at 1000 timesteps
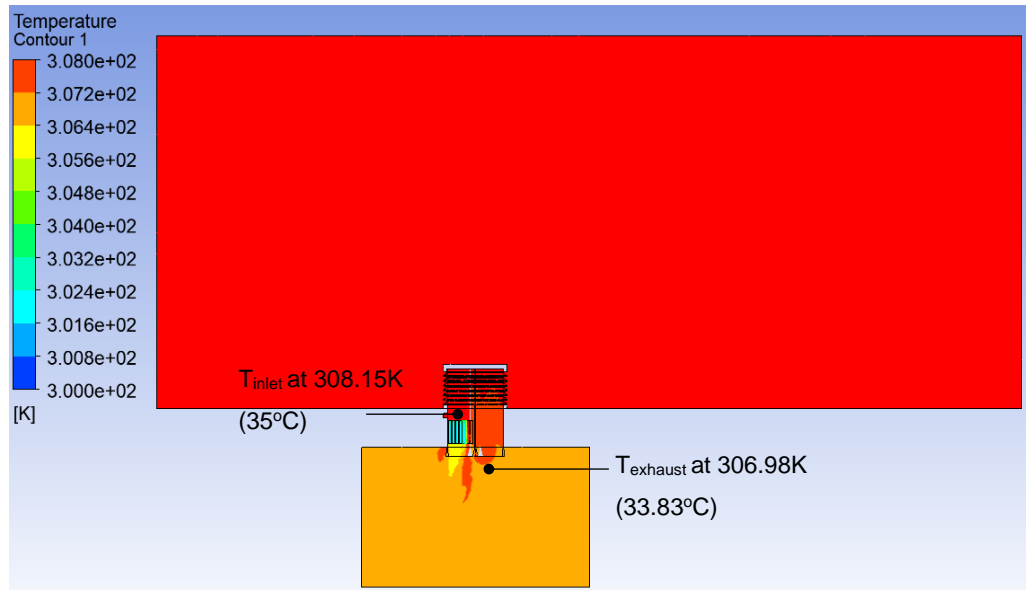
Case 2 at 1000 timesteps
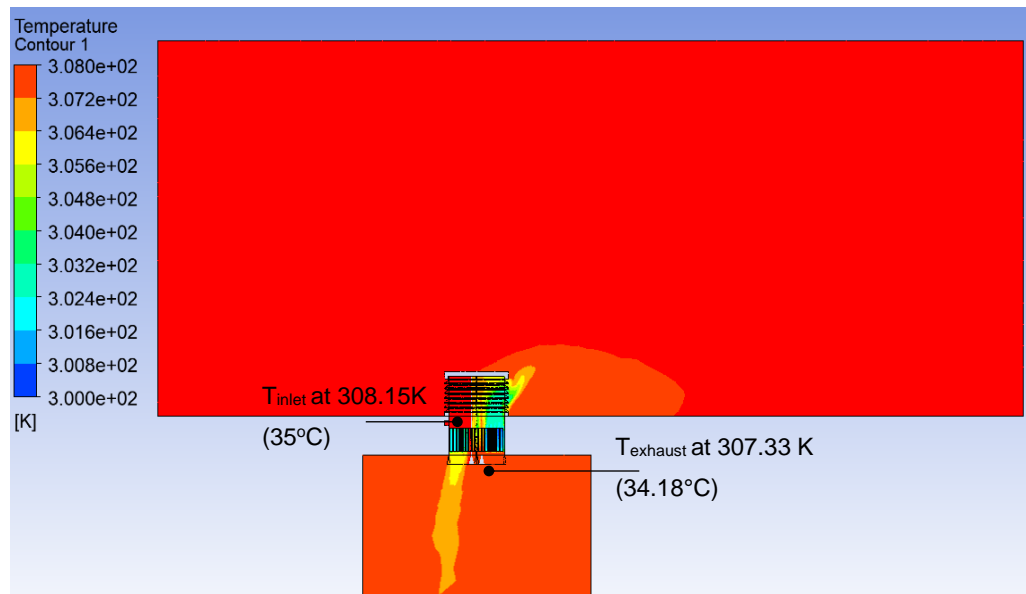
Figure 4.50. Comparison of air temperature contour for cases 1 and 2 at Vinlet 1.88m/s at 1000 timesteps

Case 1 at 2500 timesteps
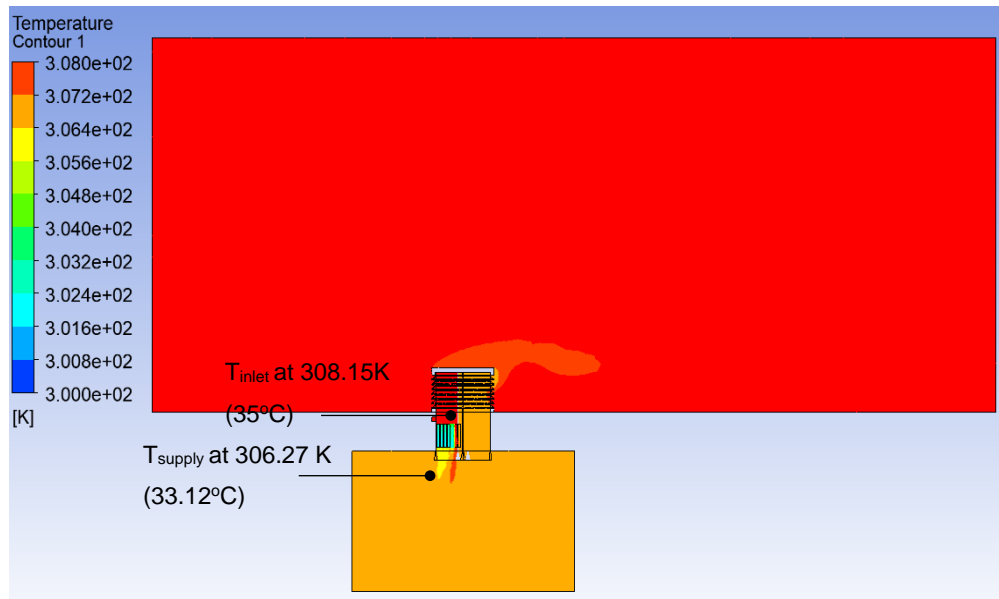
Case 2 at 2500 timesteps
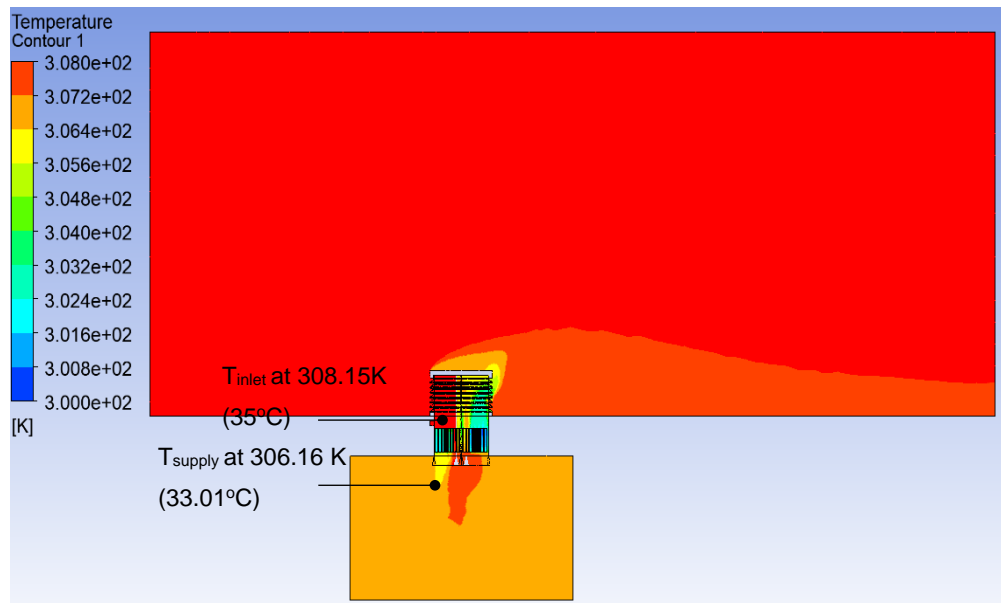
Figure 4.51. Comparison of air temperature contour for cases 1 and 2 at Vinlet 1.88m/s at 2500 timesteps

Case 1 at 5000 timesteps
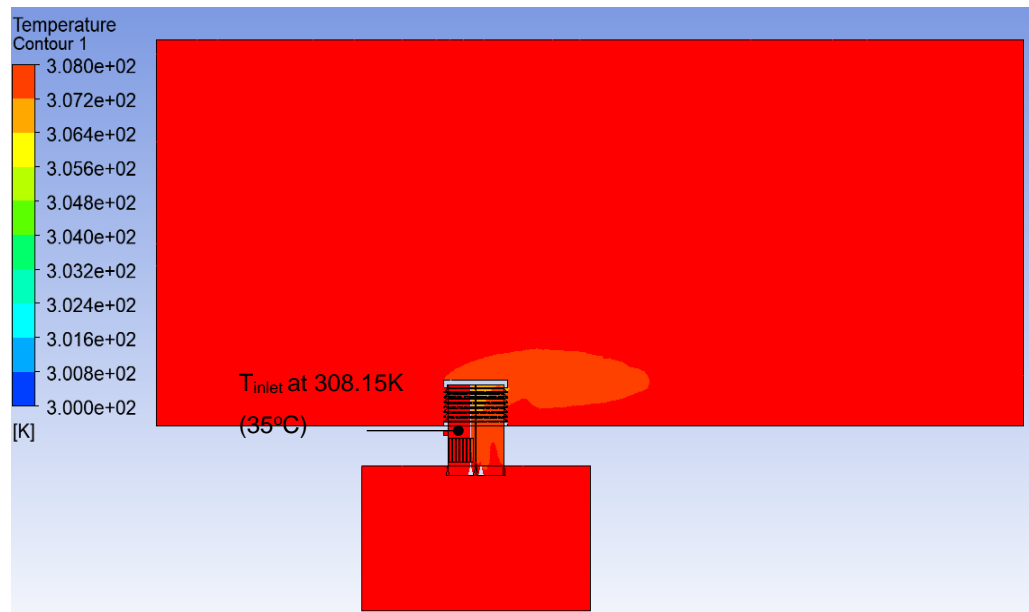
Case 2 at 5000 timesteps
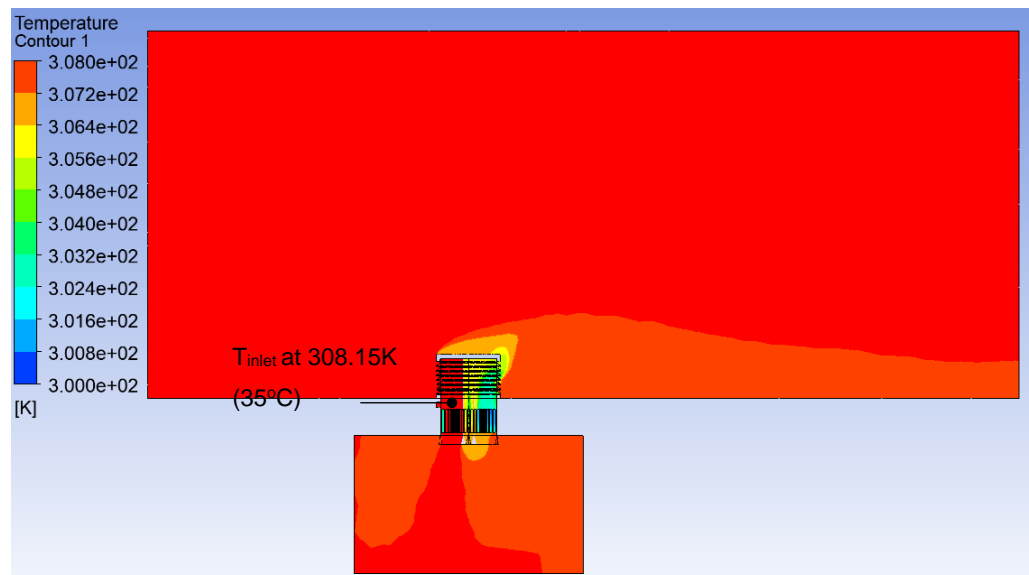
Figure 4.52. Comparison of air temperature contour for cases 1 and 2 at Vinlet 1.88m/s at 5000 timesteps

4.3.3 Thermal energy storage performance assessment of the EPCM-HMW system

The assessment of TES performance of the EPCM-HMW model was assessed based only on the PCM charging cycle. This was to understand the system's heat absorption and temperature stabilisation capability for cooling the incoming air.

4.3.3.1 Impact of varying outdoor wind speeds on thermal energy storage performance

Changes in wind speed can influence the rate of heat transfer. As a result, the impact of varying outdoor wind speeds (1.88m/s and 3m/s) on the PCM liquid fraction in Cases 1 and 2 was assessed.
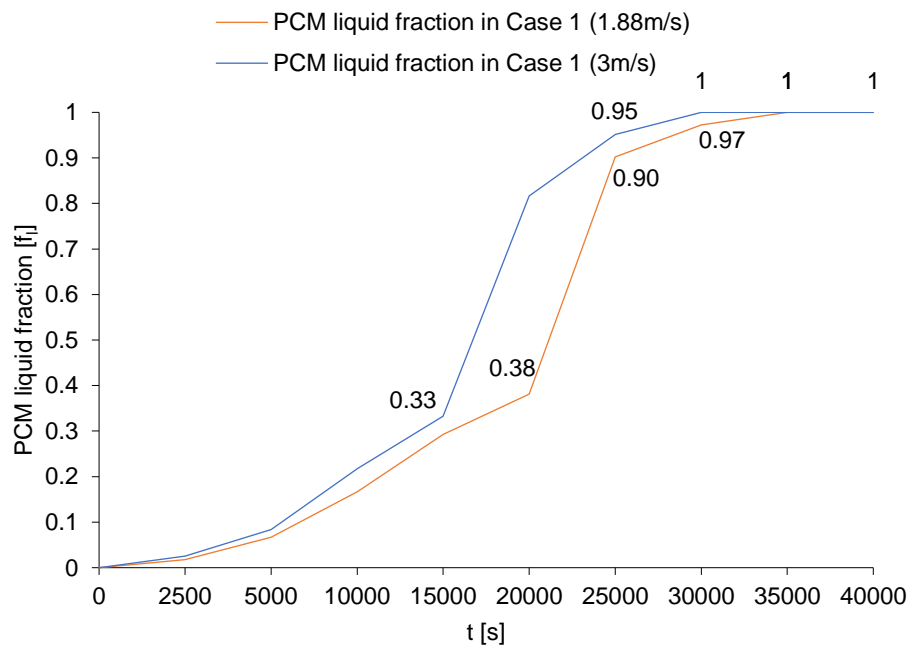
Figure 4.53. Comparison of the effect of variation in V_{inlet} on PCM liquid fraction in Case 1 (a) when V_{inlet} is 1.88 m/s and when V_{inlet} is 3 m/s.

A comparison of the PCM liquid fraction in Case 1 at 1.88 m/s and 3 m/s V_{inlet} is shown in Figure 4.53. As the V_{inlet} increased from 1.88 m/s to 3 m/s, the PCM charging rate improved significantly.

At 20,000 s, when V_{inlet} was 1.88 m/s, the liquid fraction was 0.33, but when V_{inlet} increased to 3 m/s, the liquid fraction rose to 0.38, indicating a 15% increase. After 25,000s, the liquid fraction was 0.90 with V_{inlet} at 1.88 m/s and 0.95 when V_{inlet} increased to 3 m/s, showing an increase of 5.5%. The PCM reached complete melting at 30,000s in both cases, though with V_{inlet} at 3 m/s, the melting cycle completed slightly faster.

Comparing the results in Figure 4.54(a) and (b), a faster PCM charging process was observed in the exhaust air streams when V_{inlet} increased from 1.88 m/s to 3 m/s in Case 2. However, the PCM in the EPCM-T located in the supply airstream consistently charged faster in both Cases 1 and 2. At 20,000s, the liquid fraction (f_l) of the PCM in the supply airstream was 0.35, while the PCMs in other air streams ranged between 0.18 and 0.22 (Figure 4.54(a)). Between 20,000s and 25,000s, a sharp increase in f_l occurred, reaching 0.89 in the supply airstream. Complete melting occurred at 30,000s. In contrast, the PCMs in other air streams charged more gradually, with full melting occurring between 35,000s and 40,000s.

When V_{inlet} increased to 3 m/s (Figure 4.54(b)), a similar trend was observed, but PCM charging was completed earlier. At 20,000s, the PCM liquid fraction in the supply airstream was 0.31, while the others ranged between 0.17 and 0.21. A sharp rise in f_l to 0.99 occurred between 20,000s and 25,000s. For the other PCMs, the liquid fraction remained stable between 0.31 and 0.35 until the charging cycle was completed at 30,000 s.

Increasing wind speeds accelerated the PCM charging process, indicating enhanced TES performance. The results also imply that the time required for temperature stabilisation was reduced, particularly at higher V_{inlet} values.
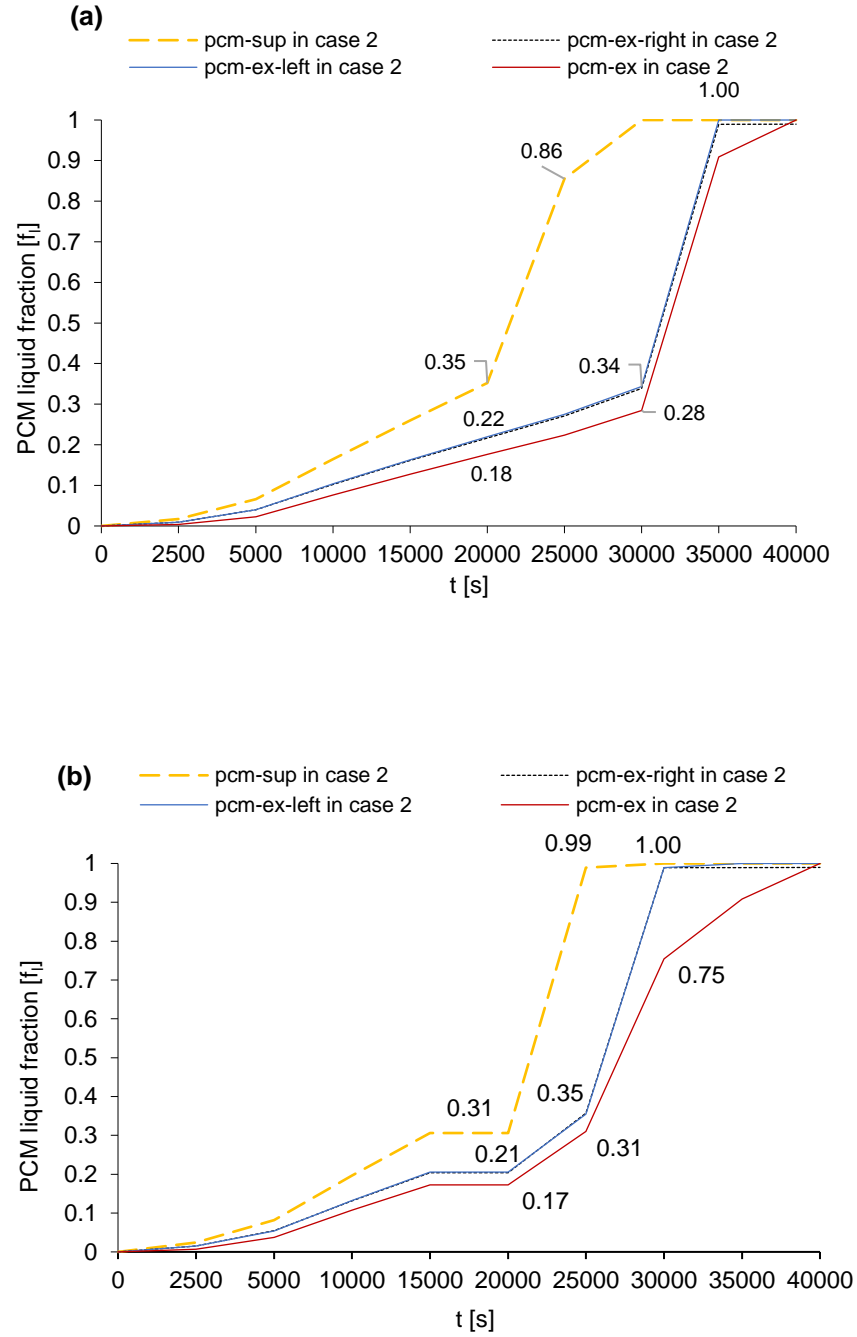
Figure 4.54. Effect of variation in PCM liquid fraction in Case 2 (a) when V_{inlet} is 1.88 m/s and (b) when V_{inlet} is 3 m/s.

4.3.3.2 Impact of E-PCMT arrangement on thermal storage performance

At V_{inlet} of 1.88m/s and V_{angle} of 0°, Case 1 and Case 2 models were assessed. This was based on variations in their PCM charging rates, PCM temperature, and air temperature stabilisation. The aim was to fully understand the impact of E-PCM-T arrangement on their overall TES performance.
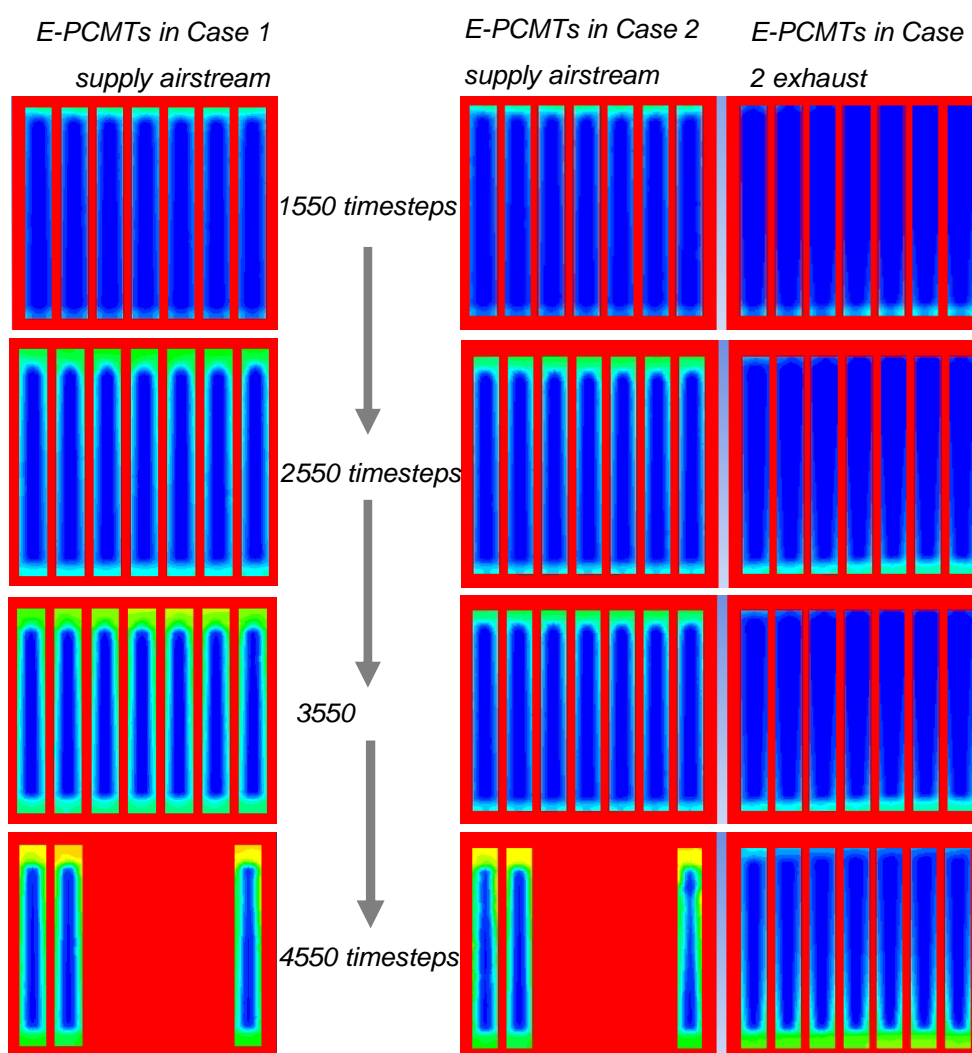
Figure 4.55. Contour showing PCM liquid fraction comparison between Case 1 and Case 2 based on the E-PCM-T arrangement in supply and exhaust airstreams.

The liquid fraction contour in Figure 4.55 graphically illustrates that from 2550 simulation timesteps, the PCM in the supply airstream in Case 1 began to melt faster than the PCM in the supply airstream in Case 2. The

liquid fraction contour also reveals that PCM melting in the exhaust airstreams occurred in a bottom-up direction. However, the PCM melting in the exhaust progressed in a top-down direction. This heat absorption at the base of the PCM in the exhaust airstream slightly improved the cooling in Case 2.
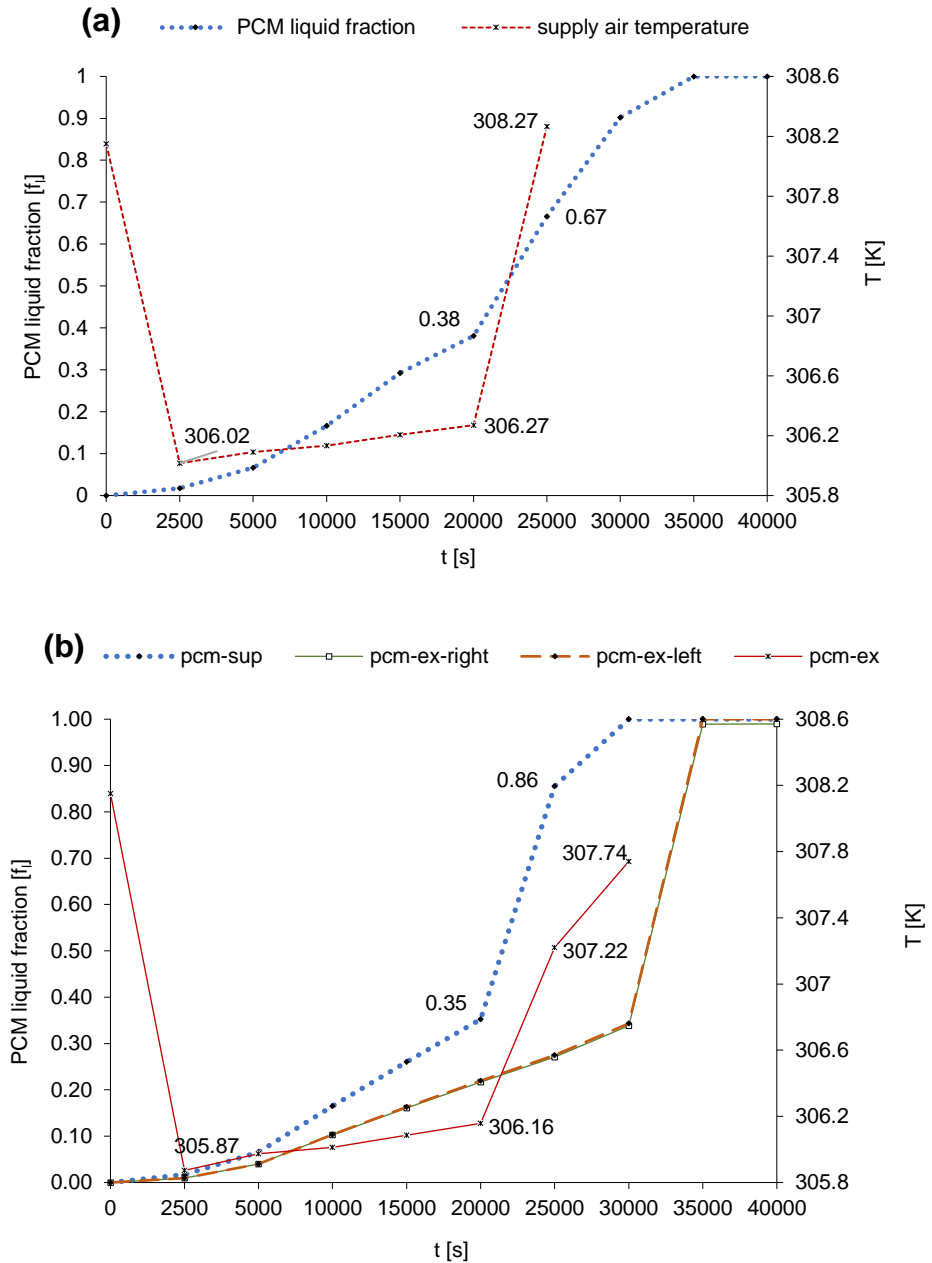
Figure 4.56. Comparison of supply air temperature T_s and PCM liquid fraction f_l in (a) Case 1 and (b) Case 2.

Figure 4.56(a) and (b) highlight the slower PCM charging cycle in Case 2 compared to Case 1. Between 2,500 s and 20,000 s, Case 2 showed a lower Tsupply value. Figure 4.56(b) compares T_{supply} and PCM liquid fractions for both cases. Case 2 retained its cooling capacity for a longer period. Between 2500 s and 20,000 s, T_{supply} was stable, ranging between 305.87 K (32.72°C) and 306.16 K, with a liquid fraction of 0.35.

At 25,000s, T_{supply} only slightly increased to 307.77 K, while the liquid fraction rose to 0.86. For both Cases 1 and 2, it was observed that T_{supply} achieved temperature stabilisation for approximately 5 hours. However, cooling (indoor temperature reduction) continued for 7 hours.

In contrast, Case 1 had a T_{supply} range of 306.02 K to 306.27 K at the same time, with a liquid fraction of 0.38. After this, a sharp rise in T_{supply} occurred, reaching 308.27 K when the liquid fraction was 0.66.
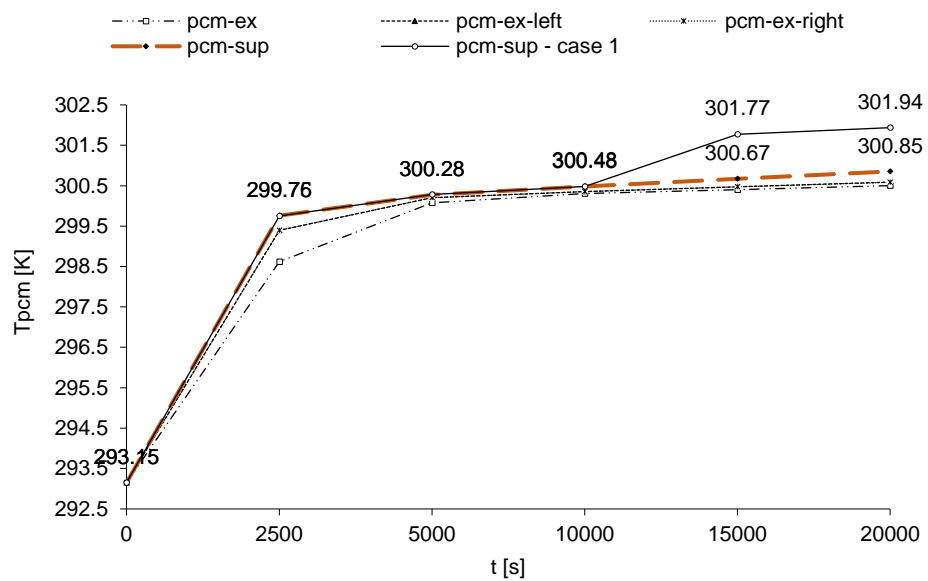
Figure 4.57. Comparison of PCM temperature T_{pcm} comparison for Case 1 and Case 2

Figure 4.57 shows an increase in T_{pcm} from an initial 293 K (20°C) for both cases. However, between 10,000s and 15,000s, Case 1 experienced a 1.1 K higher temperature difference (ΔT_{pcm}) than Case 2. The rise in Case 1 exceeded Case 2 by 0.4%. Despite this, Case 2 increased more gradually to 20,000s. This suggests the E-PCMT arrangement in all four air streams of the model significantly helped stabilise T_{supply} and extended the system's cooling performance. Basically, very minimal fluctuation occurred, which was within ±2°C temperature fluctuation, as PCM charging occurred. The results implied that effective temperature stabilisation was maintained up to 20,000s to

25,000s, slight fluctuation was observed between from 20,000 – 30,000s as the PCM charged.

4.4 Chapter's concluding remarks

4.4.1 Summary of EPCM-T parametric study

The EPCM-T parametric study examined how different EPCM-T designs performed under varying V_{inlet} of 1.88 m/s and 3 m/s, using copper and aluminium as encapsulation materials. The goal was to assess how airflow and encapsulation materials influenced the PCM's ability to absorb and store thermal energy during the charging cycle.

The following observations have been identified from the EPCM-T parametric study:

4.4.1.1 Inlet air velocity impact:

Increasing the V_{inlet} from 1.88m/s to 3m/s improved the PCM heat transfer process. At a V_{inlet} speed of 3 m/s, the PCM reached thermal equilibrium 600 minutes faster compared to when the inlet speed was 1.88 m/s, which took about 720 minutes. Higher airflow speeds led to a faster rate stabilisation air temperatures and PCM melting.

4.4.1.2 Influence of encapsulation material:

Copper encapsulation consistently showed a faster heat transfer rate compared to aluminium. For instance, at 1.88 m/s, PCM temperatures in copper-encapsulated models reached 34.7°C (307.85 K), while aluminium-encapsulated models reached 34.9°C (308.05 K). Although the temperature difference was small, copper encapsulation resulted in faster rate of temperature stabilisation. Aluminium-encapsulated models had slower heat transfer, and the temperature stabilisation was more prolonged over a longer period. This could benefit applications requiring

prolonged cooling and more stable temperature control. As a result, it was observed that the aluminium-encapsulated EPCM-T is beneficial to the EPCM-HMW system since it requires prolonged cooling and more stable temperature control.

4.4.1.3 Influence of EPCM-T shape and design:

Two EPCM-T shapes were evaluated: rectangular and cylindrical, with both shell-tube and profiled versions compared. The rectangular EPCM-Ts consistently performed better than the cylindrical versions in terms of cooling stability and TES. For example, the rectangular EPCM-T profile version maintained a more stable temperatures over time. Although the cylindrical version exhibited faster initial cooling, it was less effective in maintaining stable temperatures, particularly at higher wind speeds.

In terms of TES, the rectangular design also demonstrated better performance. This can be attributed to the fact that it showed a more controlled phase change process. The cylindrical design reached full melting earlier than the rectangular EPCM-T. But the cooling capacity reduced more rapidly. This showed that it is not suitable for prolonged heat absorption. The study concluded that the rectangular EPCM-T profile design version is the most suitable for the EPCM-HMW system, offering superior long-term cooling stability and energy storage.

4.4.1.4 Liquid fraction behaviour:

The copper-encapsulated models exhibited up to 2-3% higher liquid fraction values than aluminium in the early stages of the charging cycle, when V_{inlet} was 1.88m/s. However, when V_{inlet} increased to 3 m/s, the copper-encapsulated models reached full melting faster, at around 480 minutes. The aluminium models reached full melting at about 600 minutes. But by the end of the charging cycle, both materials had comparable performance, with only minimal differences in their liquid fraction values.

The study concluded that higher airflow velocities and copper encapsulation enhance heat transfer and accelerate PCM charging. In contrast, aluminium provides more controlled and prolonged thermal storage, making it a better choice for the EPCM-HMW system which requires extended cooling performance.

Overall, the aluminium encapsulated rectangular profile design version of the EPCM-T (Model 1B) was selected.

4.4.2 Summary of the overall performance of the EPCM-HMW system

The EPCM-HMW system's overall performance was assessed in two scenarios: Case 1, where EPCM-T units were placed in a single airstream, and Case 2, where the EPCM-T units were evenly distributed across four airstreams. The study assessed the cooling efficiency and TES of the EPCM-HMW system, based on different wind speeds and E-PCM-T arrangements.

The observations from the performance assessment of the EPCM-HMW system are summarised:

4.4.2.1 Ventilation performance based on wind speed:

The results indicated that at a low wind speed of 1.88 m/s, the lowest airflow was at P_2, near the room wall. This implied that ventilation performance was less effective at this point. Although, overall, the system at 1.88m/s windspeed, indoor airflow was still within acceptable thermal comfort limits of 140.86 L/s. This is sufficient airflow rate for 14 to 17 occupants. There was improvement in the indoor air velocity when the wind speed increased to 3m/s. However, the solar fan at a 10 Pa pressure jump also provided an additional 370 L/s airflow.

4.4.2.2 Cooling performance based on wind Speed:

Cooling performance at wind speeds of 1.88 m/s and 3 m/s was also studied. Cooling improved at lower wind speeds (1.88 m/s). In Case 2, T_{supply} reached as low as 305.87 K (32.72 °C) at 5000 s. this indicated a 0.65% temperature reduction. With 3 m/s wind speeds, Case 2 maintained more stable cooling. In this case, T_{supply} maintained a value of 307 K (33.85 °C) for a longer period. However, at specific points such as $P_{11-supply}$, the cooling effectiveness decreased with higher wind speeds.

4.4.2.3 Influence of E-PCM-T arrangement on cooling stability:

Case 2 consistently performed better than Case 1 in terms of temperature regulation and cooling stability. At 20,000 s, T_{supply} in Case 2 remained between 305.87 K (32.72 °C) and 306.16 K (33.01 °C). T_{supply} in Case 1 was between 306.02 K (32.87 °C) and 306.27 K (33.12 °C). Case 2 maintained more uniform temperature distribution, providing better long-term cooling performance. This suggests that distributing E-PCM-T units across multiple airstreams (as in Case 2) offers more efficient cooling and temperature stabilisation as compared to concentrating all the E-PCM-T units in a single airstream.

4.4.2.4 Thermal energy storage performance:

The distributed E-PCM-T arrangement impacted on the TES performance of the system. For instance, the PCM liquid fraction in the supply airstream of Case 2 reached 0.35 at 20,000 s. But in other airstreams, it ranged between 0.18 and 0.22. The E-PCM-T in the exhaust airstreams increased heat absorption. This generally enhanced the system's overall cooling effectiveness. Case 2 also achieved better stabilisation of T_{supply}, with temperatures rising more gradually than in Case 1, where temperature increases were sharper.

Overall, Case 2 is the more favourable configuration for both cooling efficiency and TES. The even distribution of E-PCM-T units across multiple airstreams results in more stable, prolonged cooling and better temperature regulation, making it a more efficient solution for long-term thermal management. However, for both Cases 1 and 2, it was observed that T_{supply} achieved temperature stabilisation for approximately 5 hours. However, cooling (indoor temperature reduction) continued for 7 hours.

Chapter 5

5   Model validation results

5.1   EPCM-HMW model validation model results

As described in 3.4.2.3, the EPCM-HMW model was verified by validating the two main components (the windcatcher and the EPCM-T) with experiment and CFD results from the literature. In this light, two separate verification models were developed to validate the airflow model of the windcatcher component of the EPCM-HMW system and the E-PCM-T heat transfer. These validation were done separately.

5.1.1   Airflow model validation
5.1.1.1 Model overview

The windcatcher component airflow model of the EPCM-HMW system was validated through CFD simulations, and the results were compared with experimental data from Calautit et al. [357]. The objective of this validation was to ensure that the model could accurately predict the airflow patterns and velocities within the EPCM-HMW system. The windcatcher component is crucial for ventilation and cooling, as it draws external air and distributes it internally. Several assumptions were made during model construction, including steady-state airflow, simplified geometry of the windcatcher, and standard atmospheric conditions (discussed in section 3.4.2.3.2). The main validation variable was wind velocity, with boundary conditions derived from the setup in Calautit et al. [357]. Before incorporating the E-PCM-T heat transfer model into the windcatcher, its airflow performance was validated to ensure reliability.

5.1.1.2 Set-up and measurements of the Calautit et al. experiment

In Calautit et al.'s study [357], a rapid-prototyped windcatcher model was tested in a closed-circuit, low-speed wind tunnel. The tunnel had an overall length of 5.6 m, with the test section measuring 0.5 m in height,

width, and 1 m in length. The windcatcher model was mounted on a revolving plate to allow airflow testing from different directions. A smoke visualisation set-up inside the tunnel was used to observe airflow patterns, as shown in Figure 5.1. Additionally, a hot-wire anemometer was employed to measure air velocity at different points within the test room and the windcatcher itself, as illustrated in Figure 5.2.
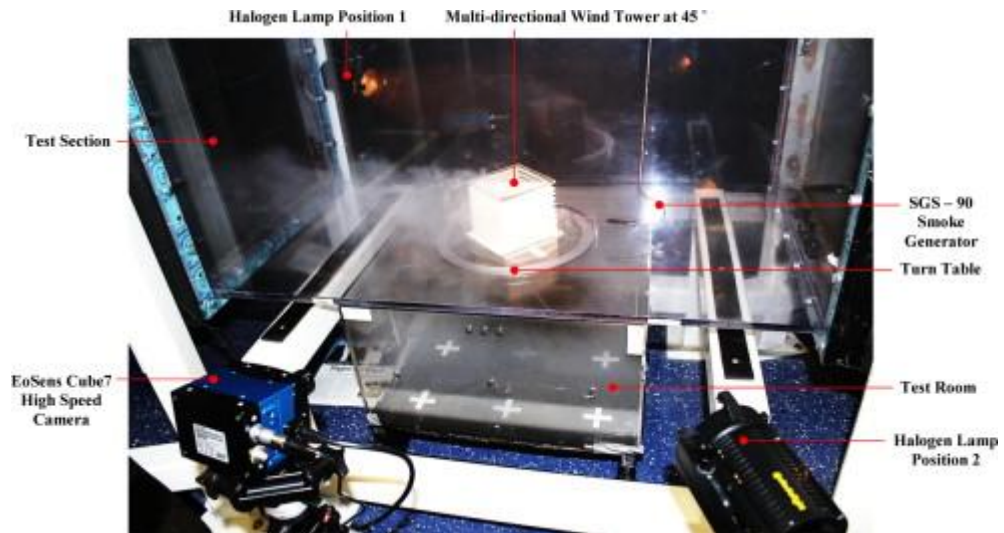
Figure 5.1. The windcatcher smoke visualisation set-up inside the Calautit et al. [357] wind tunnel experiment.

Point	X [m]	Y [m]	Z [m]
P1 (mid)	-0.165	0.165	-0.135
P2 (mid)	0	0.165	-0.135
P3 (mid)	0.165	0.165	-0.135
P4 (mid)	-0.165	0	-0.135
P5 (mid)	0	0	-0.135
P6 (mid)	0.165	0	-0.135
P7 (mid)	-0.165	-0.165	-0.135
P8 (mid)	0	-0.165	-0.135
P9 (mid)	0.165	-0.165	-0.135
P10 (bottom)	0	0	-0.22
P11 (supply)	0.025	0	-0.03
P12 (outlet)	-0.025	0	-0.03
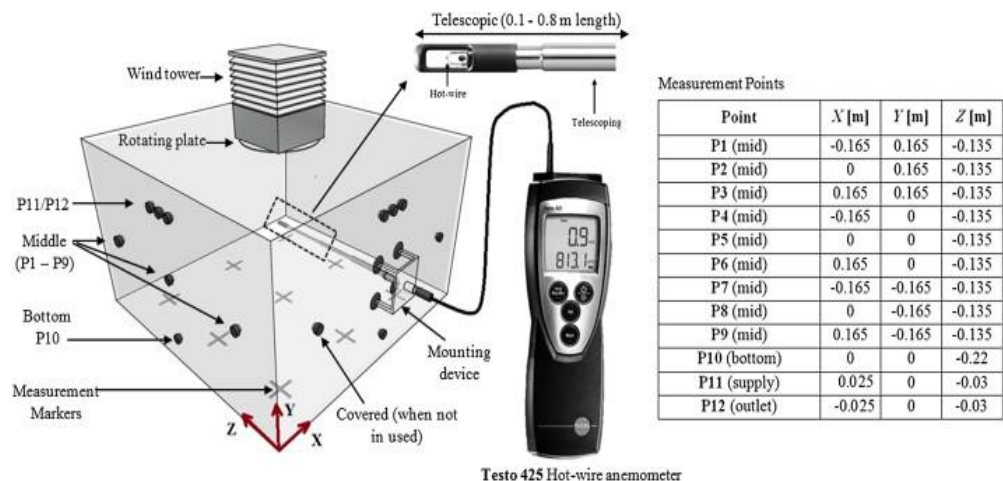
Figure 5.2. The measured points in the test room and the instruments used for measurement in the Calautit et al. [357] wind tunnel experiment.

5.1.1.3 Airflow validation results

The airflow validation compared results from Calautit et al.'s experiment with the CFD simulations from both Calautit et al. [357] and the present study. The objective was to analyse the agreement between the CFD model in the present study and the experimental data and to identify any discrepancies. Figure 5.3 graphically showed that while the current study predicted slightly lower indoor velocities, the system maintained acceptable ventilation performance.

For example, the average supply speed in the current study reached 1.61 m/s as seen in Figure 5.3. This was almost identical to the 1.62 m/s in Calautit et al.'s experiment. Indoor velocity was similarly close, at 0.54 m/s compared to 0.55 m/s (Figure 5.3). These results indicate that the model performs well in drawing external air into the system, which is vital for ventilation.

Statistical performance models, including normalized mean square error (NMSE), Fractional Bias (FB), and the fraction of predictions within a factor of two of observations (FAC2), based on equations 3.17, 3.18, and 3.19 were adopted to conduct a more in-depth validation analysis. Table 5.1 summarises the average velocities at monitor points P_1 to P_{12} and the corresponding errors calculated using these statistical performance models.
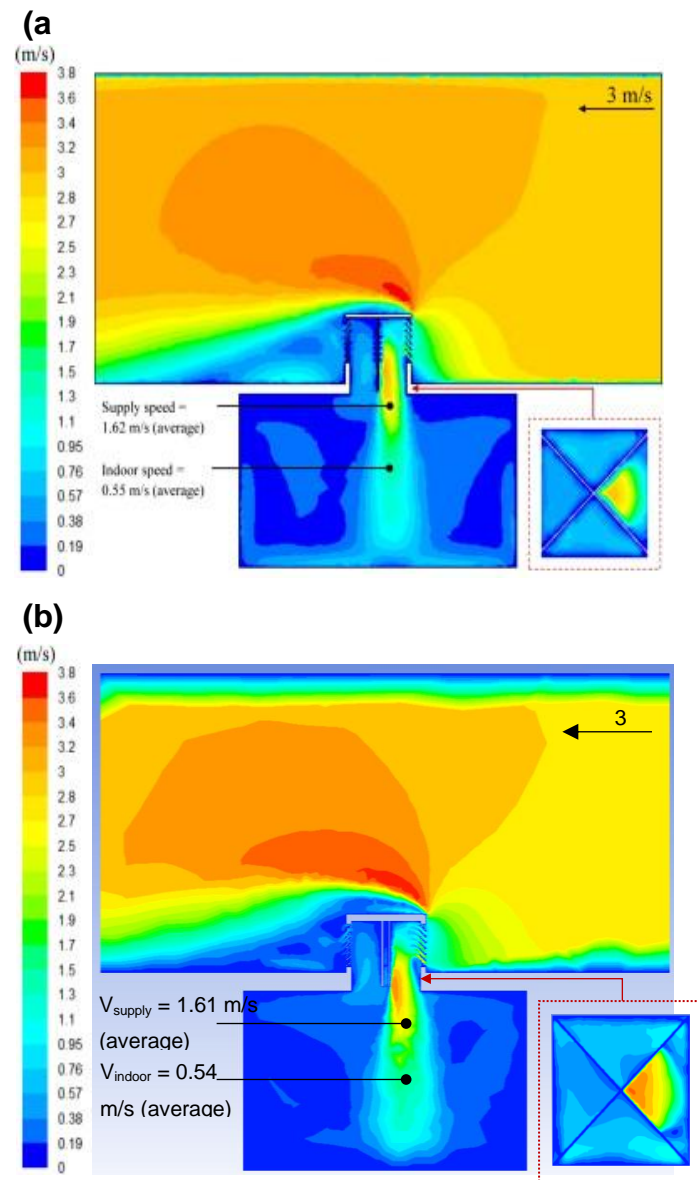
Figure 5.3. Comparison of (a) velocity contour in Calautit et al.'s study [357] with (b) velocity contour for the windcatcher component of this current study.

Table 5.1. Average weighted velocities and errors at monitor points P1 - P12 for CFD predictions and experimental observations data from the literature.

Monitor Points	P_1	P_2	P_3	P_4	P_5	P_6	P_7	P_8	P_9	$P_{10\text{-exhaust}}$	$P_{11\text{-supply}}$	$P_{12\text{-exhaust}}$
V for C_o (m/s)	0.29	0.22	0.28	0.25	1.05	0.22	0.23	0.28	0.29	0.81	2.51	0.30
V for $C_{p(L)}$ (m/s)	0.30	0.20	0.30	0.31	1.08	0.21	0.22	0.29	0.29	0.79	2.50	0.32
V for C_p [m/s]	0.32	0.21	0.17	0.30	1.19	0.21	0.47	0.16	0.27	1.19	2.82	0.37
D%	1%	0%	28%	4%	1%	0%	22%	32%	1%	15%	1%	4%
FAC2	1.12	0.93	0.59	1.21	1.13	0.96	1.60	0.57	0.92	1.47	1.12	1.23
Average FAC2	1.07											
NMSE %	3%											
	12%											

Figure 5.4. Comparison of indoor velocity for CFD data (C_P) from the present study, experimental observation data (C_o) and CFD ($C_{p(L)}$) from literature.

The bar chart in Figure 5.4 compares three data sets: experimental data from literature (orange bars), CFD data from literature (blue bars), and CFD data predictions from the current study (green bars).

Accordingly, the comparison across multiple monitor points demonstrated strong consistency between the three data sets: experimental data, literature CFD predictions, and the current CFD study. This suggested that the CFD model was successfully replicating experimental results with reasonable accuracy. The close alignment, particularly at most monitor points, validated the CFD model's ability to simulate airflow effectively.

Inadeptly, the velocities at P_1 to P_9 remained closely aligned across the data sets, with only small variations. This ranged from 0.02 to 0.05 m/s. The maximum velocity at these points was only approximately 0.4 m/s. This confirmed the model's reliability in capturing airflow at these points. At P_{10}, however, there is a noticeable divergence. The experimental data recorded a

lower velocity of 0.81 m/s, while the CFD model predicted a higher value of 1.19 m/s. This difference may have stemmed from the assumptions or boundary conditions applied in the CFD airflow model, which could have led to the overestimation at this specific point. $P_{11\text{-supply}}$ recorded the highest velocities (2.51 m/s), while P_2 and P_8 showed lower values across all metrics, indicating areas for improvement.

According to Figure 5.4, the maximum error was recorded at monitor point P_8. A significant discrepancy of 32 % was observed between the predicted CFD values and the experimental data at this point. $P_{3\text{ and }}P_7$ also recorded large deviations at 28 % and 22 % respectively (Table 5.1). These larger deviations highlight areas where the model's performance could be improved, particularly in zones where airflow behaviour may be more complex. On the other hand, as seen in Figure 5.4, the minimum error occurred at P_2 and P_6. The model showed perfect alignment with the experimental data at these points, resulting in a 0 % error. This indicated that the model performed well in some areas, but significant discrepancies existed in others.

The Fractional Bias Error (FB error) was calculated at 12 %. This suggested a slight tendency of the CFD model to have overestimated the airflow velocities at some points when compared to experimental observations. This bias, though not extreme, pointed to areas for potential refinement in the model's assumptions or boundary conditions.

The Normalized Mean Square Error (NMSE) was estimated at 3 %. This reflected a generally low level of deviation between the predicted and experimental results. This implied a strong overall model performance. In addition, the average FAC2 value of 1.07 was calculated. This suggested that the CFD model's predictions were largely within an acceptable range of the observed data. However, as shown in Table 5.1, the FAC2 values ranged from 0.57 to 1.23 across different monitor points This indicated varying levels of agreement between the predictions and experimental data.

However, despite the variations in the airflow model's accuracy across different monitor points, the overall average FAC2 value of 1.07 suggested that the CFD model provides reasonable agreement with experimental data for most monitoring locations. However, targeted improvements, particularly at points with higher errors, could further enhance the model's precision.

Precisely, the current CFD airflow model showed lower indoor velocities than Calautit et al.'s experiment, the overall ventilation performance remained adequate. The system provided sufficient air exchange to deliver fresh air, although at lower speeds. However, further refining the design could further optimise the balance between airflow efficiency and occupant comfort.

5.1.2 E-PCM-T heat transfer model validation
5.1.2.1 EPCM-T model overview

The validation of the selected aluminium encapsulated rectangular E-PCM-T heat transfer model was performed. The primary goal of the validation was to assess the CFD model's capability in accurately simulating the phase-change dynamics of the PCM. Particularly simulating its solid-to-liquid transition in response to temperature changes. This validation exercise was conducted under similar boundary conditions. It involved a detailed comparison between the spatial average liquid fraction CFD predictions from the present study, experimental observations, and the CFD predictions from Rouault et al.'s study [281]. This comparison was to ensure consistency between the CFD simulations and the experimental setup. Specifically, the extent to which the material transitioned from solid to liquid as the temperature rose above the melting point was assessed. This experimental data formed the basis for validating the predictions generated by the CFD simulations.

5.1.2.2 Set-up and measurements of the Rouault et al.'s experiment

The Rouault et al.'s experiment [281] was set up by placing aluminium encapsulated PCM tubes inside an energy storage unit. The unit is composed of 42 no. 30 mm by 40 mm by 3440 mm PCM filled aluminium encapsulated tubes layered horizontally parallel to each other inside a wooden energy storage unit. The PCM used was a commercial RT28 HC paraffin. These tubes were stacked as 6-layer bundles as illustrated in Figure 5.5.
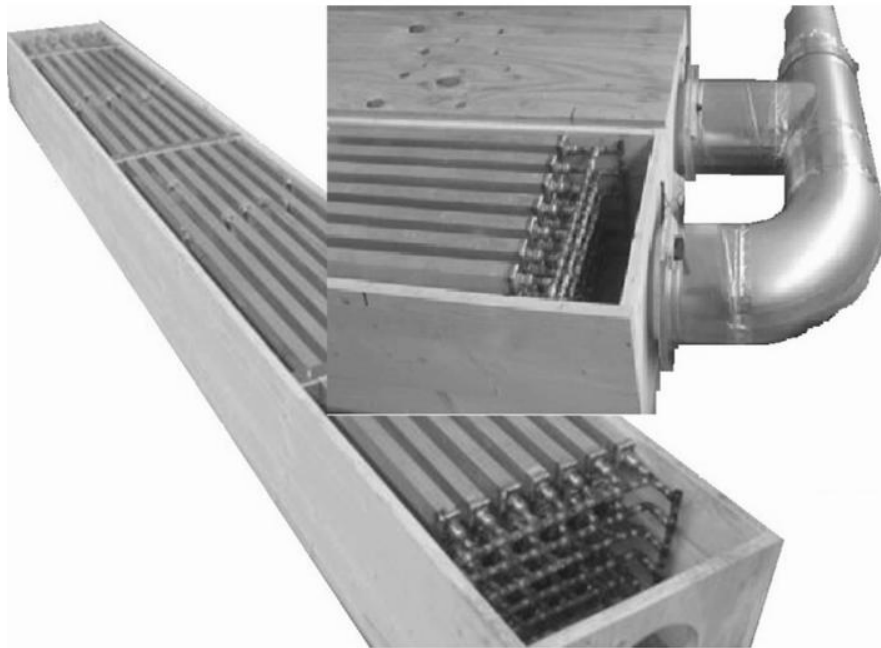
Figure 5.5. Aluminium encapsulated PCM filled tube bundles staked in 6-layered inside an energy storage unit bundle. [281].

As depicted in Figure 5.6, the Rouault et al.'s experiment [281] focused on understanding the PCM heat transfer performance in relation to the positioning of the fusion fronts during PCM charging. The fusion fronts are denoted as $s_z(x,t)$, $\delta(x,t)$ and $s_y(x,t)$ in Figure 5.6. The study further assumed that close-contact melting and heat exchange through the wooden box was negligible. Hence, crucial parameters such as the PCM liquid fraction, the encapsulation tube temperature, PCM temperature, and air temperature variation were the focus of the assessment [281]. The inlet air velocity was at a uniform value of 1.88 m/s. and the inlet air temperature was maintained at 35 °C (308.15 K).

However, temperature initialisation seen their results indicated 20 °C (293.15 K). The inlet air temperatures for both the CFD simulation in current study and Rouault et al.'s experiment was at 35°C (308.15 K). However, a key difference between the two studies was that Rouault et al. initialised their air temperature at 20°C (293.15 K), while the CFD model for the current study was initialised at 35°C (308.15 K).
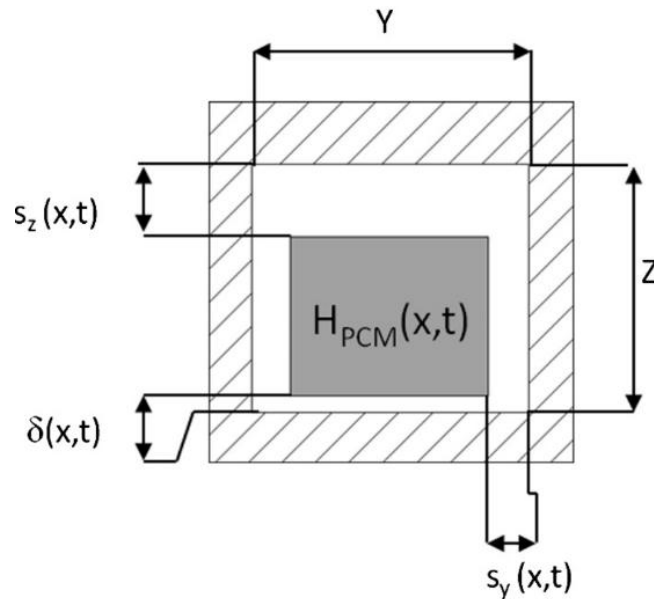
Figure 5.6. Cross-section of PCM encapsulated aluminium tubes in Rouault et al.'s experiment [281] showing the melting fonts during the PCM charging process.

Based on this, the CFD EPCM-T model in the present study was compared to the numerical and experimental data from Rouault et al.'s study [281]. However, to ensure an accurate comparison, other boundary conditions, such as inlet conditions, material properties, and heat transfer coefficients, were kept consistent with those used in Rouault et al.'s experiment. This allowed the fundamental heat transfer and airflow physics to be reliably compared between the two studies. Hence, the EPCM-T heat transfer model was monitored with the error data summarised in Table 5.2 based on the analysis interpreted from the graphs in Figures 5.7 to 5.10.

Table 5.2. Values of NMSE, FB and FAC2 statistical deviation calculations for PCM liquid fraction, encapsulation tube temperature, PCM temperature and air temperature at P_{10}.

Parameter	NMSE (%)	FB (%)	FAC2	Maximum deviation value between C_o and C_p	Comments
PCM liquid fraction	4.153	4.757	1.194	0.289	moderate NMSE and FB, but very low maximum deviation.
encapsulation Tube temperature (k)	0.003	0.524	1.005	2.048	excellent NMSE, FB, FAC2, and low maximum deviation. Best performance overall.
PCM temperature (k)	0.198	4.239	1.044	9.125	low NMSE, but higher FB and maximum deviation, indicating some limitations.
air temperature (k)	0.028	1.636	1.017	5.639	excellent NMSE and FB, but moderate maximum deviation.

5.1.2.3 PCM liquid fraction validation results

Figure 5.7 shows the comparison of PCM liquid fraction between the current CFD model (denoted as C_p), experimental data (C_o), and numerical data from the literature (C_{pL}). The model produced a Normalized Mean Square Error (NMSE) of 4.15 % and a Fractional Bias (FB) error of 4.76 %. This indicated that the CFD model performs well, although with a slight over-prediction of the liquid fraction.

The maximum deviation between C_o and C_p was 0.289, which was quite modest. The FAC2 value of 1.2 also suggested that the model's predictions were generally within the acceptable range. The graph illustrated that the current model closely followed the general trend of both experimental and numerical data but diverged slightly in the later stages of the process (around 500 minutes). At this point, C_p showed a larger discrepancy from C_o and C_{pL}.

Overall, the PCM liquid fraction model demonstrated reliable performance. It captured the main characteristics of the phase-change process.
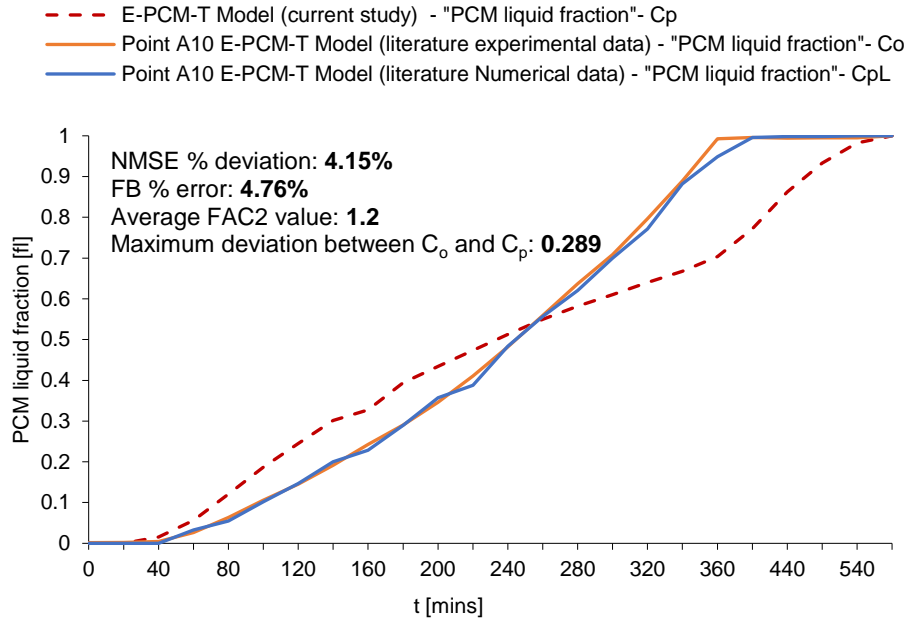
Figure 5.7. Comparison of PCM liquid fraction CFD predictions C_p in the current study, experimental observations C_o from the literature and CFD predictions C_{pL} in literature.

5.1.2.4 Encapsulation tube temperature validation results

Figure 5.8 compares the encapsulation tube temperatures. The graph showed a close correlation between CFD predictions (C_p) and both experimental and numerical results throughout the simulation period. Only minor variations were observed after 500 minutes. In this case, the model's performance was much stronger. NMSE was 0.003% and the FB error was 1%, while the FAC2 value was 1. This suggested a near-perfect alignment with the experimental and numerical data in literature.

The EPCM-T model demonstrated excellent accuracy in predicting tube temperatures. The maximum deviation between C_o and C_p was only 2.048. The model validated the strength in simulating this aspect of heat transfer, particularly for tube temperatures.
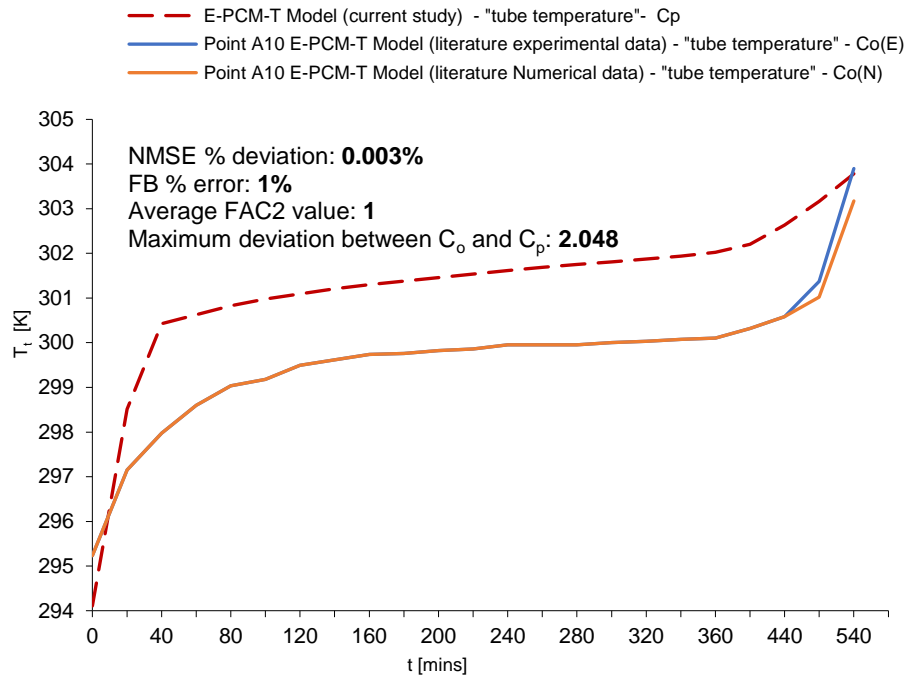
Figure 5.8. Comparison of tube temperature CFD predictions C_p in the current study, experimental observations C_o from the literature and CFD predictions C_{pL} in literature.

5.1.2.5 Air temperature validation results

As explained in section 5.1.2.2, there is a difference in initial air temperature in CFD model in the current study and that of Rouault et al.'s study [281]. Although this affected the absolute temperature values, as shown in Figure 5.9, it had minimal impact on the overall heat transfer trend over time, which was the primary focus of the validation. In CFD studies, especially when initial conditions differ slightly, it is common to prioritise matching the trends overachieving exact absolute values, as the model is typically more sensitive to relative changes in temperature rather than to the precise starting temperature.

The decision to initialise the CFD model at 35°C was intentional, aligning with the climate conditions relevant to this study. As shown in Figure 5.9, the CFD model closely followed the experimental data's trend, performing well in predicting the air temperature at P10. There was a slight over-prediction in the later stages of the simulation (after 300 minutes), but the error metrics

remained robust with an NMSE of 0.028%, an FB error of 1.6%, and a FAC2 value of 1, all indicating minimal deviation from the experimental data and confirming the model's reliability.

The maximum deviation between C_o and C_p was 5.639, slightly higher than the deviations observed for tube temperature and PCM liquid fraction. However, the deviation value still falls within acceptable limits for CFD simulations.

NMSE % deviation: **0.028%**
FB % error: **1.6%**
Average FAC2 value: **1**
Maximum deviation between C_o and C_p: **5.639**
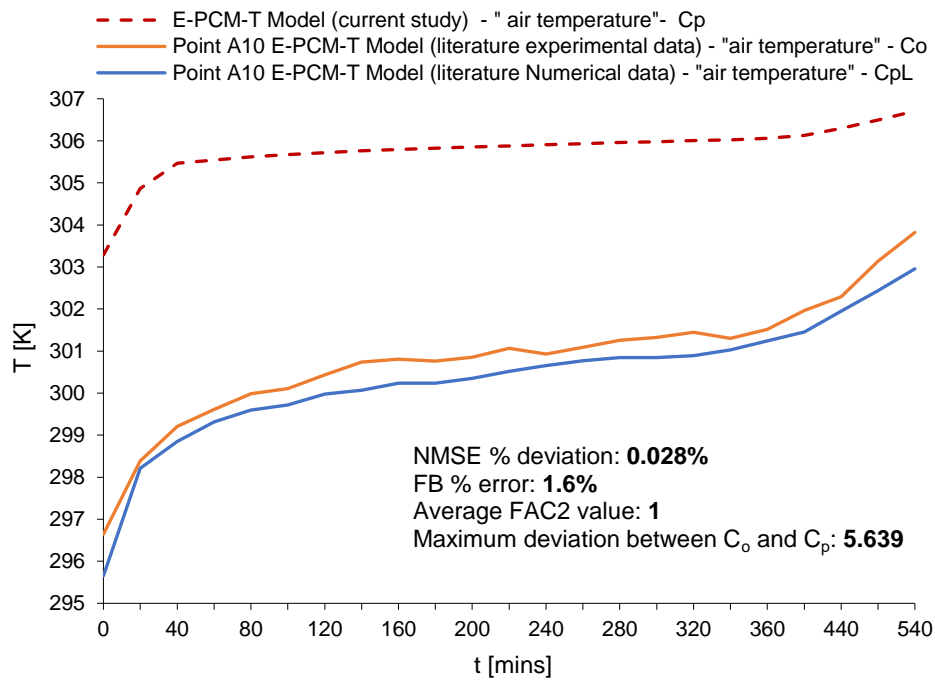
Figure 5.9. Comparison of air temperature CFD predictions C_p in the current study, experimental observations C_o from the literature and CFD predictions C_{pL} in literature.

Although the initial temperature difference was necessary to meet the objectives of this study, future work could focus on aligning the initial conditions more closely to minimise the slight over-prediction observed in the later stages. Overall, the results confirm the model's accuracy and reliability in predicting heat transfer trends under varying conditions.

5.1.2.6 PCM temperature validation results

The different initial air temperatures in both the CFD model and the experiment in the literature directly affected the starting PCM temperature. This difference in initial PCM temperature was observed in Figure 5.10.
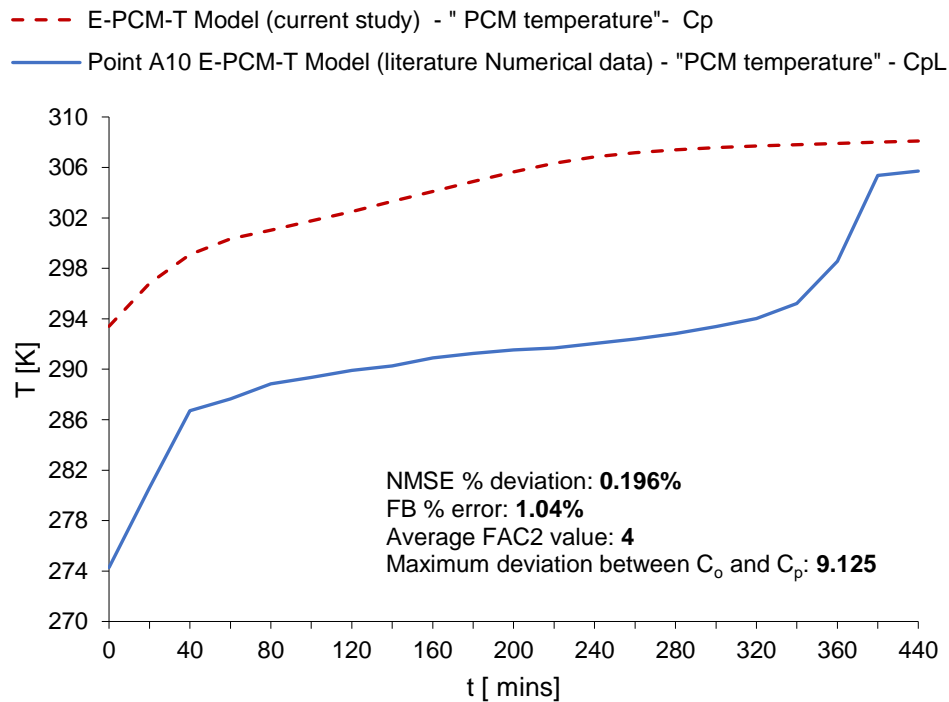
Figure 5.10. Comparison of PCM temperature CFD predictions C_p in the current study, experimental observations C_o from the literature and CFD predictions C_{pL} in literature.

The graph trend highlights the results from the PCM temperature validation, where some deviations were noted. The NMSE was 0.196%, and the FB error was 1.04%, while the FAC2 value of 4. These values indicated a considerable deviation from the experimental data, suggesting an overestimation of the PCM temperature by the CFD model. This may be due to the model's inability to simulate certain complex phase change dynamics during the simulation exercise. The maximum difference between C_o and C_p was 9.125.

The CFD model successfully captured the overall temperature trend but began to diverge from the experimental data after approximately 300 minutes. While

the predicted temperature steadied, the experimental data showed a gradual rise, suggesting that the model could benefit from further refinement to better capture the complex heat transfer dynamics in the later stages of phase change.

Overall, the EPCM-T heat transfer model demonstrated acceptable predictions, with minimal deviations from experimental data. While the PCM liquid fraction predictions were generally accurate, the largest errors occurred in PCM temperature predictions after 300 minutes. This was likely due to limitations in simulating long-term phase change dynamics. This could have stemmed from the model's inability to fully estimate the latent heat release or convective heat transfer between the PCM and encapsulating material during the phase change. Although the initial absolute temperatures varied, there was still a strong correlation between the experiment and the CFD trend. The validation results confirmed that the model was effective and reliable, with only minor discrepancies that did not significantly impact its overall accuracy.

5.1.3 Combined Model validation (EPCM-HMW + EPCM-T)
5.1.3.1 Overview of combined validation

The EPCM-HMW Case 1 which combines EPCM-T in its supply air streams, was validated against the airflow and heat transfer models discussed in sections 5.1.1 and 5.1.2. Case 1 model was validated because it served as a base model where Case 2 was developed from. This exercise was aimed to cross-verify the predicted data from the combined model with experimental measurements in literature. The goal was to ensure that the phase change behaviours and airflow dynamics of the overall EPCM-HMW model were accurately represented.

The validation compared the airflow and liquid fraction models of EPCM-HMW Case 1 with experimental data from Calautit et al. [357] and Rouault et al.'s experiment [281]. As shown in Table 5.3, the key metrics used to assess the model's accuracy were NMSE, FAC2, and FB. These metrics provided insights

into the model's performance in predicting airflow behaviour and liquid fraction profiles.

5.1.3.2 Results and comparison with EPCM-HMW CFD model data

From these results, the EPCM-HMW Case 1 model showed better alignment with the reference data (C_o) for both V_{supply} and V_{indoor}.

The results presented in Table 5.3 and Figures 5.11 and 5.12 provide a comprehensive overview of the performance of the EPCM-HMW Case 1 model. A comparison was conducted with the separate validation models previously discussed in sections 5.1.1 and 5.1.2. These results focus on airflow velocity at V_{supply} and V_{indoor}, as well as the liquid fraction of the PCM over time. This aim was to cross-validate the combined model with experimental data in literature. In Table 5.3, the NMSE, FB, and FAC2 values are used to assess the accuracy of the model predictions for V_{supply} and V_{indoor}, and the PCM liquid fraction.

Table 5.3. *Values of NMSE, FB and FAC2 statistical deviation calculations for* V_{supply}, V_{indoor} *and PCM liquid fraction, for EPCM-HMW Case 1*

Parameter	NMSE (%)	FB (%)	FAC2	Comments
V_{supply} (for Case 1)	0.500	0.667	1.000	Good agreement between observed and predicted values. The model showed acceptable accuracy.
V_{indoor} (for Case 1)	0.102	0.316	1.000	Very good accuracy with minimal bias and high consistency in predictions.
Liquid fraction (for Case 1)	0.026	0.103	0.813	good accuracy with a small error and relatively low bias.

For V_{supply}, the NMSE of 0.500 % and FB of 0.667 % indicate moderate deviations from experimental data, yet the FAC2 value of 1 suggested that the model still provided an acceptable level of accuracy. A similar trend was seen in V_{indoor}. A very strong accuracy was observed with NMSE at 0.102 % and FB at 0.316 %. FAC2 at the value of 1 indicated a good correlation. The results

for the liquid fraction exhibited minor error and low bias. The NMSE was 0.026 % and FB at 0.103 %. But the FAC2 value was at 0.813. This suggested minor deviations in the model accuracy.
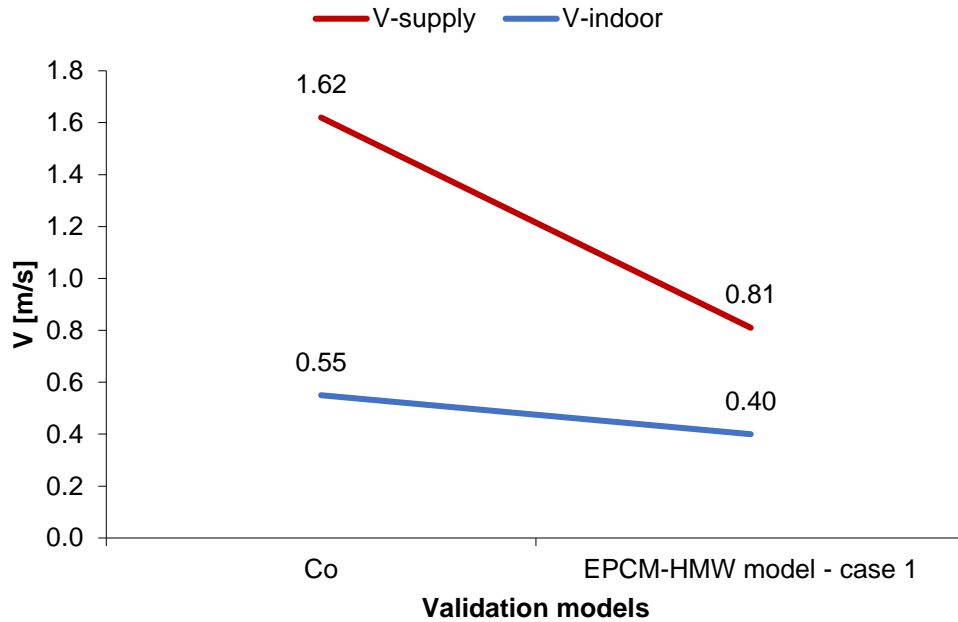
Figure 5.11. Comparison of air velocity results between experimental observations from the Calautit study at V_{supply} and V_{indoor} points with CFD predictions for Case 1 in the current study.

Figure 5.11 provides a comparison of the air velocities at V_{supply} and V_{indoor} between the experimental observations from Calautit et al. and the CFD predictions for EPCM-HMW Case 1. The predicted velocities showed lower values compared to the experimental values. V_{supply} decreased from 1.62 m/s to 0.81 m/s. V_{indoor} dropped from 0.55 m/s to 0.40 m/s. This discrepancy highlighted the need for further refinement of the airflow prediction in the CFD model, although the trends aligned reasonably well with the observed data.
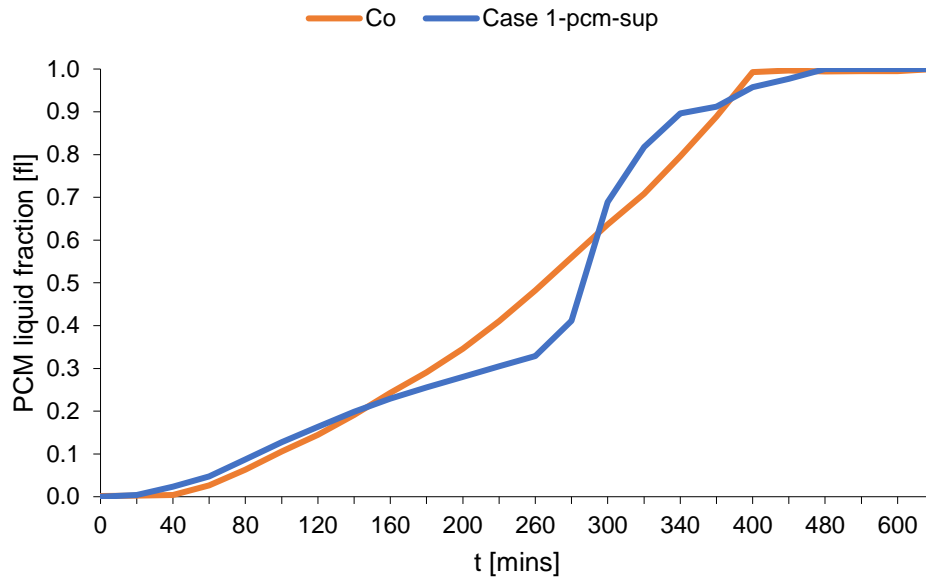
Figure 5.12. Comparison of the liquid fraction experimental observation results from Rouault et al.'s experiment and CFD results in Case 1 in the current study.

Figure 5.12 compares the PCM liquid fraction results between the experimental data from Rouault et al. [281] and the CFD predictions for Case 1. Both curves follow a similar trend. The CFD model correlated with the experimental data up until around 260 minutes into the simulation. However, the liquid fraction value in the CFD model was slightly overestimated after 260 minutes. Full melting was reached earlier than the than the experimental results. However, there was reasonably strong agreement between the two datasets. This indicated that the combined model effectively captured the PCM phase change process.

Comparing the data of the combined Case 1 model with the separate validation models analysed earlier, demonstrated improvements in terms of airflow and phase change predictions. Although there were still some deviations observed in the V_{supply} and liquid fraction predictions, the combined model showed superior accuracy and better overall consistency when validated against experimental data in literature.

5.1.4 Key observations

The section below summarises the key points deduced from the validation exercise.

5.1.4.1 Models' performance

EPCM-HMW windcatcher airflow model: The results for the validation of the windcatcher component showed good agreement between the CFD model predictions and experimental data obtained by Calautit et al. [357]. This suggested that the model captured the airflow dynamics within the system under typical operations. Moreover, based on this, the airflow rates across a wide range of wind conditions and directions were appropriately simulated in the study. This demonstrated the robustness of the CFD approach for this system. Although there was good overall agreement, small discrepancies were observed at higher wind speeds. This could be attributed to simplifications in the CFD model. For example, the simulation did not account for minor turbulence effects or interactions with surrounding environmental variables that were not included in the experimental setup.

E-PCM-T liquid fraction model: The E-PCM-T liquid fraction model showed reasonable accuracy when compared to the experimental data from Rouault et al. [281]. The model predicted phase-change behaviour well, especially in the mid-range temperature intervals. However, deviations were noted at extreme temperatures. This was identified when the CFD model tended to overpredict the phase change rate. This may have been a result of limitations in the material property data used in the simulations. Another cause of the overprediction could have been not considering complex heat transfer mechanisms like convection within the PCM module during the simulation. Additionally, the model's sensitivity to boundary conditions highlighted the importance of accurate parameter selection when applying this model in different environments.

5.1.4.2 Potential sources of error

Model simplifications: The simplification in the CFD model was one of the causes of the discrepancies between the CFD prediction data and experimental data. For instance, the airflow CFD model was assumed to be in a steady state. This was assumed in line with the CFD model in literature. However, a steady state does not usually fully capture the transient effects observed in air flow experiments. But transient data was in the literature, so steady state data provided was also used in the present study. Furthermore, all the E-PCM-T models including the combined models assumed idealised phase-change behaviour based on a constant thermal conductivity. However, in reality, these properties change with temperature and time, leading to variations in heat transfer rates that the model did not account for.

Experimental setup variations: The experimental setups described by Calautit et al. [357] and Rouault et al. [281] differed slightly from the conditions used in the CFD simulations. For example, the variability of ambient conditions was not adopted, rather constant values were used.

Numerical instabilities: Numerical instabilities and convergence issues, especially with higher wind speeds or more extreme temperature gradients, may have occurred for some of the CFD simulations in this research. The latter may have caused the overpredictions or underpredictions in the airflow rates and the liquid fraction values at the later part of the simulation exercise.

5.1.4.3 Model accuracy and limitations

The windcatcher component of the EPCM-HMW model demonstrated a high accuracy in predicting airflow behaviour at lower wind speeds. However, the model's performance declined when wind speeds increased. This may be because the model could not capture complex turbulence effects at those speeds.

The E-PCM-T liquid fraction model effectively captured the phase-change process over various conditions. However, in high temperatures, the

discrepancy in accuracy was obvious. This could be a result of the fact that natural convection and other complex material dynamics were not considered. The EPCM-T model and combined models also assumed even distribution of heat which may not occur in practical applications. Further refinement of the model will most likely improve the model's accuracy. But, despite these limitations., the models offered generally good performance predictions.

5.2 Chapter's concluding remarks

This chapter focused on validating the EPCM-HMW model by assessing the windcatcher airflow and E-PCM-T heat transfer models separately. The CFD simulation results to experimental data from Calautit et al. [357] and Rouault et al. [281] were compared with the CFD results of the current study. The validation exercise aimed to accurately predict the airflow dynamics and phase-change behaviours of the EPCM-HMW model. The airflow model shows a good correlation with the experimental data. There has been only minor over-prediction of air velocity observed at higher wind speeds.

Similarly, a high level of model accuracy was seen in the liquid fraction and temperature predictions for the EPCM-T heat transfer model. Although some deviations occurred during later phases of the phase-change process.

After validating the windcatcher and EPCM-T models separately, the combined validation of EPCM-HMW Case 1 was also validated. This showed good overall performance, though slight discrepancies were noted in the airflow and phase-change predictions. The study concluded that the EPCM-HMW and E-PCM-T system behaviour were adequately predicted. However, further model refinement will improve its predictions for both higher wind speeds and the heat transfer dynamics at later phases.

Overall, the models established a solid foundation for future research. However, there is a need to enhance the models to better capture dynamic factors that can improve model accuracy under extreme climate conditions.

Chapter 6

6 Economic feasibility of the EPCM-HMW system in the tropical savannah climate of Abuja, Nigeria

Due to frequent power outages, residential buildings in Abuja, Nigeria, rely heavily on diesel generators. The high energy cost, including the additional expense of running diesel generators, highlights the challenge of relying on AC for 24-hour home cooling. The EPCM-HMW system offers an opportunity to reduce energy consumption and operational costs in residential buildings in this region.

This chapter presents the economic feasibility of one unit of the EPCM-HMW system in Abuja, Nigeria, through a detailed cost-benefit analysis and a 20-year energy cost projection. The EPCM-HMW system was compared to a conventional AC system by analysing energy savings, operational costs, payback periods, and return on investment (ROI). The sustainability benefits of the EPCM-HMW system were also discussed in this chapter.

This economic feasibility study is required to establish the long-term viability of the EPCM-HMW system, in terms of energy cost reduction, mitigating greenhouse gas emissions, and addressing frequent power outages in Abuja. The study also serves as a foundation for calculating key economic metrics to adopt such sustainable cooling technologies in the region.

6.1 The energy landscape in Abuja

Since Abuja generally experiences high temperatures, demand for cooling is high. Several factors impact on the feasibility of using the EPCM-HMW system in Abuja's climate, they include:

i. **Expensive electricity prices:** The average cost of grid electricity is $0.27 per kWh (£0.22 / kWh).

ii. **Diesel generators:** Due to frequent power outages, backup diesel generators are often required, increasing the effective cost of energy to $0.48 per kWh (£0.39 / kWh).

iii. **High cooling demand:** Nearly year-round cooling is necessary, making energy-efficient solutions crucial.

6.2   Cost components of the EPCM-HMW system

6.2.1   Initial capital investment

The EPCM-HMW system's initial investment includes the following key components stated in Table 6.1.

Table 6.1. Initial Capital Cost Comparison

	Ductless split unit AC System		EPCM-HMW System	
	($)	(£)	($)	(£)
Ductless split AC unit (for 24,000 BTUs cooling capacity)	2,000.00	1,580.00	-	-
Windcatcher	-	-	1,880.00	1,450.00
Wall-mounted Solar Ventilation Fan	-	-	415.00	320.00
Encapsulated PCM Tubes (EPCM-T)	-	-	1, 177.00	930.00
Installation (Labor and Equipment)	450.00	350.00	650.00	500.00
Total Initial Cost	$ 2,450.00	£ 1,930.00	$ 4,122.00	£ 3,200.00

Based on the data presented in Table 6.1, local manufacturing of the EPCM-HMW system in Abuja has been estimated at $1,880.00 (£1,450.00).

Additionally, the estimated cost for the wall-mounted solar fan is $415.00 (£320.00). The cost of the EPCM-Ts is approximately $1,177.00 (£930.00). The installation cost of the EPCM-HMW system is estimated at $650.00 (£500.00) due to the specialised expertise required.

6.3 Comparison of energy use between the EPCM-HMW and traditional AC system

The energy consumption comparison presented provides an examination of each system's energy use patterns, operational efficiency, and reliance on external power between the EPCM-HMW system and a traditional AC system.

For this analysis, the ductless split AC unit has been selected as the representative system. The comparison covers both direct energy consumption (electricity used for operation) and indirect energy costs (reliance on diesel generators during power outages), providing a comprehensive view of the energy use profiles of these two systems.

6.3.1 Energy consumption estimation for a ductless split AC unit

As discussed in Section 1.1 of this thesis, traditional air conditioning (AC) systems are known for their high energy consumption. A typical single-household residential building in Abuja requires approximately 2.0 tons (24,000 BTUs) of cooling capacity of ductless split AC units.

Based on this, the AC energy consumption E_{AC} was estimated by equation 6.1:

$$E_{AC} = \frac{Cooling\ Load\ (BTU)}{EER} \times t_{operational} \times dy_{year} \qquad Equation\ 6.1$$

Where $t_{operational}$ represents AC operation as per the number of hours of operation per day. d_{year} is the number of AC operation days per year. EER (Energy Efficiency Ratio) of an AC system is 10-14 for ductless split AC

systems. For this analysis, EER is assumed to be 14. $t_{operational}$ is 8 hours per day. dy_{year} is 200 days of use per year for Abuja climate. Using equation 6.1, E_{AC} = 3,200 kWh/year.

6.3.2 The EPCM-HMW system energy consumption analysis

The EPCM-HMW system relies mainly on passive ventilative cooling. There is only very minimal solar energy use from a solar-powered fan during periods of low wind. The energy consumption of the fan can be calculated using equation 6.2, Although the energy that powers the fan is renewable. The power is accounted for as a worst-case scenario:

$$E_{EPCM-HMW} = P_{solarfan} \times t_{operational} \times dy_{year} \qquad Equation\ 6.2$$

Where $P_{solarfan}$ is the power rating solar ventilation fan, given as 100 W (0.1 kW). $t_{operational}$ represents number of hours the fan operates per day, which is assumed to be 8 hours/day. dy_{year} represents number of days the solar fan operates per year at 200 days/year. Based on this, the energy consumption of the EPCM-HMW system $E_{EPCM-HMW}$ = 160 kWh/year.

6.3.2.1 Energy efficiency improvement of the EPCM-HMW system

The energy efficiency improvement of the EPCM-HMW system compared to the ductless split AC unit can be calculated as:

$$Energy\ Efficiency\ Improvemnt\ (\%) = \left(1 - \frac{E_{EPCM-HMW}}{E_{AC}}\right) \times 100 \qquad Equation\ 6.3$$

Hence, the EPCM-HMW System consumed 95% less energy than a ductless split AC unit of the same cooling capacity, which is 20 times less energy consumption.

6.3.3 Cost of energy consumption in Abuja

The energy costs for both systems can be calculated by considering the energy use, electricity cost, rate of inflation and future discounting cost.

Electricity cost C_{elec} as of today is at \$0.22/kWh (£0.1758 kWh) at an inflation rate (r) of 34.01% (0.34). Future discount rate (d) is assumed to be 10% (0.10) for a 1–20-year (t) period.

Accordingly future electricity cost $C_{elec,t}$ is given by equation 6.4 as:

$$C_{elec,t} = C_{elec} \times (1+r)^t \qquad \text{Equation 6.4}$$

Discounted energy cost $PV_{cost,t}$ was calculated using equation 6.5.

$$PV_{cost,t} = \frac{C_{elec,t} \times E}{(1+d)^t} \qquad \text{Equation 6.5}$$

Where $PV_{cost,t}$ represents the present value of the energy cost in the year t, $C_{elec,t}$ is energy cost in year t. E represents the annual energy consumption.

Therefore, the total discounted cost of energy was calculated based on equation 6.6:

$$PV_{total} = \sum_{t=1}^{20} PV_{cost,t} \qquad \text{Equation 6.6}$$

The total discounted cost of energy per year for the ductless split AC unit was estimated at \$999.36/year (£804.48/year), whereas the EPCM-HMW system had a significantly lower discounted energy cost of \$499.68/year (£399.27/year). Over a 20-year period, the total discounted energy costs are approximately \$19,987.20 (£16,087.60) for the ductless split AC unit and \$9,993.63 (£7,981.47) for the EPCM-HMW system.

Table 6.2 shows the breakdown of the energy consumption and discounted energy costs of the two systems within the Abuja climate context.

Table 6.2. Annual energy consumption and cost comparison

System type	Average annual energy consumption	Annual energy cost	Average discounted energy cost/year	Total discounted energy cost over 20 years

	(kWh /year)	$/kWh	£/kWh	$/year	£/year	$	£
Ductless split AC unit	3,200	0.88	0.70	999.36	804.48	19,987.20	16,089.60
EPCM-HMW system (with solar fan)	160	0.68	0.55	499.68	399.27	9,993.63	7,981.47

6.3.4 Operational cost comparison

Power outages are frequent in Abuja. As a result, AC systems rely heavily on diesel generators. To calculate the operational cost of a ductless split AC unit, cost components such as the discounted cost of energy PV_{total}, backup generator fuel C_{fuel}, and maintenance costs C_{main}. This can be compared with the operational cost of the EPCM-HMW system. However, there are no backup generator fuel costs for the EPCM-HMW system because its operation is largely passive.

Cost of backup generator fuel: Assuming that the power outage rate O is 25% (0.25), and the daily generator runtime d is 4 hours. Daily fuel consumption F_{daily} was calculated based on equation 6.7.

$$F_{daily} = F_{hourly} \cdot d \qquad\qquad\qquad\qquad Equation\ 6.7$$

While the annual fuel consumption F_{annual} for 365 days Y, is derived by equation 6.8.

$$F_{annual} = F_{daily} \cdot Y \cdot O$$

Equation 6.8

Taking into consideration the inflation rate r_f is 10%, the future cost of fuel at an initial fuel price $P_{fuel,0}$ of \$1.50/litre (£1.20/litre) was derived by equation 6.9.

$$P_{fuel,t} = P_{fuel,0} \cdot \left(1 + r_f\right)^t$$

Equation 6.9

Assuming the discount rate is at 10%, the discounted fuel cost over T years is given by:

$$C_{fuel,t} = \frac{F_{annual} \cdot P_{fuel,t}}{(1+d)^t}$$

Equation 6.10

Where $P_{\text{fuel},t}$ represents future fuel price/litre at a discount rate d.

As a result, the total fuel cost over a 20-year period was derived by equation 6.11.

$$C_{fuel,total} = \sum_{t=1}^{20} C_{fuel,t}$$

Equation 6.11

The total fuel cost for a year averages at approximately \$410 / year (£328 / year). For a 20-year period, it is estimated to be a cumulative cost of \$8,200 (£ 6,456.20).

Maintenance costs: maintenance costs usually cover the cost of regular servicing, refrigerant replenishment of the ductless split AC unit, and occasional part repairs. However, the EPCM-HMW system has relatively lower maintenance costs due to fewer wear-and-tear issues with the windcatcher and PCM tubes. To calculate the annual maintenance cost $C_{maintenance}$, maintenance cost inflation rate r_m, discount rate d and time were considered for over the period of 20 years.

$$\text{Total Maintenance cost} = \sum_{t=1}^{20} \frac{\text{Maintenance cost in Year } t}{(1+d)^t} \qquad \text{Equation 6.12}$$

$$\text{Where, Maintenance Cost in Year } t = C_{maintenance} \; x \, (1 + r_m)^t \; \text{Equation 6.13}$$

It was assumed that the inflation rate for the ductless split AC unit was at 3%, while that of the EPCM-HMW system was higher, set at 5%. This increment in the inflation rate was because the EPCM-HMW system is a newly introduced system to the market and therefore has a more unpredictable inflation projection.

The total annual maintenance cost for the ductless split AC unit was calculated at an average of $412 / year (£329.50 / year). The maintenance cost for a year for the EPCM-HMW system was calculated to be $105 (£83.86 / year).

At a future discount rate of 10% over the 20-year period, it is estimated that $4,305.59 (£3,444.48) will be required to maintain the ductless split AC unit and $1,271.77 (£1,017.42) for the EPCM-HMW system.

It is assumed that the EPCM-T system will be replaced once over a 20-year period. At a discount rate of 10% and an assumed inflation rate of 5%, the replacement cost is estimated to be $4,885.25 (£3,933.60).

Table 6.3 provides a breakdown of the annual operational cost including the maintenance cost elements for the ductless split AC unit and the EPCM-HMW system.

Table 6.3. Total annual operating cost comparison

Cost Component	Ductless split AC unit ($)	Ductless split AC unit (£)	EPCM-HMW System ($)	EPCM-HMW System (£)
Generator Fuel Cost / Year	410	328.00	-	-
Total Fuel Cost (20 Years)	8,200	6,560.00	-	-
Maintenance system Cost / Year	412	329.50	105	83.86

Maintenance system Cost (20 Years)	4,305.59	3,444.48	1,271.77	1,017.42
EPCM-T replacement Cost (20 Years)	-	-	4,885.25	3,933.60
Total Annual Operating Cost	822	657.50	105	83.86
Cumulative Operating Cost (20 Years)	12,505.59	10,004.48	6,157.02	4,951.02

6.4 Energy savings (with discounted costs) and payback period

6.4.1 Energy savings

Based on the calculated energy costs with the consideration of inflation and future discounted rates, the annual energy savings projected for EPCM-HMW system was calculated using equation 6.13:

$$Annual\ energy\ savings/year = C_{energy,AC} - C_{energy,EPCM-HMW} \quad Equation\ 6.13$$

Where $C_{energy,AC}$ is the energy cost for the AC, while $C_{energy,EPCM-HMW}$ is the energy cost for the EPCM-HMW system.

Based on the equation 6.13, the calculated annual energy cost savings is estimated as \$2,707.20 (£2,152). While this was further estimated to amount to a \$54,144 (£43,040) total energy cost savings over a 20-year period.

6.4.2 Payback Period

The payback period was calculated based on a 20-year period using equation 6.14.

$$Payback\ period = \frac{C_{T(EPCMHMW)}}{annual\ energy\ savings/year} \quad Equation\ 6.14$$

$C_{T(EPCMHMW)}$ represents the total cost of investment for the EPCM-HMW system, which includes the energy cost over the 20-year period, calculated to be \$22,307.67 (£17,957.47). This total also encompasses components such

as the cumulative maintenance cost for 20 years, the replacement cost of the EPCM-T, and the operational cost of the system during that period. Based on the calculated total cost of the EPCM-HMW system and the projected energy savings, the payback period is estimated to be approximately 8.24 years.

The net savings from choosing the EPCM-HMW system over the ductless split AC unit is approximated to be $23,690.71 (£19,070.81), as determined using Equation 6.15.

$$Net\ savings = \ C_{T(AC)} - C_{T(EPCM-HMW)} \qquad\qquad Equation\ 6.15$$

$C_{T(AC)}$ represents the total cost of investment for the ductless split AC unit over a 20-year period, estimated to be $45,998.38 (£36,698.08). $C_{T(EPCM-HMW)}$ represents the total cost of investment for the EPCM-HMW system, projected at $22,307.67 (£17,883.51).

Using Equation 6.16, the return on investment (ROI) over the 20-year period was calculated to be 106.2%, demonstrating that the EPCM-HMW system provides significant long-term financial benefits.

$$ROI = \frac{Net\ savings}{C_{T(EPCMHMW)}} \times 100 \qquad\qquad Equation\ 6.16$$

Table 6.4 summarises the components that accumulated towards this ROI value.

Table 6.4. Return on investment after 20 years.

Parameter	Value ($)	Value (£)
Energy cost savings / year	2,707.2	2,152
Energy cost savings over 20 years	54,144	43,040
Total cost of the ductless split AC unit over a 20-year period	45,998.38	36,698.08
Total cost of the EPCM-HMW system over a 20-year period	22,307.67	17,883.51
20-year payback period	8.24 years	
ROI	106.2 %	

6.5 Environmental and social benefits of the EPCM-HMW system

It is clear that the EPCM-HMW system can significantly reduce energy consumption, which in turn helps lower CO_2 emissions. Implementing EPCM-HMW system as a sustainable ventilative cooling system for residential buildings align with Nigeria's commitments under the Paris Agreement. Hence, residential buildings can reduce their reliance on diesel generators during power outages. Also, carbon footprint of cooling in Abuja and other similar tropical savannah climate regions can be lowered. Additionally, the passive ventilation attribute of the EPCM-HMW system can help reduce the risks associated with SBS.

6.6 Chapter's concluding remarks

Chapter 6 presented a detailed analysis of the economic feasibility of implementing the EPCM-HMW system for ventilative cooling in a typical residential space located in Abuja, Nigeria. The chapter compared the EPCM-HMW system with a conventional ductless split AC unit by assessing the energy savings of both systems, their operational costs, payback periods, and return on investment (ROI) over a 20-year period.

The chapter first explained the energy landscape in Abuja, a city located in a tropical savannah climate region. It identified high electricity costs, reliance on diesel generators due to frequent power outages, and high cooling demand as major factors necessitating the adoption of energy-efficient systems like the EPCM-HMW system in such climates.

The economic feasibility analysis conducted established the following conclusions:

   i. **Initial capital investment:** The total initial cost of the EPCM-HMW system was calculated at $4,122 (£3,200), which is significantly higher than the ductless split AC unit at $2,450 (£1,930). The higher initial cost

of the EPCM-HMW system is attributed to the high initial cost of components such as the windcatcher, solar ventilation fan, encapsulated PCM tubes, and the specialised installation process. However, this higher upfront investment is offset by substantial long-term savings, making the EPCM-HMW system a more economically viable option over time.

ii. **Energy consumption and cost comparison:** The energy consumption of both systems was analysed. The ductless split AC unit consumed 3,200 kWh/year based on its cooling capacity of 24,000 BTUs. The EPCM-HMW system which relied more on passive ventilation using minimal solar energy, consumed only 160 kWh/year. This resulted in a 95% less energy consumption by the EPCM-HMW system compared to the ductless split AC unit. This equates to approximately 20 times less energy consumption.

iii. **Operational cost comparison:** The operational costs of the ductless split AC unit was impacted by the frequent power outages in Abuja. As a result, it relied heavily on backup diesel generators, adding significant fuel and maintenance costs to its overall operational costs. However, the EPCM-HMW system, did not incur fuel costs as it operates largely passively. The cumulative operating cost for the ductless split AC unit over 20 years was calculated to be $12,505.59 (£10,004.48), while the EPCM-HMW system's total operating cost was much lower at $6,157.02 (£4,951.02).

iv. **Energy savings and payback period:** The annual energy savings of the EPCM-HMW system were calculated to be $2,707.20 (£2,152), amounting to $54,144 (£43,040) over 20 years. Hence, payback was estimated at 8.24 years, achieving a net savings of $23,690.71 (£19,070.81) over the 20-year period.

v. **Return on investment (ROI):** A 106.2% ROI was estimated which suggested that the EPCM-HMW system better financial return in the long-run.

vi. **Environmental and social benefits:** The EPCM-HMW system reduced energy consumption and carbon emissions, supporting

Nigeria's climate goals under the Paris Agreement. By reducing reliance on diesel generators, it lowers Abuja's cooling-related carbon footprint. Additionally, its passive ventilation enhances indoor air quality, reducing SBS risks and improving occupant health.

The findings revealed that although the EPCM-HMW system requires a higher upfront investment, the short payback period of just 8.24 years offers long-term financial viability. With this, the EPCM-HMW system is a practical alternative to the use of ductless split AC unit of similar cooling capacity. In conclusion, the system's environmental benefits, such as reducing greenhouse gas emissions and reliance on diesel generators, further support its long-term viability as a sustainable cooling solution in the region.

Chapter 7

7 Conclusions and future works

7.1 Conclusions

Literature revealed the notable potential to implement PCM-integrated solar-fan-assisted multi-directional windcatchers in sub-Saharan African tropical savannah climates. This study presented the development and evaluation of an encapsulated Phase Change Material (PCM) integrated hybrid multi-directional windcatcher (EPCM-HMW) system. The system combined a hybrid solar fan-assisted multi-directional windcatcher with EPCM-Ts. The EPCM-HMW system can assist in improving indoor cooling, ventilation and temperature stabilisation in such climates. In this study, the assessment of the EPCM-HMW system and its effectiveness in achieving cooling and stabilisation of air temperature without compromising the windcatcher's ventilation efficiency was presented. The investigations were conducted through simulations and theoretical analysis and validated with experimental data from existing literature.

The key findings and conclusions drawn from the study are as follows. In addition, the study's implications, limitations, and recommended future works are also outlined in this chapter.

7.1.1 Cooling performance:

The EPCM-HMW system demonstrated robust cooling performance, using both passive cooling and PCM TES to regulate indoor temperatures effectively. The EPCM-HMW system achieved significant indoor air temperature reductions, demonstrating its effectiveness in managing cooling loads in tropical savannah climates:

i. **At low wind speed conditions:** In typical low wind conditions of 1.88 m/s, the EPCM-HMW system reduced indoor air temperatures from an outdoor peak of 308.15 K (35 °C) up to 306.97 K (33.82 °C) to 307.07

K (33.92 °C). This significant reduction was primarily attributed to the PCM's heat absorption during its charging cycle from solid to liquid, stabilising the supply air temperature.

ii. **At moderate wind speed conditions:** At higher wind speeds of up to 3 m/s, the system maintained a temperature reduction of 9% (approximately 3.15°C), reducing indoor air temperatures to 305 K (31.85 °C). This ability to maintain cooling performance under different wind speeds highlights the system's adaptability to fluctuating wind conditions

iii. **Overall cooling capacity:** With outdoor temperatures at a peak of 35°C, the EPCM-HMW system reduced indoor air temperatures to between 305 K (31.85 °C) and 307.07 K (33.92 °C). This cooling was sustained for 5 hours (20,000 s).

iv. **Role of PCM and solar fan assistance:** The solar-powered axial fan enhanced cooling by maintaining continuous airflow across the PCM tubes. The fan provided an additional 370 L/s of airflow, ensuring the PCM tubes remained effective in absorbing and releasing heat.

7.1.2 Ventilation performance:

The hybrid ventilation capabilities of the EPCM-HMW system improved indoor air quality by increasing the outdoor-to-indoor air exchange, particularly at low wind speeds:

i. **Airflow rates:** At low wind speeds of 1.88 m/s, the system maintained an airflow rate of 140.86 L/s, which was sufficient to ventilate a room designed for 14-17 occupants, meeting ASHRAE standards for ventilation. A low-pressure drop of only 10.02–10.31 Pa was also observed.

ii. **Hybrid ventilation mode:** The system's fan-assisted mode contributed to the continuous indoor air exchange. At 10Pa pressure jump, it provided an additional 370L/s airflow throughout the simulation exercise.

7.1.3 Thermal storage performance:

The integration of PCM significantly enhanced the system's thermal storage capacity, allowing it to absorb and release heat as needed to maintain indoor temperature stability:

i. **Temperature stabilisation:** The PCM used in the system operated within the phase change temperature range of 27°C to 30°C, ideal for tropical savannah climates. Very minimal fluctuation occurred, within ±2°C, as PCM charging occurred. This implied that effective temperature stabilisation was maintained up to 20,000s with slight fluctuation occurring from 20,000 – 30,000s during the duration of the PCM charging cycle. The results from the study suggested both EPCM-HMW Cases 1 and 2, the air supply offered by the system achieved temperature stabilisation for approximately 5 hours. However, cooling (indoor temperature reduction) continued for 7 hours. This implied that cool air was maintained for the active daytime hours.

ii. **Impact of EPCM-T arrangement on thermal performance:** Two primary configurations of PCM tube arrangements were evaluated:
   EPCM-HMW Case 1: All 48 PCM tubes were placed in the supply air stream, maximising the cooling effect at the air intake. This configuration resulted in a 1.08 ⁻ 1.18°C reduction in supply air temperature at low wind speeds.
   EPCM-HMW Case 2: The PCM tubes were distributed across all air streams (supply and exhaust), resulting in a more balanced but slightly lower peak cooling effect, reducing supply air temperatures by up to 3.15°C. This setup is ideal for applications requiring even temperature distribution.

iii. **Material properties:** Considering the need to achieve prolonged cooling and more stable temperature control, it was observed that the aluminium-encapsulated EPCM-T was more beneficial to the EPCM-HMW system than the copper-encapsulated ones. Also, The study concluded that the rectangular-shaped EPCM-T profile design was

more suitable for the EPCM-HMW system than the cylindrical one. This is because the rectangular-shaped EPCM-T offered superior long-term cooling stability and energy storage.

7.1.4 Implications of the results

The results of this research hold several important implications:

i. **Energy efficiency and sustainability:** The EPCM-HMW system offers a significant reduction in energy consumption for cooling, reducing the need for conventional AC. The fact that the EPCM-HMW system is 20 times lower than a conventional ductless split AC unit in energy consumption (from 3,200 kWh/year to 160 kWh/year) demonstrates its potential for large-scale application, particularly in regions with unreliable electricity grids.

ii. **Indoor comfort and health:** By stabilising indoor temperatures and improving ventilation rates, the system enhances thermal comfort while promoting better indoor air quality. This is particularly important in reducing the risk of health issues related to poor air quality, such as SBS.

iii. **Economic feasibility:** Despite a higher initial installation cost of $4,122 (£3,200) compared to $2,450 (£1,930) for a conventional ductless split AC unit, the EPCM-HMW system offered substantial long-term financial benefits. With annual energy cost savings of $2,707.20 (£2,152) and total savings of $54,144 (£43,040) over 20 years, the system achieved a net savings of $23,690.71 (£19,070.81) and a payback period of 8.24 years. Over the same 20-year period, the ROI value was estimated at a high value of 106.2%.

7.1.5 Contribution to knowledge

i. A novel design of the EPCM-HMW system offers a significant contribution to existing hybrid windcatcher designs.

ii. The outcomes of the EPCM-HMW study offer valuable scientific CFD datasets that demonstrate how cooling, ventilation, and thermal storage can be achieved together in similar systems. These findings provide a strong foundation for other researchers and practitioners to build upon.

iii. The research bridges an important research gap that has been that has been largely overlooked. The study identified the lack of hybrid windcatcher studies in tropical savannah climates. The current research highlights that windcatcher systems can work effectively in residential buildings in in tropical savannah climates. It also opens up further opportunities for practical implementation in similar regions.

iv. The study also emphasises the low operational costs of the EPCM-HMW system, showing how such hybrid windcatchers can be a viable option for low-income regions with energy challenges. This makes sustainable cooling and ventilation solutions more accessible to those who need them most.

7.1.6 Limitations of the study

Although the results derived from the study have revealed the potential of the system, there are a few limitations to this study:

i. The study used simplified CFD models. This was due to the computational expense of the simulations. Each simulation took weeks to complete, and this impacted the number of cases investigated and the need to simplify the CFD model. To achieve real-world application, more advanced modelling is required.

ii. The system's performance was based on numerical simulations and validated with experimental data in literature. Real-world field trials are necessary to fully validate the system's performance and assess operational challenges such as PCM degradation over time.

iii. The encapsulation of the PCM was not studied in-depth, due to the simplification of the model.

iv. While this study did not address the potential issue of temperature stagnation and heat accumulation at midday, it is recognised as a

possible limitation. Hence, solutions to mitigate this issue and optimise the performance of the EPCM-HMW system are suggested as part of future works.

7.2 Future works

Further research is required to refine and expand the findings of this study:

i. **Refinement of CFD models:** Future research should incorporate transient conditions and temperature-dependent material properties to improve the accuracy of CFD models.

ii. **Field testing and further validation:** Extensive field trials in diverse climatic conditions are needed to further validate the system's real-world performance, including long-term durability and maintenance requirements.

iii. **Exploration of advanced PCM materials:** Future studies should explore advanced PCM materials and PCM with different melting pints or PCMs with higher thermal conductivity and storage capacity to further enhance the system's efficiency.

iv. **Further in-depth study on the PCM encapsulation**: More in-depth study on how to improve the effectiveness of the PCM thermal performance should be considered in future studies.

v. **Future studies on the application of the EPCM-HMW System in other types of different buildings:** Aside from residential buildings, the system could be particularly beneficial in office buildings with high internal heat gains, educational institutions that require temperature stability for learning environments, and hospitals, where precise temperature control is essential. Exploring the potential for large-scale implementation across various building types would be valuable to deepen the study further.

vi. **Cooling performance optimisation:** While the EPCM-HMW system demonstrated substantial energy savings, the observed cooling

capacity was still relatively modest. Future research should focus on optimising the system's cooling performance. This can include material improvements in the TES components.

vii. **Mitigating EPCM temperature stagnation at midday hours:** To address the EPCM temperature stagnation at midday, future work should explore integrating higher-capacity solar-powered ventilation fans and further optimising the windcatcher design to improve airflow and enhance heat extraction. PCMs with higher thermal conductivity could also be explored.

Overall, the EPCM-HMW system presented a highly effective solution for passive cooling, ventilation, and TES in tropical savannah climates. Its ability to reduce and stabilise indoor temperatures, as well as improve indoor air quality and save energy makes it a viable alternative to conventional AC systems. With further research and field validation, the system holds the potential to revolutionise sustainable cooling in tropical savannah climate regions, contributing to both environmental and economical benefits.

References

[1]   GISTEMP Team, "GISS Surface Temperature Analysis (GISTEMP), version 4," 2022. Accessed: Jul. 15, 2022. [Online]. Available: https://data.giss.nasa.gov/gistemp/.

[2]   J. Hansen, R. Ruedy, M. Sato, and K. Lo, "Global surface temperature change," *Reviews of Geophysics*, vol. 48, no. 4, Dec. 2010, doi: 10.1029/2010RG000345.

[3]   N. , G. S. J. H. M. M. A. P. R. R. and D. Z. Lenssen, "Improvements in the GISTEMP uncertainty model," *J. Geophys. Res. Atmos.,* vol. 124, no. 12, pp. 6307–6326, 2019, doi: 10.1029/2018JD029522.

[4]   IPCC, "IPCC Sixth Assessment Report 2022: Working Group III: Mitigation of Climate Change - Chapter 9: Buildings," *Cambridge University Press*, 2022.

[5]   UN Environment Programme and Global Alliance for Buildings and Construction, "2021 Global Status Report for Buildings and Construction towards a zero-emissions, efficient and resilient buildings and construction sector," 2021. [Online]. Available: www.globalabc.org.

[6]   M. Santamouris, "Cooling the buildings – past, present and future," *Energy Build*, vol. 128, pp. 617–638, Sep. 2016, doi: 10.1016/j.enbuild.2016.07.034.

[7]   L. D. D. Harvey, K. Korytarova, O. Lucon, and V. Roshchanka, "Construction of a global disaggregated dataset of building energy use and floor area in 2010," *Energy Build*, vol. 76, pp. 488–496, 2014.

[8]   IEA, "Africa Energy Outlook 2019," World Energy Outlook special report, Paris, 2019. [Online]. Available: https://www.iea.org/reports/africa-energy-outlook-2019

[9]   G. Falchetta and M. N. Mistry, "The role of residential air circulation and cooling demand for electrification planning: Implications of climate change in sub-Saharan Africa," *Energy Econ*, vol. 99, 2021, doi: 10.1016/j.eneco.2021.105307.

[10]   M. A. A. Oluwafemi K. Akande and L. N. for C. and E. U. in Buildings, "Indoor Thermal Comfort for Residential Buildings in Hot-Dry climate of Nigeria," in *Adapting to Change: New Thinking on Comfort*, Cumberland Lodge, Windsor, UK, 2010.

[11]   S. O. Oyedepo, "Efficient energy utilization as a tool for sustainable development in Nigeria," *International Journal of Energy and Environmental Engineering - Springer*, 2012.

[12]   J. C. Menaut and J. Cesar, "The structure and dynamics of a West African savanna," in *Ecology of tropical savannas*, Springer, 1982, pp. 80–100.

[13]   IEA, "Share of population living in a hot climate and air conditioner ownership by selected region, 2020." [Online]. Available: https://www.iea.org/data-and-statistics/charts/share-of-population-living-in-a-hot-climate-and-air-conditioner-ownership-by-selected-region-2020

[14]   T. Randazzo, E. De Cian, and M. N. Mistry, "Air conditioning and electricity expenditure: The role of climate in temperate countries," *Econ Model*, vol. 90, pp. 273–287, Aug. 2020, doi: 10.1016/J.ECONMOD.2020.05.001.

[15]   J. Woods *et al.*, "Humidity's impact on greenhouse gas emissions from air conditioning," *Joule*, vol. 6, no. 4, pp. 726–741, Apr. 2022, doi: 10.1016/J.JOULE.2022.02.013.

[16]   IEA, "Buildings: Tracking Report," Sep. 2022.

[17]   A. Real, V. García, L. Domenech, J. Renau, N. Montés, and F. Sánchez, "Improvement of a heat pump based HVAC system with PCM thermal storage for cold accumulation and heat dissipation," *Energy Build*, vol. 83, pp. 108–116, 2014.

[18]   T. Deruelle and I. Engeli, "The COVID-19 crisis and the rise of the European Centre for Disease Prevention and Control (ECDC)," *West Eur Polit*, vol. 44, no. 5–6, pp. 1376–1400, 2021, doi: 10.1080/01402382.2021.1930426.

[19]   A. Elzaidabi, S. Omer, and S. Riffat, "A novel combined wind catcher psychometric energy core indirect evaporative cooling system," *International Journal of Low-Carbon Technologies*, vol. 5, no. 2, 2010, doi: 10.1093/ijlct/ctq008.

[20]   J. Sundell *et al.*, "Ventilation rates and health: Multidisciplinary review of the scientific literature," *Indoor Air*, vol. 21, no. 3, pp. 191–204, 2011, doi: 10.1111/j.1600-0668.2010.00703.x.

[21]   J. Drury, M. B. Rogers, T. M. Marteau, L. Yardley, S. Reicher, and C. Stott, "Re-opening live events and large venues after Covid-19 'lockdown': Behavioural risks and their mitigations," Jul. 01, 2021, *Elsevier B.V.* doi: 10.1016/j.ssci.2021.105243.

[22]   T. Ahmed, P. Kumar, and L. Mottet, "Natural ventilation in warm climates: The challenges of thermal comfort, heatwave resilience and indoor air quality," *Renewable and sustainable energy reviews*, vol. 138, p. 110669, 2021, doi: https://doi.org/10.1016/j.rser.2020.110669.

[23]   S. C. Sekhar and S. E. Goh, "Thermal comfort and IAQ characteristics of naturally/mechanically ventilated and air-conditioned bedrooms in a hot and humid climate," *Build Environ*, vol. 46, no. 10, 2011, doi: 10.1016/j.buildenv.2011.03.012.

[24] P. Nejat, J. K. Calautit, Y. Fekri, M. Sheikhshahrokhdehkordi, H. Alsaad, and C. Voelker, "Influence of terrain and atmospheric boundary layer on the ventilation and thermal comfort performance of windcatchers," *Journal of Building Engineering*, vol. 73, p. 106791, Aug. 2023, doi: 10.1016/J.JOBE.2023.106791.

[25] F. Jomehzadeh, H. M. Hussen, J. K. Calautit, P. Nejat, and M. S. Ferwati, "Natural ventilation by windcatcher (Badgir): A review on the impacts of geometry, microclimate and macroclimate," 2020. doi: 10.1016/j.enbuild.2020.110396.

[26] N. Arias-Jiménez, M. Trebilcock-Kelly, A. B. Moreno, and R. F. San-Martín, "Wind towers: Potential evaluation of natural ventilation in housing," *Arquiteturarevista*, vol. 17, no. 2, pp. 198–218, 2021, doi: 10.4013/arq.2021.172.02.

[27] D. Jafari, A. Shateri, and A. Ahmadi Nadooshan, "Experimental and numerical study of natural ventilation in four-sided wind tower traps," *Energy Equipment and Systems*, vol. 6, no. 2, pp. 167–179, 2018.

[28] M. Sadeghi, G. Wood, B. Samali, and R. de Dear, "Effects of urban context on the indoor thermal comfort performance of windcatchers in a residential setting," *Energy Build*, vol. 219, Jul. 2020, doi: 10.1016/j.enbuild.2020.110010.

[29] L. Li and C. M. Mak, "The assessment of the performance of a windcatcher system using computational fluid dynamics," *Build Environ*, vol. 42, no. 3, pp. 1135–1141, 2007, doi: https://doi.org/10.1016/j.buildenv.2005.12.015.

[30] S. Duan, C. Jing, and E. Long, "Transient flows in displacement ventilation enhanced by solar chimney and fan," *Energy Build*, vol. 103, pp. 124–130, Sep. 2015, doi: 10.1016/J.ENBUILD.2015.06.006.

[31] H. Zhang *et al.*, "A critical review of combined natural ventilation techniques in sustainable buildings," *Renewable and Sustainable Energy Reviews*, vol. 141, p. 110795, 2021.

[32] S. Zafarmandi and M. Mahdavinejad, "Technology of Modern Windcatchers: A Review," *International Journal of Architectural Engineering & Urban Planning*, vol. 31, no. 3, pp. 1–11, 2021, doi: 10.22068/ijaup.31.3.549.

[33] P. K. Sangdeh and N. Nasrollahi, "Windcatchers and their applications in contemporary architecture," *Energy and Built Environment*, vol. 3, no. 1, pp. 56–72, Jan. 2022, doi: 10.1016/J.ENBENV.2020.10.005.

[34] B. R. Hughes, J. K. Calautit, and S. A. Ghani, "The development of commercial wind towers for natural ventilation: A review," *Appl Energy*, vol. 92, pp. 606–627, 2012.

[35] J. K. Calautit, B. R. Hughes, and D. S. Nasir, "Climatic analysis of a passive cooling technology for the built environment in hot countries," *Appl Energy*, vol. 186, 2017, doi: 10.1016/j.apenergy.2016.05.096.

[36] J. K. Calautit, P. W. Tien, S. Wei, K. Calautit, and B. Hughes, "Numerical and experimental investigation of the indoor air quality and thermal comfort performance of a low energy cooling windcatcher with heat pipes and extended surfaces," *Renew Energy*, vol. 145, 2020, doi: 10.1016/j.renene.2019.06.040.

[37] S. Jafari and V. Kalantar, "Numerical simulation of natural ventilation with passive cooling by diagonal solar chimneys and windcatcher and water spray system in a hot and dry climate," *Energy Build*, vol. 256, p. 111714, Feb. 2022, doi: 10.1016/J.ENBUILD.2021.111714.

[38] M. Kahkzand, B. Deljouiee, S. Chahardoli, and M. Siavashi, "Radiative cooling ventilation improvement using an integrated system of

windcatcher and solar chimney," *Journal of Building Engineering*, p. 108409, Jan. 2024, doi: 10.1016/J.JOBE.2023.108409.

[39] D. O'Connor, J. K. Calautit, and B. R. Hughes, "A novel design of a desiccant rotary wheel for passive ventilation applications," *Appl Energy*, vol. 179, pp. 99–109, 2016, doi: 10.1016/j.apenergy.2016.06.029.

[40] H. Mahon, D. Friedrich, and B. Hughes, "Wind tunnel test and numerical study of a multi-sided wind tower with horizontal heat pipes," *Energy*, vol. 260, p. 125118, Dec. 2022, doi: 10.1016/J.ENERGY.2022.125118.

[41] K. Pelletier, C. Wood, J. Calautit, and Y. Wu, "The viability of double-skin façade systems in the 21st century: A systematic review and meta-analysis of the nexus of factors affecting ventilation and thermal performance, and building integration," *Build Environ*, vol. 228, p. 109870, Jan. 2023, doi: 10.1016/J.BUILDENV.2022.109870.

[42] K. Pelletier and J. Calautit, "Analysis of the performance of an integrated multistage helical coil heat transfer device and passive cooling windcatcher for buildings in hot climates," *Journal of Building Engineering*, vol. 48, p. 103899, May 2022, doi: 10.1016/J.JOBE.2021.103899.

[43] J. K. Calautit, A. I. Aquino, S. Shahzad, D. S. N. M. Nasir, and B. R. Hughes, "Thermal Comfort and Indoor air Quality Analysis of a Low-energy Cooling Windcatcher," in *Energy Procedia*, 2017. doi: 10.1016/j.egypro.2017.03.634.

[44] J. C. Menaut and J. Cesar, "The structure and dynamics of a West African savanna," in *Ecology of tropical savannas*, Springer, 1982, pp. 80–100.

[45] UN-Water/Africa, Economic Commission for Africa, African Union, and African Development Bank, "The Africa Water Vision for 2025: Equitable and Sustainable Use of Water for Socioeconomic Development," 2023.

[46]   S. W. Sharshir *et al.*, "Thermal energy storage using phase change materials in building applications: A review of the recent development," 2023. doi: 10.1016/j.enbuild.2023.112908.

[47]   A. H. Mosaffa, L. G. Farshi, C. A. I. Ferreira, and Ma. Rosen, "Energy and exergy evaluation of a multiple-PCM thermal storage unit for free cooling applications," *Renew Energy*, vol. 68, pp. 452–458, 2014.

[48]   S. A. Khawaja and S. A. Memon, "Novel indicators to evaluate PCM performance under different ventilation strategies by considering the impact of climate change," *Journal of Building Engineering*, vol. 74, p. 106848, 2023, doi: https://doi.org/10.1016/j.jobe.2023.106848.

[49]   L. Seidabadi, H. Ghadamian, and M. Aminy, "A novel integration of PCM with wind-catcher skin material in order to increase heat transfer rate," *International Journal of Renewable Energy Development*, vol. 8, no. 1, pp. 1–6, Feb. 2019, doi: 10.14710/ijred.8.1.1-6.

[50]   P. Abdo, B. P. Huynh, A. Braytee, and R. Taghipour, "An experimental investigation of the thermal effect due to discharging of phase change material in a room fitted with a windcatcher," *Sustain Cities Soc*, vol. 61, p. 102277, 2020, doi: https://doi.org/10.1016/j.scs.2020.102277.

[51]   P. Gadhave, F. Pathan, S. Kore, and C. Prabhune, "Comprehensive review of phase change material based latent heat thermal energy storage system," 2022. doi: 10.1080/01430750.2021.1873848.

[52]   P. Abdo, B. Phuoc Huynh, A. Braytee, and R. Taghipour, "Effect of phase change material on temperature in a room fitted with a windcatcher," in *ASME International Mechanical Engineering Congress and Exposition, Proceedings (IMECE)*, 2019. doi: 10.1115/IMECE2019-10553.

[53]   A. B. A.-A. Dhafer Al-Shamkhee Ali H.A. Al-Waeli Ghaith Yahay Abusaibaa Hazim Moria, "Passive cooling techniques for ventilation: an

updated review," *Renew. Energy Environ. Sustain*, vol. 7, no. 23, pp. 1–16, 2022.

[54] I. Oropeza-Perez and P. A. Østergaard, "Active and passive cooling methods for dwellings: A review," *Renewable and Sustainable Energy Reviews*, vol. 82, pp. 531–544, 2018, doi: https://doi.org/10.1016/j.rser.2017.09.059.

[55] B. Givoni, "Indoor temperature reduction by passive cooling systems," *Solar Energy*, vol. 85, no. 8, pp. 1692–1726, Aug. 2011, doi: 10.1016/J.SOLENER.2009.10.003.

[56] A. Al-Saggaf, H. Nasir, and M. Taha, "Quantitative approach for evaluating the building design features impact on cooling energy consumption in hot climates," *Energy Build*, vol. 211, 2020, doi: 10.1016/j.enbuild.2020.109802.

[57] K. Kosutova, T. van Hooff, C. Vanderwel, B. Blocken, and J. Hensen, "Cross-ventilation in a generic isolated building equipped with louvers: Wind-tunnel experiments and CFD simulations," *Build Environ*, vol. 154, pp. 263–280, 2019.

[58] ASHRAE-Standard55, *Thermal Environmental Conditions for Human Occupancy: ANSI/ASHRAE Standard 55-2017 (Supersedes ANSI/ASHRAE Standard 55-2013) Includes ANSI/ASHRAE Addenda Listed in Appendix N*. ASHRAE, 2017.

[59] D. Darko, K. A. Adjei, S. N. Odai, E. Obuobie, R. Asmah, and D. Trolle, "Recent climate trends for the Volta Basin in West Africa.," 2019.

[60] Global Center on Adaptation, "GCA State and Trends in Adaptation 2022 Climate Risks in Africa.," 2022.

[61] A. Albatayneh, D. Alterman, A. Page, and B. Moghtaderi, "The Impact of the Thermal Comfort Models on the Prediction of Building Energy

Consumption," *Sustainability*, vol. 10, no. 10, 2018, doi: 10.3390/su10103609.

[62] D. K. Bhamare, M. K. Rathod, and J. Banerjee, "Passive cooling techniques for building and their applicability in different climatic zones—The state of art," *Energy Build*, vol. 198, pp. 467–490, 2019, doi: https://doi.org/10.1016/j.enbuild.2019.06.023.

[63] M. Santamouris and D. Kolokotsa, "Passive cooling dissipation techniques for buildings and other structures: The state of the art," *Energy Build*, vol. 57, pp. 74–94, Feb. 2013, doi: 10.1016/J.ENBUILD.2012.11.002.

[64] N. B. Geetha and R. Velraj, "Passive cooling methods for energy efficient buildings with and without thermal energy storage–A review," *Energy Education Science and Technology Part A: Energy Science and Research*, vol. 29, no. 2, pp. 913–946, 2012.

[65] M. I. M. Azmi, N. A. C. Sidik, Y. Asako, W. M. A. A. Japar, N. M. Muhammad, and N. Razali, "Numerical Studies on PCM Phase Change Performance in Bricks for Energy-Efficient Building Application–A Review," *Journal of Advanced Research in Numerical Heat Transfer*, vol. 1, no. 1, pp. 13–21, 2020.

[66] B. Duraković, *PCM-Based Building Envelope Systems: Innovative Energy Solutions for Passive Design*. Springer Nature, 2020.

[67] Z. Emdadi, A. Maleki, M. Mohammad, N. Asim, and M. Azizi, "Coupled Evaporative and Desiccant Cooling Systems for Tropical Climate," *International Journal of Environmental Science*, vol. 2, 2017.

[68] L. Lai, X. Wang, G. Kefayati, and E. Hu, "Performance evaluation of a solar powered solid desiccant evaporative cooling system with different recirculation air ratios," *Energy Build*, vol. 270, p. 112273, 2022.

[69] D. G. L. Samuel, S. M. S. Nagendra, and M. P. Maiya, "Passive alternatives to mechanical air conditioning of building: A review," *Build Environ*, vol. 66, pp. 54–64, 2013, doi: https://doi.org/10.1016/j.buildenv.2013.04.016.

[70] B. Riangvilaikul and S. Kumar, "An experimental study of a novel dew point evaporative cooling system," *Energy Build*, vol. 42, no. 5, pp. 637–644, 2010.

[71] X. Ma, W. Shi, and H. Yang, "Improving the performance of indirect evaporative cooler for energy recovery from the perspective of nozzle configuration: A CFD model analysis," *Journal of Building Engineering*, vol. 76, p. 107195, Oct. 2023, doi: 10.1016/J.JOBE.2023.107195.

[72] J. M. Wu, X. Huang, and H. Zhang, "Numerical investigation on the heat and mass transfer in a direct evaporative cooler," *Appl Therm Eng*, vol. 29, no. 1, pp. 195–201, 2009.

[73] J. M. Wu, X. Huang, and H. Zhang, "Theoretical analysis on heat and mass transfer in a direct evaporative cooler," *Appl Therm Eng*, vol. 29, no. 5–6, pp. 980–984, 2009.

[74] Y. Fan, L. Luo, and B. Souyri, "Review of solar sorption refrigeration technologies: Development and applications," *Renewable and sustainable energy reviews*, vol. 11, no. 8, pp. 1758–1775, 2007.

[75] M. H. Hayden *et al.*, "Microclimate and human factors in the divergent ecology of Aedes aegypti along the Arizona, US/Sonora, MX border," *Ecohealth*, vol. 7, pp. 64–77, 2010.

[76] H. Paschold, W.-W. Li, H. Morales, and J. Walton, "Laboratory study of the impact of evaporative coolers on indoor PM concentrations," *Atmos Environ*, vol. 37, no. 8, pp. 1075–1086, 2003.

[77] A. Heidari, R. Roshandel, and V. Vakiloroaya, "An innovative solar assisted desiccant-based evaporative cooling system for co-production of water and cooling in hot and humid climates," *Energy Convers Manag*, vol. 185, pp. 396–409, 2019.

[78] A. Aili, X. Yin, and R. Yang, "Passive sub-ambient cooling: radiative cooling versus evaporative cooling," *Appl Therm Eng*, vol. 202, p. 117909, Feb. 2022, doi: 10.1016/J.APPLTHERMALENG.2021.117909.

[79] E. Katramiz, H. Al Jebaei, S. Alotaibi, W. Chakroun, N. Ghaddar, and K. Ghali, "Sustainable cooling system for Kuwait hot climate combining diurnal radiative cooling and indirect evaporative cooling system," *Energy*, vol. 213, p. 119045, Dec. 2020, doi: 10.1016/J.ENERGY.2020.119045.

[80] Suhendri, M. Hu, Y. Su, J. Darkwa, and S. Riffat, "Implementation of passive radiative cooling technology in buildings: A review," *Buildings*, vol. 10, no. 12, p. 215, 2020.

[81] F. Kreith and W. Z. Black, "Basic heat transfer.," 1980, doi: 10.1201/9780429445903-2.

[82] Suhendri, M. Hu, Y. Su, J. Darkwa, and S. Riffat, "Implementation of passive radiative cooling technology in buildings: A review," 2020. doi: 10.3390/buildings10120215.

[83] M. Wellons, "The Stefan-Boltzmann Law," *Physics Department, The College of Wooster, Wooster, Ohio*, vol. 44691, p. 25, 2007.

[84] M. Zeyghami, D. Y. Goswami, and E. Stefanakos, "A review of clear sky radiative cooling developments and applications in renewable power systems and passive building cooling," *Solar Energy Materials and Solar Cells*, vol. 178, pp. 115–128, 2018.

[85]   K. Panchabikesan, K. Vellaisamy, and V. Ramalingam, "Passive cooling potential in buildings under various climatic conditions in India," *Renewable and Sustainable Energy Reviews*, vol. 78, pp. 1236–1252, 2017.

[86]   R. Tang, Y. Etzion, and I. A. Meir, "Estimates of clear night sky emissivity in the Negev Highlands, Israel," *Energy Convers Manag*, vol. 45, no. 11–12, pp. 1831–1843, 2004.

[87]   S. Wijewardane and D. Y. Goswami, "A review on surface control of thermal radiation by paints and coatings for new energy applications," *Renewable and Sustainable Energy Reviews*, vol. 16, no. 4, pp. 1863–1873, 2012.

[88]   E. M. Saber, K. W. Tham, and H. Leibundgut, "A review of high temperature cooling systems in tropical buildings," *Build Environ*, vol. 96, pp. 237–249, 2016.

[89]   E. M. Saber, R. Iyengar, M. Mast, F. Meggers, K. W. Tham, and H. Leibundgut, "Thermal comfort and IAQ analysis of a decentralized DOAS system coupled with radiant cooling for the tropics," *Build Environ*, vol. 82, pp. 361–370, Dec. 2014, doi: 10.1016/J.BUILDENV.2014.09.001.

[90]   P. Rumsey and J. Weale, "Chilled beams in labs: eliminating reheat & saving energy on a budget," *ASHRAE J*, vol. 49, no. 1, p. 18, 2007.

[91]   G. Sastry, "VAV vs. radiant: side-by-side comparison," *ASHRAE J*, vol. 56, no. 5, p. 16, 2014.

[92]   M. Santamouris, *Advances in passive cooling*. Routledge, 2012.

[93]   B. Givoni, *Passive low energy cooling of buildings*. John Wiley & Sons, 1994.

[94] S. F. Ahmed, M. T. O. Amanullah, M. M. K. Khan, M. G. Rasul, and N. M. S. Hassan, "Parametric study on thermal performance of horizontal earth pipe cooling system in summer," *Energy Convers Manag*, vol. 114, pp. 324–337, 2016.

[95] Z. Chen, J. Li, G. Tang, J. Zhang, D. Zhang, and P. Gao, "High-efficiency heating and cooling technology with embedded pipes in buildings and underground structures: A review," *Renewable and Sustainable Energy Reviews*, vol. 192, p. 114209, 2024.

[96] T. Arghand, *Direct ground cooling systems for office buildings*. Chalmers Tekniska Hogskola (Sweden), 2021.

[97] R. B. Adrian R. Katili Robin Wilson, "Space Cooling in Buildings in hot and humid climates – a review of the effect of humidity on the applicability of existing cooling techniques," *SET 2015*, 2015, doi: 10.13140/RG.2.1.3011.5287.

[98] S. S. Bharadwaj and N. K. Bansal, "Temperature distribution inside ground for various surface conditions," *Build Environ*, vol. 16, no. 3, pp. 183–192, 1981.

[99] X. Gao, Z. Zhang, and Y. Xiao, "Modelling and thermo-hygrometric performance study of an underground chamber with a long vertical earth-air heat exchanger system," *Appl Therm Eng*, vol. 180, p. 115773, 2020.

[100] A. M. B. Domingues, E. S. B. Nóbrega, J. V. A. Ramalho, R. S. Brum, and R. S. Quadros, "Parameter analysis of Earth-air heat exchangers over multi-layered soils in South Brazil," *Geothermics*, vol. 93, p. 102074, 2021.

[101] K. K. Agrawal, R. Misra, T. Yadav, G. Das Agrawal, and D. K. Jamuwa, "Experimental study to investigate the effect of water impregnation on thermal performance of earth air tunnel heat exchanger for summer

cooling in hot and arid climate," *Renew Energy*, vol. 120, pp. 255–265, 2018.

[102] J. Vaz, M. A. Sattler, E. D. dos Santos, and L. A. Isoldi, "Experimental and numerical analysis of an earth–air heat exchanger," *Energy Build*, vol. 43, no. 9, pp. 2476–2482, 2011.

[103] A. A. Serageldin, A. K. Abdelrahman, and S. Ookawara, "Earth-Air Heat Exchanger thermal performance in Egyptian conditions: Experimental results, mathematical model, and Computational Fluid Dynamics simulation," *Energy Convers Manag*, vol. 122, pp. 25–38, 2016.

[104] P. Hollmuller and B. Lachal, "Cooling and preheating with buried pipe systems: monitoring, simulation and economic aspects," *Energy Build*, vol. 33, no. 5, pp. 509–518, 2001.

[105] W. R. Van Wijk and D. A. De Vries, "Periodic temperature variations in a homogeneous soil," *Physics of plant environment*, vol. 1, pp. 103–143, 1963.

[106] S. T. A. Siddique, S. F. Ahmed, and M. H. Islam, "Earth Pipe Cooling Strategy in Buildings: A Sustainable Approach," *Journal of Natural Sciences Research* , 2018.

[107] J. Gao, A. Li, X. Xu, W. Gang, and T. Yan, "Ground heat exchangers: Applications, technology integration and potentials for zero energy buildings," *Renew Energy*, vol. 128, pp. 337–349, Dec. 2018, doi: 10.1016/J.RENENE.2018.05.089.

[108] G. Sharan and R. Jadhav, "Performance of single pass earth-tube heat exchanger: An experimental study," *Journal of Agricultural Engineering*, vol. 40, no. 1, pp. 1–8, 2003.

[109] Y. Man, H. Yang, J. D. Spitler, and Z. Fang, "Feasibility study on novel hybrid ground coupled heat pump system with nocturnal cooling radiator

for cooling load dominated buildings," *Appl Energy*, vol. 88, no. 11, pp. 4160–4171, 2011.

[110] M. S. Uddin, R. Ahmed, and M. Rahman, "Performance evaluation and life cycle analysis of earth to air heat exchanger in a developing country," *Energy Build*, vol. 128, pp. 254–261, 2016.

[111] H. Zhang *et al.*, "A critical review of combined natural ventilation techniques in sustainable buildings," *Renewable and Sustainable Energy Reviews*, vol. 141, p. 110795, May 2021, doi: 10.1016/J.RSER.2021.110795.

[112] J. Atkinson, "Natural ventilation for infection control in health-care settings," 2009.

[113] H. Awbi, "Basic concepts for natural ventilation of buildings," in *CIBSE BSG Seminar: Natural and Mixed-Mode Ventilation Modelling*, 2010.

[114] H. B. Awbi, *Ventilation of buildings*. Routledge, 2002.

[115] N. Monghasemi and A. Vadiee, "A review of solar chimney integrated systems for space heating and cooling application," *Renewable and Sustainable Energy Reviews*, vol. 81, pp. 2714–2730, 2018, doi: https://doi.org/10.1016/j.rser.2017.06.078.

[116] H. M. Maghrabie *et al.*, "A review of solar chimney for natural ventilation of residential and non-residential buildings," *Sustainable Energy Technologies and Assessments*, vol. 52, p. 102082, Aug. 2022, doi: 10.1016/J.SETA.2022.102082.

[117] D. J. Harris and N. Helwig, "Solar chimney and building ventilation," *Appl Energy*, vol. 84, no. 2, pp. 135–146, 2007.

[118] X. Jianliu and L. Weihua, "Study on solar chimney used for room natural ventilation in Nanjing," *Energy Build*, vol. 66, pp. 467–469, Nov. 2013, doi: 10.1016/J.ENBUILD.2013.07.036.

[119] A. A. Imran, J. M. Jalil, and S. T. Ahmed, "Induced flow for ventilation and cooling by a solar chimney," *Renew Energy*, vol. 78, pp. 236–244, Jun. 2015, doi: 10.1016/J.RENENE.2015.01.019.

[120] U. Drori, V. Dubovsky, and G. Ziskind, "Experimental verification of induced ventilation," *Journal of Environmental Engineering*, vol. 131, no. 5, pp. 820–826, 2005.

[121] L. Shi, G. Zhang, W. Yang, D. Huang, X. Cheng, and S. Setunge, "Determining the influencing factors on the performance of solar chimney in buildings," *Renewable and Sustainable Energy Reviews*, vol. 88, Mar. 2018, doi: 10.1016/j.rser.2018.02.033.

[122] L. Shi, "Impacts of wind on solar chimney performance in a building," *Energy*, vol. 185, pp. 55–67, Oct. 2019, doi: 10.1016/J.ENERGY.2019.07.056.

[123] L. de O. Neves and F. Marques da Silva, "Simulation and measurements of wind interference on a solar chimney performance," *Journal of Wind Engineering and Industrial Aerodynamics*, vol. 179, pp. 135–145, Aug. 2018, doi: 10.1016/J.JWEIA.2018.05.020.

[124] A. Prozuments, A. Borodinecs, G. Bebre, and D. Bajare, "A Review on Trombe Wall Technology Feasibility and Applications," *Sustainability*, vol. 15, p. 3914, Feb. 2023, doi: 10.3390/su15053914.

[125] I. Blasco Lucas, L. Hoesé, and D. Pontoriero, "Experimental study of passive systems thermal performance," *Renew Energy*, vol. 19, no. 1–2, pp. 39–45, Jan. 2000, doi: 10.1016/S0960-1481(99)00013-0.

[126] G. Gan, "A parametric study of Trombe walls for passive cooling of buildings," *Energy Build*, vol. 27, no. 1, pp. 37–43, Feb. 1998, doi: 10.1016/S0378-7788(97)00024-8.

[127] P. Bevilacqua, R. Bruno, J. Szyszka, D. Cirone, and A. Rollo, "Summer and winter performance of an innovative concept of Trombe wall for residential buildings," *Energy*, vol. 258, p. 124798, Nov. 2022, doi: 10.1016/J.ENERGY.2022.124798.

[128] H. Omrany, A. Ghaffarianhoseini, A. Ghaffarianhoseini, K. Raahemifar, and J. Tookey, "Application of passive wall systems for improving the energy efficiency in buildings: A comprehensive review," *Renewable and sustainable energy reviews*, vol. 62, pp. 1252–1269, 2016.

[129] N. Ghrab-Morcos, C. Bouden, and R. Franchisseur, "Overheating caused by passive solar elements in Tunis. Effectiveness of some ways to prevent it," *Renew Energy*, vol. 3, no. 6–7, pp. 801–811, Sep. 1993, doi: 10.1016/0960-1481(93)90088-X.

[130] P. Raman, S. Mande, and V. V. N. Kishore, "A passive solar system for thermal comfort conditioning of buildings in composite climates," *Solar Energy*, vol. 70, no. 4, pp. 319–329, Jan. 2001, doi: 10.1016/S0038-092X(00)00147-X.

[131] S. Jaber and S. Ajib, "Optimum design of Trombe wall system in mediterranean region," *Solar Energy*, vol. 85, no. 9, pp. 1891–1898, Sep. 2011, doi: 10.1016/J.SOLENER.2011.04.025.

[132] F. Stazi, A. Mastrucci, and C. di Perna, "Trombe wall management in summer conditions: An experimental study," *Solar Energy*, vol. 86, no. 9, pp. 2839–2851, 2012.

[133] Z. Charqui, M. Boukendil, L. El Moutaouakil, R. Hidki, Z. Zrikem, and A. Abdelbaki, "Simulation and optimization of the thermal behavior of a Trombe wall under unsteady conditions," *Mater Today Proc*, vol. 72, pp. 3780–3785, Jan. 2023, doi: 10.1016/J.MATPR.2022.09.375.

[134] C. Song, G. Duan, D. Wang, Y. Liu, H. Du, and G. Chen, "Study on the influence of air velocity on human thermal comfort under non-uniform

thermal environment," *Build Environ*, vol. 196, p. 107808, Jun. 2021, doi: 10.1016/J.BUILDENV.2021.107808.

[135] B. R. Hughes and C. M. Mak, "A study of wind and buoyancy driven flows through commercial wind towers," *Energy Build*, vol. 43, no. 7, pp. 1784–1791, Jul. 2011, doi: 10.1016/J.ENBUILD.2011.03.022.

[136] A. Pfeiffer, V. Dorer, and A. Weber, "Modelling of cowl performance in building simulation tools using experimental data and computational fluid dynamics," *Build Environ*, vol. 43, no. 8, pp. 1361–1372, Aug. 2008, doi: 10.1016/J.BUILDENV.2007.01.038.

[137] N. Khan, Y. Su, and S. B. Riffat, "A review on wind driven ventilation techniques," *Energy Build*, vol. 40, no. 8, pp. 1586–1604, 2008.

[138] D. M. H. Rashid and N. A. Ahmed, "Study of Aerodynamic Forces on a Rotating Wind Driven Ventilator," *Wind Engineering*, vol. 27, no. 1, pp. 63–72, Feb. 2003, doi: 10.1260/030952403321833770.

[139] A. Pfeiffer, V. Dorer, and A. Weber, "Modelling of cowl performance in building simulation tools using experimental data and computational fluid dynamics," *Build Environ*, vol. 43, no. 8, pp. 1361–1372, Aug. 2008, doi: 10.1016/J.BUILDENV.2007.01.038.

[140] G.-Q. He and Y.-T. Tang, "Influence of exhaust wind cowls on wind driven ventilation | 风压通风中排风风帽的影响," *Zhejiang Daxue Xuebao (Gongxue Ban)/Journal of Zhejiang University (Engineering Science)*, vol. 57, no. 3, pp. 591–597, 2023, doi: 10.3785/j.issn.1008-973X.2023.03.017.

[141] L. O. Adekoya, "Wind energy end-use: The performance characteristics of a rotating suction cowl," *Renew Energy*, vol. 2, no. 4–5, pp. 385–389, Aug. 1992, doi: 10.1016/0960-1481(92)90071-A.

[142] E. Monahan, P. Murphy, S. Long, and A. Dowdall, "The effectiveness of passive sumps and static cowls in reducing radon levels in new build Irish dwellings," *J Environ Radioact*, vol. 248, p. 106866, Jul. 2022, doi: 10.1016/J.JENVRAD.2022.106866.

[143] N. Valibeig, S. Nasekhian, and S. Tavakoli, *The Role of Wind Catchers in Improving People's Comfort*. 2014. doi: 10.2495/ARC140091.

[144] E. H. Moghaddam, S. Amindeldar, and A. Besharatizadeh, "New Approach to Natural Ventilation in Public Buildings Inspired by Iranian's Traditional Windcatcher," *Procedia Eng*, vol. 21, pp. 42–52, Jan. 2011, doi: 10.1016/J.PROENG.2011.11.1985.

[145] P. Nejat, H. M. Hussen, F. Fadli, H. N. Chaudhry, J. Calautit, and F. Jomehzadeh, "Indoor Environmental Quality (IEQ) Analysis of a Two-Sided Windcatcher Integrated with Anti-Short-Circuit Device for Low Wind Conditions," *Processes*, vol. 8, no. 7, 2020, doi: 10.3390/pr8070840.

[146] M. Hejazi and B. Hejazi, "Cooling performance of Persian wind towers," in *Proceedings of the 4th International Conference on Harmonisation between Architecture and Nature (Echo-Architecture 2012)*, 2012, pp. 197–207.

[147] M. Rezaeian, H. Montazeri, and R. C. G. M. Loonen, "Science foresight using life-cycle analysis, text mining and clustering: A case study on natural ventilation," *Technol Forecast Soc Change*, vol. 118, pp. 270–280, 2017, doi: https://doi.org/10.1016/j.techfore.2017.02.027.

[148] A. Aryan, Z. Ehsan, S. Amin, and K. Masoud, "Wind Catchers: Remarkable Example of Iranian Sustainable Architecture," *J Sustain Dev*, vol. 3, no. 2, 2010, doi: 10.5539/jsd.v3n2p89.

[149] M. Mazidi, A. Dehghani, and C. Aghanajafi, "Wind towers' role in natural air conditioning and passive cooling of buildings in hot arid regions," *WSEAS Transactions on Fluid Mechanics*, vol. 1, no. 11, p. 959, 2006.

[150] S. Dabiri and A. Moradi, "THE REVIEW OF PERSIAN GARDEN CONCEPT IN TERMS OF ACHIEVING SUSTAINABLE CITY: CASE STUDY OF DOLATABAD GARDEN IN YAZD CITY, IRAN.," *Management Research & Practice*, vol. 6, no. 4, 2014.

[151] F. S. A. Alqatrani, "The old city of Al Zubair. The emergence and physical reality (1571–1882 Iraq)," *Bulletin of Geography. Socio-economic Series*, no. 27, pp. 17–32, 2015.

[152] C. McCabe and S. Roaf, "The wind towers of Bastakiya: assessing the role of the towers in the whole house ventilation system using dynamic thermal modelling," *Archit Sci Rev*, vol. 56, no. 2, pp. 183–194, 2013.

[153] M. N. Bahadori, "Viability of wind towers in achieving summer comfort in the hot arid regions of the Middle East," *Renew Energy*, vol. 5, no. 5–8, pp. 879–892, 1994.

[154] H. Fathy, "Natural energy and vernacular architecture," 1986.

[155] M. Alsailani, H. Montazeri, and A. Rezaeiha, "Towards optimal aerodynamic design of wind catchers: Impact of geometrical characteristics," *Renew Energy*, vol. 168, pp. 1344–1363, May 2021, doi: 10.1016/J.RENENE.2020.12.053.

[156] C. A. Varela-Boydo, S. L. Moya, and R. Watkins, "Analysis of traditional windcatchers and the effects produced by changing the size, shape, and position of the outlet opening," *Journal of Building Engineering*, vol. 33, p. 101828, Jan. 2021, doi: 10.1016/J.JOBE.2020.101828.

[157] P. Nejat and F. Jomehzadeh, "Windcatcher as a Persian sustainable solution for passive cooling," *Civ. Eng. Res. J*, vol. 6, no. 07, 2018.

[158] M. Nasri and R. Hekmatpanah, "Productivity and energy management in desert urban," *World Acad Sci Eng Technol*, vol. 4, no. 9, pp. 379–382, 2010.

[159] P. K. Sahu, "Factors Affecting Wind Tower Efficiency and Modern Design Concepts & Techniques to Increase its Effectiveness," *Journal of Sustainable Construction Engineering and Project Management*, vol. 5, no. 2, Oct. 2022, doi: 10.5281/zenodo.7188811.

[160] M. N. Bahadori, A. Dehghani-Sanij, and A. Sayigh, *Wind Towers*. Springer, 2016.

[161] M. Mahmoudi, "Wind Catcher: An attractive and charming feature of Yazd city Mahnaz mahmuodi (MS)," *The Monthly Scientific Journal of Bagh-e Nazar*, vol. 3, no. 5, pp. 91–99, 2006.

[162] P. S. Ghaemmaghami and M. Mahmoudi, "Wind tower a natural cooling system in Iranian traditional architecture," in *International Conference "Passive and Low Energy Cooling for the Built Environment*, 2005, p. 73.

[163] M. N. Bahadori, "Passive cooling systems in Iranian architecture," in *Renewable Energy*, Routledge, 2018, p. Vol1_87-Vol1_101.

[164] M. N. Bahadori, "An improved design of wind towers for natural ventilation and passive cooling," *Solar energy*, vol. 35, no. 2, pp. 119–129, 1985.

[165] C. Karakatsanis, M. N. Bahadori, and B. J. Vickery, "Evaluation of pressure coefficients and estimation of air flow rates in buildings employing wind towers," *Solar Energy*, vol. 37, no. 5, pp. 363–374, 1986.

[166] W. A. Cunningham and T. L. Thompson, "Passive greenhouse cooling with natural draft cooling towers in combination with solar chimneys," in *Proceedings of the... National Agricultural Plastics Congress (USA)*, 1987.

[167] Y. Prima and S. Prima, "Wind Catcher and Solar Chimney Integrated As An Alternative Ventilation For Urban Dense Settlements In Tropical Climate," *International Journal of Architecture and Urbanism*, vol. 3, no. 1, 2019, doi: 10.32734/ijau.v3i1.773.

[168] B. R. Hughes, J. K. Calautit, and S. A. Ghani, "The development of commercial wind towers for natural ventilation: A review," *Appl Energy*, vol. 92, pp. 606–627, Apr. 2012, doi: 10.1016/J.APENERGY.2011.11.066.

[169] S. Heidari, A. H. Poshtiri, and Z. M. Gilvaei, "Enhancing thermal comfort and natural ventilation in residential buildings: A design and assessment of an integrated system with horizontal windcatcher and evaporative cooling channels," *Energy*, vol. 289, p. 130040, Feb. 2024, doi: 10.1016/J.ENERGY.2023.130040.

[170] A. A. Dehghan, M. K. Esfeh, and M. D. Manshadi, "Natural ventilation characteristics of one-sided wind catchers: experimental and analytical evaluation," *Energy Build*, vol. 61, pp. 366–377, 2013.

[171] M. K. Esfeh, A. A. Dehghan, M. D. Manshadi, and S. Mohagheghian, "Visualized flow structure around and inside of one-sided wind-catchers," *Energy Build*, vol. 55, pp. 545–552, 2012.

[172] A. Zaki and R. Sharma, "Wind-tunnel analysis of turbulent flow in cross-ventilated buildings with windcatchers: Impact of surrounding buildings," *Build Environ*, vol. 244, p. 110826, 2023, doi: https://doi.org/10.1016/j.buildenv.2023.110826.

[173] M. Afshin, A. Sohankar, M. D. Manshadi, and M. K. Esfeh, "An experimental study on the evaluation of natural ventilation performance of a two-sided wind-catcher for various wind angles," *Renew Energy*, vol. 85, pp. 1068–1078, 2016.

[174] M. H. Ghadiri, N. Lukman, N. Ibrahim, and M. F. Mohamed, "Computational analysis of wind-driven natural ventilation in a two sided rectangular wind catcher," *International Journal of Ventilation*, vol. 12, no. 1, pp. 51–62, 2013.

[175] P. Nejat, J. K. Calautit, M. Z. A. Majid, B. R. Hughes, I. Zeynali, and F. Jomehzadeh, "Evaluation of a two-sided windcatcher integrated with wing wall (as a new design) and comparison with a conventional windcatcher," *Energy Build*, vol. 126, pp. 287–300, Aug. 2016, doi: 10.1016/J.ENBUILD.2016.05.025.

[176] A. Zaki, P. Richards, and R. Sharma, "The effect of onset turbulent flows on ventilation with a two-sided rooftop windcatcher," *Journal of Wind Engineering and Industrial Aerodynamics*, vol. 225, p. 104993, 2022, doi: https://doi.org/10.1016/j.jweia.2022.104993.

[177] M. Farouk, "Comparative study of hexagon & square windcatchers using CFD simulations," *Journal of Building Engineering*, vol. 31, p. 101366, 2020, doi: https://doi.org/10.1016/j.jobe.2020.101366.

[178] M. N. Khan and I. Janajreh, "Transevaporative Cooling Performance of a Three-Sided Wind Catcher.," *Jordan Journal of Mechanical & Industrial Engineering*, vol. 11, no. 4, 2017.

[179] H. Montazeri, "Experimental and numerical study on natural ventilation performance of various multi-opening wind catchers," *Build Environ*, vol. 46, no. 2, pp. 370–378, 2011.

[180] S. Soutullo, C. Sanjuan, and M. R. Heras, "Energy performance evaluation of an evaporative wind tower," *Solar Energy*, vol. 86, no. 5, pp. 1396–1410, 2012.

[181] A. A. Elmualim and H. B. Awbi, "Wind tunnel and CFD investigation of the performance of 'Windcatcher' ventilation systems," *International Journal of ventilation*, vol. 1, no. 1, pp. 53–64, 2002.

[182] P. Nejat, F. Jomehzadeh, H. M. Hussen, J. K. Calautit, and M. Z. Abd Majid, "Application of wind as a renewable energy source for passive cooling through windcatchers integrated with wing walls," *Energies (Basel)*, vol. 11, no. 10, 2018, doi: 10.3390/en11102536.

[183] M. N. Bahadori, A. Dehghani-Sanij, and A. Sayigh, *Wind Towers.* Springer, 2016.

[184] H. D. Mohamadabadi, A. H. Ghanbaran, and A. A. Dehghan, "The study of air distribution quality in the summer section of Iranian dry climate houses equipped with wind tower," *Sustain Cities Soc*, vol. 86, p. 104095, Nov. 2022, doi: 10.1016/J.SCS.2022.104095.

[185] M. N. Khan and I. Janajreh, "Transevaporative Cooling Performance of a Three-Sided Wind Catcher.," *Jordan Journal of Mechanical & Industrial Engineering*, vol. 11, no. 4, 2017.

[186] Q. Chen, "Ventilation performance prediction for buildings: A method overview and recent applications," *Build Environ*, vol. 44, no. 4, pp. 848–858, Apr. 2009, doi: 10.1016/J.BUILDENV.2008.05.025.

[187] A. A. Elmualim, "Effect of damper and heat source on wind catcher natural ventilation performance," *Energy Build*, vol. 38, no. 8, pp. 939–948, 2006.

[188] A. Pakari and S. Ghani, "Airflow assessment in a naturally ventilated greenhouse equipped with wind towers: Numerical simulation and wind tunnel experiments," *Energy Build*, vol. 199, pp. 1–11, 2019.

[189] A. Gharakhani, E. Sediadi, M. Roshan, and H. B. Sabzevar, "Experimental study on performance of wind catcher in tropical climate," *ARPN Journal of Engineering and Applied Sciences*, vol. 12, no. 8, 2017.

[190] J. K. Calautit, B. R. Hughes, and S. S. Shahzad, "CFD and wind tunnel study of the performance of a uni-directional wind catcher with heat

transfer devices," *Renew Energy*, vol. 83, 2015, doi: 10.1016/j.renene.2015.04.005.

[191] A. H. Chohan and J. Awad, "Wind Catchers: An Element of Passive Ventilation in Hot, Arid and Humid Regions, a Comparative Analysis of Their Design and Function," 2022. doi: 10.3390/su141711088.

[192] A. R. Dehghani-Sanij, M. Soltani, and K. Raahemifar, "A new design of wind tower for passive ventilation in buildings to reduce energy consumption in windy regions," 2015. doi: 10.1016/j.rser.2014.10.018.

[193] B. Zhang, H. Hu, H. Kikumoto, and R. Ooka, "Turbulence-induced ventilation of an isolated building: Ventilation route identification using spectral proper orthogonal decomposition," *Build Environ*, vol. 223, p. 109471, 2022, doi: https://doi.org/10.1016/j.buildenv.2022.109471.

[194] J. Li, J. Calautit, C. Jimenez-Bescos, and S. Riffat, "Experimental and numerical evaluation of a novel dual-channel windcatcher with a rotary scoop for energy-saving technology integration," *Build Environ*, vol. 230, p. 110018, 2023, doi: https://doi.org/10.1016/j.buildenv.2023.110018.

[195] M. S. Davies Wykes, E. Chahour, and P. F. Linden, "The effect of an indoor-outdoor temperature difference on transient cross-ventilation," *Build Environ*, vol. 168, p. 106447, Jan. 2020, doi: 10.1016/J.BUILDENV.2019.106447.

[196] M. Ghoulem, K. El Moueddeb, E. Nehdi, F. Zhong, and J. Calautit, "Design of a Passive Downdraught Evaporative Cooling Windcatcher (PDEC-WC) System for Greenhouses in Hot Climates," *Energies (Basel)*, vol. 13, no. 11, 2020, doi: 10.3390/en13112934.

[197] M. M. Masrour, M. Abbasi, and H. M. Hallaj, "Study of wind catchers: the mass flow rate and inlet air to the building in traditional wind catchers," *Aust J Basic Appl Sci*, vol. 6, no. 10, pp. 159–165, 2012.

[198] D. O'Connor, "A Novel Heat Recovery Device for Passive Ventilation Systems," University of Sheffield, Sheffield, 2016.

[199] N. K. Bansal, R. Mathur, and M. S. Bhandari, "A study of solar chimney assisted wind tower system for natural ventilation in buildings," *Build Environ*, vol. 29, no. 4, pp. 495–500, Oct. 1994, doi: 10.1016/0360-1323(94)90008-6.

[200] H. F. Nouanégué, L. R. Alandji, and E. Bilgen, "Numerical study of solar-wind tower systems for ventilation of dwellings," *Renew Energy*, vol. 33, no. 3, pp. 434–443, Mar. 2008, doi: 10.1016/J.RENENE.2007.03.001.

[201] F. Jomehzadeh, H. M. Hussen, J. K. Calautit, P. Nejat, and M. S. Ferwati, "Natural ventilation by windcatcher (Badgir): A review on the impacts of geometry, microclimate and macroclimate," *Energy Build*, vol. 226, p. 110396, 2020, doi: https://doi.org/10.1016/j.enbuild.2020.110396.

[202] J. Li, J. Calautit, C. Jimenez-Bescos, and S. Riffat, "Experimental and numerical evaluation of a novel dual-channel windcatcher with a rotary scoop for energy-saving technology integration," *Build Environ*, vol. 230, p. 110018, Feb. 2023, doi: 10.1016/J.BUILDENV.2023.110018.

[203] A. A. Elmualim, "Failure of a control strategy for a hybrid air-conditioning and wind catchers/towers system at Bluewater shopping malls in Kent, UK," *Facilities*, vol. 24, no. 11/12, pp. 399–411, 2006.

[204] B. R. Hughes and S. A. Ghani, "A numerical investigation into the feasibility of a passive-assisted natural ventilation stack device," *International Journal of Sustainable Energy*, vol. 30, no. 4, 2011, doi: 10.1080/1478646X.2010.503275.

[205] Y. Lavafpour and M. Surat, "Passive low energy architecture in hot and dry climate," *Aust J Basic Appl Sci*, vol. 5, no. 8, 2011.

[206] Z. Ji, Y. Su, and N. Khan, "Performance evaluation and energy saving potential of windcatcher natural ventilation systems in China," *International Journal of Architecture, Engineering and Construction*, vol. 1, no. 2, pp. 84–95, 2012.

[207] F. W. H. Yik and Y. F. Lun, "Energy saving by utilizing natural ventilation in public housing in Hong Kong," *Indoor and built Environment*, vol. 19, no. 1, pp. 73–87, 2010.

[208] R. Shanthi Priya, Mc. Sundarraja, and S. Radhakrishnan, "Experimental study on the thermal performance of a traditional house with one-sided wind catcher during summer and winter," *Energy Effic*, vol. 5, pp. 483–496, 2012.

[209] M. H. Ghadiri, N. L. N. Ibrahim, and M. Dehnavi, "The effect of tower height in square plan wind catcher on its thermal behavior," *Aust J Basic Appl Sci*, vol. 5, no. 9, pp. 381–385, 2011.

[210] M. N. Bahadori, "Natural cooling in hot arid regions," *Solar energy application in buildings*, pp. 195–225, 1979.

[211] M. Bahadori, "A passive cooling/heating system for hot arid regions," in *Proceedings of the American Solar Energy Society Conference. Cambridge. Massachusetts*, 1988, pp. 364–367.

[212] M. Bahadori and AR. Pakzad, "Performance Evaluation of New Designs of Wind Towers," in *Proceedings of the ASME 2002 Joint U.S.-European Fluids Engineering Division Conference. Volume 2: Symposia and General Papers, Parts A and B.*, Jul. 2002.

[213] B. R. Hughes, J. K. Calautit, and S. A. Ghani, "The development of commercial wind towers for natural ventilation: A review," *Appl Energy*, vol. 92, pp. 606–627, 2012.

[214] R. J. Issa and B. Chang, "Performance prediction of a multi-stage wind tower for indoor cooling," *Journal of Thermal Science*, vol. 21, no. 4, pp. 327–335, 2012, doi: 10.1007/s11630-012-0551-4.

[215] J. K. Calautit, H. N. Chaudhry, B. R. Hughes, and S. A. Ghani, "Comparison between evaporative cooling and a heat pipe assisted thermal loop for a commercial wind tower in hot and dry climatic conditions," *Appl Energy*, vol. 101, pp. 740–755, 2013.

[216] J. K. Calautit, H. N. Chaudhry, B. R. Hughes, and S. A. Ghani, "Comparison between evaporative cooling and a heat pipe assisted thermal loop for a commercial wind tower in hot and dry climatic conditions," *Appl Energy*, vol. 101, pp. 740–755, 2013.

[217] J. K. Calautit, D. O'Connor, P. Sofotasiou, and B. R. Hughes, "CFD simulation and optimisation of a low energy ventilation and cooling system," *Computation*, vol. 3, no. 2, pp. 128–149, 2014.

[218] J. K. Calautit, B. R. Hughes, and S. S. Shahzad, "CFD and wind tunnel study of the performance of a uni-directional wind catcher with heat transfer devices," *Renew Energy*, vol. 83, pp. 85–99, 2015.

[219] J. K. Calautit, H. N. Chaudhry, B. R. Hughes, and S. A. Ghani, "Comparison between evaporative cooling and a heat pipe assisted thermal loop for a commercial wind tower in hot and dry climatic conditions," *Appl Energy*, vol. 101, pp. 740–755, 2013, doi: https://doi.org/10.1016/j.apenergy.2012.07.034.

[220] S. Koohi-Fayegh and M. A. Rosen, "A review of energy storage types, applications and recent developments," *J Energy Storage*, vol. 27, p. 101047, Feb. 2020, doi: 10.1016/J.EST.2019.101047.

[221] A. Sharma, V. V. Tyagi, C. R. Chen, and D. Buddhi, "Review on thermal energy storage with phase change materials and applications,"

Renewable and Sustainable energy reviews, vol. 13, no. 2, pp. 318–345, 2009.

[222] J. Lin, Q. Zhao, H. Huang, H. Mao, Y. Liu, and Y. Xiao, "Applications of low-temperature thermochemical energy storage systems for salt hydrates based on material classification: A review," *Solar Energy*, vol. 214, pp. 149–178, Jan. 2021, doi: 10.1016/J.SOLENER.2020.11.055.

[223] S. Saha, A. R. Md. Ruslan, A. K. M. Monjur Morshed, and M. Hasanuzzaman, "Global prospects and challenges of latent heat thermal energy storage: a review," *Clean Technol Environ Policy*, vol. 23, no. 2, pp. 531–559, 2021, doi: 10.1007/s10098-020-01997-7.

[224] I. Dincer and M. A. Rosen, *Thermal energy storage: systems and applications*. John Wiley & Sons, 2021.

[225] A. A. Al-Abidi, S. Bin Mat, K. Sopian, M. Y. Sulaiman, and A. T. Mohammed, "CFD applications for latent heat thermal energy storage: a review," *Renewable and sustainable energy reviews*, vol. 20, pp. 353–363, 2013.

[226] K. Faraj, M. Khaled, J. Faraj, F. Hachem, and C. Castelain, "Phase change material thermal energy storage systems for cooling applications in buildings: A review," *Renewable and Sustainable Energy Reviews*, vol. 119, 2020, doi: 10.1016/j.rser.2019.109579.

[227] H. P. Garg, *Solar energy: fundamentals and applications*. Tata McGraw-Hill Education, 2000.

[228] K. Faraj, M. Khaled, J. Faraj, F. Hachem, and C. Castelain, "Phase change material thermal energy storage systems for cooling applications in buildings: A review," *Renewable and Sustainable Energy Reviews*, vol. 119, p. 109579, Mar. 2020, doi: 10.1016/J.RSER.2019.109579.

[229] P. Tatsidjodoung, N. Le Pierrès, and L. Luo, "A review of potential materials for thermal energy storage in building applications," *Renewable and Sustainable Energy Reviews*, vol. 18, pp. 327–349, Feb. 2013, doi: 10.1016/J.RSER.2012.10.025.

[230] C. Prieto, P. Cooper, A. I. Fernández, and L. F. Cabeza, "Review of technology: Thermochemical energy storage for concentrated solar power plants," *Renewable and Sustainable Energy Reviews*, vol. 60, pp. 909–929, Jul. 2016, doi: 10.1016/J.RSER.2015.12.364.

[231] D. Lefebvre and F. H. Tezel, "A review of energy storage technologies with a focus on adsorption thermal energy storage processes for heating applications," *Renewable and Sustainable Energy Reviews*, vol. 67, pp. 116–125, 2017.

[232] P. Tatsidjodoung, N. Le Pierrès, and L. Luo, "A review of potential materials for thermal energy storage in building applications," *Renewable and sustainable energy reviews*, vol. 18, pp. 327–349, 2013.

[233] A. H. Abedin, "A Critical Review of Thermochemical Energy Storage Systems. The Open Renewable Energy Journal, 4 (1), 42–46," 2011.

[234] S. Rashidi, J. A. Esfahani, and A. Rashidi, "A review on the applications of porous materials in solar energy systems," *Renewable and Sustainable Energy Reviews*, vol. 73, pp. 1198–1210, 2017.

[235] P. A. J. Donkers, L. C. Sögütoglu, H. P. Huinink, H. R. Fischer, and O. C. G. Adan, "A review of salt hydrates for seasonal heat storage in domestic applications," *Appl Energy*, vol. 199, pp. 45–68, 2017.

[236] D. Lefebvre and F. H. Tezel, "A review of energy storage technologies with a focus on adsorption thermal energy storage processes for heating applications," *Renewable and Sustainable Energy Reviews*, vol. 67, pp. 116–125, 2017.

[237] K. Wang, J. Y. Wu, R. Z. Wang, and L. W. Wang, "Effective thermal conductivity of expanded graphite–CaCl2 composite adsorbent for chemical adsorption chillers," *Energy Convers Manag*, vol. 47, no. 13–14, pp. 1902–1912, 2006.

[238] S. Mauran, P. Prades, and F. L'haridon, "Heat and mass transfer in consolidated reacting beds for thermochemical systems," *Heat Recovery Systems and CHP*, vol. 13, no. 4, pp. 315–319, 1993.

[239] P. Muthukumar and M. Groll, "Erratum to 'Metal hydride based heating and cooling systems: a review'[International Journal of Hydrogen Energy (2010) 35: 3817–3831]," *Int J Hydrogen Energy*, vol. 35, no. 16, pp. 8816–8829, 2010.

[240] A. Abhat and T. Q. Huy, "Heat and mass transfer considerations in a thermochemicalenergy storage system based on solid-gas reactions," *Solar Energy*, vol. 30, no. 2, pp. 93–98, 1983.

[241] G. Raam Dheep and A. Sreekumar, "Influence of nanomaterials on properties of latent heat solar thermal energy storage materials – A review," *Energy Convers Manag*, vol. 83, pp. 133–148, Jul. 2014, doi: 10.1016/J.ENCONMAN.2014.03.058.

[242] S. Kalaiselvam and R. Parameshwaran, *Thermal energy storage technologies for sustainability: systems design, assessment and applications*. Elsevier, 2014.

[243] A. H Abedin and M. A Rosen, "A critical review of thermochemical energy storage systems," *The open renewable energy journal*, vol. 4, no. 1, 2011.

[244] H. Zhang, J. Baeyens, G. Cáceres, J. Degrève, and Y. Lv, "Thermal energy storage: Recent developments and practical aspects," *Prog Energy Combust Sci*, vol. 53, pp. 1–40, Mar. 2016, doi: 10.1016/J.PECS.2015.10.003.

[245] H. M. Ali *et al.,* "Advances in thermal energy storage: Fundamentals and applications," *Prog Energy Combust Sci*, vol. 100, p. 101109, Jan. 2024, doi: 10.1016/J.PECS.2023.101109.

[246] J. A. Almendros-Ibáñez, M. Fernández-Torrijos, M. Díaz-Heras, J. F. Belmonte, and C. Sobrino, "A review of solar thermal energy storage in beds of particles: Packed and fluidized beds," *Solar Energy*, vol. 192, pp. 193–237, 2019.

[247] Y. B. Tao and Y.-L. He, "A review of phase change material and performance enhancement method for latent heat storage system," *Renewable and Sustainable Energy Reviews*, vol. 93, pp. 245–259, 2018.

[248] D. Lefebvre and F. H. Tezel, "A review of energy storage technologies with a focus on adsorption thermal energy storage processes for heating applications," *Renewable and Sustainable Energy Reviews*, vol. 67, pp. 116–125, Jan. 2017, doi: 10.1016/J.RSER.2016.08.019.

[249] H. Mehling and L. F. Cabeza, "Phase change materials and their basic properties," in *Thermal energy storage for sustainable energy consumption: fundamentals, case studies and design*, Springer, 2007, pp. 257–277.

[250] W. Aftab, A. Usman, J. Shi, K. Yuan, M. Qin, and R. Zou, "Phase change material-integrated latent heat storage systems for sustainable energy solutions," *Energy Environ Sci*, vol. 14, no. 8, pp. 4268–4291, 2021.

[251] A. Kumar and S. K. Shukla, "A review on thermal energy storage unit for solar thermal power plant application," *Energy Procedia*, vol. 74, pp. 462–469, 2015.

[252] A. Aggarwal, N. Goyal, and A. Kumar, "Thermal characteristics of sensible heat storage materials applicable for concentrated solar power

systems," *Mater Today Proc*, vol. 47, pp. 5812–5817, Jan. 2021, doi: 10.1016/J.MATPR.2021.04.174.

[253] A. Abhat, "Short term thermal energy storage," *Revue de physique appliquee*, vol. 15, no. 3, pp. 477–501, 1980.

[254] J. Lizana, R. Chacartegui, A. Barrios-Padura, and J. M. Valverde, "Advances in thermal energy storage materials and their applications towards zero energy buildings: A critical review," *Appl Energy*, vol. 203, pp. 219–239, Oct. 2017, doi: 10.1016/J.APENERGY.2017.06.008.

[255] S. M. Hasnain, "Review on sustainable thermal energy storage technologies, Part I: heat storage materials and techniques," *Energy Convers Manag*, vol. 39, no. 11, pp. 1127–1138, 1998.

[256] C. N. Elias and V. N. Stathopoulos, "A comprehensive review of recent advances in materials aspects of phase change materials in thermal energy storage," *Energy Procedia*, vol. 161, pp. 385–394, Mar. 2019, doi: 10.1016/J.EGYPRO.2019.02.101.

[257] M. K. Rathod and J. Banerjee, "Thermal stability of phase change materials used in latent heat energy storage systems: A review," *Renewable and Sustainable Energy Reviews*, vol. 18, pp. 246–258, Feb. 2013, doi: 10.1016/J.RSER.2012.10.022.

[258] Z. A. A. S. Al-Absi, M. H. M. Isa, and M. Ismail, "Application of phase change materials (PCMs) in building walls: a review," *The Advances in Civil Engineering Materials: Selected Papers of the ICACE 2018 held in Batu Ferringhi, Penang Malaysia on 9th-10th May 2018 2*, pp. 73–82, 2019.

[259] Q. Al-Yasiri and M. Szabó, "Incorporation of phase change materials into building envelope for thermal comfort and energy saving: A comprehensive analysis," *Journal of Building engineering*, vol. 36, p. 102122, 2021.

[260] S. A. Memon, "Phase change materials integrated in building walls: A state of the art review," *Renewable and sustainable energy reviews*, vol. 31, pp. 870–906, 2014.

[261] C. Amaral, R. Vicente, P. Marques, and A. Barros-Timmons, "Phase change materials and carbon nanostructures for thermal energy storage: A literature review," *Renewable and Sustainable Energy Reviews*, vol. 79, pp. 1212–1228, 2017.

[262] F. Kuznik, K. Johannes, and B. Lamrani, "Integrating phase change materials in thermal energy storage systems for buildings," in *Advances in thermal energy storage systems*, Elsevier, 2021, pp. 381–422.

[263] N. Soares, J. J. Costa, A. R. Gaspar, and P. Santos, "Review of passive PCM latent heat thermal energy storage systems towards buildings' energy efficiency," *Energy Build*, vol. 59, pp. 82–103, 2013, doi: https://doi.org/10.1016/j.enbuild.2012.12.042.

[264] R. Baetens, B. P. Jelle, and A. Gustavsen, "Phase change materials for building applications: A state-of-the-art review," *Energy Build*, vol. 42, no. 9, pp. 1361–1368, 2010, doi: https://doi.org/10.1016/j.enbuild.2010.03.026.

[265] W. Xiao, X. Wang, and Y. Zhang, "Analytical optimization of interior PCM for energy storage in a lightweight passive solar room," *Appl Energy*, vol. 86, no. 10, pp. 2013–2018, 2009, doi: https://doi.org/10.1016/j.apenergy.2008.12.011.

[266] H. Mehling and L. F. Cabeza, "Heat and cold storage with PCM," *Heat and mass transfer*, pp. 11–55, 2008.

[267] X. Xu, Y. Zhang, K. Lin, H. Di, and R. Yang, "Modeling and simulation on the thermal performance of shape-stabilized phase change material floor used in passive solar buildings," *Energy Build*, vol. 37, no. 10, pp. 1084–1091, 2005.

[268] C. Barreneche, M. E. Navarro, L. F. Cabeza, and A. I. Fernández, "New database to select phase change materials: Chemical nature, properties, and applications," *J Energy Storage*, vol. 3, pp. 18–24, 2015, doi: https://doi.org/10.1016/j.est.2015.08.003.

[269] F. Kuznik, K. Johannes, and D. David, "13 - Integrating phase change materials (PCMs) in thermal energy storage systems for buildings," in *Advances in Thermal Energy Storage Systems*, L. F. Cabeza, Ed., Woodhead Publishing, 2015, pp. 325–353. doi: https://doi.org/10.1533/9781782420965.2.325.

[270] S. E. Kalnæs and B. P. Jelle, "Phase change materials and products for building applications: A state-of-the-art review and future research opportunities," *Energy Build*, vol. 94, pp. 150–176, 2015.

[271] M. Bimaganbetova, S. A. Memon, and A. Sheriyev, "Performance evaluation of phase change materials suitable for cities representing the whole tropical savanna climate region," *Renew Energy*, vol. 148, pp. 402–416, 2020.

[272] F. Souayfane, F. Fardoun, and P.-H. Biwole, "Phase change materials (PCM) for cooling applications in buildings: A review," *Energy Build*, vol. 129, pp. 396–431, 2016.

[273] L. F. Cabeza, M. Ibanez, C. Sole, J. Roca, and M. Nogues, "Experimentation with a water tank including a PCM module," *Solar Energy Materials and Solar Cells*, vol. 90, no. 9, pp. 1273–1282, 2006.

[274] P. B. Salunkhe and P. S. Shembekar, "A review on effect of phase change material encapsulation on the thermal performance of a system," *Renewable and sustainable energy reviews*, vol. 16, no. 8, pp. 5603–5616, 2012.

[275] K. Ghasemi, S. Tasnim, and S. Mahmud, "PCM, nano/microencapsulation and slurries: A review of fundamentals,

categories, fabrication, numerical models and applications," *Sustainable Energy Technologies and Assessments*, vol. 52, p. 102084, Aug. 2022, doi: 10.1016/J.SETA.2022.102084.

[276] G. Alva, Y. Lin, L. Liu, and G. Fang, "Synthesis, characterization and applications of microencapsulated phase change materials in thermal energy storage: A review," *Energy Build*, vol. 144, pp. 276–294, 2017.

[277] M. M. Farid, A. M. Khudhair, S. A. K. Razack, and S. Al-Hallaj, "A review on phase change energy storage: materials and applications," *Energy Convers Manag*, vol. 45, no. 9, pp. 1597–1615, 2004, doi: https://doi.org/10.1016/j.enconman.2003.09.015.

[278] T. Fiedler, A. Öchsner, I. V Belova, and G. E. Murch, "Thermal conductivity enhancement of compact heat sinks using cellular metals," in *Defect and Diffusion Forum*, Trans Tech Publ, 2008, pp. 222–226.

[279] M. Liu *et al.*, "Preparation of castable phase change materials beads based on millimeter-sized nanocarbon aerogels for thermal energy storage," *Appl Therm Eng*, vol. 174, p. 115319, Jun. 2020, doi: 10.1016/J.APPLTHERMALENG.2020.115319.

[280] H. Shmueli, G. Ziskind, and R. Letan, "Melting in a vertical cylindrical tube: Numerical investigation and comparison with experiments," *Int J Heat Mass Transf*, vol. 53, no. 19–20, pp. 4082–4091, Sep. 2010, doi: 10.1016/J.IJHEATMASSTRANSFER.2010.05.028.

[281] F. Rouault, D. Bruneau, P. Sebastian, and J. Ô. Lopez, "Numerical modelling of tube bundle thermal energy storage for free-cooling of buildings," *Appl Energy*, vol. 111, 2013, doi: 10.1016/j.apenergy.2013.05.055.

[282] R. Albaldawi, Dr. A. Shyaa, and B. M.H.Hammendy, "Experimental Study on the Effect of Insertion of Copper Lessing Rings in Phase

Change Material (PCM) on the Performance of Thermal Energy Storage Unit," *Al-Khwarizmi Engineering Journal*, vol. 11, pp. 60–72, Jun. 2015.

[283] K. Merlin, D. Delaunay, J. Soto, and L. Traonvouez, "Heat transfer enhancement in latent heat thermal storage systems: Comparative study of different solutions and thermal contact investigation between the exchanger and the PCM," *Appl Energy*, vol. 166, pp. 107–116, Mar. 2016, doi: 10.1016/J.APENERGY.2016.01.012.

[284] J. Fukai, Y. Hamada, Y. Morozumi, and O. Miyatake, "Improvement of thermal characteristics of latent heat thermal energy storage units using carbon-fiber brushes: experiments and modeling," *Int J Heat Mass Transf*, vol. 46, no. 23, pp. 4513–4525, 2003.

[285] T. Nomura, C. Zhu, N. Sheng, G. Saito, and T. Akiyama, "Microencapsulation of Metal-based Phase Change Material for High-temperature Thermal Energy Storage," *Sci Rep*, vol. 5, no. 1, p. 9117, 2015, doi: 10.1038/srep09117.

[286] K. S. Raghavan and V. Kumaresan, "Thermal Properties of Natural Graphite Flake Enhanced Phase Change Material from 'T-History' Method," *Int J Thermophys*, vol. 43, no. 3, p. 39, 2022, doi: 10.1007/s10765-021-02957-z.

[287] M. Pramothraj, R. Santosh, M. R. Swaminathan, and G. Kumaresan, "Study of effect of Al and Cu microparticles dispersed in D-Mannitol PCM for effective solar thermal energy storage," *J Therm Anal Calorim*, vol. 139, no. 2, pp. 895–904, 2020, doi: 10.1007/s10973-019-08469-1.

[288] N. Pradeep, K. Paramasivam, T. Rajesh, V. Subash Purusothamanan, and S. Iyahraja, "Silver nanoparticles for enhanced thermal energy storage of phase change materials," *Mater Today Proc*, vol. 45, pp. 607–611, 2021, doi: https://doi.org/10.1016/j.matpr.2020.02.671.

[289] C. K. Oluah, E. T. Akinlabi, and H. O. Njoku, "A Concise Review of Nano-enhanced Phase Change Materials for Passive Cooling Applications in Buildings," *Trends in Manufacturing and Engineering Management: Select Proceedings of ICMechD 2019*, pp. 193–203, 2021.

[290] S. Kahwaji, M. B. Johnson, A. C. Kheirabadi, D. Groulx, and M. A. White, "A comprehensive study of properties of paraffin phase change materials for solar thermal energy storage and thermal management applications," *Energy*, vol. 162, pp. 1169–1182, 2018.

[291] E. Osterman, V. V. Tyagi, V. Butala, N. A. Rahim, and U. Stritih, "Review of PCM based cooling technologies for buildings," 2012. doi: 10.1016/j.enbuild.2012.03.022.

[292] R. Ji, Z. Zou, M. Chen, Y. Zheng, and S. Qu, "Numerical assessing energy performance for building envelopes with phase change material," *Int J Energy Res*, vol. 43, no. 12, pp. 6222–6232, 2019.

[293] S. Kamali, "Review of free cooling system using phase change material for building," *Energy Build*, vol. 80, pp. 131–136, 2014, doi: 10.1016/j.enbuild.2014.05.021.

[294] L. F. Cabeza and A. de Gracia, "Thermal energy storage (TES) systems for cooling in residential buildings," *Advances in Thermal Energy Storage Systems*, pp. 549–572, 2015.

[295] A. Pasupathy, R. Velraj, and R. V Seeniraj, "Phase change material-based building architecture for thermal management in residential and commercial establishments," *Renewable and Sustainable Energy Reviews*, vol. 12, no. 1, pp. 39–64, 2008.

[296] M. Saffari, A. de Gracia, S. Ushak, and L. F. Cabeza, "Passive cooling of buildings with phase change materials using whole-building energy simulation tools: A review," *Renewable and Sustainable Energy Reviews*, vol. 80, pp. 1239–1255, 2017.

[297] L. Yang, X. Jin, Y. Zhang, and K. Du, "Recent development on heat transfer and various applications of phase-change materials," *J Clean Prod*, vol. 287, p. 124432, Mar. 2021, doi: 10.1016/J.JCLEPRO.2020.124432.

[298] Z. A. Al-Absi, M. I. Mohd Hafizal, M. Ismail, A. Mardiana, and A. Ghazali, "Peak indoor air temperature reduction for buildings in hot-humid climate using phase change materials," *Case Studies in Thermal Engineering*, vol. 22, p. 100762, Dec. 2020, doi: 10.1016/J.CSITE.2020.100762.

[299] J. Lizana, M. de-Borja-Torrejon, A. Barrios-Padura, T. Auer, and R. Chacartegui, "Passive cooling through phase change materials in buildings. A critical study of implementation alternatives," *Appl Energy*, vol. 254, 2019, doi: 10.1016/j.apenergy.2019.113658.

[300] Y. Liang, H. Yang, H. Wang, X. Bao, and H. Cui, "Enhancing energy efficiency of air conditioning system through optimization of PCM-based cold energy storage tank: A data center case study," *Energy*, vol. 286, p. 129641, 2024, doi: https://doi.org/10.1016/j.energy.2023.129641.

[301] Y. Hu and P. K. Heiselberg, "A new ventilated window with PCM heat exchanger—Performance analysis and design optimization," *Energy Build*, vol. 169, pp. 185–194, 2018.

[302] H. Weinläder, W. Körner, and B. Strieder, "A ventilated cooling ceiling with integrated latent heat storage—Monitoring results," *Energy Build*, vol. 82, pp. 65–72, 2014.

[303] D. O'connor, J. K. S. Calautit, and B. R. Hughes, "A review of heat recovery technology for passive ventilation applications," 2016. doi: 10.1016/j.rser.2015.10.039.

[304] B. R. Hughes and S. A. A. A. Ghani, "A numerical investigation into the effect of Windvent louvre external angle on passive stack ventilation performance," *Build Environ*, vol. 45, no. 4, pp. 1025–1036, 2010.

[305] J. K. Calautit and B. R. Hughes, "Wind tunnel and CFD study of the natural ventilation performance of a commercial multi-directional wind tower," *Build Environ*, vol. 80, pp. 71–83, 2014, doi: https://doi.org/10.1016/j.buildenv.2014.05.022.

[306] P. Abdo and A. Reyes-Cubas, "Simulation of ventilation flow through a room fitted with a windcatcher incorporating phase change materials," in *American Society of Mechanical Engineers, Fluids Engineering Division (Publication) FEDSM*, 2020. doi: 10.1115/FEDSM2020-20171.

[307] C. Teodosiu, V. Ilie, and R. Teodosiu, "Appropriate CFD turbulence model for improving indoor air quality of ventilated spaces," *Modelling in Civil Environmental Engineering*, vol. 10, no. 4, pp. 28–42, 2014.

[308] F. Menter, R. Lechner, A. A. Germany GmbH Matyushenko, and S. Petersburg, "Best Practice: RANS Turbulence Modeling in Ansys CFD," 2024.

[309] Straw MP, "Computation and measurement of wind induced ventilation," Thesis, University of Nottingham, Nottingham, 2000.

[310] Z. J. Zhai, Z. Zhang, W. Zhang, and Q. Y. Chen, "Evaluation of various turbulence models in predicting airflow and turbulence in enclosed environments by CFD: Part 1—Summary of prevalent turbulence models," *HVAC&R Res*, vol. 13, no. 6, pp. 853–870, 2007.

[311] N. J. Cook, "The designer's guide to wind loading of building structures part 1: background," *Damage survey, wind data and structural classification building research establishment, Garston and Butterworths London*, 1985.

[312] Z. J. Zhai, Z. Zhang, W. Zhang, and Q. Y. Chen, "Evaluation of various turbulence models in predicting airflow and turbulence in enclosed environments by CFD: Part 1—Summary of prevalent turbulence models," *HVAC&R Res*, vol. 13, no. 6, pp. 853–870, 2007.

[313] Z. Zhang, W. Zhang, Z. J. Zhai, and Q. Y. Chen, "Evaluation of various turbulence models in predicting airflow and turbulence in enclosed environments by CFD: Part 2—Comparison with experimental data from literature," *HVAC&R Res*, vol. 13, no. 6, pp. 871–886, 2007.

[314] G. Diarce, Á. Campos-Celador, K. Martin, A. Urresti, A. García-Romero, and J. M. Sala, "A comparative study of the CFD modeling of a ventilated active façade including phase change materials," *Appl Energy*, vol. 126, pp. 307–317, 2014, doi: https://doi.org/10.1016/j.apenergy.2014.03.080.

[315] S. Hussain, P. H. Oosthuizen, and A. Kalendar, "Evaluation of various turbulence models for the prediction of the airflow and temperature distributions in atria," *Energy Build*, vol. 48, pp. 18–28, May 2012, doi: 10.1016/J.ENBUILD.2012.01.004.

[316] A. Fluent, "Fluent 6.3 Documentation," *Fluent Inc., Lebanon, NH*, vol. 63, pp. 64–65, 2006.

[317] P. C. Walsh and W. H. Leong, "Effectiveness of several turbulence models in natural convection," *Int J Numer Methods Heat Fluid Flow*, vol. 14, no. 5, pp. 633–648, 2004.

[318] A. Bekleyen and Y. Melikoğlu, "An investigation on the thermal effects of windcatchers," *Journal of Building Engineering*, vol. 34, p. 101942, 2021, doi: https://doi.org/10.1016/j.jobe.2020.101942.

[319] Y. Su, S. B. Riffat, Y. L. Lin, and N. Khan, "Experimental and CFD study of ventilation flow rate of a Monodraught™ windcatcher," *Energy Build*, vol. 40, no. 6, 2008, doi: 10.1016/j.enbuild.2007.10.001.

[320] J. Calautit, D. O'Connor, S. Shahzad, K. Calautit, and B. Hughes, "Numerical and experimental analysis of a natural ventilation windcatcher with passive heat recovery for mild-cold climates," *Energy Procedia*, vol. 158, pp. 3125–3130, 2019, doi: https://doi.org/10.1016/j.egypro.2019.01.1011.

[321] P. Nejat, J. K. Calautit, M. Z. A. Majid, B. R. Hughes, and F. Jomehzadeh, "Anti-short-circuit device: A new solution for short-circuiting in windcatcher and improvement of natural ventilation performance," *Build Environ*, vol. 105, 2016, doi: 10.1016/j.buildenv.2016.05.023.

[322] J. Li, J. K. Calautit, and C. Jimenez-Bescos, "Experiment and numerical investigation of a novel flap fin louver windcatcher for multi-directional natural ventilation and passive technology integration," *Build Environ*, vol. 242, p. 110429, 2023, doi: https://doi.org/10.1016/j.buildenv.2023.110429.

[323] K. Pelletier and J. Calautit, "Analysis of the performance of an integrated multistage helical coil heat transfer device and passive cooling windcatcher for buildings in hot climates," *Journal of Building Engineering*, vol. 48, p. 103899, 2022, doi: https://doi.org/10.1016/j.jobe.2021.103899.

[324] D. Mumovic, J. Crowther, and Z. Stevanovic, *The effect of Turbulence Models on Numerical Prediction of Air Flow within Street Canyons*. 2004.

[325] C. Teodosiu, V. Ilie, and R. Teodosiu, "Appropriate CFD Turbulence Model for Improving Indoor Air Quality of Ventilated Spaces," *Mathematical Modelling in Civil Engineering*, vol. 10, pp. 28–42, Mar. 2015, doi: 10.2478/mmce-2014-0020.

[326] Q. Chen and W. Xu, "A zero-equation turbulence model for indoor airflow simulation," *Energy Build*, vol. 28, no. 2, pp. 137–144, Oct. 1998, doi: 10.1016/S0378-7788(98)00020-6.

[327] J. Stefan, "Über die Theorie der Eisbildung, insbesondere über die Eisbildung im Polarmeere," *Ann Phys*, vol. 278, no. 2, pp. 269–286, 1891.

[328] J. H. Nazzi Ehms, R. De Césaro Oliveski, L. A. Oliveira Rocha, C. Biserni, and M. Garai, "Fixed Grid Numerical Models for Solidification and Melting of Phase Change Materials (PCMs)," *Applied Sciences*, vol. 9, no. 20, 2019, doi: 10.3390/app9204334.

[329] M. Al-Maghalseh and K. Mahkamov, "Methods of heat transfer intensification in PCM thermal storage systems: Review paper," *Renewable and Sustainable Energy Reviews*, vol. 92, pp. 62–94, 2018, doi: https://doi.org/10.1016/j.rser.2018.04.064.

[330] V. R. Voller, "Fast implicit finite-difference method for the analysis of phase change problems," *Numerical Heat Transfer*, vol. 17, no. 2, pp. 155–169, 1990.

[331] M. Zeneli, A. Nikolopoulos, S. Karellas, and N. Nikolopoulos, "Chapter 7 - Numerical methods for solid-liquid phase-change problems," in *Ultra-High Temperature Thermal Energy Storage, Transfer and Conversion*, A. Datas, Ed., Woodhead Publishing, 2021, pp. 165–199. doi: https://doi.org/10.1016/B978-0-12-819955-8.00007-7.

[332] Y. Cui, "Investigation of Phase Change Material Passive Cooling System for Buildings," Thesis, University of Nottingham, Nottingham, 2014.

[333] V. A. A. Raj and R. Velraj, "Review on free cooling of buildings using phase change materials," *Renewable and Sustainable Energy Reviews*, vol. 14, no. 9, pp. 2819–2829, 2010, doi: https://doi.org/10.1016/j.rser.2010.07.004.

[334] M. Alvarez-Rodriguez, M. Alonso-Martinez, I. Suarez-Ramon, and P. José García-Nieto, "Numerical model for determining the effective heat capacity of macroencapsulated PCM for building applications," *Appl Therm Eng*, vol. 242, p. 122478, Apr. 2024, doi: 10.1016/J.APPLTHERMALENG.2024.122478.

[335] A. Diligenskaya and A. Mandra, "Determination of Space and Time Dependent Function of Internal Heat Source in Heat Conductivity Equation," *Applied Mechanics and Materials*, vol. 698, pp. 668–673, Dec. 2014, doi: 10.4028/www.scientific.net/AMM.698.668.

[336] L. Lin *et al.*, "Numerical study on melting and heat transfer characteristics of vertical cylindrical PCM with a focus on the solid-liquid interface heat transfer rate," *J Energy Storage*, vol. 72, p. 108370, Nov. 2023, doi: 10.1016/J.EST.2023.108370.

[337] V. R. Voller and C. Prakash, "A fixed grid numerical modelling methodology for convection-diffusion mushy region phase-change problems," *Int J Heat Mass Transf*, vol. 30, no. 8, pp. 1709–1719, 1987.

[338] Z. Liu, Y. Yao, and H. Wu, "Numerical modeling for solid–liquid phase change phenomena in porous media: Shell-and-tube type latent heat thermal energy storage," *Appl Energy*, vol. 112, pp. 1222–1232, Dec. 2013, doi: 10.1016/J.APENERGY.2013.02.022.

[339] Chartered Institution of Building Services, *Environmental Design: CIBSE Guide A.* Chartered Institution of Building Services Engineers, 1999.

[340] H. B. Awbi, "Calculation of convective heat transfer coefficients of room surfaces for natural convection," *Energy Build*, vol. 28, no. 2, pp. 219–227, 1998.

[341] H. B. Awbi, *Ventilation of buildings*. Routledge, 2002.

[342] Ansys, *ANSYS FLUENT Theory Guide*, vol. 14.0. Canonsburg: ANSYS, Inc, 2011.

[343] S. Hussain, "NUMERICAL INVESTIGATIONS OF THE INDOOR THERMAL ENVIRONMENT IN ATRIA AND OF THE BUOYANCY-DRIVEN VENTILATION IN A SIMPLE ATRIUM BUILDING," 2012.

[344] S. Vardoulakis, B. E. A. Fisher, K. Pericleous, and N. Gonzalez-Flesca, "Modelling air quality in street canyons: a review," *Atmos Environ*, vol. 37, no. 2, pp. 155–182, 2003, doi: https://doi.org/10.1016/S1352-2310(02)00857-9.

[345] H. W. Coleman and F. Stern, "Uncertainties and CFD code validation," 1997.

[346] J. Franke, A. Hellsten, H. Schlünzen, and B. Carissimo, "The Best Practise Guideline for the CFD simulation of flows in the urban environment: an outcome of COST 732," in *The Fifth International Symposium on Computational Wind Engineering (CWE2010)*, 2010, pp. 1–10.

[347] Rubitherm-GmbH, "Rubitherm-GmbH. PCM RT SERIES: diverse organic PCM," Rubitherm-GmbH.

[348] M. Jurčević, S. Nižetić, M. Arıcı, A. T. Hoang, E. Giama, and A. Papadopoulos, "Thermal constant analysis of phase change nanocomposites and discussion on selection strategies with respect to economic constraints," *Sustainable energy technologies and assessments*, vol. 43, p. 100957, 2021.

[349] P. Rolka, T. Przybylinski, R. Kwidzinski, and M. Lackowski, "Thermal properties of RT22 HC and RT28 HC phase change materials proposed to reduce energy consumption in heating and cooling systems," *Renew Energy*, vol. 197, pp. 462–471, Sep. 2022, doi: 10.1016/J.RENENE.2022.07.080.

[350] J. F. Hinojosa, S. F. Moreno, and V. M. Maytorena, "Low-Temperature Applications of Phase Change Materials for Energy Storage: A Descriptive Review," Apr. 01, 2023, *MDPI*. doi: 10.3390/en16073078.

[351] Batagarawa Amina, "Assessing the thermal performance of phase change materials in composite hot humid/hot dry climates: an examination of office buildings in Abuja-Nigeria.," 2013.

[352] M. Rodríguez-Vázquez, I. Hernández-Pérez, J. Xamán, Y. Chávez, M. Gijón-Rivera, and J. M. Belman-Flores, "Coupling building energy simulation and computational fluid dynamics: An overview," *J Build Phys*, vol. 44, no. 2, pp. 137–180, Sep. 2020, doi: 10.1177/1744259120901840.

[353] D. Groulx, A. Castell, and C. Solé, "Design of latent heat energy storage systems using phase change materials," in *Advances in Thermal Energy Storage Systems*, Elsevier, 2021, pp. 331–357.

[354] Y. Dutil, D. R. Rousse, N. Ben Salah, S. Lassue, and L. Zalewski, "A review on phase-change materials: Mathematical modeling and simulations," *Renewable and Sustainable Energy Reviews*, vol. 15, no. 1, pp. 112–130, 2011, doi: https://doi.org/10.1016/j.rser.2010.06.011.

[355] S. A. Prakash, C. Hariharan, R. Arivazhagan, R. Sheeja, V. A. A. Raj, and R. Velraj, "Review on numerical algorithms for melting and solidification studies and their implementation in general purpose computational fluid dynamic software," *J Energy Storage*, vol. 36, p. 102341, Apr. 2021, doi: 10.1016/J.EST.2021.102341.

[356] A. Fluent, "ANSYSVR [ANSYS Fluent], 15.0, Help System, User's Guide/Theory Guide," *ANSYS, Inc., Canonsburg, PA, http://www. ansys. com/Products/Fluids/ANSYS-Fluent*, 2017.

[357] J. K. Calautit and B. R. Hughes, "Wind tunnel and CFD study of the natural ventilation performance of a commercial multi-directional wind tower," *Build Environ*, vol. 80, pp. 71–83, 2014, doi: 10.1016/j.buildenv.2014.05.022.

[358] J. C. Chang and S. R. Hanna, "Air quality model performance evaluation," *Meteorology and Atmospheric Physics*, vol. 87, no. 1–3, 2004, doi: 10.1007/s00703-003-0070-7.

[359] U. Authentication, "Standard Guide for Statistical Evaluation of Atmospheric Dispersion Model Performance," *Current*, vol. 05, no. Reapproved 2015, 1998.

[360] S. Hanna, D. Strimaitis, and J. Chang, "Hazard response modeling uncertainty (a quantitative method). Volume 1. User's guide for software for evaluating hazardous gas dispersion models. Final report, April 1989April 1991," Jul. 2023.

[361] National Centers for Environmental Information: National Oceanic and Atmospheric Administration (NOAA), "Hourly / Sub-Hourly Observational Data," Version 3.0.0. Accessed: Feb. 02, 2020. [Online]. Available: https://www.ncei.noaa.gov/maps/hourly/

[362] Climatestotravel, "Climates to Travel: World climate guide," 2022. [Online]. Available: https://www.climatestotravel.com/climate/nigeria

[363] Rhinoceros6-Grasshopper, "Rhino 6 Ladybug," 2021, *Rhinoceros6-Grasshopper*: 6.

[364] I. R. Abubakar, "Abuja city profile," *Cities*, vol. 41, pp. 81–91, 2014, doi: https://doi.org/10.1016/j.cities.2014.05.008.

[365] ladybug.tools, "Abuja Weather Data," 2021. [Online]. Available: http://climate.onebuilding.org/WMO_Region_1_Africa/NGA_Nigeria/NGA_FC_Abuja.651250_TMYx.zip

[366] N. C. for E. I. NOAA, "NCEI map application: Observational Data Map of hourly Weather Station Networks from around the world," 2021, *NCEI GIS Agile team*. [Online]. Available: https://gis.ncdc.noaa.gov/maps/ncei/cdo/hourly

[367] A. Sharma, V. V. Tyagi, C. R. Chen, and D. Buddhi, "Review on thermal energy storage with phase change materials and applications," *Renewable and Sustainable Energy Reviews*, vol. 13, no. 2, pp. 318–345, Feb. 2009, doi: 10.1016/J.RSER.2007.10.005.

[368] M. Liu, S. Almazmumi, P. Cao, C. Jimenez-bescos, and J. K. Calautit, "Can windcatcher's natural ventilation beat the chill? A view from heat loss and thermal discomfort," *Build Environ*, vol. 247, p. 110916, 2024, doi: https://doi.org/10.1016/j.buildenv.2023.110916.

[369] J. Franke, A. Hellsten, K. H. Schlünzen, and B. Carissimo, "The COST 732 Best Practice Guideline for CFD simulation of flows in the urban environment: A summary," *Int J Environ Pollut*, vol. 44, no. 1–4, 2011, doi: 10.1504/IJEP.2011.038443.

[370] Esri Demographics Team, "Average Household Size in Nigeria," Oct. 2023, Accessed: May 19, 2024. [Online]. Available: https://hub.arcgis.com/maps/esri::average-household-size-in-nigeria/about

[371] MB-research, "MB-Research - Supplier & Manufacturer of Internationally Comparable Regional Market Data and Digital Borders Worldwide." Accessed: May 19, 2024. [Online]. Available: https://www.mb-research.de/

[372] ANSI/ASHRAE, "ANSI/ASHRAE Addendum p to ANSI/ASHRAE Standard 62.1-2013," 2015. [Online]. Available: www.ashrae.org

[373] K. Peippo, P. Kauranen, and P. D. Lund, "A multicomponent PCM wall optimized for passive solar heating," *Energy Build*, vol. 17, no. 4, pp. 259–270, 1991.

[374] H. Nazir *et al.*, "Recent developments in phase change materials for energy storage applications: A review," *Int J Heat Mass Transf*, vol. 129, pp. 491–523, 2019.

[375] A. Sheriyev, S. A. Memon, I. Adilkhanova, and J. Kim, "Effect of phase change materials on the thermal performance of residential building located in different cities of a tropical rainforest climate zone," *Energies (Basel)*, vol. 14, no. 9, p. 2699, 2021.

[376] J. Lei, J. Yang, and E.-H. Yang, "Energy performance of building envelopes integrated with phase change materials for cooling load reduction in tropical Singapore," *Appl Energy*, vol. 162, pp. 207–217, 2016.

[377] T. D. Canonsburg, "ANSYS fluent user's guide," *ANSYS FLUENT User's Guid*, vol. 15317, p. 2498, 2017.